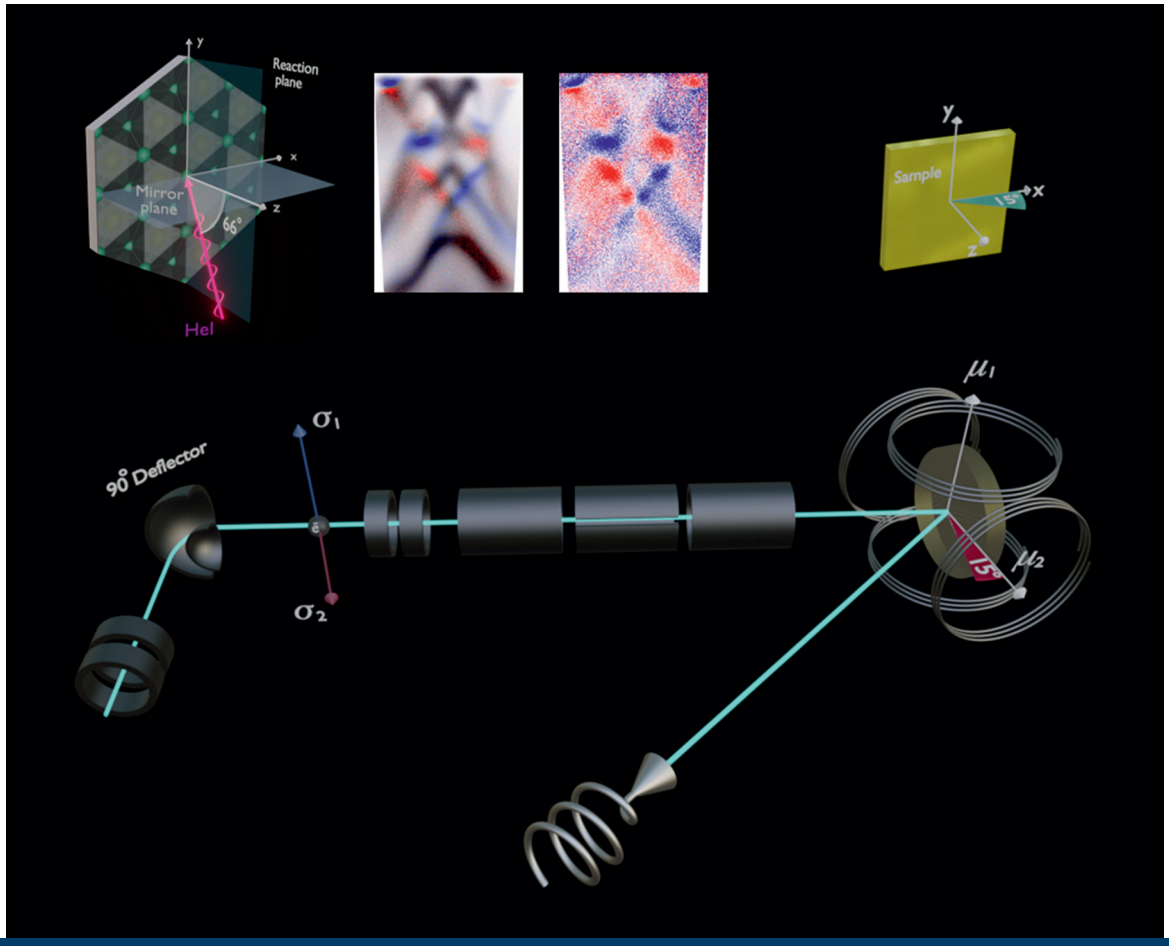

Spin-orbital mixing in the topological ladder of the two-dimensional metal $PtTe_2$

Mohammed Qahosh

Information
Band / Volume 118
ISBN 978-3-95806-872-8

Mitglied der Helmholtz-Gemeinschaft

JÜLICH
Forschungszentrum

Schriften des Forschungszentrums Jülich
Reihe Information / Information Band / Volume 118

Forschungszentrum Jülich GmbH
Peter Grünberg Institut (PGI)
Elektronische Eigenschaften (PGI-6)

Spin-orbital mixing in the topological ladder of the two-dimensional metal $PtTe_2$

Mohammed Qahosh

Schriften des Forschungszentrums Jülich
Reihe Information / Information Band / Volume 118

ISSN 1866-1777 ISBN 978-3-95806-872-8

Bibliografische Information der Deutschen Nationalbibliothek.
Die Deutsche Nationalbibliothek verzeichnet diese Publikation in der
Deutschen Nationalbibliografie; detaillierte Bibliografische Daten
sind im Internet über http://dnb.d-nb.de abrufbar.

Herausgeber und Vertrieb:	Forschungszentrum Jülich GmbH Zentralbibliothek, Verlag 52425 Jülich Tel.: +49 2461 61-5368 Fax: +49 2461 61-6103 zb-publikation@fz-juelich.de www.fz-juelich.de/zb
Umschlaggestaltung:	Grafische Medien, Forschungszentrum Jülich GmbH
Druck:	Grafische Medien, Forschungszentrum Jülich GmbH
Copyright:	Forschungszentrum Jülich 2025

Schriften des Forschungszentrums Jülich
Reihe Information / Information, Band / Volume 118

D 464 (Diss. Duisburg-Essen, Univ., 2025)

ISSN 1866-1777
ISBN 978-3-95806-872-8

Vollständig frei verfügbar über das Publikationsportal des Forschungszentrums Jülich (JuSER)
unter www.fz-juelich.de/zb/openaccess.

Contents

List of Figures

Kurzzusammenfassung

Spinpolarisation ist ein grundlegendes Konzept der Festkörperphysik mit wichtigen Implikationen für die Theorie und die Spintronik. Im Gegensatz zur ladungsbasierten Elektronik nutzt die Spintronik den intrinsischen Spin von Elektronen und ermöglicht dadurch eine schnellere und energieeffizientere Informationsverarbeitung. Die genaue Charakterisierung intrinsischer Spin-Eigenschaften ist jedoch aufgrund von Wechselwirkungen zwischen Anfangszuständen und Endzustandseffekten in Experimenten eine Herausforderung. Diese Arbeit begegnet diesen Herausforderungen durch den Einsatz hochauflösender spin- und winkelaufgelöster Photoemissionsspektroskopie (Spin-ARPES), einer leistungsstarken Methode, die eine umfassende zweidimensionale Abbildung von Spintexturen ermöglicht und somit eine genauere Bewertung intrinsischer Spinkennwerte erlaubt.

Im Mittelpunkt steht $PtTe_2$, ein Typ-II-Dirac-Halbleiter mit topologischen Oberflächenzuständen, die gemeinsam eine sogenannte „topologische Leiterstruktur“ bilden. Durch die Darstellung seiner Spintexturen wird die Natur der Spinpolarisation sichtbar gemacht. $PtTe_2$ besitzt außergewöhnliche Eigenschaften, darunter die höchste elektrische Leitfähigkeit bei Raumtemperatur unter den metallischen Übergangsmetall-Dichalkogeniden. Aufgrund seiner hohen Spin-Orbit-Torque-Effizienz zeigt es außerdem eine erhebliche Spin-Hall-Leitfähigkeit in Dünnschichten und ist damit gut für spintronische Anwendungen im Wafer-Maßstab geeignet.

Verschiedene experimentelle Geometrien wurden eingesetzt, um zu untersuchen, wie Oberflächensymmetrien und Einfallswinkel des Lichts die Spinpolarisation beeinflussen. Trifft das Licht in einer Spiegelebene auf die Probe, stimmen symmetrische Spinpolarisationen mit den berechneten Anfangszuständen überein. In Abwesenheit einer Spiegelebene treten jedoch Asymmetrien in den gemessenen Spintexturen von Oberflächen- und Volumenzuständen auf, die von den Anfangszuständen abweichen.

Einige dieser Asymmetrien sind auf die intrinsisch asymmetrische Kristallstruktur des Volumens zurückzuführen, die durch die Oberflächensensitivität von Spin-ARPES zugänglich ist – insbesondere im Rahmen des Phänomens der „versteckten Spinpolarisation“. Andere entstehen durch geometriebedingte Effekte, bei denen das Fehlen einer relevanten Spiegelebene Phasenverschiebungen im Photoemissions-Matrixelement verursacht. Zusätzlich zeigen Berechnungen, dass durch Spin-Bahn-Kopplung (SOC) induzierte Streuprozesse bis zu 15% der insgesamt beobachteten 50% Spinpolarisation in $PtTe_2$ erklären, je nach experimenteller Geometrie.

Die Ergebnisse erstrecken sich auch auf die verwandte Verbindung $PdTe_2$, bei der ähnliche Effekte auftreten, was die Übertragbarkeit der Methodik unterstreicht. Durch die Klärung von Unstimmigkeiten in Spintexturen liefert diese Arbeit wichtige Erkenntnisse über die Natur der Spinpolarisation und deren Bedeutung für die Entwicklung effizienter spinbasierter Bauelemente. Sie trägt so zum besseren Verständnis intrinsischer Spineigenschaften in SOC-Materialien bei und ebnet den Weg für deren Einsatz in zukünftigen spintronischen Technologien.

Abstract

Spin polarization is a fundamental concept in condensed matter physics, with key implications for theory and spintronics. Unlike charge-based electronics, spintronics exploits electrons' intrinsic spin, enabling faster and more energy-efficient information processing. However, accurately characterizing intrinsic spin properties is challenging due to interactions between initial electronic states and final-state effects during experimental measurements. This thesis addresses these challenges using advanced high-resolution spin- and angle-resolved photoelectron spectroscopy (spin-ARPES), a powerful technique that provides comprehensive two-dimensional mapping of spin textures, allowing for a more accurate assessment of intrinsic spin characteristics across electronic states.

This research focuses on $PtTe_2$, a type-II Dirac semimetal with topological surface states that collectively form a so-called *topological ladder*. By visualizing its spin textures, we highlight the nature of its spin polarization. $PtTe_2$ has exceptional properties, such as the highest room-temperature electrical conductivity among metallic transition metal dichalcogenides. Its high spin-orbit torque efficiency also leads to substantial spin Hall conductivity in thin films, making it well-suited for wafer-scale spintronic applications.

Various experimental geometries were employed to evaluate how surface symmetries and light incidence angles influence spin polarization. When light impinges on the sample within a mirror plane, symmetric spin-polarized maps align with corresponding initial-state calculations. Conversely, asymmetries emerge in measured spin textures of surface and bulk states when a mirror plane is absent, deviating from initial-state predictions.

Some observed asymmetries arise from the intrinsic asymmetric bulk crystal structure, accessible through the surface sensitivity of spin-ARPES, particularly within the hidden spin-polarization phenomenon. Others stem from geometry-related factors, where the absence of a relevant mirror plane introduces phase shifts in the photoemission matrix element, leading to these asymmetries. Additionally, calculations reveal that spin-orbit coupling (SOC) scattering-induced spin polarization accounts for up to 15% of the total observed 50% polarization in $PtTe_2$, that is revealed based on the adapted experimental geometry.

Furthermore, findings extend to the related compound $PdTe_2$, where similar behaviors reinforce the applicability of the developed methodologies. By addressing ambiguities in spin texture observations, this research provides critical insights into the nature of spin polarization and its implications for the efficient design of spin-based devices. Ultimately, this thesis enhances the fundamental understanding of intrinsic spin properties in SOC materials, paving the way for their integration into next-generation spintronic technologies.

1. Introduction

Spin polarization, the alignment of electron spins, is a fundamental concept in condensed matter physics with significant implications for both foundational research and emerging technologies [1, 2]. It underpins phenomena like topological surface states [3] and plays a critical role in the development of spintronics. Unlike conventional electronics, spintronics utilizes the electron's intrinsic spin quantum number rather than its charge [4], enabling the design of high-speed, energy-efficient information technologies [5, 6]. However, accurately characterizing intrinsic spin properties in solids remains challenging. The interplay between initial electronic states and experimental final-state effects complicates data interpretation.

Spin- and angle-resolved photoemission spectroscopy (spin-ARPES) is a powerful technique for exploring the occupied electronic structure of solids by measuring final-state momentum of emitted electrons [7–12]. Despite its advantages, spin-ARPES data interpretation is often hindered by final-state effects, such as interatomic interference from non-equivalent atomic sites and scattering events during photoemission. These effects are particularly pronounced in materials with strong spin-orbit coupling (SOC), where spin mixing of orbital characters and SOC-induced scattering can distort observed spin polarization. Additionally, sample surface symmetries, along with the polarization and incidence angle of light, can introduce extrinsic spin polarization, further complicating the extraction of intrinsic spin textures.

Transition metal dichalcogenides (TMDs), which exhibit strong SOC [13], provide a rich field for exploring these effects. These materials offer tunable electronic properties [14, 15], long spin-life time [16]. Some TMDs that incorporate heavy metals like Mo, W, Pt, and Pd exhibit non-trivial band topologies [17] and show promise as spin-source materials, largely due to their efficient charge-to-spin conversion capabilities [14, 18, 19]. These materials are important candidates for spin-orbit torque (SOT) applications, where SOT-induced magnetization switching is critical to advancing spintronic devices [20–24].

Among TMDs, Pd and Pt selenides and tellurides exhibit a so-called *topological ladder* in the chalcogen-derived p-band manifold [25] with several resulting spin-polarized topological states [19]. In particular, $PtTe_2$ is notable for its high room-temperature electrical conductivity among metallic TMDs [26], and its strong SOT efficiency, yielding substantial spin Hall conductivity in thin-film forms, making it well-suited for wafer-scale spintronic device applications [27]. $PtTe_2$ is also a type-II Dirac semimetal [28, 29], featuring topological surface states (TSSs), part of the *topological ladder*, which exhibit spin-momentum locking akin to topological insulators [30, 31]. While its bulk Dirac node lies below the Fermi level at an approximate binding energy of $E_{binding} \sim 0.1$ eV [29], $PtTe_2$ hosts non-trivial TSSs near the Fermi level, especially along the $\bar{\Gamma} - \bar{M}$ direction in reciprocal space, a property it shares with its sister compound $PdTe_2$ [19]. These Fermi-level-accessible TSSs, exhibit-

ing helical spin textures [32], are likely to impact observable behavior in transport experiments. Given these compelling characteristics, we selected $PtTe_2$ to investigate its spin-resolved band structure, with an emphasis on distinguishing intrinsic initial-state properties from final-state effects in spin-resolved measurements.

Prior research (e.g. [32–42]) has often encountered difficulties in verifying spin textures in momentum space due to limitations in probing specific regions or selected k-points in energy-momentum space. These constraints have sometimes led to ambiguous asymmetries in observed spin textures, such as those noted in Ref. [33], which are often attributed to sample imperfections or final-state effects. Furthermore, incomplete spin reversals between $+\boldsymbol{k}$ and $-\boldsymbol{k}$ momenta, that are not connected by a mirror symmetry as reported in [35], complicate the analysis of intrinsic spin properties. Therefore, the determination of topological properties of these materials requires probing spin-momentum dependence over the full Brillouin zone in order to access the Bloch wave functions, including their spin and orbital characters, as well as phases, that enter the quantum geometric tensor [43, 44].

Recent technological advancements in 2D spin detection, including momentum microscopes [45] and lens-deflector systems in hemispherical analyzers [46], have expanded the capabilities of spin-resolved measurements. These techniques enable comprehensive 2D mapping of photoemission spin textures, visualized as k_x-k_y maps at specific binding energies or as $E(k_{||})$ maps along targeted $k_{||}$ directions. Spin detectors with broader energy and momentum accessibility are instrumental in revealing true initial-state properties in materials. By encompassing a more extensive view of energy-momentum and momentum-momentum space, these advancements reduce the uncertainties associated with measured spin textures of a limited dataset, permitting a more accurate assessment of intrinsic spin textures across electronic states. This capability holds substantial implications for spintronics, where detailed knowledge of spin textures is necessary for the efficient design of spin-based devices. Enhanced measurement accuracy also deepens the fundamental understanding of SOC materials, improving their potential in spin-polarized current applications and advancing the integration of SOC materials into spintronic technologies.

ARPES studies have revealed that the spectra of $PtTe_2$ [29, 32, 47] and related compounds [19, 48–50] feature numerous topological surface states (TSSs) forming a *topological ladder*, However, the precise nature of its spin polarization remains unclear. This thesis utilizes the advanced spin-ARPES spectrometer at the Peter Grünberg Institute 6 of Forschungszentrum Jülich (PGI-6) to visualize the spin textures of the *topological ladder* in $PtTe_2$, to distinguish initial-state properties from final-state effects. By employing different experimental geometries, we examine their influence on the observed spin polarization. One geometry preserves the mirror symmetry of the material, a critical feature that simplifies the system by eliminating asymmetries introduced during the measurement process. This enables direct observation of intrinsic spin configurations: those governed solely by the material's inherent electronic structure and symmetry properties, free from distortions or artifacts caused by experimental conditions. In contrast, the other geometry introduces asymmetries that highlight the influence of final-state effects. This dual-approach goes beyond $PtTe_2$ to provide a more accurate interpretation of measured spin textures and their connection to initial-state properties.

The structure of this thesis is as follows:

Chapter 2 provides an overview of fundamental theoretical concepts related to electronic band structure. Photoemission spectroscopy, the primary technique used in this thesis, is introduced and explained in detail. The chapter also addresses the scattering of hot photoexcited electrons by neighboring atomic potentials during their transit to the detector.

Chapter 3 details the experimental setup of the high-resolution spin-ARPES laboratory at PGI-6. It also includes an overview of the ARPES beamline at the PHELIX end station, which operates in the soft X-ray range at the Solaris National Synchrotron Radiation Center in Kraków, Poland.

Chapter 4 presents spin-integrated ARPES data on bulk $PtTe_2$, acquired using different photon energies ($h\nu$). The orbital character of the $PtTe_2$ valence band is discussed based on 30-layer slab *ab initio* calculations. The effect of light polarization on photoemission intensity is examined within the framework of photoemission matrix elements, comparing results based on the free-electron final state model and the scattering final state model, where the EDAC code [51] was used in the later. This chapter also introduces various experimental geometries, defined by the alignment of the photoemission reaction plane (containing the light incidence direction and the sample surface normal) with the mirror planes of the sample surface. Spin-integrated ARPES data are compared across these geometries: one type of configuration yields symmetric spin-integrated maps, while another displays asymmetries absent in the initial state, as confirmed by theoretical calculations.

Chapter 5 explores the origin of spin polarization in E(k) and (k_x-k_y) maps obtained from spin-ARPES for non-magnetic and centrosymmetric bulk $PtTe_2$. The geometry-based analysis developed in Chapter 3 is applied to spin-resolved measurements. Here, one type of geometry preserves the symmetry of a mirror plane, resulting in symmetric spin-polarized maps, while other geometries produce asymmetric spin-polarized maps that differ from the symmetric initial-state spin textures. Potential sources of these asymmetries are discussed, attributing some of them to the intrinsic crystal structure and others to final-state effects.

Chapters 6, 7 extend the investigation to the sister compounds $PdTe_2$ and $PtSe_2$, respectively, where similar results are observed. This reinforces the feasibility of applying the main methodology of this thesis to ARPES and spin-ARPES studies more broadly, aiding in the separation of initial-state from final-state effects in measured data.

2. Theoretical background

2.1 Electrons in a lattice

An electron in a periodic solid no longer behaves like a free electron in vacuum. Instead it experiences the periodic potential field provided by the atomic ions. Here, I will shortly discuss two simple models used typically to describe electrons in such a crystalline solid. The first model is the *free electron model*: in which valence electrons of the constituent atoms become conduction electrons that obey the Pauli exclusion principle, and move in a three dimensional potential well (simulating the crystal) with infinitely high walls representing the crystal surfaces. These electrons acquire a traveling plane wave $\psi(\boldsymbol{r}) = e^{i\boldsymbol{k}.\boldsymbol{r}}$, that satisfies the free-particle Schrödinger equation $[\frac{\hbar^2}{2m}\nabla^2 + E]\psi(\boldsymbol{r}) = 0$. This suggests a continuous energy range for the electron from zero to infinity as it is shown for the 1D case in Fig. 2.2 (a). However, this model fails to answer some major questions like how to distinguish between metals, semimetals, semiconductors and insulators. The second model which answers the previous question is the *band structure model* which was formulated by Felix Bloch in 1928: it states that the eigenfunction solution of the Schrödinger equation for an electron in a periodic potential can be chosen to have the form of a product of a plane wave $e^{i\boldsymbol{k}.\boldsymbol{r}}$ and a periodic function $u_{n\boldsymbol{k}}(\boldsymbol{r})$ that has the periodicity of the crystal lattice:

$$\psi_{n\boldsymbol{k}}(\boldsymbol{r}) = u_{n\boldsymbol{k}}(\boldsymbol{r}) \cdot e^{i\boldsymbol{k}.\boldsymbol{r}} \tag{2.1}$$

where $u_{n\boldsymbol{k}}(\boldsymbol{r}) = u_{n\boldsymbol{k}}(\boldsymbol{r} + \boldsymbol{R})$; for all translation vectors of the lattice $\boldsymbol{R}$.

Figure 2.1 is a one-dimensional schematic representation showing the lattice potential for a row of atoms (a linear lattice), a periodic function of the lattice periodicity, the real part of a plane wave, and the real part of the Bloch wave function. These Bloch eigenstates are solutions of the Schrödinger equation which considers also the *perturbing periodic potential* $V(\boldsymbol{r}) = V(\boldsymbol{r} + \mathbf{R})$, $\forall$ $\mathbf{R}$:

$$\left(\frac{\hbar^2}{2m}\nabla^2 + \Big[E_n(\boldsymbol{k}) - V(\boldsymbol{r})\Big]\psi_{n\boldsymbol{k}}(\boldsymbol{r})\right) = 0 \tag{2.2}$$

Here, $\boldsymbol{k}$ is the Bloch vector, that is a reciprocal space wave vector in units $\frac{1}{length}$. $E_n(\boldsymbol{k})$ is the energy of the electron which is a continuous function of the Bloch vector $\boldsymbol{k}$, such that this continuous range of energies is referred to as the energy band and labeled by the band index n. The existence of the band index occurs because for a given Bloch vector $\boldsymbol{k}$ there are many independent eigenstates and hence many energy eigenvalues; each refer to a distinct band index n. The number of different Bloch vectors in each band is equal to the number of primitive unit cells

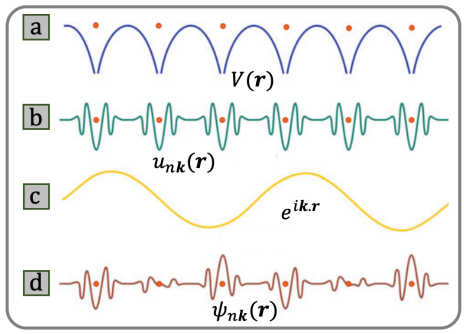

Figure 2.1: **Schematic representation of Bloch eigenstates of a 1D lattice.** (a) The potential energy $V(\boldsymbol{r})$ of a linear lattice. (b) A Bloch periodic function $u_{\boldsymbol{k}}(\boldsymbol{r})$ that has the lattice periodicity. (c) The real part of a plane wave $e^{i\boldsymbol{k}.\boldsymbol{r}}$. (d) Bloch wave function which is a product of (b) and (c). Taken from [52].

in the crystal[1]. Because the energy eigenvalues are periodic in the reciprocal space $E_n(\boldsymbol{k}) = E_n(\boldsymbol{k} + \boldsymbol{G})$, where $\boldsymbol{G}$ is a reciprocal lattice vector, the Bloch vectors are restricted to the first Brillouin zone **BZ** which is a Wigner-Seitz primitive cell in the reciprocal space.

To clarify the capability of the band theory do distinguish between the electronic properties of different materials, a very simplified periodic potential of square well array known as Kronig-Penney potential (shown in the inset of Fig. 2.2 (b) with a,b and V_0 representing the well, the barrier width and the barrier height respectively) can be introduced into Eq.(2.2). Following the math derivation in solid state physics books as in Kittel [53] and the solution of problem number {1} in chapter {**8**} from Ashcroft and Mermin [54], one would get the equation :

$$-\left(\frac{\alpha^2-\beta^2}{2\alpha\beta}\right)sin(\alpha a)sinh(\beta b) + cos(\alpha a)cosh(\beta b) = cos(k(a+b)) \tag{2.3}$$

where $\alpha = \left(\frac{2mE}{\hbar^2}\right)^{\frac{1}{2}}$ and $\beta = \left(\frac{2m(V_\circ - E)}{\hbar^2}\right)^{\frac{1}{2}}$.

When the left-hand side (L.H.S) of Eq.(2.3) is plotted as a function of the electron's kinetic energy E, which is contained in α and β, one can see regions exceeding ± 1 which are the limiting values of the right-hand side (R.H.S), as shown in Fig. 2.2 (b). These regions don't have Bloch-like solutions to the wave equation, hence, forbidden energy regions are formed (*energy gaps*). On the other hand, the gray shaded regions which are within the limits of the allowed range ± 1 represent allowed energy values. A special interesting case is when the periodic potential is reduced to the periodic delta function via reducing the barrier width b$\rightarrow$0 and increasing the barrier height $V_0 \rightarrow \infty$. Then Eq.(2.3) reduces to :

$$\left(\frac{P}{\alpha a}\right)sin(\alpha a) + cos(\alpha a) = cos(ka) \tag{2.4}$$

where $P = \frac{\beta^2 ba}{2}$ is the scattering power of the potential barrier. Similarly, when plotting the L.H.S of Eq.(2.4) as a function of (αa) as shown in Fig. 2.2 (c), allowed

[1]For a 3D crystal that is having (n_1,n_2,n_3) primitive unit cells along ($\boldsymbol{a}$,$\boldsymbol{b}$,$\boldsymbol{c}$) directions in real space, there would be $N = n_1 n_2 n_3$ Bloch vectors and hence each degenerate band would be able to take $2N$ electrons considering the electron spin.

and forbidden regions are formed and interestingly the energy gaps happen at the zones boundaries as indicated which can be explained due to the Bragg reflections. The Bragg condition in one-dimension is $k = \pm\frac{n\pi}{a}$, where a is the lattice constant and n is an integer. At these special wave vectors, traveling waves can not propagate in the lattice, instead a wave traveling to the right will be Bragg-reflected to the left and vice versa, and through successive reflections back and forth a standing wave will be formed.

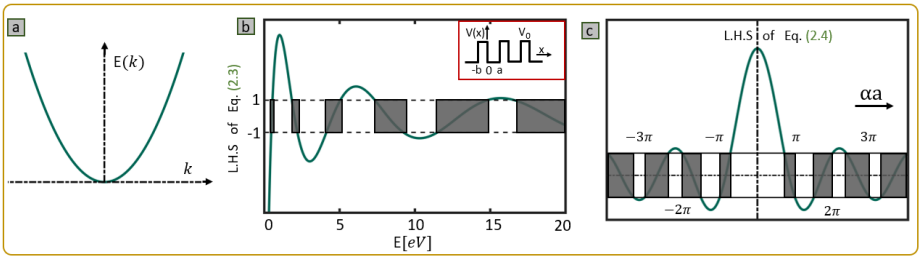

Figure 2.2: **Free electron band dispersion compared to the perturbed case due to the periodic potential of the crystal lattice.**(a) band dispersion $E(k)$ for a free electron in one-dimensional lattice. (b) L.H.S of Eq. (2.3) as a function of E (which is contained in α and β) for a square periodic array shown in the inset and calculated for a=10 Å, b=1.2 Å, and $V_\circ$= 10 eV representing the well, the barrier width and the barrier height respectively. The gray shaded regions represent allowed energy values where the L.H.S is within the limits of the R.H.S ±1. (c) L.H.S of Eq. (2.4) as a function of E, which is a special case of (b) where the periodic potential is reduced to the periodic delta function (b→0 and $V_0 \to \infty$) and the figure was plotted for a barrier scattering power $P = \frac{3\pi}{2}$. Energy gaps happen at Bragg-reflections where standing waves are formed instead of traveling ones in the lattice.

The ground state of a system is achieved through filling subsequently the energy levels with electrons staring with the lowest energy. The energy level filled with the last electron is called the *Fermi energy* E_F. The uppermost completely filled band is called the valence band while the next entirely empty band is called the conduction band. The location of the Fermi energy level is very critical for the optical and electrical properties of the crystal. If E_F level crosses at least a band, the material will be a metal where it will require a small amount of energy to excite an electron from E_F occupied state into an empty state within the same band. On the other hand, if E_F level is located within the previously discussed band gap the material is either a semiconductor or an insulator where the later happens if the energy gap is larger. In this case a large amount of energy is needed in order to lift an electron from a state in the valence band overcoming the energy gap into a state in the conduction band. This manifests the vital rule of the energy gaps which was introduced successfully through the band theory model, unlike the free electron model.

2.2 Spin-orbit coupling

Spin is an angular momentum degree of freedom of the electron which has been recognized as a relativistic effect of quantum mechanics in 1928 by Dirac [55, 56]. Spin-orbit coupling (SOC) is a related relativistic quantum mechanical phenomenon which describes the coupling between the electrons spin and the magnetic field created by the electrons orbital motion. This results because an electron orbiting the nucleus on a trajectory with velocity $\mathbf{v}$ experiences an electric field $\mathbf{E}$ from the potential gradient of the nucleus as a magnetic field $\mathbf{B}$ due to the Lorentz transformation[2][57].

Introducing these relativistic quantum mechanical concepts would predict the fine structure splitting of the energy levels. Using the *non-relativistic* Schrödinger theory in treating non relativistic systems, like the light Hydrogen atom[3], is very successful, however, there are measurable corrections of the order of $(\frac{v}{c})^4$ which have to be put in by hand [58]. This fine structure is partly due to the relativistic variation of mass with velocity, and partly due to the spin of the electron. Now, using the *relativistic* Schrödinger equation (also known as Klein–Gordon equation) would predict the variation of the mass alone for spin-less particles, but would not give correct results for the fine structure, the Zeeman effect and other phenomena which depend on the spin of the electron [59]. Therefore in order to include the effect of the spin-orbit coupling on the quantum mechanical basis, an equation that has the relativity built into it from the beginning is necessary, namely the *Dirac* equation. A thorough derivation of the Dirac theory can be found in quantum mechanics textbooks as refs. [58, 59]. Here I will limit the discussion to show that using the *Dirac equation* emerges the concepts of electrons spin, spin-orbit coupling and other fine structure corrections. Following Shankar [58]:

The **free-particle** *non-relativistic* Schrödinger equation is :

$$i\hbar\frac{\partial\left|\Psi\right\rangle}{\partial t}=\frac{p^2}{2m}\left|\Psi\right\rangle \tag{2.5}$$

Using the Einstein relativistic energy law :

$$\mathcal{H}=(c^2p^2+m^2c^4)^{1/2} \tag{2.6}$$

The corresponding **free-particle** *relativistic* Schrödinger equation is:

$$i\hbar\frac{\partial\left|\Psi\right\rangle}{\partial t}=(c^2p^2+m^2c^4)^{1/2}\left|\Psi\right\rangle \tag{2.7}$$

but this equation treats space and time asymmetrically[4]. One solution is to use

$$\mathcal{H}^2=c^2p^2+m^2c^4 \tag{2.8}$$

[2]Lorentz transformation: $\mathbf{B}=\frac{1}{c}(\mathbf{v}\mathrm{x}\mathbf{E})$. From the electrons frame of reference (rest frame), the nucleus is orbiting the electron inducing an effective magnetic field, $\mathbf{B}$, felt by the electron.

[3]The typical semiclassical velocity is small compared to speed of light; $\frac{v}{c}\sim\frac{1}{137}$ in the ground state [58].

[4]Expanding the square root in equation (2.7): $i\hbar\frac{\partial|\Psi(\mathbf{p},t)\rangle}{\partial t}=mc^2(1+\frac{p^2}{2m^2c^2}-\frac{p^4}{8m^4c^4}+...)\left|\Psi(\mathbf{p},t)\right\rangle$ implies first and second derivative of time and space respectively; $\mathbf{p}=-i\hbar\nabla$ and $p^2=-\hbar^2\nabla^2$.

and using the quantum mechanical operator $\mathbf{p} = -i\hbar\nabla$ to obtain the so called *Klein-Gordon* equation which is the relativistic generalization of the Schrodinger equation:

$$\left(\frac{1}{c^2}\frac{\partial^2}{\partial t^2} - \nabla^2 + \frac{m^2c^2}{\hbar^2}\right)\Psi = 0 \tag{2.9}$$

This equation satisfies the desired symmetry treatment of space and time, but it is of second order. Dirac's idea was to *linearize* this equation supposing the quantity inside the square root in equation (2.6) can be written as a perfect square of a quantity that is linear in $\mathbf{p}$. Hence, ending up with the **free-particle** *linearized relativistic* Schrodinger equation (**free-particle** *Dirac* equation):

$$i\hbar\frac{\partial\,|\Psi\rangle}{\partial t} = (c\boldsymbol{\alpha}\cdot\mathbf{p} + \beta mc^2)\,|\Psi\rangle \tag{2.10}$$

Where, $\boldsymbol{\alpha}$ is a vector of 4×4 matrices, that can be written in terms of the Pauli spin-matrices, $\boldsymbol{\sigma}$, while β is a matrix of same rank, that can be expressed in terms of the 2×2 unit matrix I_2:

$$\boldsymbol{\alpha} = \begin{pmatrix} 0 & \boldsymbol{\sigma} \\ \boldsymbol{\sigma} & 0 \end{pmatrix},\ \beta = \begin{pmatrix} I_2 & 0 \\ 0 & -I_2 \end{pmatrix},\ \sigma_1 = \begin{pmatrix} 0 & 1 \\ 1 & 0 \end{pmatrix},\ \sigma_2 = \begin{pmatrix} 0 & -i \\ i & 0 \end{pmatrix},\ \sigma_3 = \begin{pmatrix} 1 & 0 \\ 0 & -1 \end{pmatrix}.^{5}$$

This implies that the Hamiltonian acts on a four-component wave function Ψ called *Lorentz* spinor, that can be written in terms of two-component spinors called large and small components, ψ and χ respectively; $\Psi = [\psi, \chi]^T$.

Now, coupling to electric ϕ and magnetic $\mathbf{A}$ potentials would be through the following Hamiltonian[6]:

$$\mathcal{H} = [(\mathbf{p} - q\mathbf{A}/c)^2c^2 + m^2c^4]^{\frac{1}{2}} + q\phi \tag{2.11}$$

which gives:

$$i\hbar\frac{\partial\,|\Psi\rangle}{\partial t} = (c\boldsymbol{\alpha}\cdot(\mathbf{p} - q\mathbf{A}/c) + \beta mc^2 + q\phi)\,|\Psi\rangle \tag{2.12}$$

In order to show that the Dirac equation describes a spin-$\frac{1}{2}$ particle we set $\phi = 0$ to get:

$$\mathcal{H}\Psi = (c\boldsymbol{\alpha}\cdot\boldsymbol{\pi} + \beta mc^2)\Psi = E\Psi \quad ; \qquad (\boldsymbol{\pi} = \mathbf{p} - q\mathbf{A}/c) \tag{2.13}$$

Writing $\boldsymbol{\alpha}$ and β explicitly in equation (2.13) we get:

$$\begin{pmatrix} E - mc^2 & -c\boldsymbol{\sigma}\cdot\boldsymbol{\pi} \\ -c\boldsymbol{\sigma}\cdot\boldsymbol{\pi} & E + mc^2 \end{pmatrix}\begin{pmatrix} \psi \\ \chi \end{pmatrix} = \begin{pmatrix} 0 \\ 0 \end{pmatrix} \tag{2.14}$$

ending up with the large and small two-component spinors coupled in the following two equations:

$$(E - mc^2)\psi - (c\boldsymbol{\sigma}\cdot\boldsymbol{\pi})\chi = 0 \tag{2.15}$$

$$(E + mc^2)\chi - (c\boldsymbol{\sigma}\cdot\boldsymbol{\pi})\psi = 0 \tag{2.16}$$

[5] $\boldsymbol{\alpha}$ and β obey these conditions: $\alpha_i^2 = \beta^2$ $(i = 1, 2, 3)$, $\alpha_i\alpha_j + \alpha_j\alpha_i = 0$ $(i \neq j)$, $\alpha_i\beta + \beta\alpha_i = 0$.

[6] This is done via substituting $(\mathbf{p} \Rightarrow \mathbf{p} - \frac{q\mathbf{A}}{c})$ and $(\mathcal{H} \Rightarrow \mathcal{H} - q\phi)$ in Eq.2.5.

Writing the small component χ in term of the large component ψ using equation (2.16) [7], substituting in equation (2.15), retaining only terms up to order $(\frac{v}{c})^2$ and following the simplification done by Shanker [58], we get the equation for the large component only:

$$\left(\frac{(\mathbf{p}-q\mathbf{A}/\mathbf{c})^2}{2m}-\frac{q\hbar}{2mc}\boldsymbol{\sigma}\cdot\mathbf{B}\right)\psi=E_s\psi \tag{2.17}$$

where $-\frac{q\hbar}{2mc}\boldsymbol{\sigma}\cdot\mathbf{B}=-(\frac{g}{2})\frac{q\hbar}{2mc}\boldsymbol{\sigma}\cdot\mathbf{B}=(\frac{g}{2})\frac{e}{mc}\mathbf{S}\cdot\mathbf{B}=-\boldsymbol{\mu}\cdot\mathbf{B}=\mathcal{H}_{int}$

Equation (2.17) manifests that it describes a spin-$\frac{1}{2}$ particle with g-factor=2, and $\mathcal{H}_{int}$ represents the interaction of electron with an external magnetic field.

Now to see the origin of the spin-orbit coupling, we apply the Dirac equation to the case where an electron is affected by a potential :

$$V(r)=e\phi(r)=\frac{-e^2}{r};\qquad\text{(similar to an electron in a Hydrogen atom)} \tag{2.18}$$

This time the coupled equations of the large and small spinor components would be:

$$(E-V-mc^2)\psi-(c\boldsymbol{\sigma}\cdot\mathbf{p})\chi=0 \tag{2.19}$$

$$(E-V+mc^2)\chi-(c\boldsymbol{\sigma}\cdot\mathbf{p})\psi=0 \tag{2.20}$$

Following the same analysis done above i.e. writing the small component in term of the large component using equation (2.20) and substituting in equation (2.19) but this time retaining terms up to order $(\frac{v}{c})^4$ [see Shanker [58] for the details] we get a Hamiltonian for the large spinor component only:

$$\mathcal{H}_{(\psi)}=\underbrace{\frac{\boldsymbol{p}^2}{2m}+V(r)}_{\mathrm{H}^{(o)}}+\underbrace{\frac{\boldsymbol{p}^4}{8m^3c^2}}_{\delta\mathrm{H}_{(relativistic)}}+\underbrace{\frac{1}{2m^2c^2}\frac{1}{r}\frac{\mathrm{d}V(r)}{\mathrm{d}r}\boldsymbol{S}\cdot\boldsymbol{L}}_{\delta\mathrm{H}_{(spin-orbit)}}+\underbrace{\frac{\hbar^2}{8m^2c^2}\nabla^2V(r)}_{\delta\mathrm{H}_{(Darwin)}} \tag{2.21}$$

The first term represents the conventional Hamiltonian, while the second term introduces the relativistic correction due to the change of the mass with velocity. The fourth term , referred to as the Darwin term, which has no classical analogue.

The focal point is the third term (the spin-orbit coupling) which describes the coupling between the spin and the magnetic field created by the electrons orbital motion [57]. This term involves the radial derivative of the potential, indicating that the primary contribution to the spin-orbit coupling occurs near the nucleus. Consequently, SOC is most pronounced for electronic core levels, associated with electrons tightly bound to the core. Additionally, in regions of small radial distances, the potential adopts a Coulomb-like potential ($V(r)=-\frac{Z}{r}$) with a radial derivative proportional to the atomic number Z[8]. Therefore, SOC is expected to be large for

[7] $\chi=\left(\frac{c\boldsymbol{\sigma}\cdot\boldsymbol{\pi}}{E+mc^2}\right)\psi$. The denominator $(E+mc^2)=(E_{Schrödinger}+2mc^2)\cong 2mc^2$; where at low velocities $E_{Schrödinger}\ll mc^2$, and the numerator is of the order mvc. Hence, $|\frac{\phi}{\psi}|\cong\frac{1}{2}(\frac{v}{c})\ll 1$. This clarifies why ψ and ϕ are called large and small components respectively.

[8] In Hydrogen-like atoms the Coulomb potential is $V(r)=\frac{Ze^2}{r}$. For an electron orbiting a nucleus of an atom with atomic number Z, the expectation value of the orbit's radius scales with the atomic number as $\langle r\rangle\propto\frac{1}{z}$: Hence $\delta\mathrm{H}_{(spin-orbit)}\propto\frac{1}{r}\frac{\mathrm{d}V(r)}{\mathrm{d}r}\propto Z^4$ [60].

heavy atoms, but small for lighter ones. This clarifies the presence of heavy atoms in materials characterized by properties derived from spin-orbit coupling. The term involves the scalar product $\boldsymbol{S} \cdot \boldsymbol{L}$, causing the atomic energy levels to split based on the relative orientation of the electron's spin and orbital angular momentum. As an example of such splitting, is the splitting of the p energy level into the two distinct separated levels $p_{3/2}$ and $p_{1/2}$ [61]. The existence of such scalar product means that L_z and m_s are no longer good quantum numbers, however, the total angular momentum quantum number $\boldsymbol{J} = \boldsymbol{L} + \boldsymbol{S}$ is a good quantum number and the SOC term can be written as [62, 63]:

$$\delta \mathrm{H}_{SOC} = \frac{1}{2m^2c^2}\frac{1}{r}\frac{\mathrm{d}V(r)}{\mathrm{d}r}\boldsymbol{S}\cdot\boldsymbol{L} = \frac{a}{2}(j(j+1) - l(l+1-s(s+1))) \tag{2.22}$$

where

$$a = \frac{\hbar^2}{2m^2c^2}\frac{1}{r}\frac{\mathrm{d}V(r)}{\mathrm{d}r} \tag{2.23}$$

Up to this point, the concept of the SOC has been explained on the atomic level. Furthermore, the effect of the SOC extends to crystals, significantly shaping the electronic band structure of solids, despite being a relativistic effect predominantly treated as a weak perturbation. A notable example, is the semiconductor GaAs: within the tight binding picture and neglecting spin, the valence band maximum, at the Γ point, is a degenerate p-orbital character band (with orbital angular momentum l=1). Including the effect of SOC splits the band into a fourfold degenerate $p_{3/2}$ (with a total angular momentum $j = 3/2$) level and a twofold degenerate $p_{1/2}$ (with a total angular momentum $j = 1/2$) level, separated in energy by 0.34 eV of the what so-called *SO-gap* [64, 65]. The impact is thoroughly illustrated in Figure 2.3.

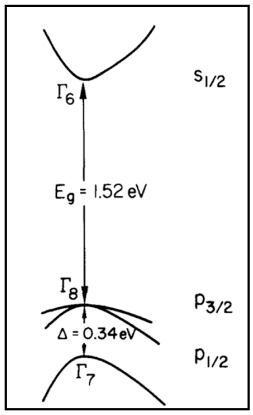

Figure 2.3: **Spin-orbit coupling effect on the band structure of the semiconductor GaAs**. Band structure at the Γ point of GaAs. The SOC splits the valence band maximum into a fourfold degenerate $p_{3/2}$ and a twofold degenerate $p_{1/2}$ energy levels with a *SO-gap* of 0.34 eV. Figure taken from [64].

In the two cases recently examined, namely the atomic and the crystal perspectives, the splittings of the atomic orbitals and bands respectively, resulting from SOC, were based on the total angular momentum quantum number $\boldsymbol{J}$ depending on the relative orientation of the spin $\boldsymbol{S}$ and the orbital angular momentum $\boldsymbol{L}$. However, focusing on the solid state picture, the bands remain degenerate; that is,

they are still occupied with an equal number of electrons with opposite spin polarizations along any quantization axis, canceling out any net spin polarization. This degeneracy arises from the combination of the time reversal symmetry with the real space inversion symmetry of the crystal, a phenomenon known as the *Kramers degeneracy* :

$$\left.\begin{aligned}\text{Time reversal symmetry}(\mathcal{TRS}) : E(\boldsymbol{k},\uparrow) = E(-\boldsymbol{k},\downarrow)\\ \text{Inversion symmetry}(\mathcal{IS}) : E(\boldsymbol{k},\uparrow) = E(-\boldsymbol{k},\uparrow)\end{aligned}\right\} \Rightarrow E(\boldsymbol{k},\uparrow) = E(\boldsymbol{k},\downarrow) \tag{2.24}$$

Equation 2.24 implies that in order to have spin polarized electronic states the degeneracy must be lifted. This can be accomplished by either breaking the time reversal symmetry $\mathcal{TRS}$ or breaking the inversion symmetry of the crystal $\mathcal{IS}$.

2.3 The Rashba effect

In magnetic systems $\mathcal{TRS}$ is inherently broken, allowing for spin-polarized bands. While, in non-magnetic systems, achieving this involves actions such as doping the material with magnetic impurities to induce a magnetic field or through applying an external magnetic field, subsequently breaking $\mathcal{TRS}$. On the other hand, in systems where $\mathcal{TRS}$ is preserved but inversion symmetry $\mathcal{IS}$ is violated, the potential will not be symmetric such that $V(\mathbf{r}) \neq V(-\mathbf{r})$, hence, a non-vanishing potential gradient $\nabla V(\mathbf{r}) \neq 0$ and in turn an electric field $E(\mathbf{r})$ will arise. In the relativistic limit, the electron will experience the electric field as an effective magnetic field $\boldsymbol{B}_{effective}$ through Lorentz transformation and the electron spin $\boldsymbol{S}$ will couple with $\boldsymbol{B}_{effective}$ splitting up the degenerate band into separate spin polarized bands based on the relative orientation of $\boldsymbol{B}_{effective}$ and $\boldsymbol{S}$. This manifists the relativistic SOC origin of the Rashba effect[9]. This coupling term is called Rashba or Bychkov-Rashba Hamiltonian [66, 67]:

$$\mathcal{H}_R = \alpha_R \boldsymbol{\sigma} \cdot (\boldsymbol{p} \times \boldsymbol{E}) = \alpha_R \boldsymbol{\sigma} \cdot (\boldsymbol{k} \times \boldsymbol{E}) = \alpha_R(E) \boldsymbol{\sigma} \cdot (\boldsymbol{k} \times \hat{\boldsymbol{e}}) \tag{2.25}$$

Where the last two equalities apply only for plane wave eigenstates as it is the case for a free 2D electron gas with a potential gradient along the perpendicular direction $\hat{\mathbf{z}}$ [57]. The Rashba parameter α_R represents the effect's strength and depends on the atomic number Z and the symmetry-breaking electric field E [68] as illustrated in note 9. The 2D electron gas picture can be realized in semiconductor heterostuctures, where at the interface in these structures the electrostatics between the nearest atoms create an electric dipole, hence, an effective electric field needed for the Rashba effect [69]. This also extends to surfaces where the periodicity of the crystal potential is truncated[10]. At these boundaries, surface electronic states may form inside bulk energy band gaps and electrons occupying these states are confined on the surface. A prominent example is the surface states of $Au(111)$ [70],

[9] Starting with the SOC Hamiltonian and using a symmetry-breaking surface electric field $E\hat{\mathbf{z}}$: $\delta H_{SOC} = \frac{1}{2m^2c^2}\frac{1}{r}\frac{\mathrm{d}V(r)}{\mathrm{d}r}\boldsymbol{S}\cdot\boldsymbol{L} = \frac{1}{2m^2c^2}\frac{1}{r}\frac{\mathrm{d}V(r)}{\mathrm{d}r}\left(\frac{\hbar}{2}\boldsymbol{\sigma}\right)\cdot(\boldsymbol{r}\times\boldsymbol{p}) = \frac{\hbar}{4m^2c^2}\boldsymbol{\sigma}\cdot\left(\frac{\mathbf{r}}{r}\frac{\mathrm{d}V(r)}{\mathrm{d}r}\times\boldsymbol{p}\right) = \frac{\hbar}{4m^2c^2}\boldsymbol{\sigma}\cdot(\nabla V(r)\times\boldsymbol{p}) = \frac{\hbar}{4m^2c^2}\boldsymbol{\sigma}\cdot(\boldsymbol{p}\times\boldsymbol{E}) = \frac{\hbar^2}{4m^2c^2}\boldsymbol{\sigma}\cdot(\boldsymbol{k}\times\boldsymbol{E}) = \frac{\hbar^2 E}{4m^2c^2}\boldsymbol{\sigma}\cdot(\boldsymbol{k}\times\hat{\boldsymbol{z}}) = \alpha_R(E)\boldsymbol{\sigma}\cdot(\boldsymbol{k}\times\hat{\boldsymbol{z}}) = Eq.2.25$

[10] At the crystal surface, **z** and **-z** belong to two distinct environments: vacuum and the crystal, respectively.

where the spin split surface states are very clearly measured using the photoemission Spin-ARPES method [71].

For a 2D electron gas confined in the (x, y) plane and subject to a symmetry-breaking surface electric field $E\hat{\mathbf{z}}$, the Hamiltonian can be expressed as:

$$\mathcal{H} = \mathcal{H}_{\text{kinetic}} + \mathcal{H}_R = \frac{\boldsymbol{p}^2}{2m^*} + \alpha_R \boldsymbol{\sigma} \cdot (\boldsymbol{k} \times \hat{\boldsymbol{e}}_z) \tag{2.26}$$

where $\mathcal{H}_R$ describes the Rashba SOC as additional contribution to kinetic energy, while m^*, $\boldsymbol{p}$ and $\boldsymbol{k}$ are the electron effective mass, its in-plane *parallel* momentum, and its in-plane wave vector respectively. The corresponding eigenenergies are

$$\mathcal{E}_{\pm}(k) = \frac{\hbar^2 k^2}{2m^*} \pm \alpha_R k = \frac{\hbar^2}{2m^*}(k \pm k_R)^2 - E_R \tag{2.27}$$

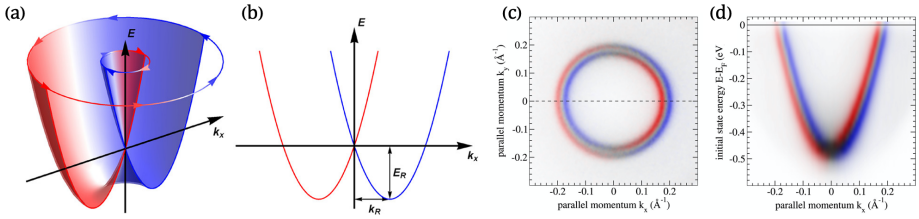

Figure 2.4: **Rashba effect in a structure inversion asymmetric environment.** (a) A schematic illustration 3D view of the spin texture of the Rashba split bands, where the inner band has a clockwise spin chirality while the outer one has a counterclockwise spin chirality for the in-plane S_y-spin component where red (blue) refer for the spin-up (spin-down) component. A 2D view is shown in (b) where E_R and k_R are labeled representing the energy difference and the momentum offset between the high symmetry point $k = 0$ and the vertex of the spin polarized split parabola. (c-d) Experimental realization of the Rashba effect measured using Spin-ARPES from $Au(111)$ surface state excited via p-polarized 6.05 eV photons. (c) Spin and intensity map measured at Fermi energy showing the concentric circles with opposite spin helicity similar to the Fermi energy cut that would have been taken from (a). (d) Spin resolved and intensity band dispersion measured along the dashed line in (c) at $k_y = 0$ in agreement with the schematic illustration (b). Measured spin component is S_y in agreement with the illustration in (a-b). (Figs.(a-b) taken from [72] and Figs.(c-d) from [71]).

The $\pm$ refer to the eigenstates having opposite in-plane spin polarization and are normal to the electron wave vector. This induces helical spin textures in k-space where the spin of the electron is locked to a certain momentum (*spin-momentum locking*). One can see clearly through equation 2.27 (except the high symmetry point $k = 0$) that the initially degenerate free electron parabola will split into two distinct spin polarized parabolas that are shifted by $(k_R = m\alpha_R)$ but in opposite directions for the opposite spin components, while both parabolas are lowered in energy by $\left(E_R = \frac{m\alpha_R^2}{2}\right)$ as illustrated in Fig. 2.4. It is also important to note that the energy difference in the spin-polarized split bands ($\Delta\mathcal{E}$=$\mathcal{E}_+ - \mathcal{E}_-$=$2\alpha_R k$) is linear in k.

This Rashba effect has been discussed for e.g. 2D electron gas, heterostuctures etc. where structure inversion asymmetries exist. On the other hand, it is also important to note that in *bulk* inversion asymmetry (BIA) systems, that is, crystal

structures that lack a center of inversion, we can have a spin splitting even if $\boldsymbol{B} = 0$ which is know as the *Dresselhaus* effect (D-1) [73]. Unlike the linear Rashba effect, the energy difference in this case scales with k as ($\Delta\mathcal{E}_{\text{Dresselhaus}} \propto k^3$) [57].

2.4 The Photoelectron emission spectroscopy

Photoelectron emission spectroscopy (PES) has been one of the most widely used techniques to study the electronic structure of atoms, molecules, solids and adsorbates [74]. It refers to all the methods that are based on the application of the photoelectric effect which was originally discovered by Hertz in 1887 [75], where it was discovered that electrons can be removed from a solid when it is being illuminated by electromagnetic radiation. It was until 1905 when Albert Einstein [76] postulated the quantization of the electromagnetic field rather than the emission mechanism via introducing the concept of photon where he successfully explained the relation between the maximum kinetic energy for an electron emitted from Fermi level and the frequency ν of the light used rather that its intensity though the following substantial photoelectric equation

$$E_{kin}^{max} = h\nu - \Phi_{\circ} \tag{2.28}$$

where h is Planck's constant and $\Phi_{\circ}$ is the material work function which is a characteristic constant of the sample surface that refer to the potential barrier preventing the valence electrons from escaping (typically 4–5 eV for metals). Einstein was awarded the Nobel Prize in Physics in 1921 for his discovery.

Figure 2.5 (a) shows a schematic picture of a modern angle-resolved photoemission experiment, and a schematic view of the photoemission principle is illutrated in Fig. 2.5 (b). The photon source can be vacuum ultra-violet (VUV) line spectra of discharge lamps e.g. He-discharge lamp (HeI_{α}: 21.22 eV and $HeII_{\alpha}$: 40.82 eV), a laser, or a synchrotron radiation facility which provides light over a broad range of photon energies from the ultraviolet up to hard x-rays [77]. Based on the photon energy used, one can either investigate the valence band states by using the ultraviolet photoemission (UPS), or via using the x-ray photoemission spectroscopy (XPS) to probe the core-level states that are at high binding energies. He-lamp is around 0.2-0.5 mm in diameter, while the laser or synchrotron light beam can be finely focused down to $< 50\ \mu m$. Even though the line width for the discharge lamp is a few meV and for the x-ray is $\sim$ 1eV, an additional monochromator can be used to enhance the energy resolution and to suppress the background intensities. So, when the light impinges a sample, that has to be a single crystal aligned properly to perform momentum resolved measurements, electrons will be ejected into vacuum in all directions. However, the electron energy analyzer is characterized by a finite acceptance angle that is defined by an electron optical entrance lens system, which makes the emission direction defined by (ϑ, φ) a free experimental parameter. Here ϑ is the polar angle with respect to the surface normal, and φ is the azimuthal angle defined with respect to the experimental geometry or the crystal axis. Hence, via collecting these photoelectrons and recording their kinetic energies E_{kin} together with their emission angles (ϑ, φ), it is possible to determine the postemission momentum $p = \sqrt{2m_e E_{kin}}$ and its component parallel to the surface

$$\boldsymbol{p}_{||_{vacuum}} = \left(\sqrt{2m_e E_{kin}} \cdot sin(\vartheta) \cdot cos(\varphi)\hat{\boldsymbol{k}}_x + \sqrt{2m_e E_{kin}} \cdot sin(\vartheta) \cdot sin(\varphi)\hat{\boldsymbol{k}}_y\right) \tag{2.29}$$

which is conserved during the whole photoemission process, and the perpendicular to the surface component

$$\boldsymbol{p}_{\perp_{vacuum}} = \sqrt{2m_e E_{kin}} \cdot cos(\vartheta)\hat{\boldsymbol{k}}_z \tag{2.30}$$

which is not conserved due to the broken symmetry at the surface.

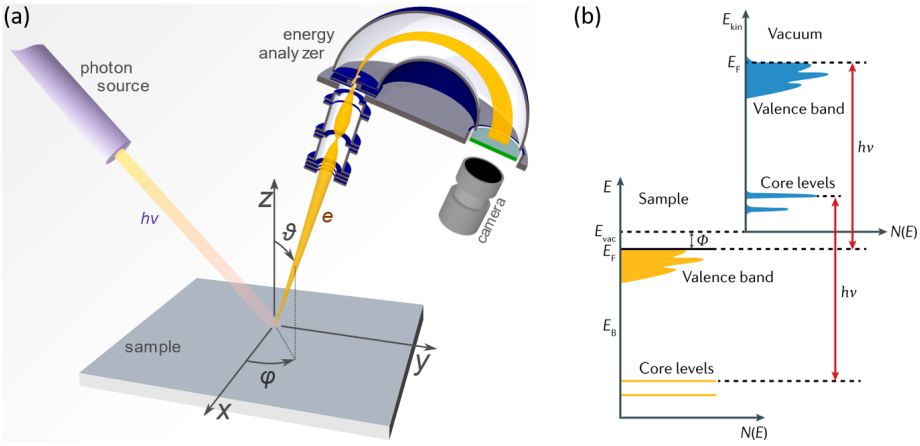

Figure 2.5: **Geometry and principle of the photoemisssion process.** (a) Schematic picture showing the geometry of the photoemission process. (b) Principle of the photoemission process: energy distribution of the photoelectrons $N(E)$ collected by the spectrometer (blue shaded regions in the right-top panel) referring to the density of states occupied in the sample (yellow shaded regions in the right-bottom panel), reflecting a broad valence electronic distribution (labeled: Valence band) and sharp emission lines from the core levels (labeled: Core levels). (a) Taken from [78] and (b) taken from [79].

In general, most of the photon energies used in the photoemission experiments are within the ultraviolet (UV) range, in particular ($h\nu$<100 eV). At this low energy, the photon momentum $\boldsymbol{k}_{h\nu} = \frac{2\pi}{\lambda_{h\nu}}$ during the photoemission process can be neglected. It is ($\boldsymbol{k}_{HeI_\alpha} = 0.008$ Å^{-1}) for the HeI$_\alpha$ discharge line typically used in photoemission experiments, and ($\boldsymbol{k}_{100eV} = 0.05$ Å^{-1}) for 100 eV photons, both are much smaller compared to the typical size of the Brillouin-zone $\frac{2\pi}{a}$ for a solid, and hence, can safely be neglected. On the other hand, if the photon energy is high enough as in the case of using 1487 eV photons where $\boldsymbol{k}_{1487eV} = 0.76$ Å^{-1} (the Al K$_\alpha$ line used in x-ray photoemission), then the corresponding momentum can not be neglected and must be taken into consideration [80]. Therefore, neglecting the photon momentum and taking advantage of the total energy and momentum conservation of the electron, one can derive the relation between the pre-emission and post-emission electronic states

$$E_{kin} = h\nu - \Phi_\circ - E_B \tag{2.31}$$

$$\begin{aligned}\boldsymbol{p}_{||_{(vacuum\equiv crystal)}} = \hbar\boldsymbol{K}_{||_{(vacuum\equiv crystal)}} = \sqrt{2m_e E_{kin}} \cdot sin(\vartheta)\hat{\boldsymbol{k}}_\rho = \\ \left(\sqrt{2m_e E_{kin}} \cdot sin(\vartheta) \cdot cos(\varphi)\hat{\boldsymbol{k}}_x + \sqrt{2m_e E_{kin}} \cdot sin(\vartheta) \cdot sin(\varphi)\hat{\boldsymbol{k}}_y\right)\end{aligned} \tag{2.32}$$

Here, E_{kin} is the photoelectron kinetic energy, E_B is the pre-emission binding energy of the electron inside the material. $\boldsymbol{p}_{||} = \hbar \boldsymbol{K}_{||}$ is the parallel component to the surface of the photelectron which is equal to the parallel component of the crystal momentum for the electron prior emission inside the material in the *extended zone scheme*, but can always be traced back into the first Brllouin zone by subtracting the correct reciprocal lattice vectror $\boldsymbol{G}$ ($\boldsymbol{p}_{||BZ^{1st}} = \boldsymbol{p}_{||BZ^{higher-order}} - \boldsymbol{G}$).

The experimental energy resolution is determined by the bandwidth of the light source and the energy resolution of the detector: $(\Delta E_{total})^2 = (h\Delta v)^2 + (\Delta E_{detector})^2$. The main contribution into the momentum resolution is from the detector $\Delta\vartheta$, hence, using Eq. (2.32) to derive the momentum resolution:

$$\Delta \boldsymbol{K}_{||} \approx \sqrt{2m_e E_{kin}/\hbar^2} \cdot cos(\vartheta) \cdot \Delta\vartheta \tag{2.33}$$

One can see that the lower the photon energy and hence the slower the photoelectrons E_{kin}, and the larger polar angle ϑ (can be reached by measuring outside the 1^{st} BZ) the higher the momentum resolution achieved.

2.5 Three-step model of photoemission

The photoemission process can be understood within the so-called *three-step model* which divides the photoemission of a *single* electron into three sequential steps that have to be connected quantum mechanically to allow the electronic wave function to propagate from one step to another:

- *Optical excitation* of the electron in the bulk. This step contains the electronic structure information of the material.
- *Transport* of the excited (hot) electron to the surface, which is described by the effective mean free path representing the elastic and inelastic scattering experienced by the electron during its journey to the surface. The inelastic-scattering shows up as background in the spectra that is typically being ignored.
- *Transmission* of the electron through the surface into the vacuum, where the photoelectron takes the form of a free electron plane wave in the vacuum that extends to the detector.

The three steps are labeled with ③,④ and ⑤ respectively in Fig. 2.6. In the coming sections I will discuss these steps and mostly elaborate on the first step, but for a detailed description the reader is recommended to check the literature available on the subject in e.g. [79–86]. Here it is very important to distinguish between the different electronic wave vectors during this process:

- $\boldsymbol{k}_i$: initial wave vector of the electron before it gets excited.
- $\boldsymbol{k}_f$: final wave vector of the excited electron while remaining in the bulk.
- $\boldsymbol{K}$: wave vector of the photoelectron after being ejected into vacuum.

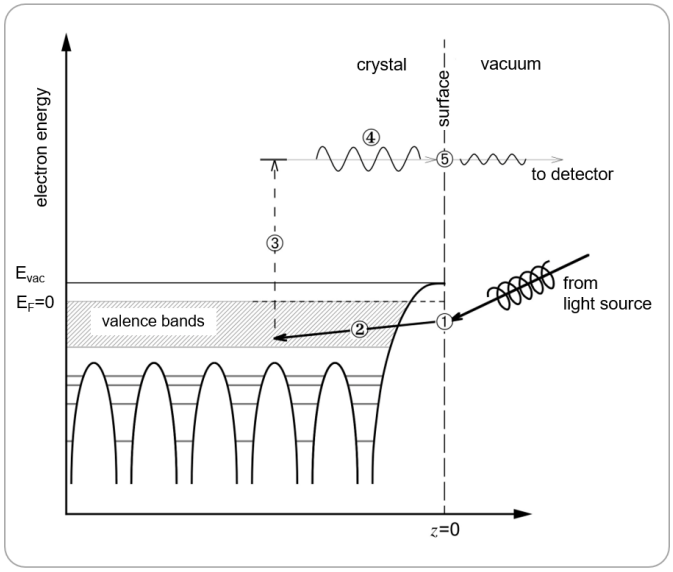

Figure 2.6: **Schematic representation of the three step model.** Steps labeled ③,④ and ⑤ are the steps of the three step model representing the optical excitation, traveling of the photoelectron to the surface and its transmission into the vacuum respectively. Furthermore, steps ① and ② represent refraction and penetration of the electromagnetic wave into the material respectively. Taken from [83].

2.5.1 1^{st} step: Photoexcitation

In order to extract the encoded electronic structure information from the 1^{st} step of the three step model, the photoemission process needs to be formulated theoretically. The starting point is to imagine the ground state of a system as a reservoir of N-electron system that will interact with the electromagnetic wave of the incoming photon such that a *single* electron will be removed from the reservoir leaving a $(N-1)$ electrons in that reservoir besides the photoexcited electron. Then, the aim is to derive a formula that can describe the total photoemission intensity (total photocurrent). The foundation stone is *Fermi's golden rule*:

$$w_{i\to f} = \frac{2\pi}{\hbar}|\langle\Psi_f^N|H_{int}|\Psi_i^N\rangle|^2\delta(E_f^N - E_i^N - h\nu) \tag{2.34}$$

which describes the transition probability $w_{i\to f}$ of the N-particle system from the initial state $|\Psi_i^N\rangle$ to one of the possible excited final states $|\Psi_f^N\rangle$. Here, the delta function ensures the energy conservation where E_i^N and E_f^N are the initial- and final-state energies of the N-particle system, while H_{int} is the perturbing Hamiltonian which will be described in the next Sec.(2.5.1.1).

2.5.1.1 Photoemission matrix element

The Hamiltonian describing an electron in a unperturbed solid is

$$H_\circ = \frac{\boldsymbol{p}^2}{2m_e} + V(\boldsymbol{r}) \tag{2.35}$$

The sample in general represents a many-body system that will be involved as a whole in the photoemission process once it is being shined by some sort of light. However, a simplified view of the process is through a single-electron picture, such that the electron will interact with the electromagnetic field $\boldsymbol{A}$ which is expressed mathematically through the canonical replacement $\boldsymbol{p} \rightarrow (\boldsymbol{p} - \frac{e}{c}\boldsymbol{A})$ in Eq. (2.35). This can be understood as a force experienced by the electron from the oscillating electric field of the electromagnetic wave that will change its momentum, to get the perturbed Hamiltonian

$$\begin{aligned} H &= \frac{(\boldsymbol{p} - \frac{e}{c}\boldsymbol{A})^2}{2m_e} + V(\boldsymbol{r}) \\ &= \underbrace{\frac{\boldsymbol{p}^2}{2m_e} + V(\boldsymbol{r})}_{\mathrm{H}_{(o)}} - \underbrace{\frac{e}{2m_e c}(\boldsymbol{A}\cdot\boldsymbol{p} + \boldsymbol{p}\cdot\boldsymbol{A}) + \frac{e^2}{2m_e c^2}\boldsymbol{A}^2}_{\mathrm{H}_{(perturbing)}} \\ &\approx H_\circ - \frac{e}{m_e c}\boldsymbol{A}\cdot\boldsymbol{p} \\ &= H_\circ - \frac{e}{m_e c}(\boldsymbol{A}_\circ e^{i(\boldsymbol{q}\cdot\boldsymbol{r} - wt)})\cdot\boldsymbol{p} \\ &= H_\circ - \underbrace{\frac{e}{m_e c} e^{i\boldsymbol{q}\cdot\boldsymbol{r}}(\boldsymbol{A}_\circ\cdot\boldsymbol{p})}_{\mathrm{H}_{(int)}} e^{-iwt} \\ &= H_\circ + H_{(int)} e^{-iwt} \end{aligned} \tag{2.36}$$

On the second line, the quadratic term in $\boldsymbol{A}$ describes two-photon processes and can be neglected for weak radiation in the linear optical regime[11]. Also, $-\frac{e}{2m_e c}(\boldsymbol{A}\cdot\boldsymbol{p} + \boldsymbol{p}\cdot\boldsymbol{A}) = -\frac{e}{2m_e c}(2\boldsymbol{A}\cdot\boldsymbol{p} + i\hbar\nabla\cdot\boldsymbol{A}) \approx -\frac{e}{m_e c}\boldsymbol{A}\cdot\boldsymbol{p}$, where the dipole approximation assumption ($\boldsymbol{A}$ is constant over atomic dimensions and hence $\nabla\cdot\boldsymbol{A} = 0$ in the bulk) was used which holds in the ultraviolet regime typically used in photoemission experiments [82, 84]. We used $\boldsymbol{A} = \boldsymbol{A}_\circ e^{i(\boldsymbol{q}\cdot\boldsymbol{r} - wt)}$ for the electromagnetic field with a photon momentum $\boldsymbol{q}$. One can see that the final form represented in Eq. (2.36) shows the weak perturbation that is periodic in time and hence can be used in Fermi's golden rule Eq. (2.34) when it is reduced into a single electron system with single -initial and -final wave functions

$$w_{i\rightarrow f} = \frac{2\pi}{\hbar}|\langle\phi_f^{\boldsymbol{k}}|H_{int}|\phi_i^{\boldsymbol{k}}\rangle|^2 \cdot \delta(\mathcal{E}_f - \mathcal{E}_i - h\nu) \tag{2.37}$$

with the so-called *photoemission matrix element*

$$M_{f,i}^{\boldsymbol{k}} = \langle\phi_f^{\boldsymbol{k}}|H_{int}|\phi_i^{\boldsymbol{k}}\rangle = -\frac{e}{m_e c}\langle\phi_f^{\boldsymbol{k}}|e^{i\boldsymbol{q}\cdot\boldsymbol{r}}(\boldsymbol{A}_\circ\cdot\boldsymbol{p})|\phi_i^{\boldsymbol{k}}\rangle \tag{2.38}$$

The photon wave can probe length scales of order $\lambda = \frac{2\pi}{q}$ which is large compared to the atomic dimensions for the mostly used ultraviolet light in mapping the band structure (using HeI$_\alpha$ = 21.22 eV $\rightarrow \lambda$= 584 Å$\gg$ lattice constant a$_\circ \sim$ Å). Expanding the photon plane wave $e^{i\boldsymbol{q}\cdot\boldsymbol{r}} = 1 + i\boldsymbol{q}\cdot\boldsymbol{r} + ... \approx 1$ (dipole approximation) with $\boldsymbol{q}\cdot\boldsymbol{r} \sim 2\pi\frac{a_\circ}{\lambda} \ll 1$, leads to the simplified form

[11] However, in the case of high photon intensities as those achieved in ultrafast pulses, the quadratic term becomes relevant.

$$M_{f,i}^{\boldsymbol{k}} = -\frac{e}{m_e c}\langle\phi_f^{\boldsymbol{k}}|\boldsymbol{A}_\circ\cdot\boldsymbol{p}|\phi_i^{\boldsymbol{k}}\rangle \tag{2.39}$$

$$= -\frac{e}{m_e c}\langle\phi_f^{\boldsymbol{k}}|\boldsymbol{A}_\circ\cdot\frac{im_e}{\hbar}[H_\circ,\boldsymbol{r}]|\phi_i^{\boldsymbol{k}}\rangle$$

$$= -\frac{ie}{\hbar c}\langle\phi_f^{\boldsymbol{k}}|H_\circ\boldsymbol{A}_\circ\cdot\boldsymbol{r}-\boldsymbol{A}_\circ\cdot\boldsymbol{r}H_\circ|\phi_i^{\boldsymbol{k}}\rangle$$

$$= -\frac{ie}{\hbar c}(\mathcal{E}_f-\mathcal{E}_i)\langle\phi_f^{\boldsymbol{k}}|\boldsymbol{A}_\circ\cdot\boldsymbol{r}|\phi_i^{\boldsymbol{k}}\rangle$$

$$= -\frac{i}{\hbar c}(\mathcal{E}_f-\mathcal{E}_i)\langle\phi_f^{\boldsymbol{k}}|\boldsymbol{A}_\circ\cdot\underbrace{e\boldsymbol{r}}_{\mu}|\phi_i^{\boldsymbol{k}}\rangle \tag{2.40}$$

where in the last line μ is a reminder of the electric dipole moment form, and that's why Eq. (2.40) is known as the *dipole matrix element*. Classically, the state of polarization of the electromagnetic wave is specified by the direction of the electric field $\boldsymbol{\epsilon}$, so $\boldsymbol{A}$ can be written as $A_\circ\boldsymbol{\epsilon}$, and the matrix element becomes

$$M_{f,i}^{\boldsymbol{k}} = \underbrace{-\frac{e}{m_e c}A_\circ\langle\phi_f^{\boldsymbol{k}}|\boldsymbol{\epsilon}\cdot\boldsymbol{p}|\phi_i^{\boldsymbol{k}}\rangle}_{\text{velocity form}} = \underbrace{-\frac{i}{\hbar c}A_\circ(\mathcal{E}_f-\mathcal{E}_i)\langle\phi_f^{\boldsymbol{k}}|\boldsymbol{\epsilon}\cdot e\boldsymbol{r}|\phi_i^{\boldsymbol{k}}\rangle}_{\text{length form}} \tag{2.41}$$

$$\Rightarrow \qquad M_{f,i}^{\boldsymbol{k}} \propto \langle\phi_f^{\boldsymbol{k}}|\boldsymbol{\epsilon}\cdot\boldsymbol{p}|\phi_i^{\boldsymbol{k}}\rangle \propto \langle\phi_f^{\boldsymbol{k}}|\boldsymbol{\epsilon}\cdot\boldsymbol{r}|\phi_i^{\boldsymbol{k}}\rangle \tag{2.42}$$

Indeed, the simplified *length form* of the matrix element, $\langle\phi_f^{\boldsymbol{k}}|\boldsymbol{\epsilon}\cdot\boldsymbol{r}|\phi_i^{\boldsymbol{k}}\rangle$ is extremely valuable. In order to stress the importance of this term, we can start looking at the atomic picture. Because atomic orbitals are described with a time-independent potential V, Schrödinger's equation can be solved using the technique of separation of variables, so that any wave function will have the form $\Psi_{n,l,m_l}(r,\vartheta,\varphi) = R_{n,l}(r)Y_{l,m_l}(\vartheta,\varphi)$, where $R_{n,l}(r)$ is the radial wave function part and $Y_{l,m_l}(\vartheta,\varphi)$ is the angular wave function part that is written in terms of spherical harmonics. Therefore, the initial and final single electron wave functions $|\phi_i^{\boldsymbol{k}}\rangle$ and $|\phi_f^{\boldsymbol{k}}\rangle$, respectively, appearing in the matrix element expression can be factorized into radial and spherical harmonics parts. Moreover, the operator $(\boldsymbol{\epsilon}\cdot\boldsymbol{r})$ can also be expressed in terms of the spherical harmonics (e.g. $Y_{1,0}$ for linearly polarized light, while $Y_{1,\pm m}$ for circularly polarized light). This implies that the total expression for the matrix element $\langle\phi_f^{\boldsymbol{k}}|\boldsymbol{\epsilon}\cdot\boldsymbol{r}|\phi_i^{\boldsymbol{k}}\rangle$ can be fully calculated using spherical harmonics products which give nonzero outcome based on well known rules between the quantum numbers l, m_l of the initial and final states. Although this description is based on the atomic level, within the frame work of the tight-binding model, the band structure can be resolved on the basis of atomic orbitals as will be shown in Sec. 4.6.

2.5.1.2 Noninteracting electrons picture

The first approach to look at the photoemission is through the so-called noninteracting electrons picture. This way, one can factorize the initial- and final-state N-electron wave functions as this

$$|\Psi_i^N\rangle = \mathcal{A}|\phi_i^{\boldsymbol{k}}\rangle|\Psi_i^{N-1}\rangle \tag{2.43}$$

$$|\Psi_f^N\rangle = \mathcal{A}|\phi_f^{\boldsymbol{k}}\rangle|\Psi_f^{N-1}\rangle \tag{2.44}$$

where $\mathcal{A}$ is an antisymmetry operator that ensures the antisymmetrization of the N-electron wave function to satisfy the Pauli principle. $|\phi_i^{\boldsymbol{k}}\rangle$ represents the *single*-electron wave function before being excited by the photon, and $|\phi_f^{\boldsymbol{k}}\rangle$ refer to the photoexcited electron while still in the solid. Both wave functions are having the same wavevector $\boldsymbol{k}$ because $\boldsymbol{k_i}$=$\boldsymbol{k_f}$ as a result of the momentum conservation during the photoemission process. As the name *noninteracting electrons* indicates, exciting an electron from the initial state of the N-electron system into a final state will not affect the remaining $(N-1)$ electrons, hence, $|\Psi_f^{N-1}\rangle = |\Psi_i^{N-1}\rangle$ and Eq. (2.34) becomes:

$$\begin{aligned} w_{i\to f} &= \frac{2\pi}{\hbar}|\langle\Psi_f^{N-1}\phi_f^{\boldsymbol{k}}|H_{int}|\phi_i^{\boldsymbol{k}}\Psi_i^{N-1}\rangle|^2\cdot\delta(E_f^N-E_i^N-h\nu) \\ &= \frac{2\pi}{\hbar}|\langle\phi_f^{\boldsymbol{k}}|H_{int}|\phi_i^{\boldsymbol{k}}\rangle|^2\cdot|\langle\Psi_f^{N-1}|\Psi_i^{N-1}\rangle|^2\cdot\delta(E_f^N-E_i^N-h\nu) \\ &= \frac{2\pi}{\hbar}|\langle\phi_f^{\boldsymbol{k}}|H_{int}|\phi_i^{\boldsymbol{k}}\rangle|^2\cdot\delta(\mathcal{E}_f-\mathcal{E}_{\boldsymbol{k}}-h\nu) \\ &= \frac{2\pi}{\hbar}|M_{f,i}^{\boldsymbol{k}}|^2\cdot\delta(\mathcal{E}_f-\mathcal{E}_{\boldsymbol{k}}-h\nu) \end{aligned} \tag{2.45}$$

where $M_{f,i}^{\boldsymbol{k}} = \langle\phi_f^{\boldsymbol{k}}|H_{int}|\phi_i^{\boldsymbol{k}}\rangle$ is the *one*-electron dipole matrix element discussed in Sec. 2.5.1.1. In the last two equalities, $\mathcal{E}_{\boldsymbol{f}}$ and $\mathcal{E}_{\boldsymbol{k}}$ are the single electron energies for the wave functions $|\phi_f^{\boldsymbol{k}}\rangle$ and $|\phi_i^{\boldsymbol{k}}\rangle$ respectively. The desired total photoemission current will be the sum over all possible transition combinations between the initial and final states $I = \sum_{i,f} w_{i\to f}$. To simplify the picture, we can consider a single transition between an initial and a final state along each wavevector $\boldsymbol{k}$, this will be exactly Eq. (2.45) where it represents a sharp peak in the photoemission spectrum modified by the matrix element. Hence, covering all the directions (wavevectors $\boldsymbol{k}$) is constructing the desired band structure $\mathcal{E}_{\boldsymbol{k}}$.

2.5.1.3 Interacting electrons picture

The other way to look at the photoemission process is through the so-called interacting electrons picture. However, as one can guess from the name of the method that, the treatment of removing a single electron is not as trivial as it is compared to the noninteracting electrons picture described previously. Here we can not factorize the total wave function into a single electron's wave function and a remaining $(N-1)$ electrons wave function as it was done in Eq. (2.43) and Eq. (2.44). Even though, the problem can be simplified via considering an instantaneous removal of the electron, which takes place on a timescale of $10^{-15}s$, from the system of the so-called *sudden approximation*, such that the photoexcited electron will not have the time to interact with the remaining $(N-1)$ electrons system[12]. This way the final total wave function can be factorized as in Eq. (2.44). Similarly, one can still simplify the initial total wave function using the Hartree-Fock formalism, justifying the factorization in Eq. (2.43). However, the most critical difference here compared to the *noninteracting* picture is that, the remaining excited $(N-1)$ electrons system after removing an electron is not the same as before i.e. $|\Psi_f^{N-1}\rangle \neq |\Psi_i^{N-1}\rangle$. Indeed, $|\Psi_f^{N-1}\rangle$ can be any of the excited mth final eigenstate $|\Psi_m^{N-1}\rangle$ with the corresponding

[12]This approximation is valid only when the photoelectron has sufficiently high kinetic energy to leave the system before the remaining $(N-1)$ electrons have time to respond.

eigenenergy E_m^{N-1} or even a linear combination of multiple of them. The transition probability in this case will be

$$\begin{aligned} w_{i\to f} &= \frac{2\pi}{\hbar}|\langle\Psi_f^{N-1}\phi_f^{\boldsymbol{k}}|H_{int}|\phi_i^{\boldsymbol{k}}\Psi_i^{N-1}\rangle|^2\cdot\delta(E_f^N - E_i^N - h\nu) \\ &= \frac{2\pi}{\hbar}\sum_m|\langle\Psi_m^{N-1}\phi_f^{\boldsymbol{k}}|H_{int}|\phi_i^{\boldsymbol{k}}\Psi_i^{N-1}\rangle|^2\cdot\delta(\mathcal{E}_f + E_m^{N-1} - E_i^N - h\nu) \\ &= \frac{2\pi}{\hbar}|\langle\phi_f^{\boldsymbol{k}}|H_{int}|\phi_i^{\boldsymbol{k}}\rangle|^2\cdot\sum_m|\langle\Psi_m^{N-1}|\Psi_i^{N-1}\rangle|^2\cdot\delta(\mathcal{E}_f + E_m^{N-1} - E_i^N - h\nu) \\ &= \frac{2\pi}{\hbar}|M_{f,i}^{\boldsymbol{k}}|^2\cdot\sum_m|\langle\Psi_m^{N-1}|\Psi_i^{N-1}\rangle|^2\cdot\delta(\mathcal{E}_f + E_m^{N-1} - E_i^N - h\nu) \end{aligned} \tag{2.46}$$

and the total photoemission intensity will include the sum over all possible transitions for the single electron along a defined direction $\boldsymbol{k}$ and the sum over all the possible excited states left for the $(N-1)$ electrons

$$I = \frac{2\pi}{\hbar}\sum_{f,i}|M_{f,i}^{\boldsymbol{k}}|^2\cdot\sum_m|\langle\Psi_m^{N-1}|\Psi_i^{N-1}\rangle|^2\cdot\delta(\mathcal{E}_f + E_m^{N-1} - E_i^N - h\nu) \tag{2.47}$$

where $|\langle\Psi_m^{N-1}|\Psi_i^{N-1}\rangle|^2$ is the probability that removing an electron from the system will leave it in the mth excited state. If the final $(N-1)$ electrons, after absorption a photon by the electron, happens to be in one single final state $m = m_\circ$ and the corresponding initial eigenstate happens to be the same $|\Psi_i^{N-1}\rangle = |\Psi_{m_\circ}^{N-1}\rangle$, then the photoemission will give a delta spectrum assuming a non-zero matrix element $|M_{f,i}^{\boldsymbol{k}}|^2 \neq 0$. This reminds us with the *noninteracting* picture. The significance of this method shows up in the strongly correlated materials, where removing a single electron will affect the remaining $(N-1)$ electrons strongly, leaving $|\Psi_f^{N-1}\rangle$ as a linear combination of more that one excited state. Hence, $|\Psi_i^{N-1}\rangle$ will overlap with all of them in Eq. (2.47) producing broadened peaks in the photoemission spectra unlike the *noninteracting* delta spectra.

2.5.2 2nd step: Transport of the hot electron to the surface

In this step the excited electron propagates towards the surface. During this journey the electron experiences elastic and inelastic scattering mainly dominated by the scattering due to other electrons and defects in the material, in addition to the phonons scattering. The elastic scattering will change the direction of propagation of the photoelectron and, hence, changing the angular distribution of the filtered electrons in the vacuum. On the other hand, *inelastic* means that the electron will lose part of its kinetic energy and may thus be visible at different lower kinetic energy in the measured band structure, within the so-called secondary electrons which typically appear as broad featureless background. The only unscattered electrons give rise to sharp features in the measured spectrum which can be related to the initial electronic band structure of the material. In order to have a clue of the probing depth of the photoemission process and to have an idea of how long an electron can travel in the material towards the surface before it gets scattered, a quantity known as inelastic mean free path λ_{in} (IMFP), which is defined as the average distance between two subsequent inelastic scattering events, is typically used to describe the

exponentially damping photoelectron intensity I compared to its initial value $I_\circ$ along a path d (considering the emission angle) [83, 87]

$$I = I_\circ exp\Big(-\frac{d}{\lambda_{in}}\Big) \tag{2.48}$$

Actually, λ_{in} was found experimentally to behave similarly in different materials producing the so-called universal curve as shown in Fig. 2.7. One can see the minimum of the curve, minimum values of (IMFP), is happening within ∼(20-120) eV kinetic energies of the emitted electrons which are the conventional mostly used VUV photon energies in laboratories and synchrotrons. This reflects the extreme surface sensitivity of the photoemission technique, which in turn refers that most of the photoemission signal is coming from the topmost surface layer of the material making it an advantage in probing surface states. Thus, this clarifies the need for the ultra-high vacuum system to do such experiments. On the other hand, if the aim is to look at the bulk band structure, one can see that going into the x-ray energy range increases the (IMFP), making the process less sensitive to the surface and more sensitive to the bulk.

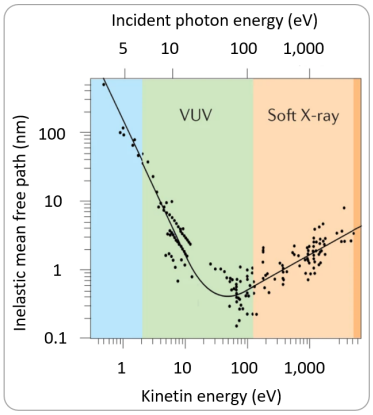

Figure 2.7: **Universal curve of the inelastic mean free path.** Universal curve of the inelastic mean free path of the photoemitted electrons as a function of their kinetic energies (bottom axis), and the photon energies used (top axis: calculated using 4 eV work function and exciting electrons located at Fermi level). Dots represent measured values and the black line is the corresponding least square fit to the data. Taken from [86].

The increase in λ_{in} with increasing kinetic energy of the excited electron in the x-ray regime can be understood in terms of the scattering cross-section. Although the density of states of a free-electron gas increases as $\sqrt{E}$, which would increase the scattering rate and thus reduce λ_{in}, the electron–electron scattering cross-section decreases more rapidly with energy. As a result, the overall scattering probability decreases, leading to an increase in the inelastic mean free path. In contrast, the increase in λ_{in} observed in the low-energy regime is not straightforward to explain due to the complex role of electronic screening effects [88], leaving the universal curve under debate.

2.5.3 3^{rd} step: Transmission through surface to vacuum

In this last step of the photoemission process, the hot electron will try to leave the surface of the material into vacuum. Out of this process, one can relate the momentum of the electron in vacuum $\boldsymbol{K}$ to its momentum inside the solid $\boldsymbol{k}_f$=$\boldsymbol{k}_i$. However, as it was indicated in Sec. 2.4 only the parallel component of the momentum $\boldsymbol{K}_{||} = \boldsymbol{k}_{f_{||}}$ will be conserved through the transmission process, while the

perpendicular component is not $\boldsymbol{K}_\perp \neq \boldsymbol{k}_{f_\perp}$ (see Fig. 2.8 (a)). This can be understood due to the existence of the surface potential barrier, which can be related to the symmetry of the crystal, such that the electron will get diffracted at the surface. Moreover, the periodic potential of the crystal does not exist in vacuum making the dispersion relation of the electron in solid differs from that in vacuum. In order to fully determine the initial band structure $E(\boldsymbol{k}_i)$, one needs to determine the perpendicular component as well, in addition to the parallel component and the binding energy (from the kinetic energy). To do that, a widely used assumption, in particular, a nearly-free electron dispersion for the final bulk Bloch states is made

$$E_{kin}(\boldsymbol{k}_f) + V_\circ = \frac{\hbar^2}{2m_e}\boldsymbol{k}_f^2 = \frac{\hbar^2}{2m_e}(\boldsymbol{k}_i + \boldsymbol{G})^2 \tag{2.49}$$

where $\boldsymbol{G}$ is a reciprocal lattice vector, and it is important to include it here to include all possible excitation directions of the electron. $V_\circ$ is known as the inner average effective potential experienced by the electron in the solid, in another language it describes the energy loss during the transmission through the surface potential barrier (here we neglect photon momentum) that acts as an offset for the free-electron final state approximation (see Fig. 2.8 (b)). In metals with nearly parabolic bands it is the sum of the bottom of the valence bands and the work function $V_\circ = E_{\text{valence band bottom}} + \Phi_\circ$. Generally, it is determined via optimizing the agreement of the experimental data with the calculated band structure. In the next Sec. 2.5.4, the derivation of the perpendicular initial state component is illustrated.

2.5.4 Derivation of the $k_\perp$ momentum component

Although the only momentum component that is conserved through the transmission process (3^{rd} step of the three step model) is the parallel component, one can still recover the orthogonal component inside the material assuming a nearly free-electron band dispersion for the final state of the excited electron, while still in the solid, that is offset by a potential $V_\circ$, and assuming the shortest $\boldsymbol{G}$ vector allowing a vertical transition between the initial and final states, neglecting photon momentum, as shown in Fig. 2.8(b), to get

$$E_{kin}(\boldsymbol{k}_f) = \frac{\hbar^2\boldsymbol{k}_f^2}{2m_e} - V_\circ \tag{2.50}$$

and assuming no energy dissipation (no inelastic collisions) happens at the surface, then the kinetic energy of the excited electron in the material will equate the kinetic energy in the vacuum, hence

$$E_{kin}(\boldsymbol{k}_f) = \frac{\hbar^2\boldsymbol{k}_f^2}{2m_e} - V_\circ = E_{kin}(\boldsymbol{K}) = \frac{\hbar^2\boldsymbol{K}^2}{2m_e} \tag{2.51}$$

that is

$$E_{kin}(\boldsymbol{k}_f) = E_{kin}(\boldsymbol{K}) = E_{kin} = \frac{\hbar^2(\boldsymbol{k}_{f_{||}}^2 + \boldsymbol{k}_{f_\perp}^2)}{2m_e} - V_\circ = \frac{\hbar^2(\boldsymbol{K}_{||}{}^2 + \boldsymbol{K}_\perp{}^2)}{2m_e} \tag{2.52}$$

and using the conservation of the parallel momentum stated in Eq. (2.32), then

$$\boldsymbol{k}_{f_{||}} = \boldsymbol{K}_{||} = \sqrt{\frac{2m_e}{\hbar^2}E_{kin}} \cdot sin(\vartheta)\hat{\boldsymbol{k}_\rho} \tag{2.53}$$

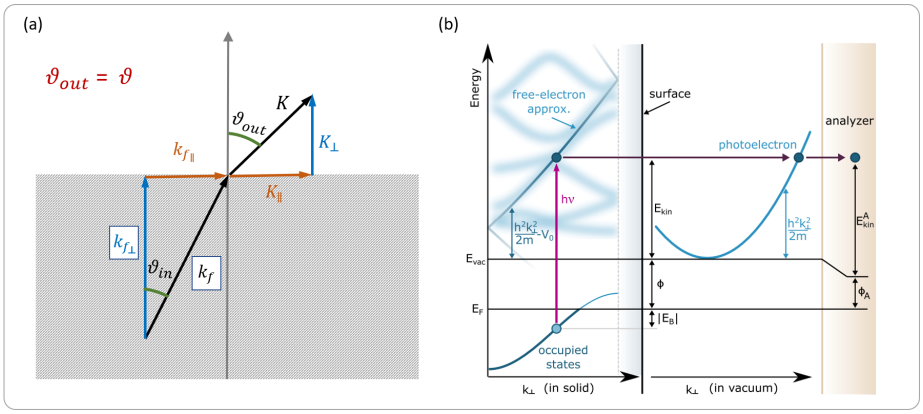

Figure 2.8: **Schematic picture of what is happening to the electrons momentum during the transmission process and illustration of the nearly free-electron final state approximation.** (a) Schematic picture showing the conservation of the in-plane electrons momentum ($\boldsymbol{k}_{f_{||}} = \boldsymbol{K}_{||}$) during the transmission process from the solid to vacuum, unlike the perpendicular component that loses part of its magnitude due to the surface potential barrier ($\boldsymbol{k}_{f_\perp} \neq \boldsymbol{K}_\perp$). (b) The three step model showing the free-electron final state approximation offset by the inner potential $V_\circ$ in the reduced zone scheme for the excited electron inside the material. $V_\circ$ plays a compensation rule for the discontinuity of the momentum perpendicular component at the surface as derived in the text and shown in the picture. The detected kinetic energy is measured with respect to the analyser work function Φ_A as indicated, such that for the photoelectron to be measured its energy must over come the work function of the analyser as well as the sample. In the rest of the context we will ignore this difference in the work function and consider only the sample work function. (b) Taken from [82].

substituting this in Eq. (2.52) for the desired $\boldsymbol{k}_{f_\perp}$ part

$$\begin{aligned} E_{kin} &= \frac{\hbar^2}{2m_e} \cdot \left(\left(\sqrt{\frac{2m_e}{\hbar^2} E_{kin}} \cdot sin(\vartheta) \right)^2 + \boldsymbol{k}_{f_\perp}^2 \right) - V_\circ \\ &= \frac{\hbar^2}{2m_e} \cdot \left(\frac{2m_e}{\hbar^2} E_{kin} \cdot sin^2(\vartheta) + \boldsymbol{k}_{f_\perp}^2 \right) - V_\circ \\ &= E_{kin} \cdot sin^2(\vartheta) + \frac{\hbar^2}{2m_e} \boldsymbol{k}_{f_\perp}^2 - V_\circ \end{aligned} \tag{2.54}$$

rewriting in term of $\boldsymbol{k}_{f_\perp}$

$$\boldsymbol{k}_{f_\perp}^2 = \frac{2m_e}{\hbar^2} \Big(E_{kin} + V_\circ + E_{kin} \cdot sin^2(\vartheta) \Big) = \frac{2m_e}{\hbar^2} \Big(E_{kin} \cdot cos^2(\vartheta) + V_\circ \Big) \tag{2.55}$$

ending up with the final expression for the perpendicular momentum component in the material

$$\boldsymbol{k}_{f_\perp} = \sqrt{\tfrac{2m_e}{\hbar^2} \cdot (E_{kin} cos^2(\vartheta) + V_\circ)} \hat{\boldsymbol{k}}_z \tag{2.56}$$

Experimentally, $\boldsymbol{k}_{f_\perp}$ is determined using normal emission i.e. setting $\vartheta = 0$ in Eq. (2.56), and changing the photon energy, hence, changing E_{kin} which would require a tunable light source as it is in synchrotrons. However, if the final state deviates a lot from the nearly free-electron approximation, this model fails and here comes the need to compare with the band structure calculation.

2.6 Electron scattering

In a photoemission experiment, electrons emitted from a material are resolved. The time-reversed of this picture is the low energy electron diffraction (LEED) experiment. In LEED a free electron beam $e^{i\boldsymbol{k}_f \cdot \boldsymbol{r}}$, produced by an electron gun, impinge a surface of the measured material and the reflected or transmitted electrons are analyzed. From point of view of the electron, any material is approximately a collection of muffin tin potentials, and the first order of scattering is a single atomic-like scattering on these potentials, which essentially results in atomic-like scattering state, but with the atomic potential replaced by its muffin-tin counterpart [89–91]. To clarify this, I will discuss the one-electron approximation scattering picture focusing on region of interest for ARPES experiments adapting the partial wave analysis method.

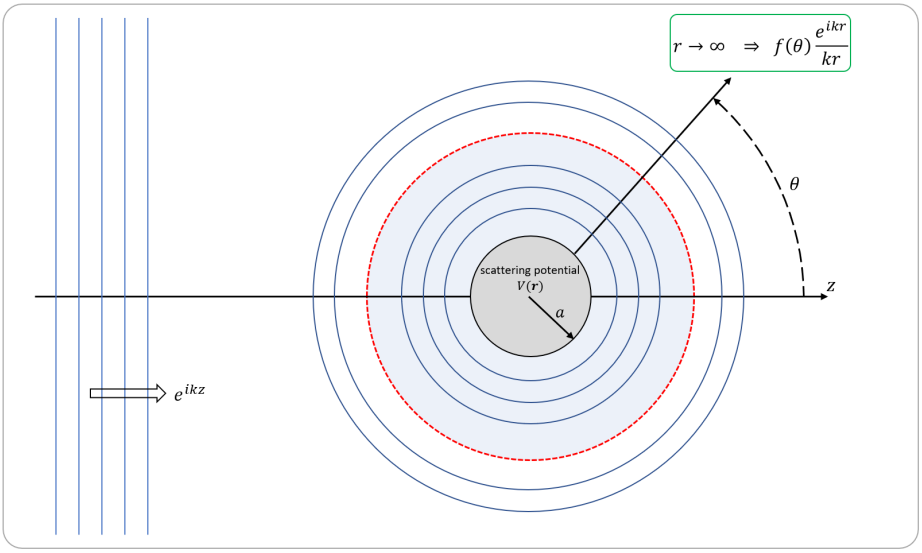

Figure 2.9: Schematic geometry showing the scattering of an electron by a potential $V(\boldsymbol{r})$ of range a. The blue shaded intermediate region sandwiched between the scattering potential and the red-circle is the region where the centrifugal potential term can not be neglected. In the limit $r \to \infty$, the asymptotic behaviour is an outgoing spherical wave $\frac{e^{ikr}}{kr}$ modulated by the scattering amplitude $f(\theta)$.

Let us imagine a quantum mechanical free-electron wave propagating along the positive z-direction, where it is going to be scattered by the potential $V(\boldsymbol{r})$ of range a centered at the origin as schematically shown in Fig. 2.9. The scattered wave is an outgoing spherical wave. In three dimensions one can think of sound waves bouncing

off a basketball. The solution of the Schrödinger equation in the intermediate blue shaded region in Fig. 2.9 can be demonstrated to be [62]

$$\psi(r,\theta,\varphi) = A\Big\{ \underbrace{e^{ikz}}_{incident\ wave} + \underbrace{\sum_{l,m} C_{l,m} h_l^{(1)}(kr) Y_l^m(\theta,\varphi)}_{scattered\ wave} \Big\} \tag{2.57}$$

where Y_l^m is a spherical harmonic with the non-negative integer l, and the integer m; $-l \leq m \leq 1$. $h_l^{(1)}$ is the Hankel function of the first kind that goes asymptotically (i.e. $r \to \infty$) as an outgoing spherical wave $\sim \frac{e^{ikr}}{kr}$. In the case of a spherically symmetric scattering potential $V(\boldsymbol{r}) = V(r)$, only terms with $m = 0$ in Eq. 2.57 survive. Hence,

$$\psi(r,\theta) = A\Big\{ e^{ikz} + \sum_{l=0}^{\infty} \sqrt{\frac{2l+1}{4\pi}} C_l h_l^{(1)}(kr) P_l(cos\theta) \Big\}^{13} \tag{2.58}$$

For large values of r, the Hankel function $h_l^{(1)}$ goes like $(-i)^{l+1}\frac{e^{ikr}}{kr}$, so

$$\psi(r,\theta) \approx A\Big\{ e^{ikz} + f(\theta)\frac{e^{ikr}}{r} \Big\} \ ; \qquad (r \to \infty) \tag{2.59}$$

where

$$f(\theta) = \frac{1}{k}\sum_{l=0}^{\infty} (-i)^{l+1} \sqrt{\frac{2l+1}{4\pi}} C_l P_l(cos\theta) \tag{2.60}$$

and $f(\theta)$ is the so-called *scattering amplitude*, which is the amplitude in the direction θ of the spherical wave resulting from the scattering of an initial plane wave [92]. Hence, Eq. 2.60 tells us how to calculate the scattering amplitude $f(\theta)$ in terms of the partial wave amplitudes C_l. Therefore, all that remains is to determine the amplitudes C_l for the given scattering potential in the problem (which is replaced in the atomic-like scattering case by its muffin-tin counterpart). This is done through solving the Schrödinger equation inside the scattering potential region and applying the boundary conditions to match the wave function in the exterior region [62].

Another way of looking at the scattering amplitude is to write it in terms of the so-called phase shifts. To do that, the incident plane can be expanded in terms of spherical waves [62]

$$e^{ikz} = \sum_{l=0}^{\infty} i^l (2l+1) j_l(kr) P_l(cos\theta) \tag{2.61}$$

where, j_l is the Bessel function, and asymptotically (as $r \to \infty$) Eq. 2.61 takes the form [93, 94]

$$e^{ikz} \approx \sum_{l=0}^{\infty} i^l (2l+1) P_l(cos\theta) \frac{i}{2k} \Big\{ \underbrace{\frac{e^{-i(kr-\frac{l\pi}{2})}}{r}}_{incoming\ wave} - \underbrace{\frac{e^{i(kr-\frac{l\pi}{2})}}{r}}_{outgoing\ wave} \Big\} \tag{2.62}$$

The scattering of each l^{th} angular momentum term (partial wave) of the expansion can be calculated independently. Now, the total wave function in Eq. 2.58 can be demonstrated asymptotically (as $r \to \infty$) to have the form [94]

[13] $Y_l^0 = \sqrt{\frac{2l+1}{4\pi}} P_l(cos\theta)$; where P_l is the l^{th} Legendre polynomial.

$$\psi(r,\theta) \approx \sum_{l=0}^{\infty} i^l (2l+1) e^{i\delta} P_l(cos\theta) \frac{i}{2k} \Big\{ \underbrace{\frac{e^{-i(kr-\frac{l\pi}{2}+\delta_l)}}{r}}_{incoming\ wave} - \underbrace{\frac{e^{i(kr-\frac{l\pi}{2}+\delta_l)}}{r}}_{outgoing\ wave} \Big\} \tag{2.63}$$

after some algebra this can be re-arranged to have the following form

$$\psi(r,\theta) \approx \sum_{l=0}^{\infty} i^l (2l+1) P_l(cos\theta) \frac{i}{2k} \Big\{ \underbrace{\frac{e^{-i(kr-\frac{l\pi}{2})}}{r}}_{incoming\ wave} - \underbrace{\frac{e^{i(kr-\frac{l\pi}{2}+2\delta_l)}}{r}}_{outgoing\ wave} \Big\} \tag{2.64}$$

One can see that by comparing Eq. 2.64 with Eq. 2.62 that the only difference is the introduced phase shift $e^{i2\delta_l}$ in the outgoing-wave part. This can be explained as follows: in order to have equal outgoing flux to the incoming flux, the maximum the scattering potential can do is to change the relative phase of the incoming and the outgoing waves. We also see the modification is happening only for the outgoing wave. The number 2 in the phase shift $e^{i2\delta_l}$ can be explained as a result of the interaction of the wave twice with the scattering potential; once in its way to the scattering potential and once in its way away from the potential after getting scattered. Therefore, the total wave function in Eq. 2.64 is called the *distorted plane wave*, where it differs from the incident free-electron plane-wave by just the phase shift $e^{i2\delta_l}$. Now, the scattering amplitude $f(\theta)$ can be expressed in terms of these phase shifts [94, 95]

$$f(\theta) = \frac{1}{2ik} \sum_{l=0}^{\infty} (2l+1)(e^{2i\delta_l} - 1) P_l(cos\theta) \tag{2.65}$$

These phase shifts can be calculated numerically by matching the radial part of the Schrödinger equation inside and outside the scattering potential of radius a (or its muffin-tin counterpart) [92]. Indeed, the amplitudes of the scattering factor, $\frac{1}{2ik}(e^{2i\delta_l} - 1) = t_l$, form the elements of the so-called t-matrix $\mathbf{t}$ [96].

Polar plots of the atomic-scattering amplitude $|f(\theta)|$ for an electron being scattered by a single Ni atom (left panel) and a single oxygen atom (right panel) are presented in Fig. 2.10 for some selected kinetic energies of the incident electron ranging from 60-1000 eV [97]. One can see that at lower kinetic energies, the scattering is important in several directions. However, at higher kinetic energies of the incident electron the scattering is dominated by the forward scattering at $\theta = 0°$ while scattering in other directions decreases appreciably.

The domination of the forward scattering by a single atom can be explained where the scattering atom acts as a rough converging electrostatic lens [97]. This is illustrated in Fig. 2.11. This means that at high electrons kinetic energies above 500 eV, most of the scattering is expected to happen along the chain of atoms [92, 97]. For electron scattering by atomic chains with different orientations, the reader is encouraged to check Ref. [97].

To summarize, this is the one-electron and one scattering potential picture in the LEED experiment i.e. the sum of a free-electron incoming wave and a spherical wave outgoing of the atomic scattering potential. The corresponding photoemission picture is the time-reversed LEED (TR-LEED), i.e. the sum of a spherical wave incoming onto the atomic scattering potential and an outgoing free-electron.

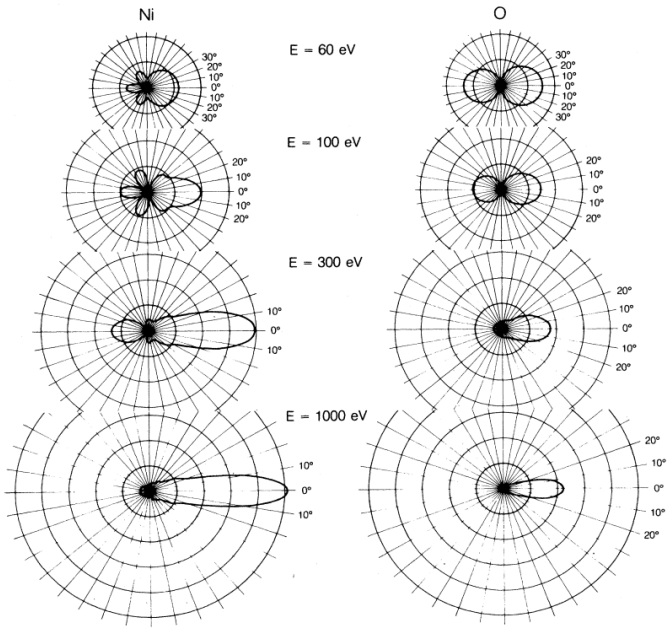

Figure 2.10: **Atomic-scattering amplitude**. Atomic-scattering amplitude $|f(\theta)|$ for an electron being scattered by a single Ni atom (left) and a single oxygen atom (right) at some selected kinetic energies of the incident electron. Figure taken from [97].

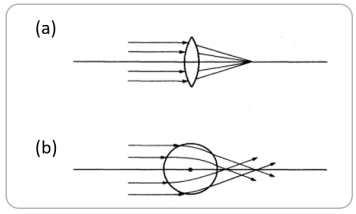

Figure 2.11: **Forward focusing by a single atom**. (a) Parallel light being focused by a converging lens. (b) Parallel beam of electrons *classically* being forwardly focused by a single atom. Figure Taken from [97].

Let us now discuss the case of a photoelectron excited from a valence state ψ_i. Here, each atomic site is considered as a scattering potential. The corresponding photoemission picture (TR-LEED), is the sum of an outgoing free-electron wave and N spherical waves incoming on each of the N scattering sites [90]. The initial state wave function is typically written as a two-component spinor in the form of the tight binding wave function, and spin is assumed to be conserved upon the transition. Within the tight-binding formalism, see Appendix A, the initial state wave function can be written as $\psi_i = \sum_j C_j \cdot \phi_j$, where $j \in \{\boldsymbol{r}_z, n, l, m\}$, $\boldsymbol{r}_z$ are positions of ions, and n, l, m are the atomic quantum numbers.

Within the dipole approximation, the photoemission dipole matrix element in the length form as shown in Sec. 2.5.1.1 is written as

$$M_{f,i}(\boldsymbol{k}_f) \propto \langle \psi_f(\boldsymbol{k}_f) | \boldsymbol{\epsilon} \cdot \boldsymbol{r} | \psi_i \rangle, \tag{2.66}$$

where $\boldsymbol{\epsilon}$ is the light polarization vector and $\boldsymbol{r}$ is the position operator. This *length* form of the matrix element is appropriate for atomic photoionization [89]

while the velocity form may be more appropriate depending on the particular case [90]. Substituting the tight binding form of the initial state ψ_i in Eq. 2.66, the matrix element can be written as

$$\langle\psi_f(\boldsymbol{k}_f)|\boldsymbol{\epsilon}\cdot\boldsymbol{r}|\psi_i\rangle = \sum_j C_j\langle\psi_f(\boldsymbol{k}_f)|\boldsymbol{\epsilon}\cdot\boldsymbol{r}|\phi_j\rangle, \tag{2.67}$$

that is, it is a coherent sum of matrix elements related to all the participating orbitals ϕ_j. The coherent sum, even from orbitals at different sites, is expected because the electromagnetic field of the typically used light in photoemission is spatially constant over the atomic sites {e.g. $\lambda_{HeI_\alpha} = 584$ Å $\gg$ Pt–Te bond length $= 2.73$ Å in $PtTe_2$ [98]}. Equation 2.67 can be interpreted as a sum of emissions originating from atomic-like emitters at different sites, where their interference leads to angular intensity variations, i.e., a diffraction pattern [90]. Indeed each atom can be associated with an atomic dipole vector that reflects the symmetry of the initial state orbital. When this atomic dipole vector is mathematically dotted with the electric field it gives the amplitude of the spherical wave emitted from that atom, and the amplitude of finding the photoelectron at the observer $\boldsymbol{k}_f$ is the coherent sum of the contributions from each atom [99]. This visualization is the LEED picture and one should keep in mind that photoemission is TR-LEED.

The principle of atomic-like emitters is best understood by looking at photoemission from valence states of oriented molecules as shown in Fig. 2.12. Let us think of a diatomic molecule e.g. H_2, where the two atomic sites of the H-atoms are indicated by the red and blue spheres in Fig. 2.12. Let us assume two identical atomic orbitals ϕ centered on the two sites. The resulting bonding and antibonding molecular orbitals are $\psi_+ = \frac{\phi_1+\phi_2}{\sqrt{2}}$ and $\psi_- = \frac{\phi_1-\phi_2}{\sqrt{2}}$ respectively. When a photoelectron is excited from ψ_+ or ψ_-, two spherical waves will be emitted *coherently* from the two sites (within the LEED picture) [90]. *Let us focus on the left panel of Fig.* 2.12. The two atomic sites are aligned along the y-axis. In the bonding case (i-ii) the two spherical waves emitted from the two sites are in-phase where $\Delta\varphi = 0$, while in the antibonding (iii-iv) the two spherical waves are out-phase where $\Delta\varphi = \pi$. In (i) and (iii), the separation distance between the two sites is $\frac{\lambda}{2}$, while in (ii) and (iv) it is λ, where λ is the wavelength of the *coherently* emitted two spherical waves. The outgoing black arrows (LEED picture) refer to polar angles where the interference of the emitted waves is maximum constructive interference. One can see that the interference pattern resulting from the bonding states (i-ii) is reversed compared to the antibonding states (iii-iv), which is illustrated by the arrows. Importantly, the angular distribution of photoemission in valence band is affected strongly by the bond-length d between the atomic sites. This effect is obvious when comparing (i) and (iii), where $d = \frac{\lambda}{2}$, with (ii) and (iv) respectively that have $d = \lambda$. The interference pattern is also affected by the bond orientation as well. This is illustrated in the middle and right panels of Fig. 2.12 where the atomic sites are along the x-axis and diagonally respectively. In Fig. 2.12, direction of arrows would be reversed into the atomic sites in the photoemission picture (TR-LEED).

To summarize, the photoemission amplitude along a final wave vector $\boldsymbol{k}_f$, defined by the angles $(\theta, \varphi$; see Fig. 2.5), is a coherent sum of the photoemission amplitudes from all the atomic-emitters participating in the photoemission process taking into account the relative phase shift which depends on the relative positions of emitter atoms. Based on Fig. 2.12 for the two emitters case defined by the real space vectors

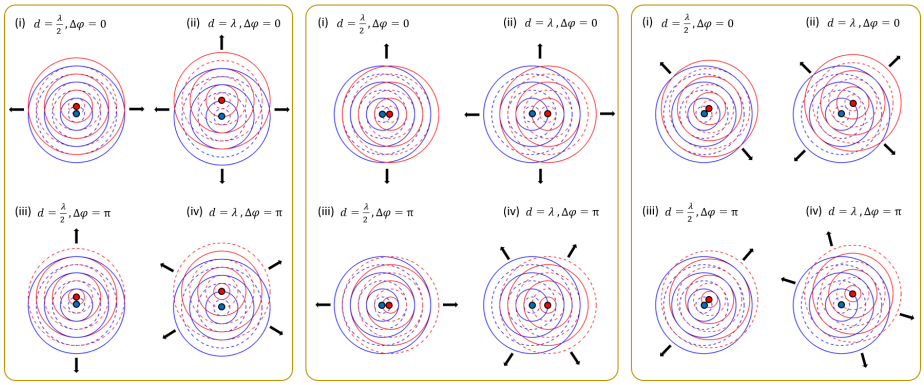

Figure 2.12: **LEED picture of two atomic sites emitters**. Left panel: Spherical waves emitted from two atomic sites emitters red-and blue spheres. Bond with length d is along the y-axis. λ is the wavelength of the *coherently* emitted spherical waves. $\Delta\varphi$ is the phase shift between the primary emitted spherical waves. (i-ii) Emission from bonding states. (iii-iv) Emission from antibonding states. Wave fronts of the spherical waves are indicated by the red and blue lines. Full lines refer to maxima while broken lines refer to minima. Arrows indicate polar angles where maximum constructive interference happen. Middle and right panels are similar to the left panel, but the bond is along the x-axis and diagonally aligned respectively. For the left panel I got inspired by [90], while middle and right panels are produced based on left panel.

$\boldsymbol{R}_{red}$ and $\boldsymbol{R}_{blue}$, the corresponding relative phase is $e^{i\boldsymbol{k}_f\cdot(\boldsymbol{R}_{red}-\boldsymbol{R}_{blue})}$.

However, scattering of the spherical waves has not been taken into consideration. Indeed, each spherical wave gets scattered by the neighboring atomic sites (scatterers). To illustrate this, let us look at the middle panel of Fig. 2.12. Now let us assume the blue atomic-site is the emitter, but now the red atomic-site is the scatterer. The blue lines represent the originally emitted spherical waves, while the red lines represent the scattered waves. In (ii) and (iii), the phase shift between the original (blue) and the scattered (red) waves is 0, while in (i) and (iv) the phase shift is π. One can see an expected reverse of the angular intensity of photoemission comparing the 0 phase shift case with the π phase shift case. Therefore, scattering is expected to lead to additional interference in the measured photoemission signal. If more scatterers exist and multiple scattering back and forth is included, then more complex diffraction patterns are expected.

Within this picture, the key challenge to evaluate Eq. 2.67 is in establishing the form of the final state ψ_f. But, we know from the boundary conditions that in the far-field the photoemission detectors are assumed to measure free electrons. Therefore, in the most simple approach, the final state is approximated by a plane wave characterized only by the direction and wave number of the emitted electron such that $\psi_f = e^{i\boldsymbol{k}_f\cdot\boldsymbol{r}}$ throughout all space where the effect of the scattering potential is neglected in the final state [100]. Using the spherical-harmonic addition theorem [101] together with Eq. 2.61, ψ_f can be written as a partial wave expansion around each site. This leads for each site separately to the dipole selection rules known from atomic physics [102, 103]. The free-electron final state (FEFS)

matrix element can be written as $M_{free}(\boldsymbol{k}_f) \propto (\boldsymbol{\epsilon} \cdot \boldsymbol{k}_f)\langle e^{i\boldsymbol{k}_f \cdot \boldsymbol{r}}|\psi_i(\boldsymbol{k}_i, \boldsymbol{r})\rangle$[14], where $\boldsymbol{\epsilon}$ is the light polarization [90, 100, 104, 105]. Substituting the tight-binding form of the initial state, we get $M_{free}(\boldsymbol{k}_f) \propto (\boldsymbol{\epsilon} \cdot \boldsymbol{k}_f) \sum_j C_j \langle e^{i\boldsymbol{k}_f \cdot \boldsymbol{r}}|\phi_j\rangle$. Since within the tight-binding formalism only discrete sites $\boldsymbol{r}_j$ representing the orbitals are considered, the FEFS matrix element is essentially a Fourier transform of the initial wave function times the polarization dependent factor [106]. Therefore, different sites $\boldsymbol{r}_j$ will lead to phase shifts $e^{i\boldsymbol{k}_f \cdot \boldsymbol{r}_j}$, and the FEFS matrix element will have the form $M_{free}(\boldsymbol{k}_f) \propto (\boldsymbol{\epsilon} \cdot \boldsymbol{k}_f) \sum_j e^{i\boldsymbol{k}_f \cdot \boldsymbol{r}_j} C_j |\phi_j\rangle$. This approximation is very useful in qualitative description of phenomena that depend on relative positions of emitter atoms, with an important application in orbital tomography [107]. It can also be used to explain the asymmetries in final spin-polarization from spin-mixed initial states [46].

However, the free-electron approximation fails to describe photoemission perpendicular to the polarization of light because of the factor $|\boldsymbol{\epsilon} \cdot \boldsymbol{k}_f|^2$ [108, 109]. Because the photoemission intensity, I, as described in Sec. 2.5.1.2 and Sec. 2.5.1.3 is proportional to the matrix element such that $I \propto |M_{free}|^2$. It also fails to describe circular dichroism in ARPES (CD-ARPES) [109], where CD-ARPES is defined as the difference in photoemission intensity between right-and left-handed circularly polarized light ($I_{RCP} - I_{LCP}$). But, the polarization vectors for left and right circular light are complex conjugates of each other (i.e. $\boldsymbol{\epsilon}_{RCP} = \boldsymbol{\epsilon}^*_{LCP}$), and $(I_{RCP} - I_{LCP}) \propto (|\boldsymbol{\epsilon}_{RCP} \cdot \boldsymbol{k}_f|^2 - |\boldsymbol{\epsilon}_{LCP} \cdot \boldsymbol{k}_f|^2)$. Therefore, for the plane wave final state CD-ARPES does not exist in the electric dipole approximation where it predicts zero dichroism signal for all $\boldsymbol{\epsilon}$ and $\boldsymbol{k}_f$.

To overcome these shortcomings of the FEFS method, the so-called independent atomic center approximation (IACA) was adapted. In the IACA, emission from atomic emitters happens independently but *coherently* [100, 110]. Therefore, the final state ψ_f in the IACA is computed independently for each atom. The contribution of each atomic orbital ϕ_j in the coherent sum at observer $\boldsymbol{k}_f$ is a product of three amplitudes: the weight of the atomic orbital C_j representing the orbital's contribution into the initial wave function ψ_i, the phase factor amplitude arises from the real space shift of the orbital's site with respect to origin, hence, the extra path length it needs to reach the detector, and the amplitude representing the optical excitation of the initial orbital ϕ_j into an allowed quantum mechanically final state [110, 111]. In order to apply this to the equation of the matrix element Eq. 2.67, one needs to further assume that each orbital ϕ_j overlaps only with the scattering state of its own muffin tin potential. This approximation neglects any overlap with the scattering states from the neighboring sites. It also neglects multiple scattering as well. Despite this deficiency, this approach improves the description in many cases and allows for non-vanishing CD-ARPES signal [90]. It also takes into account the distortion of the plane wave intensity into different directions due to the atomic potential [108].

For the atomic photoionization and within the formalism of the IACA, the probability amplitude of detecting a photoelectron at $\boldsymbol{k}_f$ is found by adding coherently the amplitude of spherical waves of all angular momentum components into which the initial state can make an optical transition [99]. The partial wave expansion in spherical harmonics Y_l^m naturally leads to dipole selection rules $\Delta l = \pm 1$, with

[14] $M_{free}(\boldsymbol{k}_f) \propto \langle \psi_f | \boldsymbol{A} \cdot \boldsymbol{P} | \psi_i \rangle$, where $\boldsymbol{A} = \hat{\boldsymbol{\epsilon}} A_0 e^{i\boldsymbol{q}\cdot\boldsymbol{r}} \approx A_0 \hat{\boldsymbol{\epsilon}}$ (in the electric dipole approximation; see Sec. 2.5.1.1) and $\boldsymbol{p} = -i\hbar\nabla$. Using the hermiticity of $\boldsymbol{p}$ and operating with ∇ on the free-electron final state $\psi_f = e^{\boldsymbol{k}_f \cdot \boldsymbol{r}} \Longrightarrow M_{free}(\boldsymbol{k}_f) \propto (\hat{\boldsymbol{\epsilon}} \cdot \boldsymbol{k}_f)\langle e^{i\boldsymbol{k}_f \cdot \boldsymbol{r}}|\psi_i\rangle$.

$\Delta m = 0$ for linear light and $\Delta m = \pm 1$ for circular $C\pm$ light [112, 113], with related radial integrals and phase shifts, previously tabulated for selected atoms [89]. Therefore, for a particular initial state atomic orbital $\psi^{(i)}_{n,l,m}$, the final state of the atomic photoionization is a coherent sum of the available allowed $l \pm 1$ final state channels, i.e. one must sum over the possible final states which can be reached by photoemission from a given atomic orbital. For example, allowed emission from a p orbital of Y_1^{-1} angular part with a circular C_+ light is into Y_0^0 (s orbital) and Y_2^0 (d orbital) channels. Importantly, $l \pm 1$ channels generically exhibit different orbital phase shifts $\delta_{l\pm1}$, where δ is the induced shift in the sinusoidally oscillating character of the radial wave function in the limit of large radius. The atomic photoionization cross section is proportional to the cosine of the phase-shifts difference $cos(\delta_{l+1} - \delta_{l-1})$ which represents interference between the outgoing $l+1$ and $l-1$ waves indicating final state interference already for atomic photoionization [89, 114]. In the case of a surface of a periodic solid, one needs to consider the Bloch wave function of the form $\psi_i = e^{i\boldsymbol{k}_{i||}\cdot\boldsymbol{r}} \cdot u(\boldsymbol{r})$, where $u(\boldsymbol{r})$ is in-plane periodic. Since the IACA matrix element acts as a Fourier transform, the free-electron term $e^{i\boldsymbol{k}_{i||}}$ determines the non-vanishing intensity of the final parallel wavevector for a certain energy eigenvalue, $E(k_f)$. Within this scheme, for an ideal 2D system it leads to appearance of sharp dispersive features in the ARPES spectra that are routinely interpreted as initial bands. The $u(\boldsymbol{r})$ acts as a form factor, which determines the angular intensity distribution through the participating atomic scattering wave functions and interatomic phase shifts. In case of surface sensitive photoemission measurements, the meaning of the perpendicular momentum $k_{i\perp}$ is not well defined for a semi-periodic system of the terminated crystal. Within IACA, one can assume a final state dampening due to inelastic mean-free path, that effectively leads to broadening of the measured $k_{f\perp}$ dispersion in the $h\nu$-dependent experiment.

2.7 WIEN2k

The WIEN2k program performs quantum mechanical calculations to exploit the periodic nature of solids. It is based on the augmented plane wave plus local orbitals (APW+lo) basis set method to solve the Kohn–Sham equations for the ground state density, total energy, and energy bands of a many-electron system, for detailed information the reader can follow [115, 116] . Following the Bloch theorem discussed in Sec. 2.1, the wave function $\Psi(\boldsymbol{r})$ of the solid can be written as

$$\Psi(\boldsymbol{r}) = \phi_{\boldsymbol{G}}(\boldsymbol{r})e^{i\boldsymbol{G}\cdot\boldsymbol{r}} = \phi_{\boldsymbol{G}}(\boldsymbol{r})e^{i(\boldsymbol{k}+\boldsymbol{K})\cdot\boldsymbol{r}} = \phi_{\boldsymbol{k}n}(\boldsymbol{r})e^{i\boldsymbol{k}\cdot\boldsymbol{r}} \tag{2.68}$$

where the reciprocal lattice vector $\boldsymbol{G}$ can be written as $\boldsymbol{G}$=$\boldsymbol{k}$+$\boldsymbol{K}$ such that $\boldsymbol{k}$ is a vector within the 1^{st} BZ and $\phi_{\boldsymbol{k}n}(\boldsymbol{r})$ are the so-called Kohn–Sham orbitals. A direct way to get these Kohn–Sham orbitals is to expand them in term of plane waves,

$$\phi_{\boldsymbol{k}_n}(\boldsymbol{r}) = \sum_{\boldsymbol{K}} c_{\boldsymbol{K}}^{n,\boldsymbol{K}} e^{i\boldsymbol{K}\cdot\boldsymbol{r}} \tag{2.69}$$

to get

$$\Psi_{\boldsymbol{k}_n}(\boldsymbol{r}) = \sum_{\boldsymbol{K}} c_{\boldsymbol{K}}^{n,\boldsymbol{K}} e^{i(\boldsymbol{k}+\boldsymbol{K})\cdot\boldsymbol{r}} \tag{2.70}$$

However, describing the highly oscillating valence wave functions in the vicinity of the atomic cores due to the steep potential requires large number of basis functions i.e. high $\boldsymbol{K}$ values. One way to solve this disadvantage is to merge the core electrons into the nuclei to form pseudopotentials, making the valence electrons wave functions moving in such potentials much smoother and describable in much smaller number of plane waves. Another way which is implemented by WIEN2k is the full-potential method that takes all electrons into account and it is based on augmenting the plane wave basis functions with more localized functions of the so-called linearized augmented plane wave plus local orbitals {(L)APW+lo} method.

This method divides the real space unit cell into two regions Fig. 2.13: non-overlapping spheres[15], called Muffin-tin (MT) regions, centered at the nuclear sites and interstitial region (I) in-between these spheres. In the I-region, electrons are far from the atomic nuclei and behaves like free electrons in a slowly varying potential, hence, can be described as plane-waves, while in the MT-spheres, electrons are strongly bind to the nuclei and can be described by atomic-*like* functions. The potential can then be defined as

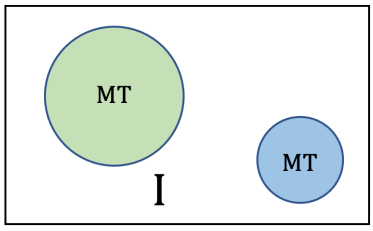

Figure 2.13: **Muffin-tin approximation.** Partitioning the real space into Muffin-tin spheres (MT) centered at nuclei, and interstitial region I.

[15]To increase the computational efficiency, the sizes of the spheres are chosen as large as possible and the radii of these spheres satisfy R_{MT}(f-orbitals) > R_{MT}(d-orbitals) > R_{MT}({s,p}-orbitals).

$$V(\boldsymbol{r}) = \begin{cases} V(\boldsymbol{r}) & \boldsymbol{r} \in \text{MT} \\ \text{constant} & \boldsymbol{r} \in \text{I} \end{cases}$$

and the corresponding APW basis functions in the two different regions are given by

$$\phi^{APW}_{\boldsymbol{k}_n}(\boldsymbol{r}, E_l) = \begin{cases} \sum_{lm} A_{lm,\boldsymbol{k}_n} u_l(r, E_l) Y_{lm}(\hat{\boldsymbol{r}}) & \boldsymbol{r} \in \text{MT} \\ \frac{1}{\sqrt{\Omega}} e^{i\boldsymbol{k}_n \cdot \boldsymbol{r}} & \boldsymbol{r} \in \text{I} \end{cases}$$

where Ω is the volume of the unit cell, Y_{lm} are spherical harmonics, A_{lm} is an expansion coefficient to be determined via matching $\phi^{APW}_{\boldsymbol{k}_n}(\boldsymbol{r}, E_l)$ at the boundary between the Muffin-tin regions and the interstitial, and $u_l(r, E_l)$ are solutions of the radial Schrödinger equation for the spherical potential $V(\boldsymbol{r})$ and energy E_l.

A disadvantage in the APW-method is that E_l is needed to be determined exactly in order to describe the wave function, and because of the way $u_l(r, E_l)$ depends on energy, this creates a non-linear eigenvalue problem making the method computationally costly as it needs to be solved iteratively.

The APW is typically linearized via expanding the basis functions in the Muffin-tin spheres based, additionally, on the energy derivative of $u_l(r, E_l)$ of the so-called linearized augmented plane wave LAPW to get the following basis functions

$$\phi^{LAPW}_{\boldsymbol{k}_n}(\boldsymbol{r}, E^1_l) = \begin{cases} \sum_{lm} \{A_{lm,\boldsymbol{k}_n} u_l(r, E^1_l) + B_{lm,\boldsymbol{k}_n} \dot{u}_l(r, E^1_l)\} Y_{lm}(\hat{\boldsymbol{r}}) & \boldsymbol{r} \in \text{MT} \\ \frac{1}{\sqrt{\Omega}} e^{i\boldsymbol{k}_n \cdot \boldsymbol{r}} & \boldsymbol{r} \in \text{I} \end{cases}$$

This way the LAPW method is more flexible compared to the APW where it is not necessary to know the exact E_l value, instead for any linearization energy E^1_l chosen close to E_l it is possible to obtain the radial function $u_l(r, E_l)$ through a Taylor expansion : $u_l(r, E_l) = u_l(r, E^1_l) + (E_l - E^1_l)\dot{u}_l(r, E^1_l) + O\{(E_l - E^1_l)^2\}$. The expansion coefficients $A_{lm,\boldsymbol{k}_n}$ and $B_{lm,\boldsymbol{k}_n}$ are determined by matching the value and the slope of the augmenting function to a plane wave at R_{MT}.

A special treatment is needed for the so-called semi-core states where part of their charge leaks out of the MT sphere. Mainly in these states more that one n quantum number will have the same l quantum number and correspondingly more that one energy, however, in the LAPW method there is only one linearization energy E_l for every l, this can be solved via introducing local orbitals confined to the Muffin-tin spheres and zero in the interstitial region

$$\phi^{LO}_{lm} = \begin{cases} \{A_{lm} u_l(r, E^1_l) + B_{lm} \dot{u}_l(r, E^1_l) + C_{lm} u_l(r, E^2_l)\} Y_{lm}(\hat{\boldsymbol{r}}) & \boldsymbol{r} \in \text{MT} \\ 0 & \boldsymbol{r} \in \text{I} \end{cases}$$

where they add an additional radial function at a new linearization energy E^2_l. Despite the fact that the LAPW method succeeds in linearizing the eigenvalue problem, however, that will be on the cost of the optimal shape of the basis functions inside the Muffin-tin sphere.

A more efficient way to linearize the APW with the same basis size as the APW is to use the standard APW basis set at fixed energy E_l to keep the linearized eigenvalue problem and add to it local orbital set (lo) which is different than (LO) of the so-called APW+lo method, with lo given by

$$\phi^{lo}_{lm} = \begin{cases} \{A_{lm} u_l(r, E^1_l) + B_{lm} \dot{u}_l(r, E^1_l)\} Y_{lm}(\hat{\boldsymbol{r}}) & \boldsymbol{r} \in \text{MT} \\ 0 & \boldsymbol{r} \in \text{I} \end{cases}$$

here, the coefficients A_{lm} and B_{lm} are determined by normalization and equating the local orbital to zero at R_{MT}.

An example of the calculation done using WIEN2k is shown in Fig. 2.14 (a)

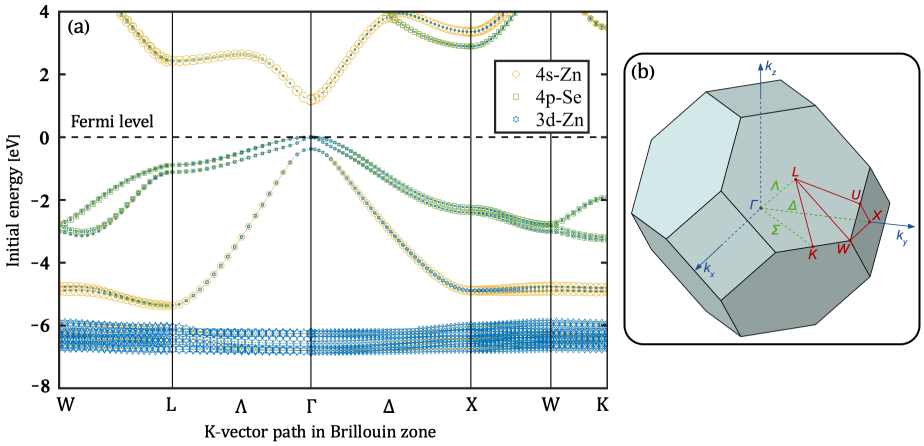

Figure 2.14: **Band structure of FCC** $ZnSe$ **using WIEN2k.** (a) Electronic band structure of the FCC $ZnSe$ using WIEN2k along the high symmetry lines indicated in the corresponding 1^{st} Brillouin zone along side the symmetry labels schematically shown in (b). Band characters of Zn 4s, Se 4p, and Sn 3d levels are indicated by yellow circles, green squares and blue hexagons respectively, where the size of the symbol represents the orbital weight. In the figure, the zero of the energy scale is adjusted to the valence band maximum.

for the FCC semiconductor $ZnSe$ which is calculated along the high symmetry directions labeled in the corresponding 1^{st} Brillouin zone shown in Fig. 2.14 (b).

The figure shows the orbital characters of the valance and conduction bands through different symbols as indicated through the legend, additionally, the weight of those characters is reflected through the size of the symbol used to represent it. Within the framework of the tight binding model, see Appendix A.4, one can imagine that these orbital characters weights are squared of the expansion coefficients $c_{\boldsymbol{k}}^{j\alpha}$ appear in Eq. A.9 for their respective orbitals α's at positions j's. Based on the electron configuration of the zinc atom Zn:$[Ar]4s^2\ 3d^{10}$, the 3d-orbital is completely filled, which means that these electrons behave like core electrons with their charge density mostly located close to the Zn nucleus reflecting the nearly non-dispersive group of bands within the energy range [-7,-6] eV. The valence bands within the energy range [-6,0] eV are mainly a mixture of Se 4p and Zn 4s orbitals, while the conduction bands are mostly made out of the Zn 4s orbital.

3. Experimental setup

Within the scope of this PhD thesis, the electronic band structures of various transition metal dichalcogenides (TMDCs) have been investigated using high-resolution spin- and angle-resolved photoemission spectroscopy (S-ARPES). The S-ARPES system was enhanced with a newly designed universal 5-axis cryocooled manipulator from PREVAC, offering five degrees of freedom for precise control over the sample under investigation. This chapter provides a detailed explanation of the S-ARPES setup, including the operating principles of both the ARPES system and the spin detectors. In addition, an overview of the sample preparation procedures, carried out in the preparation chamber before conducting spin- and angle-resolved measurements, will be discussed in detail.

3.1 Need for Ultra-High Vacuum (UHV)

To accurately collect the energy, momentum, and spin information from photoemitted electrons, the ejected electrons must travel into the analyzer without scattering and proceed to the detector. This necessitates an ultra-high vacuum (UHV) environment, which is essential for imaging the material's initial band structure. In our S-ARPES setup, we maintain a base pressure of $< 5{\cdot}10^{-11}$ mbar. These UHV conditions are achieved using a series of turbomolecular pumps, which are typically pre-pumped by another stage of turbomolecular pumps, with the entire system being initially evacuated by oil-free scroll pumps.

At this ultra-high vacuum level, using the equation of state $PV = nR_oT$, the density of residual molecules inside the analysis chamber is $\sim 10^{12}\ \frac{particles}{m^3}$ [1]. The *mean free path*, λ, of a particle (e.g., electron) at this pressure is $\sim 10^6$ m[2], which represents the average distance an electron can travel in this UHV environment before undergoing a collision [117]. This path length is sufficiently long to ensure that photoelectrons emitted from the sample can reach the detector without scattering.

Using the kinetic theory of gases, one can estimate the impingement rate, J, which is defined as the number of molecules per second striking a unit area at constant pressure. At atmospheric pressure, outside the vacuum system, $J_{atmosphere} \sim 2.8 \times 10^{23}\ \frac{molecules}{s{\cdot}cm^2}$[3]. On the other hand, at our UHV system with a pressure

[1] $PV = nR_oT = \frac{N}{N_A}R_oT \Longrightarrow \tilde{n} = \frac{N}{V} = \frac{P}{k_BT} \sim 10^{12}\ \frac{particles}{m^3}$ (at $T = 298K, P = 5{\cdot}10^{-11}\ mbar$).

[2] $\lambda = \frac{1}{\sqrt{2}\sigma\tilde{n}}$; $\sigma = \pi d^2$ is the collision cross-section (with $d = 3.74 \times 10^{-10}$ m for air molecules).

[3] $J = \frac{1}{4}\frac{N}{V} < v >= \frac{1}{4}\frac{N_An}{V}\sqrt{\frac{8R_oT}{\pi M}} = \frac{1}{4}\frac{N_AP}{R_oT}\sqrt{\frac{8R_oT}{\pi M}}$; $M_{air} = 0.02896\frac{kg}{mole}, R_o = 8.3145\frac{J}{K{\cdot}mole}$

$(T = 298K, P_{atmosphere} \sim 1\text{bar} \Longrightarrow J_{atmosphere} \sim 2.8 \times 10^{23}\frac{molecules}{s{\cdot}cm^2})$,

$(T = 298K, P_{UHV} \sim 5 \cdot 10^{-11}\text{mbar} \Longrightarrow J_{UHV} \sim 1.4 \times 10^{10}\frac{molecules}{s{\cdot}cm^2})$

$\sim 5 \cdot 10^{-11}$ mbar, $J_{UHV} \sim 1.4 \times 10^{10}$ $\frac{molecules}{s \cdot cm^2}$. Since there are roughly 10^{15} $\frac{atoms}{cm^2}$ on a typical metal surface, then $\frac{10^{15}}{S \cdot J}$ is the coverage time needed to form a full mono-layer where $S \leq 1$ is the so-called *sticking coefficient*, which is a measure of the probability that incident molecules stick on a surface. Assuming every molecule hitting the sample will get adsorbed on its surface, i.e. S=1, then at room temperature and atmospheric pressure, the sample surface will get contaminated completely within just $\sim$ 3 nsec. However, inside our analysis chamber the sample can service for $\sim$ 20 hours at room temperate and $S = 1$ before just one layer of residual gases in the chamber contaminate it. This of course can vary depending on the nature of the sample under investigation, its temperature as the sticking coefficient increases at low temperatures, and the type of residual gases in the chamber[4].

3.2 The High-Resolution S-ARPES setup

Spin and angle-resolved photoemission spectroscopy (S-ARPES) is a highly powerful technique for probing the energy, momentum and spin-resolved electronic band structure of solids. Our experimental setup consists of three interconnected chambers: the load lock chamber, the preparation chamber and the main chamber. A schematic illustration of the laboratory-based S-ARPES apparatus is shown in Fig. 3.1. The three chambers are connected, but can be sealed from each other using UHV valves, allowing for individual venting or pumping. The load lock chamber is equipped with a garage containing three sample slots and a wobble stick for transferring samples to the manipulator in the preparation chamber. The compact design of the load lock chamber facilitates rapid pumping. The subsequent sections will provide a detailed discussion of the preparation and main chambers.

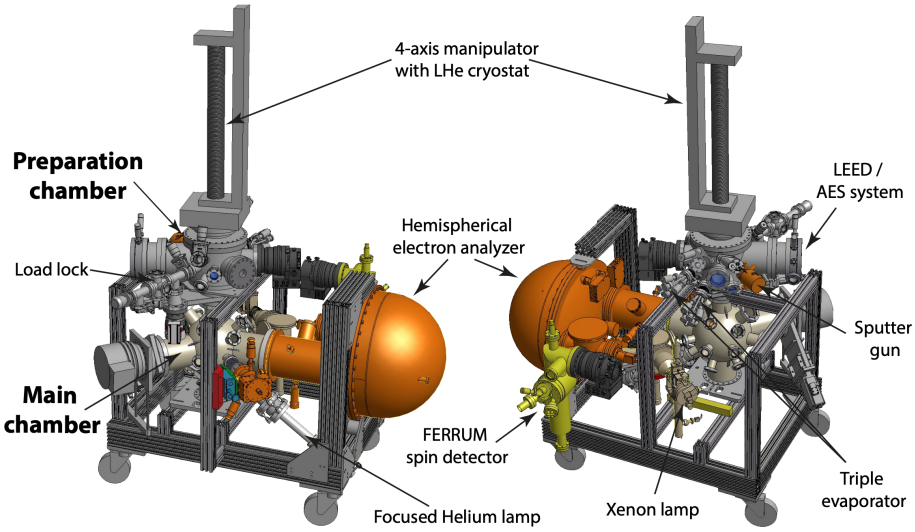

Figure 3.1: 3D schematic representation of the spin-ARPES apparatus viewed from two angles, highlighting and labeling key components critical to its operation.

[4]In the 10^{-11} mbar range, most of the residual gas is H_2 and CO. With a sticking coefficient $S_{CO/Pt} \sim 0.7$ the converge time for a Pt-sample is $\sim$ 28 hours.

3.2.1 Preparation Chamber

Figure 3.2 shows a top view of a 3D sketch of the preparation chamber, with labels indicating the most important components, which will be explained separately. As the name suggests, all sample preparation processes are carried out in this chamber before the sample is transferred via the manipulator to the main chamber for measurements.

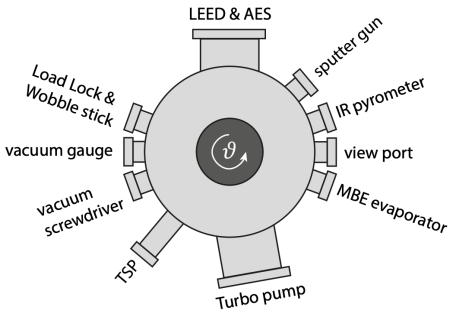

Figure 3.2: Top view of the preparation chamber, with labels indicating the most important components.

Ultra-clean Sample Surface

Photoemission experiments are highly sensitive to the top atomic layers of a material. To accurately extract the encoded information about the surface electronic structure from the photoemitted electrons, it is essential to detect them without scattering caused by impurities on the sample surface. This necessitates the presence of atomically clean and flat surfaces. Conventionally, two methods are employed to achieve this:

(i) **Cleaving single crystals inside the UHV chambers**: This method employs two techniques to achieve cleavage. The first technique involves the scotch tape method (see Fig. 3.3(a), upper two slots), where scotch tape is adhered to one side of the cleavable single crystal and folded around a circularly shaped copper wire on the opposite side (see Fig. 3.3(b)). The second technique uses a cleaving post (see Fig. 3.3(a), third slot), which consists of a small ceramic post (approximately 2 mm in diameter) glued to the cleavable side of the sample using silver epoxy (see Fig. 3.3(d)). The load-lock wobble stick is then employed to either pull out the scotch tape (see Fig. 3.3(c)) or to knock off the ceramic post (see Fig. 3.3(e)), thereby exposing a freshly cleaved sample surface suitable for ARPES characterization. For van der Waals (vdWs) bonded systems, such as transition metal dichalcogenides and bulk 3D topological insulators, the scotch tape method is particularly advantageous due to the weak interlayer bonding along the c-axis, facilitating cleavage along this direction and yielding sharp spectral features. However, this method often results in atomically flat and clean but small areas that may not accommodate larger light sources with bigger beam spots.

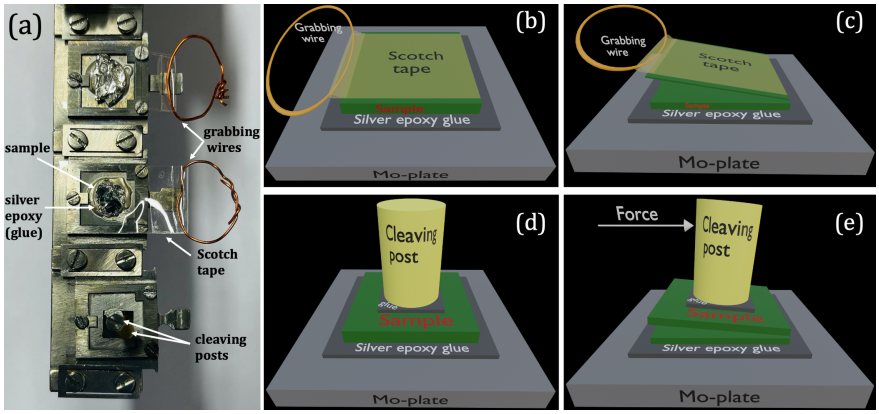

Figure 3.3: (a) Various single-crystal samples glued onto sample holders using silver epoxy. Two samples are equipped with scotch tape on top, while one features ceramic posts, both prepared for cleaving under ultra-high vacuum conditions. Copper wire rings are utilized to remove the tape and prevent it from falling into the vacuum chamber. (b)-(e) Schematic representation of the cleaving techniques utilizing both the tape and the ceramic post. The size of the Mo-plate is 10×10 mm^2.

(ii) **In-situ grown thin films**: This technique involves the use of molecular beam epitaxy (MBE) to grow samples, allowing them to be transferred to the ARPES setup without breaking ultra-high vacuum (UHV) conditions, thereby maintaining a highly clean environment. This method produces large and flat surfaces ideal for ARPES measurements. However, it is time-consuming due to the necessary transfer process from PGI-9, where samples are typically grown, to PGI-6, as our laboratory lacks a direct MBE chamber connected to the ARPES chamber.

Heater

One of the most widely employed techniques in surface science for achieving atomically flat and clean surfaces is annealing. This process utilizes a custom-designed heater specifically for this purpose. The heater incorporates a slot that accommodates the sample, which is affixed to a sample holder. A tungsten-coiled filament is positioned on the backside of the sample holder, and a power supply is connected to generate a current of up to approximately 2.3 A. This current flows through the tungsten filament, heating it and thermally emitting electrons into the vacuum environment. These emitted electrons are subsequently accelerated toward the sample holder, which is maintained at a high voltage of approximately 1000 V via a separate power supply.

The electron bombardment results in the heating of both the sample holder and the mechanically fixed sample, facilitating the desorption of adsorbed contaminants, primarily water, from the surface. The temperature of the sample is monitored using a remote-sensing pyrometer, which operates at temperatures exceeding 300°C and is positioned outside the preparation chamber, allowing it to view the sample through a visible light viewport. Additionally, the heater can be employed to smooth the sample surface following the deposition of materials, which is achieved through either

single or triple evaporators, as will be detailed later.

Sputter Cleaning

Surfaces of samples can be etched using a process known as sputtering. Figure 3.4 illustrates the operational principle of the sputtering gun, which is mounted in the UHV preparation chamber of the ARPES system. Argon gas from an external container is introduced into the gas cell via the leak valve. A high potential difference is applied between the cathode and the anode, resulting in the emission of electrons from the cathode that ionize the argon atoms within the cell, thereby generating a plasma of argon ions and free electrons.

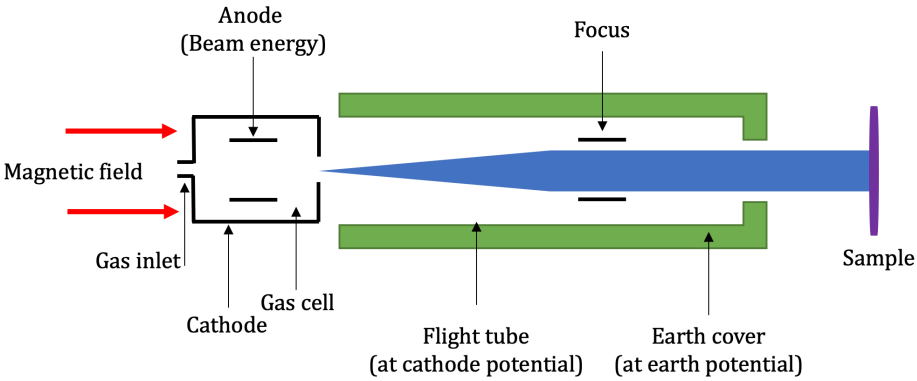

Figure 3.4: Diagram showing the operation principle of the sputter gun, labelled with the most important parts.

The longitudinal magnetic field produced by an external permanent magnet forces the electrons in the cell to follow spiral trajectories, increasing their path lengths and subsequently enhancing the probability of collisions that produce additional ions. The argon ions are repelled from the anode, acquiring kinetic energy approximately equal to that of the anode, and are attracted toward the cathode. A small aperture is present at the cathode, allowing the energetic argon ions to escape into the flight tube, where a focusing element is employed to refocus the broadened beam size caused by space charge limitations, particularly for low-energy beams.

The highly energetic argon ions bombard the target material (sample), facilitating momentum exchange that effectively removes contaminants adhering to the surface and may even eject some of the top layers of the sample, i.e. etching the sample. These ion collisions generate a measurable current through the sample, referred to as the sample current I_{sample}. The parameters that can be optimized to achieve a clean surface include the sample current, sputtering duration, ion beam kinetic energy and argon partial pressure. In this thesis, this method has been extensively employed to clean the copper plate of the head stage in the newly mounted five-axis manipulator during the cooling process, enabling the measurement of the lowest attainable temperatures using the Fermi-Dirac fitting analysis technique.

Electron-Beam Vacuum Deposition of Thin Films

Electron-beam evaporation is regarded as one of the most widely used methods for depositing thin layers of various materials onto desired substrates. The preparation chamber of our vacuum system is equipped with both triple and single evaporators from the company FOCUS electronics GmbH, which are utilized for this deposition process.

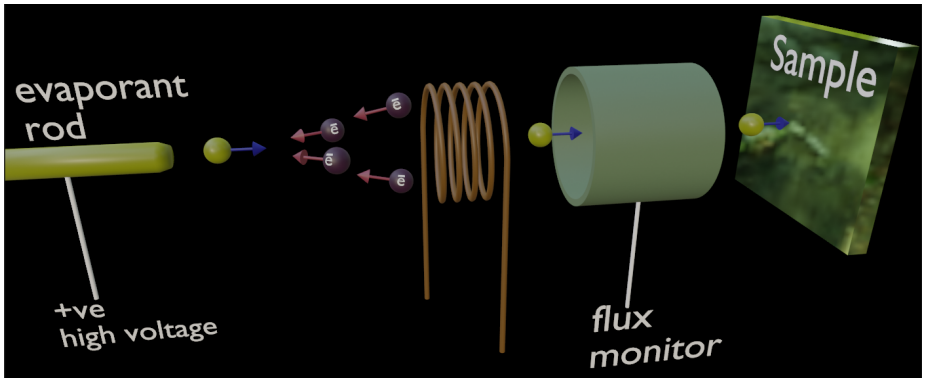

Figure 3.5: 3D schematic representation of the e-beam evaporation process used for depositing a material onto the sample.

Figure 3.5 illustrates the operational principle of the deposition process in a 3D sketch. In this setup, a tungsten filament is heated via an electric current to a temperature enough to provide the thermal energy needed to overcome the material's work function. At this elevated temperature, some electrons gain sufficient energy to escape from the filament's surface, generating an electron beam that can be accelerated towards an evaporant rod, which is maintained at a high positive adjustable voltage (positive electrode). This electron beam bombards the head of the evaporant rod, heating it up, leading to the evaporation of material from the rod's apex. The bombardment generates an electron emission current I_{em} within the rod, which is continuously measured. As the evaporated atoms travel towards the sample, they pass through a flux monitor, which measures the ion flux that is directly proportional to the flux of the evaporated atoms.

By controlling I_{em} and the rod voltage, the flux rate of the evaporated atoms can be precisely adjusted for a desired duration, allowing for accurate definition of the layer thickness of the deposited material. The setup includes both triple and single evaporators [118]. At their outlets, a shutter positioned between the flux monitor and the sample can be opened or closed by a rotary drive, enabling fine flux adjustment before exposure. In the case of the triple evaporator, there are three distinct cells, each functioning similarly to the single evaporator, allowing for the simultaneous or sequential evaporation of up to three different materials

Five - Axis Liquid He Cryostat Manipulator

The system has been enhanced with a customized universal 5-axis manipulator from the company PREVAC, which provides five degrees of freedom. It can move spatially along three axes (x, y, z), with x and y movements limited to $\pm$ 12.5 mm around the

central axis of the manipulator. The deferentially pumped rotary seal, featuring two isolated pumping stages, enables continuous azimuthal rotation θ of 360° through the vacuum wall of the UHV system.

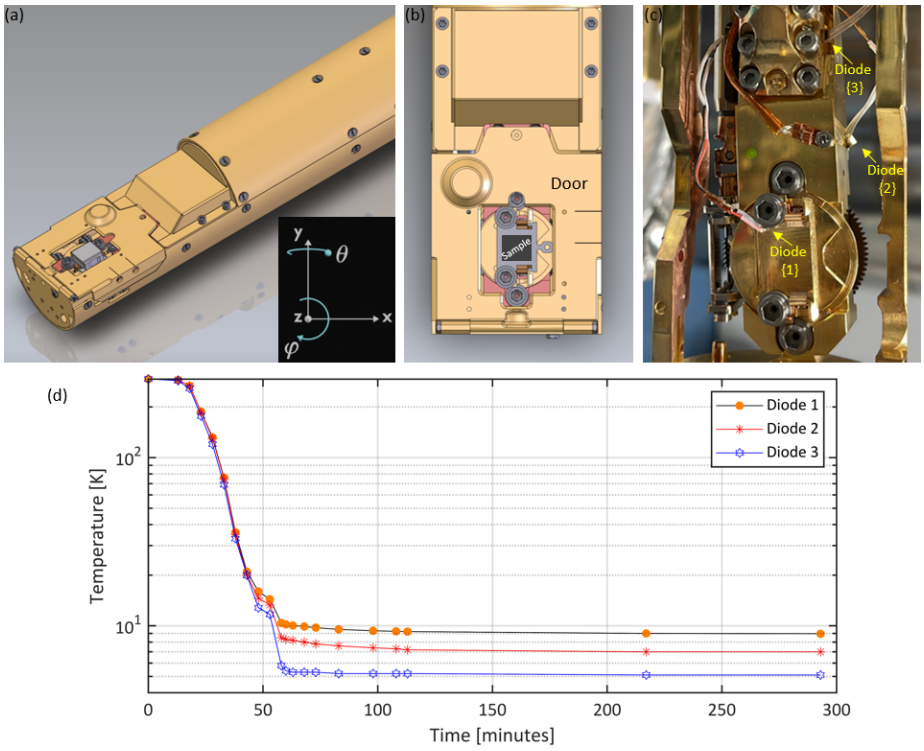

Figure 3.6: (a) 3D design for the end parts of the manipulator. Inset shows allowed degrees of freedom. (b) Font view of (a) showing a sample fixed by two screws. Other screws away from the sample are for tightening the head stage to the rest of the manipulator body to achieve a better sample cooling while the door is closed. (c) A real front picture with the three diodes labeled during a cooling test. (d) Temperature change over time during a cooling process recorded by the three diodes shown in (c).

The back side of the head stage of the manipulator is connected to the main body and secured by two nuts. This configuration allows for unlimited polar rotation φ around the z-axis when the sapphire plates slide over each other. Figure 3.6(a) shows a 3D design of the end parts of the manipulator, with the inset showing the allowed degrees of freedom. A front view of the design is presented in Fig. 3.6(b).

All movements are facilitated by stepper motors controlled via software installed on a PC. After transferring the sample from the load lock to the manipulator using the wobble stick mounted in the load lock and sealing the load lock from the preparation chamber, the sample can be mechanically secured into the head stage by tightening a pair of screws using a vacuum screwdriver (see Fig. 3.6(b)), pressing the sample holder against the head stage.

The manipulator features two concentric cylinders that accommodate one end of a transfer cooling line, while the other end is immersed in a dewar containing liquid helium. The transfer line is designed to utilize capillary action, allowing liquid He to

flow from the dewar to the manipulator, where it is pumped from the two concentric cylinders by a rough pump. In principle, the faster the He is pumped, the lower the achievable sample temperature.

The other two screws, located away from the sample as seen in Fig. 3.6(b), are used to secure the manipulator's head to the rest of the body, ensuring thermal contact necessary for achieving the minimum temperature while cooling the sample. Additionally, the head of the manipulator is equipped with a door, as labeled in Fig. 3.6(b), that can be closed with the vacuum screwdriver during cooling, providing an additional shield to enhance cooling efficiency.

Figure 3.6(c) shows a photo of the head of the manipulator, with the cover shield being removed, prepared for a cooling test. Three diodes are labeled in the figure. While diodes 2 and 3 are permanent, diode 1 was mounted directly and fixed under the screw to the closest point to where the sample is going to be placed. Figure 3.6(d) shows the temperatures over time read by the three diodes during a cooling process. Diode 1, closest to sample shows that we could achieve a minimum temperature of $\sim$ 9K.

Lamp-based VUV Spin-ARPES

Noble gas discharge lamps are the predominant vacuum ultraviolet (VUV) light sources utilized in laboratory-based ARPES-setups. The operating principle of these VUV light sources is typically founded on the cold cathode capillary discharge method [119, 120], wherein a high potential difference is applied between the two electrodes of the discharge tube, which is continuously filled with a noble gas. This generated electric field excites the noble gas atoms, causing some of their electrons to be elevated to higher energy levels or to be completely ejected as free electrons, thus producing plasma within the discharge tube.

As the excited atoms and cations relax, they emit light at characteristic wavelengths that depend on the specific noble gas filling the discharge tube. For photoemission experiments, it is crucial to use light sources that provide photon energies sufficient to overcome the work function of the material under investigation (typically around 4.5 eV for metals). This necessitates the emission of photons in the ultraviolet range, specifically with wavelengths shorter than 200 nm. Due to the absorption of these photons by air, noble gas discharge lamps emitting light in this range must be integrated into a vacuum system to ensure effective operation.

Helium Lamp

The helium discharge lamp is particularly notable as the most common light source used in ARPES setups, and the S-ARPES laboratory at PGI-6 is equipped with the **HIS 13** helium discharge lamp. In this system, applying a high voltage across a discharge capillary tube filled with helium gas, creates a plasma through ionization and excitation processes. When the electric field accelerates free electrons, these energetic electrons collide with neutral helium atoms, leading to excitation or ionization. In excitation, one of the helium atom's electrons is promoted from the $1s$ orbital to a higher energy level, such as ($2p$, $3p$, or $4p$), while in ionization, an electron is completely removed, forming a singly ionized helium ion (He^+).

The excited helium atom can exist in one of two quantum states: parahelium (singlet state, $S = 0$), where the two electrons have opposite spins, or orthohelium

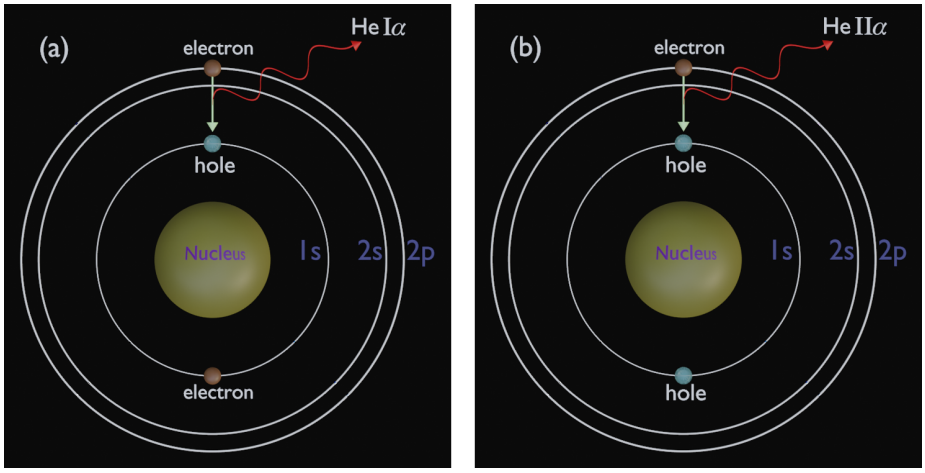

Figure 3.7: Generation of the most intense resonance lines HeI_α (a) and $HeII_\alpha$ (b) are being generated in (a) and (b), depicting the transitions from the first excited state to the ground state for the He-atom and He^+ ion correspondingly.

(triplet state, $S = 1$), where the electrons have parallel spins [121]. These states follow different selection rules for transitions, which affect the emission spectrum of the lamp.

Parahelium states have symmetric spin wavefunctions but antisymmetric spatial wavefunctions, allowing them to decay quickly via electric dipole transitions, emitting strong HeI spectral lines, such as HeI_α, HeI_β, and HeI_γ. In contrast, orthohelium states have antisymmetric spin wavefunctions and symmetric spatial wavefunctions, making their transitions spin-forbidden in electric dipole radiation, which significantly prolongs their lifetimes [122].

Similarly, when He^+ ions are excited and return to lower energy states, they emit HeII spectral lines, including $HeII_\alpha$, following the same selection rules that restrict transitions to those with $\Delta l = \pm 1$, meaning that electrons move between orbitals of different angular momentum (e.g., $\mathbf{p} \rightarrow \mathbf{s}$ transitions are allowed, while $\mathbf{s} \rightarrow \mathbf{s}$ transitions are forbidden).

These emission lines are well-resolved and exhibit extremely narrow linewidths of only a few meV, making them highly suitable for high-energy resolution photoemission measurements without the necessity of a monochromator. The strongest spectral lines, HeI_α (21.22 eV, 58.43 nm) and $HeII_\alpha$ (40,81 eV, 30.38 nm), are illustrated in Fig. 3.7(a) and Fig. 3.7(b), respectively.

As previously mentioned, the helium lamp must be connected to the UHV system. However, plasma ignition within the capillary discharge tube occurs at a significantly higher pressure of approximately $5 \cdot 10^{-3}$ mbar in the first pumping stage. To accommodate this, the setup includes two differential pumping stages that connect the lamp to the main analysis UHV chamber, effectively reducing the pressure in the chamber to $< 6 \cdot 10^{-9}$ mbar during measurements (at the base pressure of $\sim 3 \cdot 10^{-11}$ mbar in our case).

The light generated within the capillary discharge tube is directed and focused onto the sample using a toroidal gold-coated mirror after exiting the light capillary.

This mirror allows the beam spot to be focused down to approximately $\sim 1.1\ mm$ in diameter on the sample [123], enabling selective probing of different regions in inhomogeneous samples.

The Electron Spectrometer

The core component of the ARPES spectrometer is the *MB Scientific* A1 hemispherical electron energy analyzer, which generates a simultaneous 2D intensity map as a function of energy and momentum. It features a mechanoelectrostatic lens deflector system and two concentric conductive hemispheres with a constant voltage difference applied between them. A schematic diagram, labeled with the most significant elements, is depicted in Fig. 3.8(a). Photoelectrons emitted from the grounded sample enter the imaging lens system, which facilitates the mapping of emission angles over approximately $\pm 15°$ in both the k_x and k_y directions.

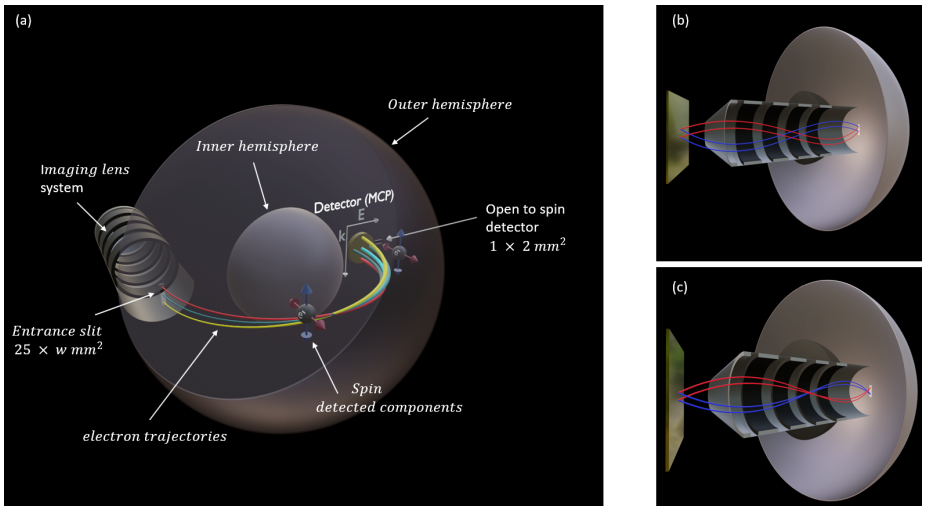

Figure 3.8: **Schematic 3D representations of the MB Scientific A1 hemispherical electron energy analyzer and the mechanoelectrostatic lens deflector system**. In (a), photoelectrons are filtered within the analyzer based on their kinetic energies (horizontally, shaded cyan trajectories) and their emission angles (vertically, red, cyan, and yellow trajectories) on the detector (MCP). This configuration provides a simultaneous 2D intensity map versus energy and momentum. An opening next to the MCP indicates the two spin components (blue and red arrows) that can be filtered using the spin detector. (b) and (c) illustrate the spatial and angular modes, respectively, through which the lens system projects photoelectrons onto the entrance slit of the analyzer.

Depending on the lens mode selected by adjusting the voltages applied to the lens deflector system, electrons will be projected onto the entrance slit of the outer hemisphere while preserving either their:

- **Spacial distribution**: In this mode, electrons emitted at different angles from the same spot on the sample will be projected onto the corresponding spot on the entrance slit (see Fig. 3.8(b)).

- **Angular distribution**: In this mode, electrons emitted from different locations on the sample but with the same emission angle will converge and be projected onto a single spot on the entrance slit (see Fig. 3.8(c)).

Only photoelectrons with kinetic energies that fall within a narrow energy window centered around the pass energy E_p will be transmitted through the analyzer. For the $MB\ Scientific$ A1 spectrometer, this energy window has a width of approximately 10% of E_p. These selected photoelectrons follow trajectories, based on their kinetic energies and emission angles, from the entrance slit to the detector on the opposite side of the analyzer.

Electrons within this energy window, having exactly E_p kinetic energy, will follow the central trajectory. In contrast, those with lower or higher energies will end up closer to the inner or outer hemisphere, respectively. Electrons with kinetic energies that fall outside this energy window will be absorbed or scattered by the inner or outer hemisphere. By varying the voltages between the typically grounded sample and the entrance slit of the analyzer, a wide range of initial kinetic energies can be filtered.

The energy resolution of the hemispherical analyzer is expressed by the following equation [124]:

$$\Delta E_{analyzer} = E_P \cdot \left(\frac{w}{2R_o} + \frac{\alpha_{max}^2}{2} \right) \approx E_P[eV] \cdot \frac{w[mm]}{R_o[mm]} \tag{3.1}$$

where E_P is the pass energy, w is the width of the entrance slit, α_{max} is the maximum value of the entrance angle and $R_o = \frac{R_1+R_2}{2}$ (20 cm for the $MB\ Scientific$ A1 spectrometer) is the mean radius of the two concentric hemispheres of radii R_1 and R_2. An additional angular aperture in front of the entrance slit leads to the approximation $\frac{\alpha_{max}^2}{2} = \frac{w}{2R_o}$.

This formula indicates that lower pass energy and smaller slit widths result in improved energy resolution; however, this also decreases the intensity of the transmitted electrons. Therefore, it is essential to find an optimal balance between energy resolution and intensity for effective measurements.

Resolution of the setup with the newly upgraded 5-Axis manipulator

The total energy resolution ΔE_{total} of an experimentally measured spectrum is primarily determined by three factors: the analyzer resolution $\Delta E_{analyzer}$, which depends on the combination of pass energy E_P and slit width w used during the experiment, the linewidth of the exciting photon $\Delta E_{h\nu}$, and the thermal broadening $\Delta E_{thermal}$ caused by the sample temperature. These factors combine according to the following relation:

$$\Delta E_{total} = \sqrt{\Delta E_{analyzer}^2 + \Delta E_{h\nu}^2 + \Delta E_{thermal}^2} \tag{3.2}$$

The photon energy $h\nu$ resolution is extremely high due to the sharp spectral line, with values of ($\Delta E_{h\nu}^{He} \sim 1$ meV and $\Delta E_{h\nu}^{Xe} \sim 600$ μeV) [125, 126]. At the Fermi level, the temperature effect on the sample introduces an unavoidable broadening of approximately $4k_BT$, as dictated by Fermi-Dirac (FD) statistics [127].

At room temperature, this FD broadening dominates the total energy resolution, for most cases contributing approximately 100 meV, regardless of analyzer settings

or the negligible contribution from the photon energy resolution[5]. With the recently upgraded five-axis manipulator, the sample can be cooled to temperatures as low as 9K. Under these low-temperature conditions, using analyzer settings with $\Delta E_{analyzer} \sim 1$ meV, and neglecting the photon source broadening, a total energy resolution of approximately 3 meV can be achieved.

Geometry of the Spin-Integrated measurements (ARPES)

This section shows the geometry of the spin-integrated measurements conducted in the S-ARPES laboratory at PGI-6 (See Fig. 3.9(a)). The sample is aligned for normal emission, positioning its surface within the xy-plane and at a distance of 35 mm along the z-direction from the lens of the spectrometer. Three different sources for electron excitations are utilized, represented by the green, red and blue arrows corresponding to helium lamp, 6 eV laser and xenon lamp [125], respectively. The He light impinges on the sample within the yz-incidence plane at an angle of 24° relative to the sample surface, while the laser and xenon lights strike the sample within the xz-incidence plane at an angle of 45° from the right and left, respectively.

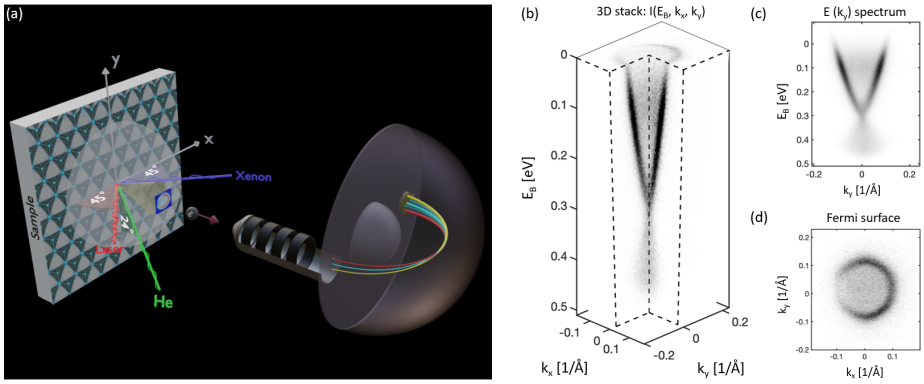

Figure 3.9: (a) Visualization of the ARPES geometry in PGI-6. In this case, the sample is in normal emission, where the normal to the surface is the z-axis while the sample surface is within the xy-plane. Three different sources of light: helium lamp, xenon lamp and 6 eV laser are represented by the light pointing arrows; green, blue and red respectively, with the corresponding incident angles indicated. A transparent hemisphere represents the photoemitted electrons from the sample in all directions, while the shaded yellow cone is the part of this hemisphere that is being imaged by the spectrometer in the normal emission. Note the entrance slit which is vertical enabling imaging the angular distribution along the y-direction by the spectrometer in one shot. (b) A typical 3D-data set, measured for the topological insulator Bi_2Se_3 and collected from individual energy-momentum maps $E(k_y)$ for a set of deflections along the x-direction using the A1 lens deflector system. Slicing this cube of data produces band dispersion maps (c) and constant energy cuts (d).

Photoelectrons are emitted from the sample in all directions, as indicated by the hemisphere in Fig. 3.9(a). However, only a cone of electrons, represented by the yellow shaded area in the 3D sketch, will enter the lens, which has an acceptance angle of ±15° in both the x and y directions. The elongated entrance slit of the

[5]However, some states are not strongly affected; see e.g. the topological surface states of Bi_2Se_3 measured at room temperature as presented in Fig. 3.9(c).

spectrometer allows for filtering all electrons with emission angles within the range of [−15°,+15°] in the y-direction, enabling energy dispersion mapping along the k_y direction for a fixed k_x value (see $E(k_y)$ spectrum of Fig. 3.9(c)).

The mechanoelectrostatic lens deflector system can be used to deflect the electron cone onto the slit in the x-direction, according to a chosen set of deflections, allowing for mapping in the k_x direction. The A1 lens deflector system facilitates mapping significant portions of the Brillouin zone without requiring sample rotation. This approach generates a three-dimensional dataset of the surface electronic structure (see Fig. 3.9(b) for the I(E_B, k_x, k_y) mapping).

Various cuts can be extracted from this 3D dataset along the k_x or k_y directions to map the band dispersions $E(k_x)$ and $E(k_y)$, respectively. Constant energy cuts can also be taken along the energy direction; like the Fermi energy cut (see Fig. 3.9(d) for the Fermi surface). Depending on the photon energy used to eject electrons from the sample, different areas of the Brillouin zone are mapped[6].

Additionally, by rotating the sample off-normal around the y-axis, larger k_x values of the Brillouin zone can be probed, allowing for the exploration of equivalent cones similar to the yellow cone depicted in the 3D sketch of Fig. 3.9(a), but horizontally off-normal along the equator of the photo-emitted electron hemisphere.

3.2.2 FERRUM Spin Detector

The system is equipped with the highly efficient spin detector, namely FERRUM [128]. As the name indicates, the heart of this detector is an iron film. The mechanism of the spin detection of this detector is based on the exchange scattering of electrons at a magnetized target, where a high *asymmetry* in the intensity of the scattered low kinetic energy electrons is observed depending on the electron spin component being filtered with respect to the magnetization direction of the scattering target. Figure 3.10 depicts a 3D visualization of the spin detector showing the scattering geometry and the electron spin components (the in-plane σ_1, and the out-plane σ_2) that FERRUM is able to detect. The principle of work of this detector will be discussed in the next section.

Preparing the scattering target: The scattering target is a ferromagnetic thin film of iron that is deposited onto a surface of W(100) single crystal. Prior to iron deposition, the W-substrate has to be cleaned, and this is done combining the following two methods. First, hot oxygen treatment, where a silver tube is heated up and selectively allows only the diffusion of oxygen from atmosphere maintaining a partial pressure of $\sim 5{\cdot}10^{-8}$ mbar O_2 in the FERRUM chamber, then the W-substrate single crystal is periodically heated up to $\sim$ 1200K in 15 cycles with a heating time of 10 seconds each and a waiting time of 50 seconds in between (this is controlled automatically via a power supply). This way, carbon contaminations segregate from the bulk of the W-crystal into the surface and get oxidized and desorbed. Second, oxide-flash, where the substrate is flashed raising its temperature to $\sim$ 2300K removing the tungsten-and carbon-oxides. Once the W(100) single crystal is clean, an electron-beam evaporator is used to evaporate iron with an evaporation rate of $\sim$ 0.11Å/sec. for 15 min. growing an iron film of $\sim$ 60 mono-

[6]Using the helium lamp (He I_α=21.22 eV) as an excitation source and probing a metal material with a typical work function of $\sim$ 4.5 eV and using the full acceptance angle of the lens 30°, it is possible to map $\sim$ 1.047 [1/Å] of the BZ in both k_x and k_y directions.

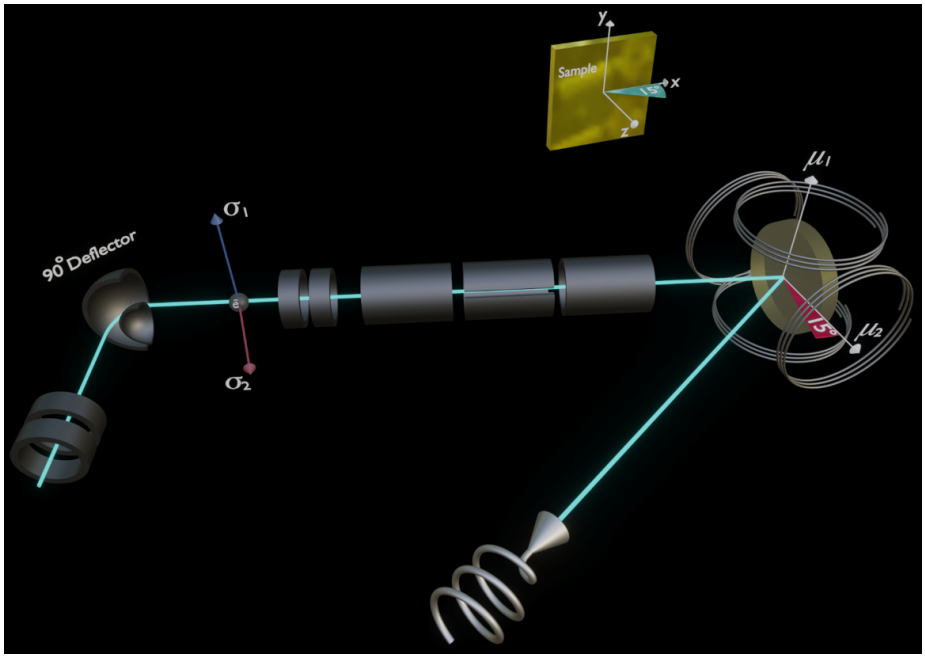

Figure 3.10: 3D schematic drawing of the FERRUM spin detector. σ_1 and σ_2 are the in-plane and out-plane spin components that can be filtered via magnetizing the scattering target along the μ_1 or μ_2 directions respectively, using the corresponding pair of magnetizing coils.

layers. As this film is very sensitive to surface contamination by adsorbates, oxygen is dosed, selectively using the heated silver tube, to oxidise and passivate the iron film. Finally, in order to heal and enhance the quality of the thin film and to remove the excess of oxygen, the film is annealed for $\sim$ 10 min. reaching a temperature of $\sim$ 800K.

Geometry of Spin-ARPES Measurement

FERRUM spin detector at PGI-6 is able to filter the two spin components, in-plane σ_1 and the out-plane σ_2, as it is visualized in Fig. 3.10. While the sample is in normal emission geometry (i.e. the z-axis is normal to the sample surface), it is possible to filter the in-plane spin component σ_1 via magnetizing the evaporated iron thin film onto the W-single crystal, using the horizontally aligned pair of coils, along the μ_1 direction. However, the scattering W-crystal is off-normal by 15°, hence, the sample has to be rotated around the z-axis by 15° in order to filter pure out of plane spin component σ_2 (see Fig. 3.10 rotated sample in the background), where in this case this is done through magnetizing the iron thin film, using the other two vertically aligned pair of coils, along the μ_2 direction.

Photoelectrons leave the hemispherical analyzer through a 1×2 mm^2 opening next to the MCP (see Fig. 3.8(c)) and get directed via a 90° deflector into the scattering target, where they will be accelerated or decelerated hitting the target with a kinetic energy of 5.5 eV. Once the pair of coils is chosen to filter the selected

spin component, the scattering target will be magnetized along the corresponding positive- and negative-direction of the quantization axis consecutively[7]. At this low kinetic energy, the intensity of the scattered electrons from the target is highly asymmetric based on the relative orientation of the spin component with respect to the magnetization direction of the scattering target.

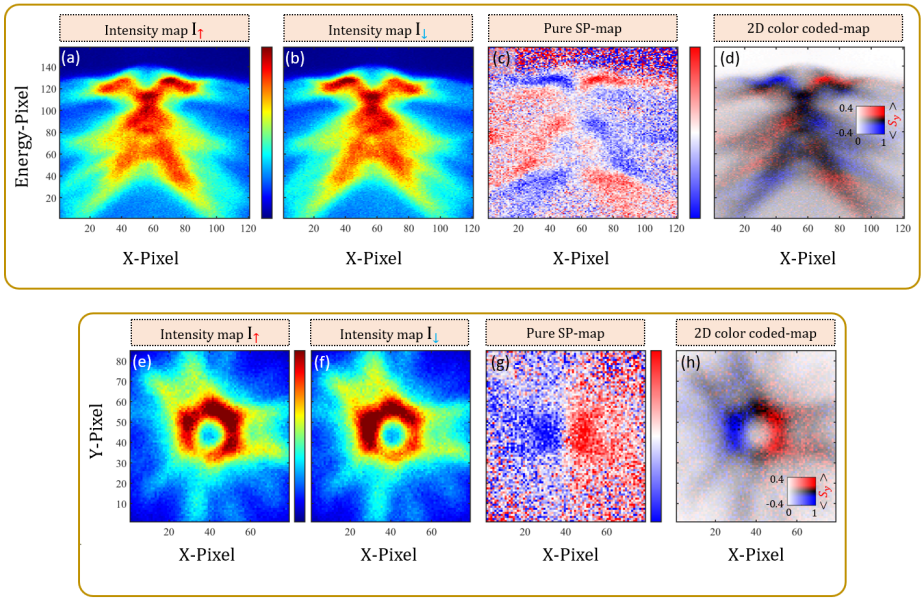

Figure 3.11: **HeI-driven spin-resolved maps for the in-plane S_y spin component of the bulk topological insulator Sb_2Te_3.** Upper panel (each figure 158 × 121 pixels): (a),(b) raw data of the spin-polarized band dispersion maps that show the intensity $I_\uparrow$ and $I_\downarrow$ respectively for the opposite scattering target magnetizations measured pixel-by-pixel. While the x-deflection is fixed, 158-energy pixels are scanned. This corresponds to a vertical line in (a). At energy-pixel 158, the scattering target is being re-magnetized and an equivalent vertical line in (b) is being scanned. This is done similarly for the 121-points along the x-direction. (c) Pure spin-resolved band dispersion map plotted by taking the difference between (a) and (b) and dividing by the sum of (a) and (b) as well as by the Sherman function based on equation 3.3. The spin polarization false color scale is saturated between -40% and 40%. (d) Spin-resolved band dispersion map plotted using the 2D color code shown in the inset where intensity and spin-polarization are simultaneously plotted. Lower panel (each figure 85 × 79 pixels; $E_{binding} \sim 0.5$ eV): (e),(f) raw data of the spin-polarized momentum maps that show the intensity $I_\uparrow$ and $I_\downarrow$ for the opposite scattering target magnetizations measured pixel-by-pixel. While the y-deflection is fixed the x-deflection is scanned, which corresponds to a horizontal line in (e). At x-pixel 79 the scattering target is being re-magnetized and an equivalent horizontal line in (f) is being scanned. This is done similarly for the 85-points along the y-direction. (g),(h) Produced in a similar way to (c) and (d) in the upper panel respectively. Measurements were done at room temperature using an unpolarized HeI-light ($h\nu = 21.22$ eV).

Unlike spin-integrated measurements, spin-resolved measurements are collected

[7]To filter the in-plane S_y-spin component (σ_1), the scattering target is magnetized along μ_{1_+} then re-magnetized along μ_{1_-}.

pixel-by-pixel using the mechanoelectrostatic lens deflector system of the A1 spectrometer. This system enables spin filtering any k-point from the 3D-ARPES data set, highlighting the necessity of the deflector in both the x- and y-directions. Since such spin-resolved measurements are time consuming,in this thesis typically $E(k)$- and the constant energy cut (k_y vs. k_x) spin-resolved maps have been the most often performed spin-resolved measurements. See upper panel of Fig. 3.11 for the spin-resolved band dispersion maps, and the lower panel of Fig. 3.11 for the spin-resolved momentum maps.

Spin-resolved data acquisition method: for the spin-resolved band dispersion maps $E(k)$, the data is collected point-by-point along the k-direction, such that at each k-point, the energy scale is scanned twice, for the opposite scattering target magnetizations. For the spin-resolved momentum maps (k_y vs. k_x), the data is collected point by point along the k_y direction, such that at each k_y point, the k_x scale is being scanned twice, for the opposite scattering target magnetizations. *This way, by frequently re-magnetizing the target, a long-term fluctuation effect in the intensity of the light source is minimized.* A detailed explanation is presented in the caption of Fig. 3.11. The scattered electrons, with the asymmetry in their intensity based on the magnetization direction of the scattering target relative to their spin direction, will be collected using a channeltron. The spin-polarization is then calculated based on the following relation:

$$I_{SP} = \frac{1}{S} \cdot \frac{I_{\mu_{+i}} - I_{\mu_{-i}}}{I_{\mu_{+i}} + I_{\mu_{-i}}}, \tag{3.3}$$

where, I_{SP} is the intensity of the spin-polarization. I_{μ_+} and I_{μ_-} are intensities of the scattered electrons from the scattering target that is magnetized along the positive and negative direction respectively. The effective Sherman function (S=0.29), is the asymmetry in a fully polarized electron beam. (i=1,2) represents the magnetization direction of the scattering target aiming to filter the in-plane σ_1 or the out-plane σ_2 spin components respectively.

3.3 UV 206-nm laser system

The S-ARPES system is equipped with a VUV laser system from *LEOS* company with the main components schematically shown in Fig. 3.12. The laser master box produces vertically-polarized infra-red (IR) light of 824 *nm* wavelength that is being directed via the two mirrors (1) into the first cavity. A half-waveplate (2) rotates the polarization into horizontally-polarized IR light that will in-turn be directed and aligned through mirror (3) into the input coupler (4) where the light beam goes through the optical path in-between the input coupler (4), the output coupler (7), and the two folding mirrors (4) and (5) passing through the *non-linear* crystal at the center of the optical path.

The optical axis of the half-waveplate is aligned such that it allows part of the vertically polarized light to get through such that when it combines with the horizontally-polarized light that goes through the input coupler produces elliptically polarized light that is being reflected at the reflecting mirror (8) into the yellow box (9) which in-turn reads this as an indication of the alignment of the optical path which is being transmitted as an error signal to the piezoelectric transducer ($6'$). The feedback signal is used to control the length of the optical path via moving the

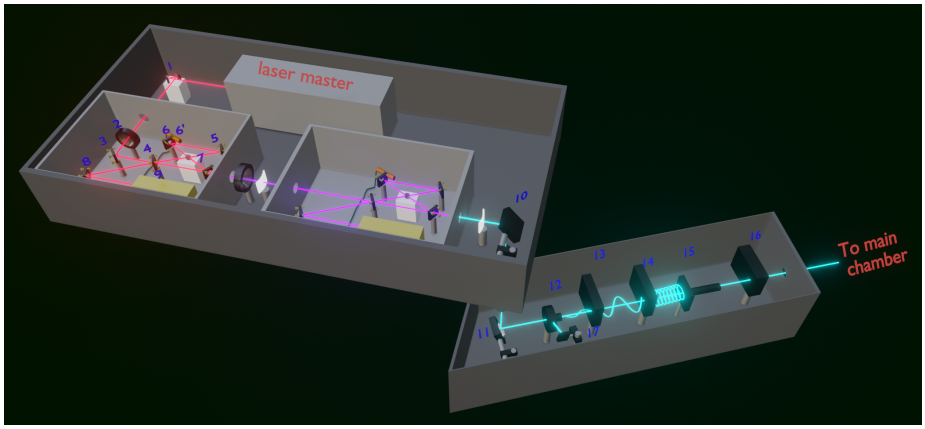

Figure 3.12: **Schematic 3D visualization of the $\sim$ 6 eV laser system.** In the upper box, the laser master generates IR 824 *nm* wavelength vertically-polarized that is being guided into the first cavity where, using a non-linear crystal, part of the 824 *nm* beam is converted into $\sim$ 412 *nm*. Similar process happens in the second cavity leaving it with a UV $\sim$ 206 *nm* wavelength. In the lower box, the laser beam can be vertically, horizontally or, circularly if needed, get polarized and directed into the main chamber. Main components in the laser system are shown and labeled with numbers to be referred to within the text.

folding mirror (6), hence, increasing the coupling in the first cavity. The frequency of the laser beam leaves the first cavity with doubled frequency; half the original wavelength $\sim$ 412 *nm*. A similar treatment happens to the laser beam in the second cavity and the frequency again gets doubled leaving the second cavity with $\sim$ 206 *nm* wavelength. A reflecting mirror (10) is used to guide the laser beam into the lower box where it gets again reflected via mirror (11) to be guided into the main chamber. To assure linearly polarized light, a polarizer (12) filtering a specific electric field component is used. Via using a half-waveplate (13) which is mounted on a stepper motor that allows to rotate the optical axis of the $\frac{\lambda}{2}$-waveplate in order to produce a vertically or a horizontally polarized light. A $\frac{\lambda}{4}$-waveplate (14), if needed, is used in order to convert the linearly polarized light into circularly polarized light. Afterwards, the laser beam is being focused using a telescope (15) and a focusing lens (16) to enter through an optical window into the main chamber to hit the sample and excite electrons. As the polarizer (12) selects only the electric field component that is parallel to its transmission axis, part of the scattered light as one can see in Fig. 3.12 is measured using a photodiode (17) where this signal is being used as a real-time normalizer for the laser-spin measurements.

3.3.0.1 Doubling the frequency of the laser beam

When the electromagnetic field of a lightwave propagates through a medium, it exerts forces on the valence electrons, hence, distorting the charge distribution of the medium creating a polarization wave. If the driven oscillator is a linear isotropic medium, the polarization P will be directly proportional to the applied field E and given by the following relation

$$P = \epsilon_o \chi E \tag{3.4}$$

where χ is the electric susceptibility, a dimensionless constant that characterizes the medium's response to the field.

At higher electric field strengths, however, the linear approximation breaks down, as polarization cannot increase indefinitely in proportion to E. This leads to the emergence of nonlinear effects. To account for this, the polarization can be expressed as a power series in E, incorporating higher-order susceptibilities:

$$P = \epsilon_o(\chi E + \chi_2 E^2 + \chi_3 E^3 + ...) \tag{3.5}$$

where χ_2, χ_3, etc., represent higher-order nonlinear susceptibilities that become increasingly significant as the electric field strength increases [129].

For a lightwave of the form $E = E_o sin(wt)$ incident on the medium, the polarization response is

$$\begin{aligned} P &= \epsilon_o \chi E_o sin(wt) + \epsilon_o \chi_2 E_o^2 sin^2(wt) + \epsilon_o \chi_3 E_o^3 sin^3(wt) + ... \\ &= \epsilon_o \chi E_o sin(wt) + \frac{\epsilon_o \chi_2}{2} E_o^2 (1 - cos(2wt)) + \frac{\epsilon_o \chi_3}{4} E_o^3 (3sin(wt) - sin(3wt)) + ... \end{aligned} \tag{3.6}$$

In the case of *linear* medium, the first-order susceptibility χ dominates, and the reradiated light corresponds to a refracted wave with a reduced speed v but the same frequency ω as the incident wave. The polarization in this case corresponds to an oscillatory current. On the other hand, in a *non-linear* medium, such as a nonlinear crystal as it is the case in our laser system, higher-order terms contribute significantly. This results in the generation of new frequency components, such as second harmonic generation (SHG), where a frequency-doubled wave at 2ω is produced in the first cavity, and fourth harmonic generation (FHG), where a wave at 4ω is generated in the second cavity (where w is the original frequency of the IR laser master).

3.3.0.2 Converting linearly- to circularly- polarized light

A waveplate has a slow axis and a fast axis, characterized by indices of refraction n_s and n_f along these axes, respectively. If the linearly polarized light is travelling along the slow (fast) axis, then the same linearly polarized light will still get out from the waveplate, however, the wave will be delayed by an amount proportional to n_s (n_f) and the thickness of the waveplate t through this relation $\{delay_{(s/f)} = \frac{2\pi n_{(s/f)} t}{\lambda}\}$ where λ is the vacuum wavelength of the light. Therefore, a waveplate has what so-called retardance [129–132] $\Gamma = \frac{2\pi(n_s - n_f)t}{\lambda}$ which is how much slowness one gets along the slow axis compared to the fast axis. Hence, using $\frac{\lambda}{4}$-waveplate delays the component parallel to the slow axis by $\frac{\lambda}{4}$ of the wavelength more than the component parallel to the fast axis producing elliptically polarized light. In order to produce circularly polarized light, the polarization axis of the linearly polarized light, coming out of the $\frac{\lambda}{2}$-waveplate, has to be at 45° with respect to the fast and slow axes of the $\frac{\lambda}{4}$-waveplate [130, 131]. This will result in equal amounts of light parallel to the slow- and fast-axis with same amplitudes and circulating around the optic axis, hence, the name circular polarization. The direction of polarization either clockwise

(right-handed) or counterclockwise (left-handed) is determined by the slow-axis of the $\frac{\lambda}{4}$-waveplate that determines which component of the electric field will be slowed down more, and in our setup this is controlled via a stepper motor onto which the $\frac{\lambda}{4}$-waveplate is being mounted. The way we used in order to define the slow- and fast-axis of the $\frac{\lambda}{4}$-waveplate is the following: we used two polarizers and we rotated the transmission axis of the second one such that the measured intensity was minimum, this way we make sure the transmission axes of the two polarizers are orthogonal. We used $\frac{\lambda}{4}$-waveplate in-between the two polarizers, and using the stepper motor, we rotated it to align one of the transmission axes along the transmission axis of the first polarizer at which the measured intensity was also minimum. Then, the $\frac{\lambda}{4}$-waveplate was rotated 45° to make sure that the transmission axis of the first polarizer is 45° sandwiched in-between the slow- and fast-axis of the $\frac{\lambda}{4}$-waveplate (equivalently: we searched for the maximum intensity).

3.4 PHELIX beamline at Solaris

Some of the spin-integrated measurements and all dichroic measurements in this thesis were done at the PHELIX end station that operates in the soft X-ray range, at the Solaris National Synchrotron Radiation Centre in Kraków, Poland. Solaris is an electron based synchrotron. The electrons are initially produced by an electron gun, where a high voltage cathode of BaO is heated under vacuum up to 1000 C° providing the electrons with a sufficient thermal energy to escape the surface of the material via the process of thermal emission. An electric field is used to accelerate the electron beam up to 2.8 MeV. Then, a 40 meters length linear accelerator consisting of a row of cavities, in which an electromagnetic field oscillates, is used to accelerate the electron beam to a maximum energy of 600 MeV. Electrons are then introduced through a transfer line into the storage ring in which the kinetic energy of the electron beam is ramped to 1.5 GeV. Bending magnets are used to curve the electron beam between adjacent straight sections of the storage ring. To maintain the trajectory of electrons while accelerating them, the magnetic field produced by the bending magnets must be increased in synchrony with the particle's speed. This is the reason the system is referred to as a *synchrotron*.

The circulating beam is stored for many hours inside the ring on a fixed stable orbit. Synchrotron radiation is emitted as the electrons beam follows curved paths. The radiation required for photoemission experiments at the PHELIX beamline is sent through an Apple II-type elliptically polarizing undulator, which consists of four rows of magnets. Two of these rows are movable, while the other two remain fixed in position. Each magnetic array contains four types of magnet blocks with identical magnetic properties but varying in size and direction of magnetization, as depicted in Fig. 3.13. The undulator has a periodic length, λ_u, of 58 mm, and with 44 periods, the total length of the magnetic structure amounts to 2600 mm. By adjusting the position of the two movable magnetic arrays relative to the fixed ones, a phase shift, δ, is introduced, which alters the polarization of the emitted light, as shown schematically in Fig. 3.13. At the PHELIX end station, when the phase shift is $\delta = 0 \cdot \lambda_u$, horizontally polarized light is produced. Circularly polarized light is achieved with a phase shift of $\delta = \pm\frac{1}{4} \cdot \lambda_u$, while the vertically polarized light is obtained when $\delta = \frac{1}{2} \cdot \lambda_u$. Theoretical analyses for an elliptically polarized undulator can be found in [133–138].

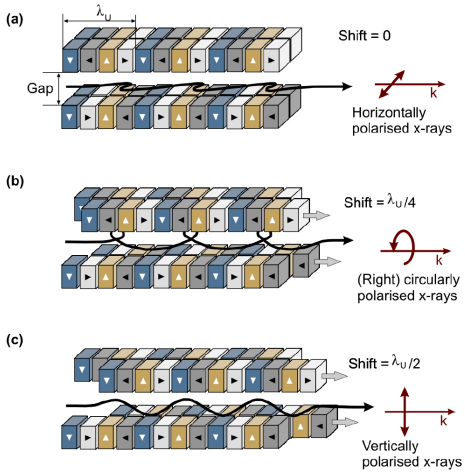

Figure 3.13: APPLE II type undulator schematically showing different phase shift δ settings producing horizontally polarized light when $\delta = 0 \cdot \lambda_u$ (a), circularly polarized light when $\delta = \pm\frac{1}{4} \cdot \lambda_u$, vertically polarized light when $\delta = \frac{1}{2} \cdot \lambda_u$ and elliptically polarized light when δ is in-between. Taken from Ref. [139].

The radiation from the undulator will then be monochromatized and focused into the photoemission chamber by the beamline. Schematic drawing of the most important optical elements of the PHELIX beamline is shown in Fig. 3.14. The undulator light is collimated through a collimating mirror and directed into the plane grating monochromator (PGM), where it gets reflected from the plane mirror inside the PGM chamber onto the grating. The working principle of the PGM is based on the diffraction of the incoming light on a plane grating with a constant line spacing [140].

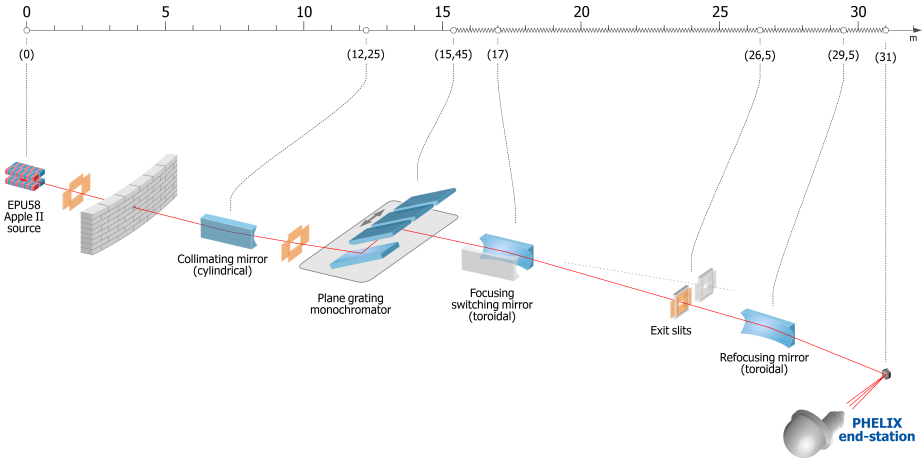

Figure 3.14: Schematic of the most important optical elements of PHELIX end station with their positions along the beamline. Taken from Ref. [141].

When the collimated light hits the grating, it is diffracted at different angles de-

pending on the wavelength of the light. The beamline works with three gratings: 600 lines/mm suitable for 50–300 eV, 800 lines/mm for 200–1000 eV and 1200 lines/mm for 400–1500 eV [141]. By rotating the plane mirror inside the PGM chamber and the grating of the monochromator, the desired energy gets refracted into the forward direction where it gets focused by a focusing mirror onto the exit slit. The width of the exit slit determines the final energy resolution, where it allows light of a specific wavelength to pass through, blocking most of others. The exit slit is directly followed by a refocusing mirror which finally produces a small beam spot on the specimen inside the spectrometer. A top view of the 3D model of the PHELIX end-station showing its main components is shown in Fig. 3.15, with the light beam incidence angle of 54.7° with respect to the lens axis.

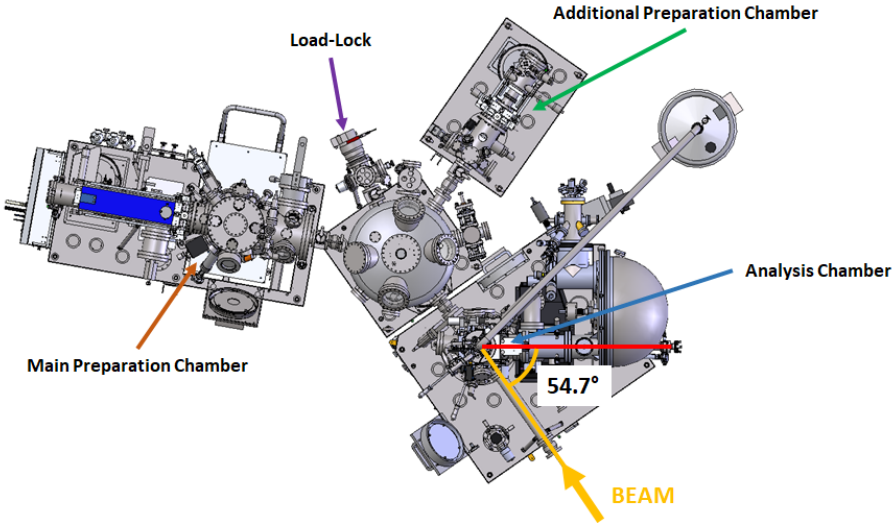

Figure 3.15: 3D model top-view of PHELIX end-station showing its main components. Angle of beam incidence with respect to the lens axis is 54.7° .Taken from Ref. [141].

4. ARPES-based electronic structure of $PtTe_2$

This chapter presents a detailed investigation of the electronic structure of $PtTe_2$, a transition metal dichalcogenide (TMDC), using angle-resolved photoemission spectroscopy (ARPES). The ARPES measurements reveal key electronic features, including sharp surface states and diffuse bulk electronic regions, with a focus on the topological surface states (TSS).

The chapter explores how varying light polarization, specifically s- and p-polarized light, affects the photoemission intensities, as observed in the spin-integrated momentum maps from the ARPES spectra. These variations are analyzed within the framework of matrix element, linking the sensitivity to the light polarization to the orbital character of the valence bands. Different orbitals exhibit distinct responses to s- and p-polarized light, resulting in notable differences in spectral weights.

A central focus of the chapter is the investigation of asymmetries in the measured spectral weights of $PtTe_2$. This analysis is conducted by comparing spin-integrated momentum maps along high-symmetry directions in the reciprocal space, specifically the $\bar{\Gamma} - \bar{K}$ and $\bar{\Gamma} - \bar{M}$ directions, while varying the alignment of the sample with respect to the incident light. In geometries where the reaction plane, defined by the light incidence angle and normal to the sample surface, coincides with one of the mirror planes of the crystal surface, the electronic band structure and photoemission intensities display symmetry with respect to the mirror plane. However, when the sample was rotated such that the incident light no longer impinged within a crystal mirror plane, pronounced asymmetries emerged in the ARPES data, manifested as changes in intensity and shifts in the positions of both surface and bulk electronic features.

These asymmetries are attributed not to sample defects or imperfections, but rather to the specific alignment of the crystal relative to the incident light, as well as intrinsic structural asymmetries within the crystal itself. In particular, regions associated with topological surface states exhibited pronounced asymmetry, underscoring the influence of experimental geometry on these measurements.

A comparative analysis presented in this chapter demonstrates that while theoretical band structure calculations predict symmetric behavior, experimental data may deviate from these predictions due to experimental factors. Understanding these asymmetries is crucial for interpreting ARPES studies and highlights the need to consider experimental conditions when analyzing photoemission spectra.

4.1 Crystal structure of $PtTe_2$

$PtTe_2$ is a member of the transition metal dichalcogenides (TMDCs) family materials. It is characterized by the octahedral 1T-phase structure, where the hexagonally packed layer of the transition metal plane formed out of Pt atoms is sandwiched

between two chalcogen layers composed of Te atoms. Figures 4.1(a) and 4.1(b) represent a top- and side views, respectively, of the crystal structure of $PtTe_2$. Within a monolayer, the two Te layers are 180° rotated with respect to each other, producing a Pt-centered $PtTe_6$ octahedron [142], as shown in the bulk unit cell of $PtTe_2$ depicted in Fig. 4.1(c), giving rise to a trigonal structure when projected onto the (001) plane.

Within the individual $PtTe_2$ monolayer, which itself contains three layers of atoms (Te-Pt-Te), the intralayer Pt-Te bonds are strong covalent bonds, whereas the monolayers are coupled via the weak van der Waals forces, allowing the crystal to cleave along the layer surface preserving its properties [143]. The three atomic planes (Te-Pt-Te) are stacked in the AbC order, in which Te atoms in different atomic planes occupy different positions A and C in the direction perpendicular to the layer (see Fig. 4.1(b)).

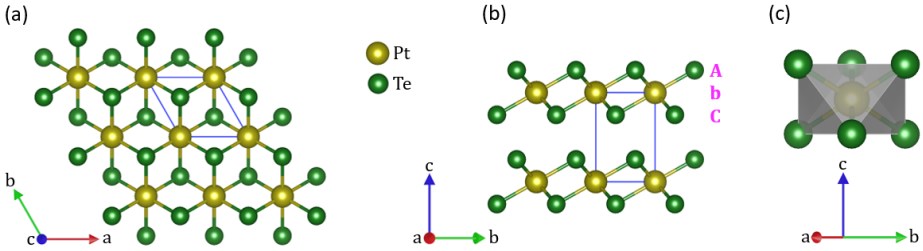

Figure 4.1: **Crystal structure of bulk single crystal $PtTe_2$.** (a),(b) Top and side views of $PtTe_2$ crystal structure, respectively. Atom colour code: yellow, metal-Pt; green, chalcogen-Te. The label AbC in (b) represents the stacking sequence where the upper- and lower-case letters represent the chalcogen and metal elements, respectively. (c) Bulk unit cell, indicated by the solid blue line in (a) and (b).

4.2 Symmetry operations of bulk $PtTe_2$

The compound $PtTe_2$ crystallizes in the $P\bar{3}m1$ space group (No. 164). Its crystal structure exhibits twelve distinct symmetry operations, which are detailed below and illustrated in Fig. 4.2. In the figure, each circle represents an atom, and the circle labeled '1' signifies the identity operation for an atom within the unit cell enclosed by the parallelogram. The labels '1' through '12' inside the circles correspond to the listed symmetry operations, establishing a one-to-one correspondence. In all the symmetry operations: x and y are translations along the in-plane lattice constants **a** and **b** respectively, i.e. $\mathbf{x} = x\,\hat{a}$ and $\mathbf{y} = y\,\hat{b}$. While z is a translation along the out of plane **c** lattice constant; $\mathbf{z} = z\,\hat{c}$.

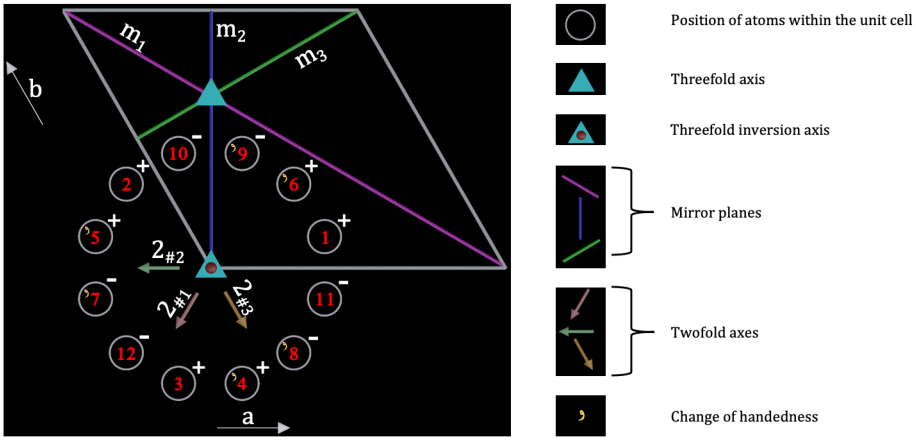

Figure 4.2: **Diagram for $P\bar{3}m1$ (No. 164) space group**. Left: space group diagram showing the equivalent atomic positions generated by the twelve symmetry operations present in $PtTe_2$ bulk single crystal. In this diagram m_1, m_2, and m_3 refer to the three mirror planes operators, $2_{\#1}$, $2_{\#2}$, and $2_{\#3}$ represent three twofold axes, and '+' and '–' indicate atomic positions either above or below the $z = 0$ plane, respectively. Right: explanation of the symbols used in the left panel. Figure produced based on explanation in [144].

symmetry operators:

1. x, y, z : Identity; I
2. $\bar{y}$, $x - y$, z : Anticlockwise 3-fold rotation axis; 3^+
3. $\bar{x} + y$, $\bar{x}$, z : Clockwise 3-fold rotation axis; 3^-
4. $\bar{y}$, $\bar{x}$, z : Mirror plane; m_1
5. $\bar{x} + y$, y, z : Mirror plane; m_2
6. x, $x - y$, z : Mirror plane; m_3
7. $\bar{x}$, $\bar{y}$, $\bar{z}$: Center of inversion, $\bar{I}$
8. y, $\bar{x} + y$, $\bar{z}$: Anticlockwise 3-fold inversion axis; $\bar{3}^+$
9. $x - y$, x, $\bar{z}$: Clockwise 3-fold inversion axis; $\bar{3}^-$
10. y, x, $\bar{z}$: Twofold axis $2_{\#1}$
11. $x - y$, $\bar{y}$, $\bar{z}$: Twofold axis $2_{\#2}$
12. $\bar{x}$, $\bar{x} + y$, $\bar{z}$: Twofold axis $2_{\#3}$

4.3 ARPES on bulk $PtTe_2$

Figure 4.3 provides an overview of the ARPES measurements of $PtTe_2$. The measurements were conducted for two distinct sample orientations, determined by the relative alignment of the three mirror planes present in the bulk single crystal (discussed in Sec. 4.2) and the incidence angle of the light[1]. A schematic illustration of the first orientation is shown in Fig. 4.3(a), where the light impinges the sample within one of the $(\bar{M}-\bar{\Gamma}-\bar{M})$ mirror planes.

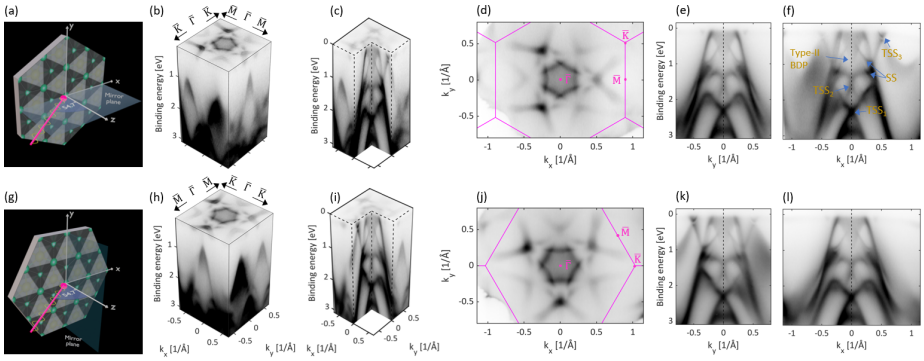

Figure 4.3: **Experimentally determined electronic band structure of $PtTe_2$.** *Upper panel*: (a) schematic geometry showing one of the three mirror planes of bulk $PtTe_2$, oriented such that the incident light beam interacts with the sample within this plane, thereby maintaining the symmetry rules of the mirror plane. (b) Three-dimensional ARPES data set for $PtTe_2$. (c) A three-quarter view of (b) to enhance visualization of the band structure. (d) ARPES Fermi surface map of $PtTe_2$ ($E_F \pm 200$ meV). (e),(f) In-plane band dispersion along the high-symmetry directions $\bar{\Gamma}-\bar{K}$ and $\bar{\Gamma}-\bar{M}$, respectively. (d)-(f) Cuts taken from the 3D data set in (b). Measurements shown in panels (b) through (f) were conducted using the geometry depicted in (a). The labels denote surface states (SS), topological surface states (TSS1, TSS2, TSS3), and the type-II bulk Dirac cone ($h\nu = 108$ eV; p-polarized light, probing close to an A-plane in the three-dimensional Brillouin zone along the k_z direction). *Lower panel*: (h) through (l) replicate the measurements shown in (b) through (f), but were obtained using the geometry depicted in (g), where one of the three mirror planes of bulk $PtTe_2$ is oriented such that no mirror plane symmetry is preserved for the entire system of the sample and the incident light.

The measurements were performed using p-polarized light of $h\nu = 108$ eV probing close to an A-plane of the three dimensional Brillouin zone[2][3]. The first A-plane in

[1] The significance of these two orientations will be thoroughly examined in Sec. 4.10 and, Sec. 5.1 in the context of spin-resolved measurements.

[2] Through Eq. 2.56, for the normal emission $\vartheta = 0$, using inner potential $V_\circ = 16$ eV, $h\nu = 108$ eV and for electrons emitted from Fermi-level with $E_B = 0$ with a typical metallic work-function $w = 4.5$ eV, then $k_z \approx 5.60\text{Å}^{-1}$. For a lattice vector $c \approx 5.22$Å along the out-plane direction $\Rightarrow k_z \approx \{4{\cdot}\frac{2\pi}{c} + \frac{\pi}{c} \equiv 4{\cdot}b_3 + \frac{b_3}{2} \equiv 4{\cdot}b_3 + \text{A}\}$, indicating the probing close to the A-plane highlighted by the cyan-frames in Note 3.

[3] $PtTe_2$ bulk Brillouin zone. Reciprocal lattice vectors are indicated by the vectors b_1, b_2, and b_3. Blue-frame represents the Γ-plane, while cyan-frames refer to A-planes in reciprocal space.

the reciprocal space for a trigonal crystal structure is defined by A-plane $\equiv \frac{1}{2}\,\boldsymbol{b}_3$, where $\frac{\boldsymbol{b}_3}{b_3}$ is a unit vector along the out-plane direction k_z.

Let us first discuss panels (b)-(f) of Fig. 4.3, which were obtained using the experimental geometry depicted in panel (a). The ARPES data from $PtTe_2$ were collected as a 3D matrix $E(k_x, k_y)$, as shown in panel (b). To enhance the visualization of the band structure, three-quarters of this matrix are plotted in panel (c). The Fermi surface map and the in-plane band dispersion maps along the high-symmetry directions of the surface Brillouin zone, $\bar{K} - \bar{\Gamma} - \bar{K}$ and $\bar{M} - \bar{\Gamma} - \bar{M}$, are shown in panels (d)-(f), respectively, which were extracted as cuts from the data matrix displayed in panel (b). The wavevector positions of the features in the ARPES Fermi surface map[4] in panel (d) indicate a threefold symmetry, confirming the absence of twin domains in the measured $PtTe_2$ crystal.

As will be discussed below, the sharp features observed in the band dispersion in panels (e) and (f) primarily correspond to topologically trivial surface states (SS) and topological surface states (TSS1, TSS2, TSS3). The TSS2 state has been experimentally well-resolved in a related compound $PdTe_2$, as reported in Ref. [25]. Additionally, regions of relatively diffuse spectral weight, indicative of a projected bulk band structure, are observed, including the region associated with the type-II bulk Dirac cone located approximately 1 eV below the Fermi level [29]. Both the topological surface states and the type-II bulk Dirac cone arise from a series of band inversions within the Te p-orbital manifold. These inversions result from the disparity in bandwidth between the out-of-plane p_z orbitals and the in-plane $p_{x,y}$ orbitals along the k_z direction in reciprocal space [25], as further elaborated in Sec. 4.5. The topological surface state centered around the binding energy of approximately 2.3 eV has been identified as a surface Dirac cone in $PtTe_2$ and related compounds [25, 28, 29, 48, 49].

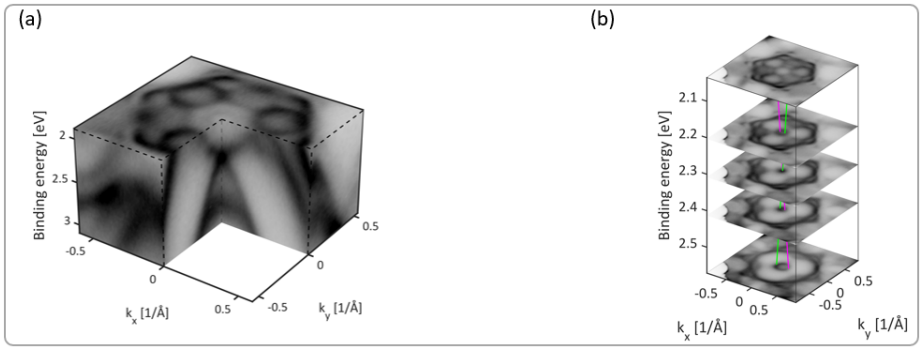

Figure 4.4: **Experimentally determined surface Dirac cone in $PtTe_2$.** (a) Part of the 3D data set showing the surface Dirac cone centered at $E_{binding} \sim 2.3$ eV which is being referred to as TSS1 in Fig. 4.3(c). (b) Selected constant energy cuts, clarifying with the aid of the magenta and green lines, closing and re-opening of the cone while increasing the binding energy.

For the second orientation, the sample was rotated by 30° around the out-of-plane z-axis relative to the first orientation. This aligns the sample such that the

[4]Fermi surface: is the surface in momentum space where, in the limit of zero interactions as $T \Rightarrow 0$, separates occupied from unoccupied electron states.

incident light beam impinges the sample ***not*** within any of the three $\bar{M} - \bar{\Gamma} - \bar{M}$ mirror planes as shown in panel (g). Measurements obtained at this configuration are presented in panels (h) through (l). ARPES Fermi surface maps in Figs. 4.3(j) and 4.3(d) are connected by 30° rotation around the out-plane k_z-axis, consistent with the 30° rotation of the crystal. Additionally, Fig. 4.3(k) is now equivalent to Fig. 4.3(f), while Fig. 4.3(l) is equivalent to Fig. 4.3(e).

A portion of the 3D data stack from Fig. 4.3(h), which encompasses the surface Dirac cone, is presented in Fig. 4.4(a). Additionally, selected constant energy contours are shown in Fig. 4.4(b), demonstrating the closing and reopening of the Dirac cone with increasing binding energy, as illustrated by the green and magenta lines.

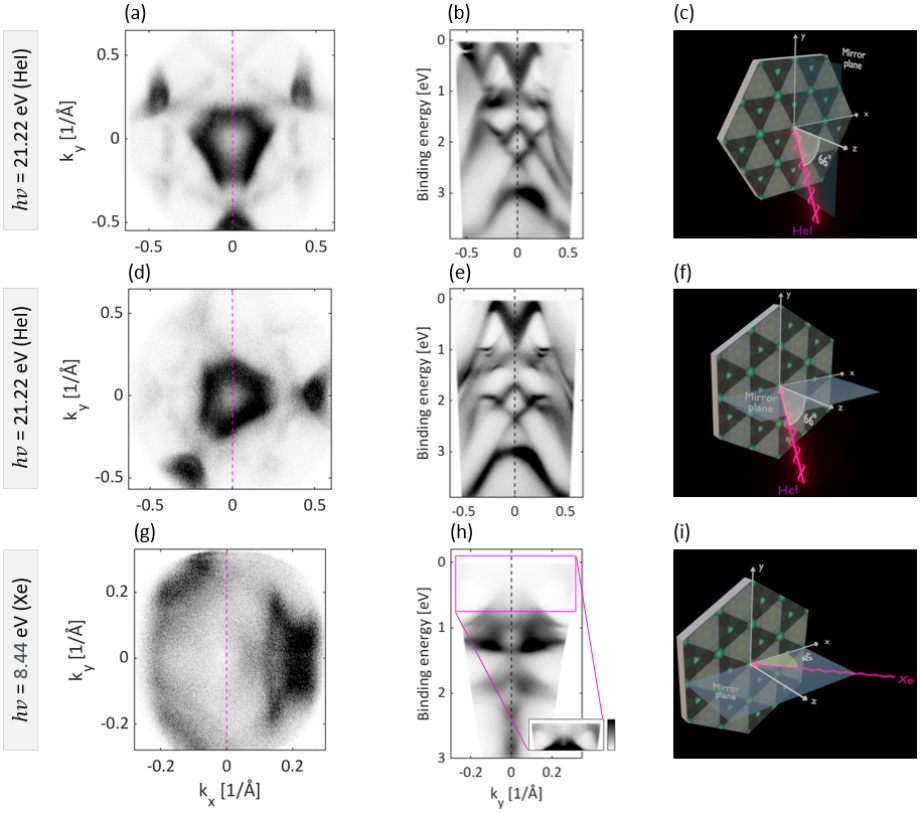

Figure 4.5: **ARPES on cold $PtTe_2$ using PGI-6 lab. based HeI and Xe light sources.** (a),(d),(g) Fermi surfaces ARPES momentum maps from cold $PtTe_2$. HeI radiation ($h\nu$ = 21.22 eV) was used in (a),(d). Xe radiation ($h\nu$ = 8.44 eV) was used for (g). (b),(e),(h) Energy-momentum bands dispersion maps probed along the dashed-magenta lines in the corresponding Fermi maps (a),(d),(g) respectively. Fermi surfaces maps (a),(d),(g) and the corresponding bands dispersion maps were measured using the experimental geometries (c),(f),(i) respectively. Energy-momentum maps were measured along the slit of the analyzer.

A clearer depiction of the surface states of $PtTe_2$ is provided in Fig. 4.5, which was measured on a *cold* $PtTe_2$ sample at a temperature of approximately 45 K using

PGI-6 lab-based light sources. Panel (a) shows the Fermi surface ARPES momentum map obtained with He I radiation ($h\nu$ = 21.22 eV). The corresponding energy-momentum band dispersion map, shown in panel (b), was measured along the dashed magenta line in (a). Both panels (a) and (b) were obtained using the schematic geometry illustrated in panel (c). The middle panels (d)-(f) present measurements equivalent to those in (a)-(c), but with the sample rotated by $\varphi = 30°$ around the z-axis, as depicted in panel (f). The lower panels (g)-(i) replicate the measurements in (d)-(f), but were conducted using Xe radiation ($h\nu$ = 8.44 eV). The energy-momentum maps in (a), (d) and (g) were measured along the slit of the spectrometer, that is aligned along the y-axis. The incident light in (c) and (f) is within the yz-plane, while it is within the xz-plane in (i).

Panel (e) of Fig. 4.5 reveals that the surface states (SS) at $E_{binding} \approx 1$ eV are clearly visible, exhibiting nearly flat dispersion. These surface states are also observable in the energy-momentum map measured with Xe radiation, as shown in Fig. 4.5(h). The upper branches of the surface Dirac cone merge with the diffuse projected bulk spectral weight. Along the $\bar{\Gamma} - \bar{K}$ direction shown in Fig. 4.5(e), they retain their general shape and persist as surface resonances distinctly separated from the bulk diffuse spectral weight curving away from the $\bar{\Gamma}$ point. However, they continue to disperse at lower binding energies along the $\bar{\Gamma} - \bar{M}$ direction, as seen in Fig. 4.5(b), after emerging from the bulk diffuse manifold. Furthermore, the photoemission intensity at the type-II bulk Dirac cone region varies significantly between He I and Xe radiation. This variation in ARPES intensity with different photon energies highlights the bulk nature of the Dirac cone.

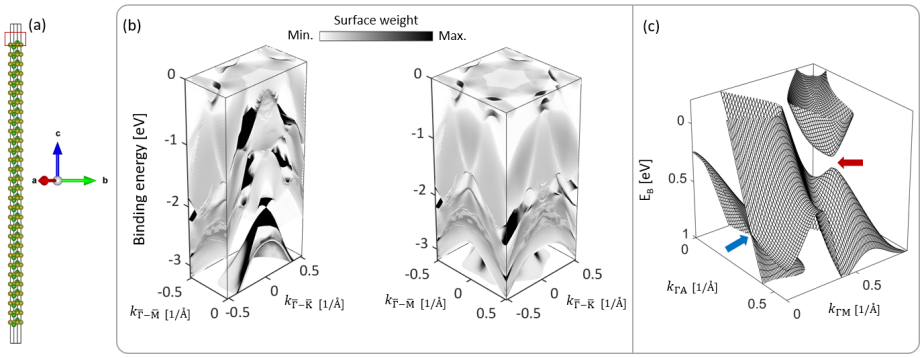

Figure 4.6: **Calculated electronic band structure of $PtTe_2$.** (a) A unit cell of 30-layers slab as visualized via VESTA, with the real space lattice vectors shown in the inset. (b) 3D-calculated band structure of $PtTe_2$ for the slab shown in (a). Contribution from the outermost atomic orbitals of the top surface Pt and Te atoms are included in the calculations. These atoms are enclosed by the red-square in (a). (c) Bulk band structure for $E_B(k_{\Gamma M}, k_{\Gamma A})$. Red arrow indicates the local bulk band gap, while the blue arrow indicates the type-II bulk Dirac cone.

In order to compare the presented experimental work with theory, the band structure of $PtTe_2$ has been calculated using WIEN2k for a 30-layers slab, where a monolayer is equivalent to three atomic layers Te-Pt-Te. A 3D-visualization of the unit cell of the 30-layers structure is shown in Fig. 4.6(a) which is visualized via VESTA program using the structure file that is being used in WIEN2k calculations.

The 3D-data set of the calculated band structure representing $E(k_{\bar{\Gamma}-\bar{M}}, k_{\bar{\Gamma}-\bar{K}})$ is shown in Fig. 4.6(b)[5] where the contribution from the outermost atomic orbitals of the top surface Pt and Te atoms are included in the calculations[6]. These orbitals weights are indicated by the gray level scale. The weights of separate orbitals for the distinct bands will be discussed in Sec. 4.6. Figure 4.6(c) presents the bulk band structure for $E_B(k_{\Gamma M}, k_{\Gamma A})$. The type-II bulk Dirac cone, previously referenced in Fig. 4.3(f), is highlighted with the blue arrow, while a local bulk band gap is marked with the red arrow.

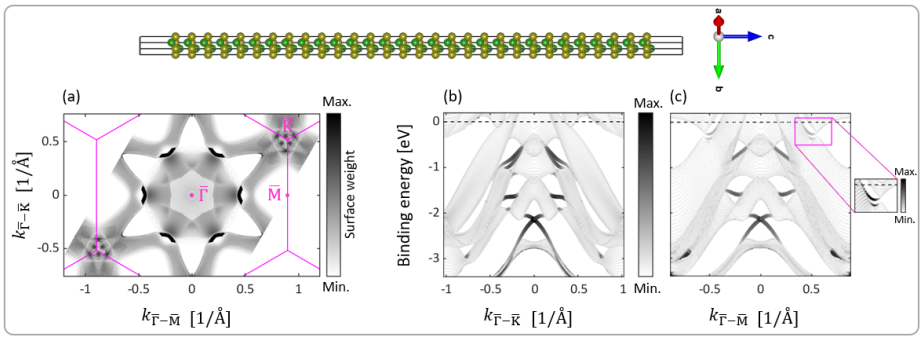

Figure 4.7: **Calculated Fermi map and electronic band structure along high symmetry directions of reciprocal space.** (a) Fermi surface map constant energy cut from the 30-layers calculations presented in Fig. 4.6(b). (b),(c) Calculations of the band structure along the high symmetry directions of the surface Brillouin zone $\bar{K}-\bar{\Gamma}-\bar{K}$ and $\bar{M}-\bar{\Gamma}-\bar{M}$, respectively. Outermost atomic-orbitals of the top surface Pt and Te atoms are included in the calculations (a-c).

Fermi surface map (averaged over $\Delta E = 0.03$ eV) taken from the calculated band structure of the slab is plotted in Fig. 4.7(a). Energy-momentum maps along the high symmetry directions $\bar{K}-\bar{\Gamma}-\bar{K}$ and $\bar{M}-\bar{\Gamma}-\bar{M}$ are shown in Figs. 4.7(b) and (c) respectively. In agreement with the experimentally measured data in Fig. 4.3, multiple surface states are clearly visible, particularly, the surface Dirac cone at $\sim$ 2.0 eV which is resolved and plotted separately in Fig. 4.8. Additionally, there is the previously mentioned TSS3 crossing Fermi level in Fig. 4.7(c) that appears as arcs in the Fermi map at $k_{||} \sim \pm 0.5$ (Å^{-1}) midway along the $\bar{\Gamma}-\bar{M}$ direction in Fig. 4.7(a). These topological surface states are hosted within the local bulk band gap indicated by the red arrow in Figure 4.6(c). The slab calculations reveal clearly the surface states labeled in Fig. 4.3 as (SS) along $\bar{\Gamma}-\bar{K}$ direction, while one branch appears to be much more pronounced along $\bar{\Gamma}-\bar{M}$ direction.

Experimentally selected constant energy k_x-k_y contours are plotted in Fig. 4.9(a) and Fig. 4.9(b) for the two different geometries discussed in the upper and lower panels of Fig. 4.3 respectively. The corresponding k_x-k_y contours that are produced

[5] A grid of 51×51 k-points was employed for this calculation, with 51 k-points sampled along the $\boldsymbol{b}_1$ direction and 51 k-points along the $\boldsymbol{b}_2$ direction of the reciprocal space.

[6] As described in Sec. 2.7, the solid is divided into non-overlapping Muffin-tin spheres centered at the atomic positions, and the WIEN2k calculations account for the electronic charge distribution within these spheres. For valence orbitals, however, the charge is not entirely confined within the Muffin-tin spheres, indicating that the surface weight obtained from the calculations is an approximation.

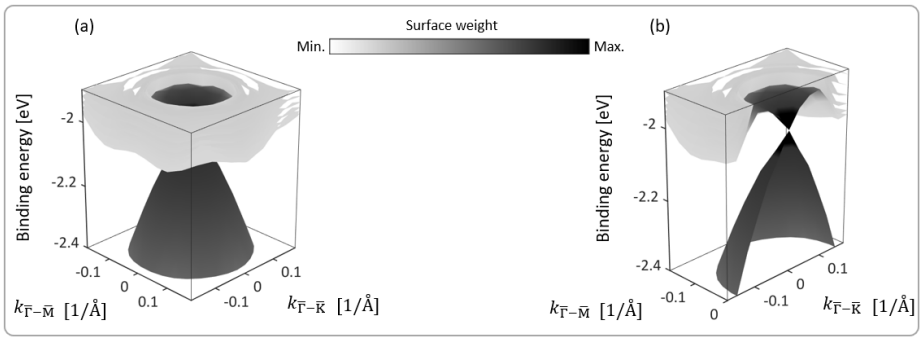

Figure 4.8: **Calculations of the surface Dirac cone.** (a) Section of the $E_{binding}(k_x, k_y)$ band structure in the region of the Dirac cone at $E_{binding} \sim 2$ eV. (b) Same as (a) but only for negative momenta along $\bar{\Gamma} - \bar{M}$ to visualize the Dirac point. Outermost atomic-orbitals of the top surface Pt and Te atoms are included in the calculations (a-b).

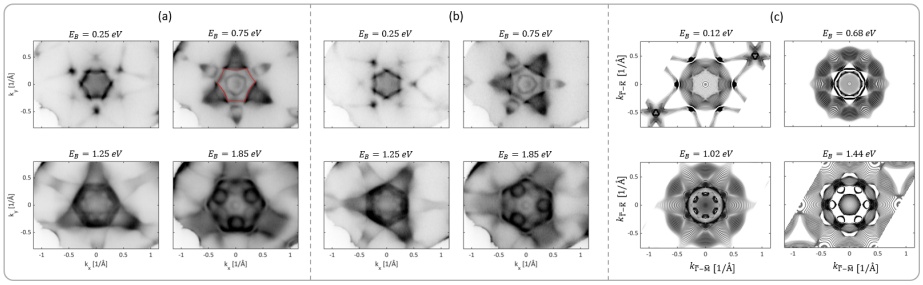

Figure 4.9: **Experimentally determined and theoretically produces k_x-k_y constant energy contours of $PtTe_2$.** (a), (b) Selected experimental constant energy contours of $PtTe_2$ ($h\nu$= 108 eV, P-pol.) that were measured at two different geometries explained in the upper and lower panels of Fig. 4.3 respectively. (c) Corresponding theoretical constant energy contours that are plotted from the 30-layers slab calculations. Each is at the indicated binding energy.

via the 30-layers slab calculations are also presented in Fig. 4.9(c).

The surface state SS together with the surrounding diffuse bulk manifold, produce the warped shape in the momentum map labeled with $E_{binding}$ = 0.75 eV of Fig. 4.9. A red frame indicating this warping is plotted in Fig. 4.9(a) for the corresponding map. This momentum map evolves into ($E_{binding}$ = 1.25 eV)-labeled momentum map of Fig. 4.9 which is a constant energy cut taken from the 3D-data set at binding energy corresponds to the lower part of the surface state SS. The contour corresponds to $E_{binding}$ = 1.85 eV is measured above the upper legs of the surface Dirac cone TSS1.

4.4 Thickness-Driven Metal-to-Semiconductor Transition in $PtTe_2$

The calculations presented in Fig. 4.10(a) illustrate the behaviour of the electronic band structure of $PtTe_2$ when its bulk structure is thinned down to a single layer, i.e. triatomic layer formed of Pt-layer sandwiched between two Te-layers. The calculation shows bands crossing the Fermi level in the bulk down to 2-layers which

reflects the metallic nature of $PtTe_2$. This has been experimentally reported in Ref. [32] for the (2 to 6) layers of $PtTe_2$ thin films. On the other hand, calculations show a semiconducting case for the one-layer where Fermi level is located in-between the valence and the conduction bands. The semiconducting case has recently been experimentally verified in a single layer of $PtTe_2$ in Ref [47]. The indirect band-gap predicted in a monolayer of $PtTe_2$ positions this material as a promising candidate for applications in valleytronics, similar to the indirect band gap predicted in its sister compound, $PtSe_2$ [33].

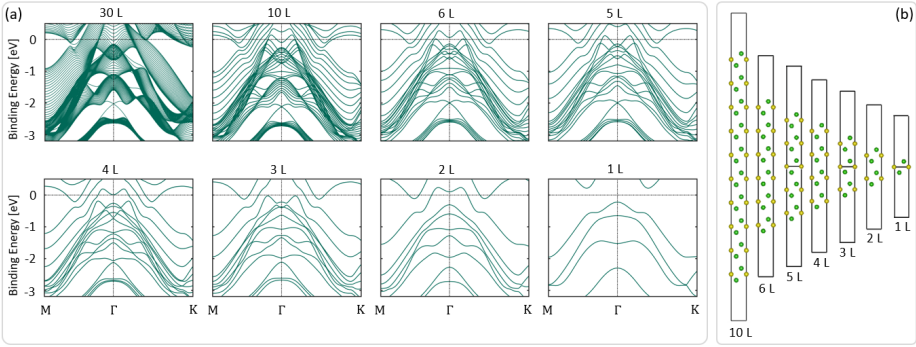

Figure 4.10: **Electronic properties of $PtTe_2$ across different layer thicknesses** (a) Theoretical calculations for the electronic band structure of $PtTe_2$ with different thicknesses (1-6, 10 and 30 layers). (b) Corresponding unit cells with the number of layers labeled.

4.5 Origin of topological phenomena based on tight-binding analysis

In this section we analyse the band structure of the 1T-type MX_2 of the family of TMDCs based on the tight-binding model. The orbital weight due to the transition metal, M, in the band structure is significantly bellow the Fermi level. As a result, focusing exclusively on the p-orbital manifold of the chalcogen provides a valid approximation [145].

Following the crystal structure discussed in Sec. 4.1, the unit cell exhibits threefold rotationally symmetric along the c-axis. The resulting crystal field splits the triply degenerate energy levels of Te (neglecting spin) $p_{x,y,z}$ into p_z and $p_{x,y}$ manifolds. Spin orbit interaction (SOI) further splits the $p_{x,y}$ manifold into the singlets R'_4 and $R_{5,6}$ levels with distinct energy levels that no longer have degeneracy, and additionally it modifies the energetic separation of p_z and $p_{x,y}$. Furthermore, the presence of two chalcogen sites within the unit cell leads to the creation of bonding and anti-bonding splittings of the p-energy levels. All these factors together create a hierarchy of energy levels at the Γ ($\mathbf{k}$=(0,0,0)) and A ($\mathbf{k}$=(0,0,π/c)) points of the Brillouin zone, as illustrated in Fig. 4.11. The hopping of electrons along the c-axis for the p_z orbitals, as denoted by the intra-layer hopping t_3 and inter-layer hopping t_4 in Fig. 4.11(a), is significantly larger when compared to the planar $p_{x,y}$ orbitals. This induces a strong k_z dispersion and a larger bandwidth for the p_z-derived bands compared to the $p_{x,y}$-derived bands, leading to the emergence of multiple band cross-

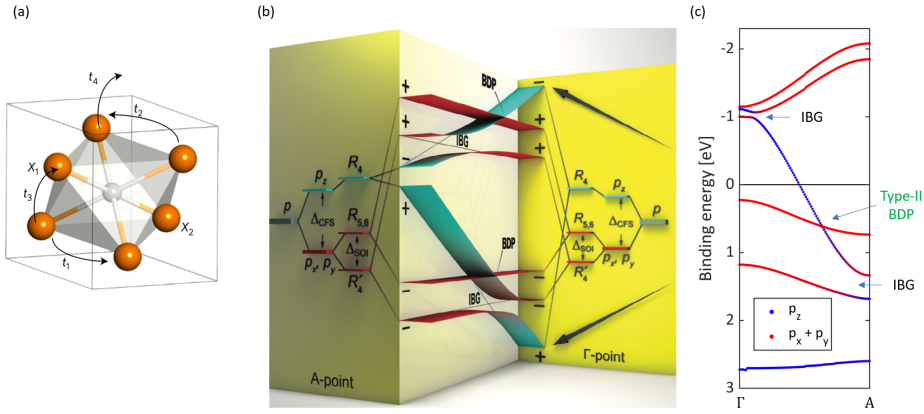

Figure 4.11: **Formation of topological phenomena from the single chalcogen p-orbital manifold in 1T-TMDCs**. (a) Crystal structure of the 1T-TMDCs discussed in detail in Sec. 4.1 showing the hopping of electrons within the same sub-layer (t_1=t_2), between the two sub-layers (t_3) within the same monolayer and the inter-layer hopping (t_4) used in the tight binding model to create the energy levels in (b). (b) Schematic diagram showing splitting of the chalcogen p-orbital derived energy levels at the Γ and A points of the Brillouin zone as a result of the combination of the crystal field splitting (CFS), spin orbit interaction (SOI) and the bonding and anti-bonding splittings. The sufficiently high band width of the p_z-orbital character bands compared to the planar $p_{x,y}$-derived bands along the out of plane high symmetry line Γ-A, leads to multiple band crossings forming ladder of topological phenomena including protected bulk Dirac points and band gaps with inverted parity hosting spin polarized surface states. The double group representation (R_i) and the parity (+/-) are labelled. (c) Out of plane bulk band dispersions along the Γ-A direction of the Brillouin zone from DFT calculations of $PtTe_2$, projected onto the chalcogen $p_{x,y}$(red) and p_z(blue) orbitals, demonstrating (b). (a) Adapted from [25], (b) reproduced from [145].

ings *within the same p-orbitals manifold* [25, 145, 146][7]. Some of these crossings are protected by the symmetry of the crystal lattice, resulting in the so-called bulk Dirac points (BDP). This is the case for the crossings of the bonding and anti-bonding split bands of R_4 and $R_{5,6}$, where, for a given Hamiltonian $H(k)$, the overlapping matrix element $< R_4|H(k)|R_{5,6} >$ equals zero, indicating no hybridization between the corresponding wave functions. On the other hand, the hybridization between the split bands of R_4 and R_4' is not protected, leading to a parity-inverted band gap (IBG) that hosts spin-polarised Dirac states at the surface. All this combined produces a so-called *topological ladder*. The DFT calculations of $PtTe_2$ illustrate this phenomenon, as shown in Fig. 4.11(c). These calculations depict the out-plane bulk band dispersions along the Γ-A direction of the BZ, projected onto the chalcogen $p_{x,y}$ (red) and p_z (blue) orbitals.

[7]Unlike the majority of other systems where different atomic manifolds contribute to the formation of such topological phenomena as e.g. in the topological insulator Bi_2Se_3 where the topological surface state hosted in the inverted band gap results from the crossings of p_z-derived bands of both Bi and Se manifolds [147].

4.6 Orbital characters of bulk $PtTe_2$ valence bands

Figure 4.12 and Fig. 4.13 show surface orbital characters of the 30-layers $PtTe_2$ slab calculation. The quantization axis for the complex orbitals is chosen perpendicular to the surface as shown in the inset. One can see that the surface Dirac cone centered at $E_B \sim 2$ eV (TSS1) is formed predominantly from the out-plane orbitals Pt $5d\ Y_2^0 = d_{z^2}$ and Te $5p\ Y_1^0 = p_z$ with admixtures of Pt $6s\ Y_0^0$ orbital.

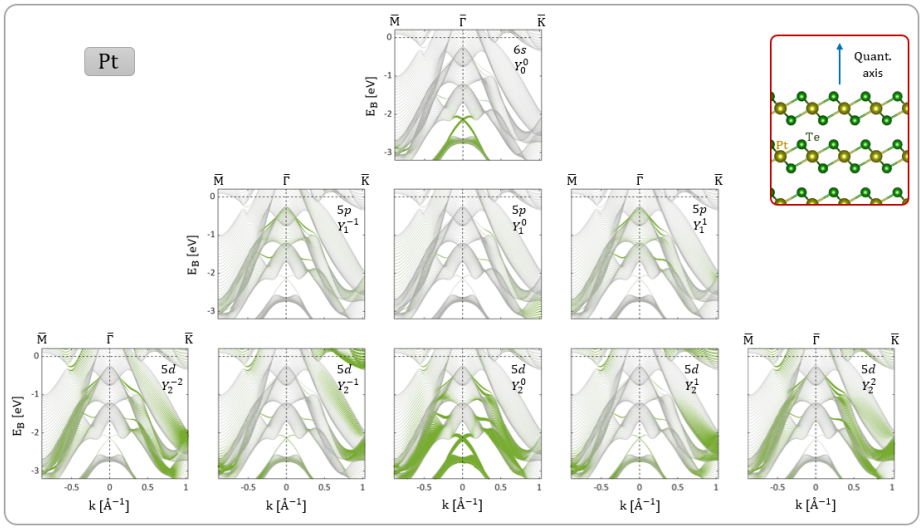

Figure 4.12: **Band characters for the Pt surface atom of the 30L $PtTe_2$ slab calculation.** Band characters for the Pt surface atom of the 30L $PtTe_2$ slab calculation for s, p and d complex orbitals for the quantization axis normal to the surface as indicated in the inset. The bands are plotted along $\bar{M} - \bar{\Gamma} - \bar{K}$ trajectory of the reciprocal space. The size of symbols represents the corresponding orbital weight.

The surface states at $E_B \sim 1.5$ eV are formed from Te $5p\ Y_1^0$, Te $5p\ Y_1^{\pm 1}$ and Pt $5d\ Y_2^0$ orbitals. The surface states at $E_B \sim 0.8$ eV (SS) are formed predominantly from Te $5p\ Y_1^0$ and Te $5p\ Y_1^{\pm 1}$ with admixtures of Pt $5d\ Y_2^0$ and Pt $5d\ Y_2^{\pm 2}$ orbitals. The surface states close to Fermi level (TSS3) that appear only along the $\bar{\Gamma} - \bar{M}$ direction are formed predominantly from the out-plane Te $5p\ Y_1^0$ orbital with admixtures of Pt $5d\ Y_2^0$, $Y_2^{\pm 1}$ and $Y_2^{\pm 2}$ orbitals. This demonstrates that in $PtTe_2$ the valence bands wave functions are strongly mixed between Te and Pt sites.

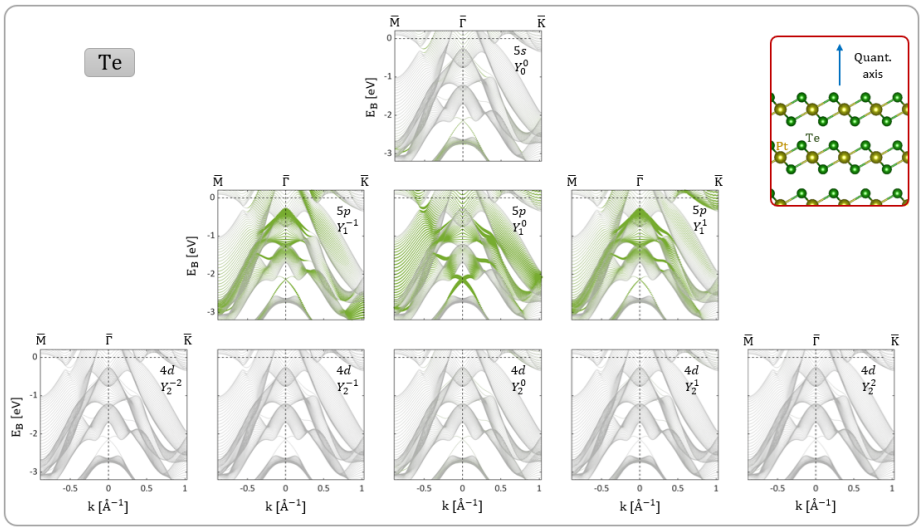

Figure 4.13: **Band characters for the Te surface atom of the 30L $PtTe_2$ slab calculation.** Band characters for the Te surface atom of the 30L $PtTe_2$ slab calculation for s, p and d complex orbitals for the quantization axis normal to the surface as indicated in the inset. The bands are plotted along $\bar{M} - \bar{\Gamma} - \bar{K}$ trajectory of the reciprocal space. The size of symbols represents the corresponding orbital weight.

4.7 Ionization cross sections

Figure 4.14 shows photoionization cross sections for the valence orbitals of $PtTe_2$, taken from Ref. [148], for the photon energy range relevant to the work presented in this thesis. Let us assume, to a first approximation, that the photoemission signal detected via ARPES originates from the contributing orbitals that have been discussed in Sec. 4.6. The vertical black-dashed line indicates the cross sections at the He-I radiation energy. One can see that at this energy the ARPES signal is dominated by the Pt 5d and Te 5p orbitals. The cross section of Pt 5d is $\sim$ 6-times larger than the Te 5p cross section, however, this is probably partly compensated by the longer inelastic mean free path IMFP (discussed in Sec. 2.5.2) of Pt sites which are located under the Te sites (see Fig. 4.1). At this energy, the cross section of Pt 6s is over two orders of magnitude smaller. Therefore, we conclude that at He-I photon energy only Pt 5d and Te 5p orbitals contribute significantly to the ARPES signal.

The relative contribution of Te is highest at $h\nu$ near 200 eV, where contribution from Pt 5d is only $\sim 2\times$ larger than those from Te orbitals, therefore, likely compensated by the IMFP effect. We conclude that at $\sim$ 200 eV, Pt 5d and Te 5p contribute approximately equally.

At all energies, the cross section of Pt 6s orbital is much smaller than cross sections of other orbitals, therefore, one can neglect its contribution in the approximate analysis. All these considerations are approximate in the sense that they are not taking into account the itinerant nature of the valence orbitals. Furthermore, the far field signals originated from different orbitals need to be added coherently, which will lead to interferences as explained in Sec. 2.6.

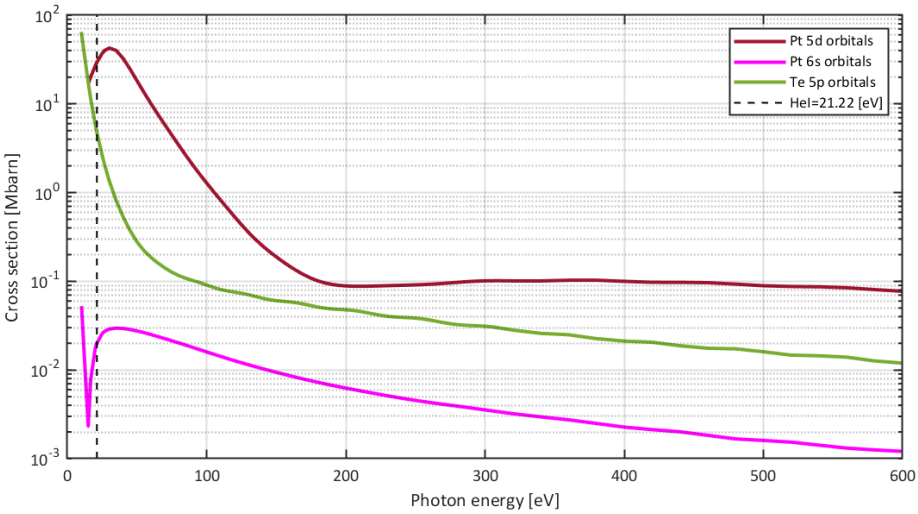

Figure 4.14: **Photoionization cross sections of Pt and Te atoms.** Ionization cross sections of the valence band orbitals of Pt and Te atoms for the photons energies range that is relevant to the work presented in this thesis. Vertical dashed line indicates He-I radiation energy of $h\nu = 21.22$ eV. Figure re-plotted from Ref. [148].

Panels (a)-(d) of Fig. 4.15 are energy-momentum band dispersion maps of $PtTe_2$ along $\bar{K} - \bar{\Gamma} - \bar{K}$ measured using some selected photon energies. Panel (a) was measured using the unpolarized He-I radiation energy. Panels (b)-(d) were measured using p-polarized light using the corresponding indicated energies. One can see the bigger momentum range probed with increasing photon energies, where same range of angles was covered, in consistent with Eq. 2.32. Despite the tendency towards becoming more bulk sensitive with increasing photon energy, one can still see the surface Dirac cone centered at $E_B \sim 2.3$ eV. One can as well see that the photoemission intensity of the surface Dirac cone is modulated as a function of photon energy, where it is most pronounced at $h\nu = 500$ eV and suppressed at $h\nu = 60$ eV. Similar observations of variation of ARPES photoemission intensity as a function of $h\nu$ have been experimentally reported in the surface state of Al(100) in Ref. [149, 150] and in the surface state of BiTeI in Ref. [151].

Panels (e)-(p) present a summary of ARPES measurements of $PtTe_2$ measured using p-polarized light and $h\nu = 500$ eV. Using $h\nu = 500$ eV probes $\sim$ two BZs of $PtTe_2$ as shown in panel (g) of the Fermi surface map and the corresponding energy-momentum map of panel (h) in addition to the constant energy contours of panels (k)-(p) where the reciprocal lattice vectors b_1 and b_2 are labeled.

The IMFP when probing using 500 eV (the soft x-ray regime) is $\sim$ 2-times longer compared to the IMFP when probing using the 60 eV (the VUV regime) (see Fig. 2.7). This bulk sensitivity is reflected more clearly in the energy-momentum maps of panels (h),(i) where ARPES intensity is pronounced in the region of certain bulk structures. On the other hand, the surface Dirac cone is still clearly pronounced as illustrated in panel (j) in the momentum maps close to it.

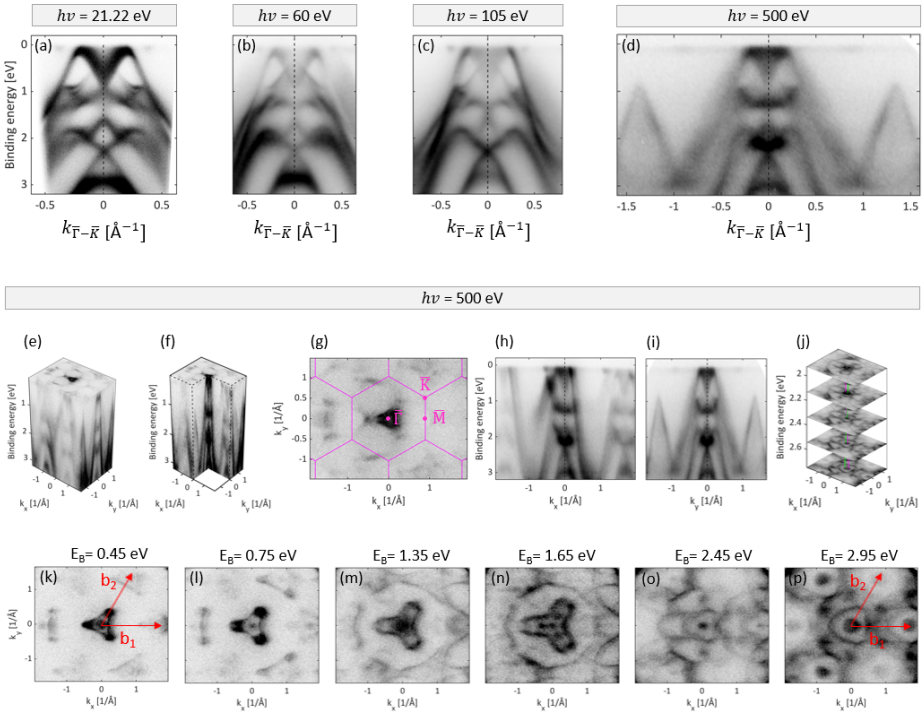

Figure 4.15: **Measured band structure of $PtTe_2$ at selected photon energies.** (a)-(d) Experimentally determined electronic band dispersion of $PtTe_2$ along the high symmetry direction $\bar{\Gamma} - \bar{K}$. (a) Measured using the unpolarized He-I radiation energy. (b)-(d) Measured using P-polarized light with photon energies indicated in the upper panel 60 eV, 105 eV and 500 eV respectively. (e)-(p) Summary of $PtTe_2$ electronic band structure using $h\nu = 500$ eV. Measurements were performed on cold $PtTe_2$ (T $\sim$ 88 K). Reciprocal lattice vectors b_1, b_2 are labeled in (k) and (p).

4.8 Different orbital responses to s- and p-polarized light

In Fig. 4.16 we show different response of bulk $PtTe_2$ valence electronic bands when measured using either s- or p-polarized light. Panel (a) shows the energy-momentum map measured along $\bar{M} - \bar{\Gamma} - \bar{M}$ as indicated by the dashed-magenta line in the corresponding Fermi surface map in panel (b). Panels (a),(b) were measured using p-polarized light, $h\nu = 108$ eV, where the sample was aligned such that the normal to the sample surface is along the axis of the spectrometer lens, as schematically illustrated in panel (c), and the yellow sinusoidal wave refers to the electric field of the light. Panels (d)-(f) are equivalent but measured using s-polarized light at the same geometry, as shown in (f).

Panels (g)-(h) were measured using p-polarized light, $h\nu = 165$ eV, but in this case the sample was rotated around the y-axis by $\theta = 54.7°$ such that the direction of the incident light coincides with the out-plane z-axis, with respect to the sample surface, as illustrated in the corresponding geometry in panel (i). With this geometry, the p-polarized light is seen as s-polarized light by the sample surface.

Panels (a),(d) and (g) were measured through probing along the slit of the ana-

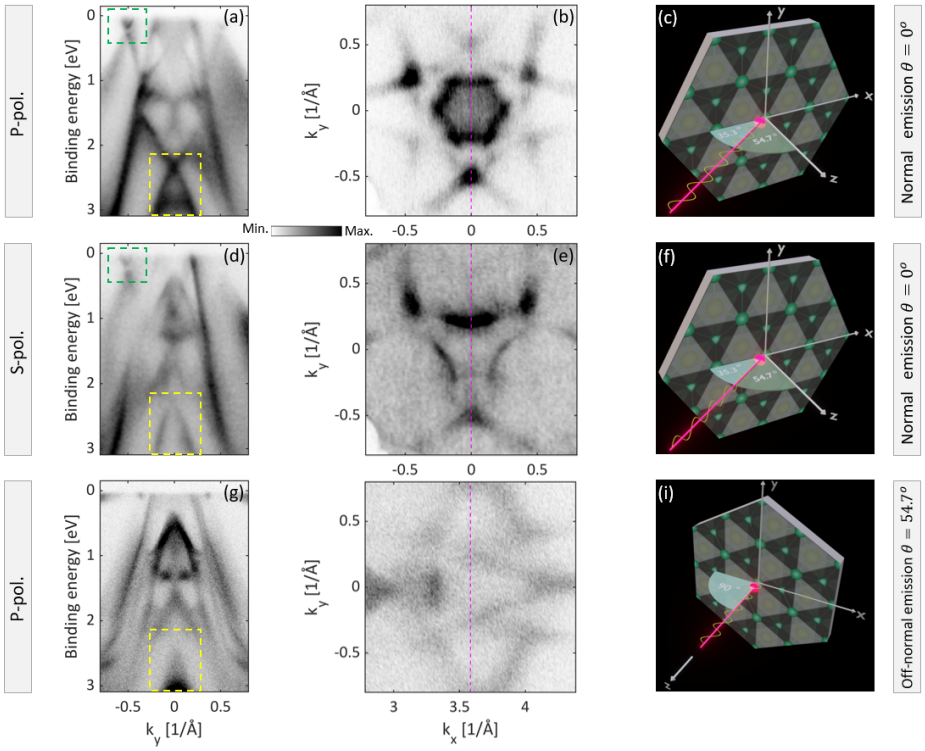

Figure 4.16: **Different orbital character response using s- and p-polarized light.** (a) Measured band dispersion map of $PtTe_2$ along $\bar{\Gamma} - \bar{M}$, probed along the magenta line of the corresponding Fermi surface map in (b) (Fermi map: $E_B = E_F \pm 0.2$ eV). (a),(b) Measured using p-polarized light, $h\nu = 108$ eV, as illustrated in (c) where the sinusoidal wave indicates the electric field polarization direction of the light when sample was in normal emission. (d)-(f) Same, but measured using s-polarized light, $h\nu = 108$ eV, as illustrated by its electric field direction in (f). (g)-(i) Also same, but measured using p-polarized light, $h\nu = 165$ eV, where sample was off-normal rotated by $\theta = 54.7°$ as schematically illustrated in (i). (g) Measured along $\bar{\Gamma} - \bar{K}$. Yellow rectangles enclose the surface Dirac cone at $E_B \sim 2.3$ eV, while the green rectangles enclose the topological surface state (TSS3) crossing the Fermi level. (a),(d),(g) Probed along the slit of the analyzer which is aligned along the y-axis. Band dispersion maps and Fermi maps were normalized by the measured mirror current at the beam-line indicating the intensity of the light while taking measurements.

lyzer which is aligned along the y-direction. Band dispersion as well as Fermi surface maps are normalized by a mirror current at the beam-line reading the intensity of the light used during ARPES experiments.

As discussed in Sec. 4.6, the surface Dirac cone at $E_B \sim 2.5$ eV is predominantly formed from the out-plane orbitals Pt $5d\ Y_2^0 = d_{z^2}$ and Te $5p\ Y_1^0 = p_z$ with admixtures of Pt $6s\ Y_0^0$ orbitals. But, at $h\nu = 108$ eV the cross section of Pt $6s\ Y_0^0$ can be neglected, therefore, ARPES signal can be considered to be originating from the out-plane orbitals only. The p-polarized light has an out-plane component of its oscillating electric field, contrary to the totally in-plane oscillating electric field

in case of the s-polarized light. As a result, one would expect the coupling between out-plane orbitals and p-polarized light to differ from that with s-polarized light.

This selective orbital-light coupling is clearly seen in the stronger ARPES signal of the Dirac cone in panel (a) compared to panel (d) (see yellow rectangles). Additionally, in panel (g) even though we started with p-polarized light, the rotated sample $\theta = 54.7°$ sees the light as s-polarized and this is demonstrated in the reduced ARPES signal of the Dirac cone in (g) compared to (a) and consistent with (d). A similar logic can also be applied to the surface states crossing the Fermi level (TSS3), where these states show stronger ARPES signal when excited using p-polarized light as seen in panel (a) compared to the panel (d) (see green rectangles) due to the out-plane nature of Te $5p\ Y_1^0$ orbitals that predominantly form these states. On the other hand, the surface states at $E_B \sim 0.8$ eV exhibit a mixture of in-plane and out-plane orbitals, as discussed in Sec. 4.6, making it challenging to provide a straightforward explanation solely from this perspective.

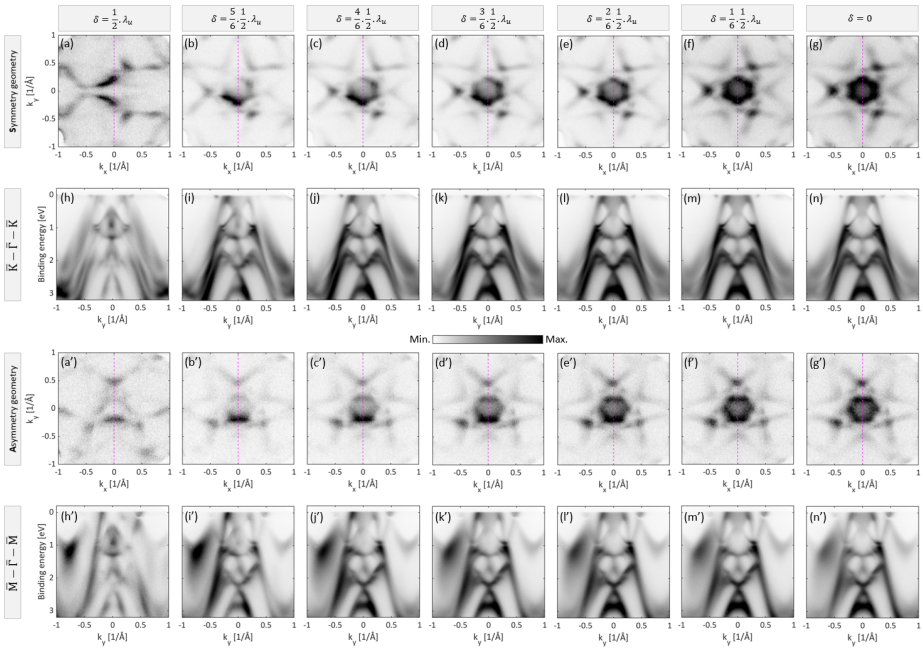

Figure 4.17: **$PtTe_2$ valence bands response to different light polarizations.** (a)-(g) Fermi surface maps of $PtTe_2$, aligned in the *symmetry geometry* shown in Fig. 4.3(a), measured using different light polarizations by changing the phase of the undulator δ, starting with s-polarization (a) passing through elliptical polarizations (b),(c) then circular polarization (d) and again elliptical polarizations (e),(f) ending up with p-polarization (g). (h)-(n) Corresponding energy-momentum band dispersion maps along $\bar{K} - \bar{\Gamma} - \bar{K}$ probed along the slit of the spectrometer which is defined along the magenta-dashed lines in the corresponding Fermi surface maps. (a′)-(n′) Same, but measured using the *asymmetry geometry* shown in Fig. 4.3(g), and (h′)-(n′) were measured along $\bar{M} - \bar{\Gamma} - \bar{M}$. All spectra were normalized by the measured mirror current at the beam-line indicating the intensity of the light while taking measurements.

Figure 4.17 shows the response of $PtTe_2$ valence bands to different light po-

larizations, where maps were normalized by the mirror current at the PHELIX end-station. The polarization of light was changed by changing the phase of the undulator δ (see Sec. 3.4). Panels (a)-(g) present Fermi surface maps of $PtTe_2$ measured using different light polarizations at the corresponding indicated phases. At the PHELIX end-station, when the phase is half of the undulator wavelength, $\delta = \frac{1}{2} \cdot \lambda_u$, the light is vertically polarized and its Fermi surface map is shown in panel (a). The phase was reduced with a step size of factor $\frac{1}{6}$, to have elliptically polarized light as in panels (b) and (c), then it was circularly polarized as in panel (d), and again elliptically polarized as in panels (e) and (f), and finally the phase was reduced to $\delta = 0$ to have a horizontally polarized light with its corresponding Fermi surface map shown in panel (g). Panels (h)-(n) are the energy-momentum maps long $\bar{K} - \bar{\Gamma} - \bar{K}$, which were probed along the dashed-magenta lines plotted in the corresponding Fermi maps. Panels (a′)-(n′) are similar, but measured for the asymmetry geometry alignment of the sample as shown by the Fermi maps in panels (a′)-(g′), and the corresponding energy-momentum bands in this case are along $\bar{M} - \bar{\Gamma} - \bar{M}$. Within the tight binding picture, each point in these measured spectra is defined by a wavefunction which within the atomic picture is a linear combination of atomic orbitals. Therefore different structures and different photoemission intensities can be thought of as different coupling of the orbitals consisting these structures with different polarizations of light. The smooth increase in the ARPES intensity of the surface Dirac cone while moving from vertically to horizontally polarized light is a clear example.

4.9 Light polarization effect on ARPES experiment

The atomic photoemission matrix element, as discussed in Sec. 2.5.1.1, can as well be expressed as described in Ref. [104][8]

$$M_{\boldsymbol{k}_f \boldsymbol{k}} \propto 2\pi \frac{N}{V} \underbrace{\boldsymbol{\epsilon} \cdot (i\boldsymbol{k}_f - \tfrac{1}{\lambda}\boldsymbol{e}_\perp)}_{\text{I}} \times \underbrace{\langle \boldsymbol{k}_f - \boldsymbol{k}_{h\nu} + \frac{i}{\lambda}\boldsymbol{e}_\perp | \boldsymbol{0}, k \rangle}_{\text{II}} \underbrace{\delta(\boldsymbol{k}_{||} - \boldsymbol{k}_{f||} + \boldsymbol{k}_{h\nu||} + \boldsymbol{K}_{||})}_{\text{III}} \underbrace{\frac{1}{i(k_\perp - k_{f\perp} + k_{h\nu\perp}) + 1/\lambda}}_{\text{IV}}$$

where $\boldsymbol{k}$, $\boldsymbol{k}_f$, $\boldsymbol{k}_{h\nu}$ and $\boldsymbol{K}$ are the initial state electron's wave vector, the final state electron's wave vector, the momentum vector of the incoming light and a reciprocal lattice vector respectively. $\boldsymbol{e}_\perp$ is the surface normal vector. The second term (II) represents the angular distribution of photoelectrons based on local orbital properties. The third and forth terms (III), (IV) refer for the conservation of parallel and perpendicular momentum respectively. Now, let's focus on the term (I) which has the dot product between the polarization of the light used during ARPES experiments and the wave vector of the final state of the electron. This term accounts for the limited lifetime of the outgoing electron from the solid due to electron-electron and

[8] An equivalent expression for emission from atomic orbitals, within the free-electron final state approximation, is given by the differential cross section relation $\frac{d\sigma}{d\Omega} \propto (\hat{\boldsymbol{\epsilon}} \cdot \boldsymbol{k})^2 |Y_l^m(\vartheta_k, \varphi_k)|^2$ [152], where $\hat{\boldsymbol{\epsilon}}$ is the light polarization, and $\boldsymbol{k}$ is the wave vector of the emitted electron defined by the emission angles ϑ_k and φ_k (see Fig. 2.5).

electron-phonon interactions through introducing the parameter λ which represents damping of the wave inside the solid [153, 154]. Therefore, the free-electron plane wave of the outgoing electron is modified into the damped plane wave $e^{i\boldsymbol{k}_f \boldsymbol{r}} e^{r_\perp/\lambda}$. In order to investigate the influence of this term on the photoemission matrix element, one needs to evaluate the *projection* of the *polarization vector* $\boldsymbol{\epsilon}$ on the final state wave vector $(i\boldsymbol{k}_f - \frac{1}{\lambda}\boldsymbol{e}_\perp)$. Figure 4.18(a) shows a typical ARPES geometry where the light beam $h\nu$ impinges the sample within the yz-incidence plane making an angle α with respect to the out-plane normal.

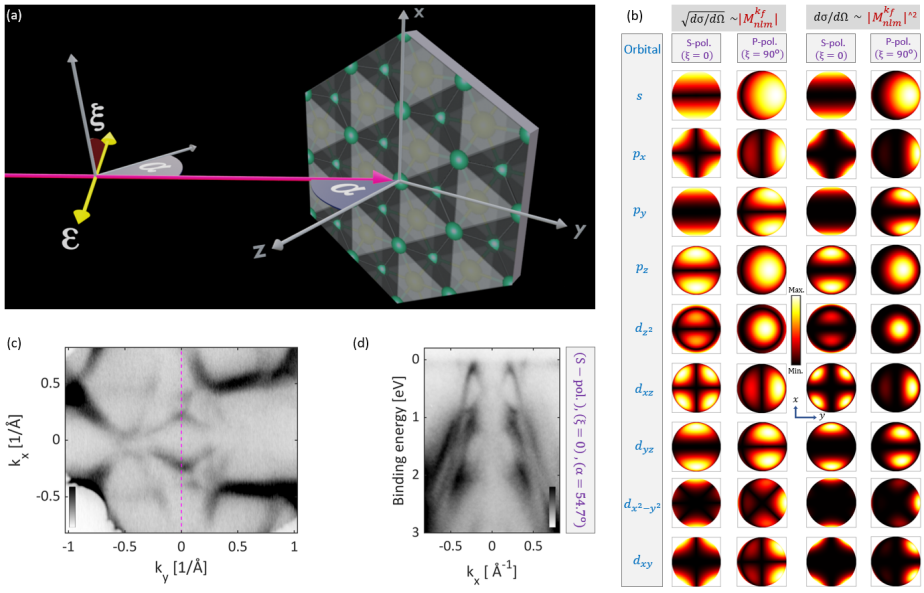

Figure 4.18: **Effect of light polarization and the experimental geometry on the measured ARPES spectra.** (a) Typical ARPES experimental geometry where a beam of light $h\nu$ impinges the sample within the yz-plane with an angle α with respect to the sample normal $\hat{z}$. The polarization of light is defined by its electric field vector $\boldsymbol{\epsilon}$. The angle ξ defines the ratio between the principle components of the electric field. (b) Calculated angular distributions $\sqrt{d\sigma/d\Omega}$ and $d\sigma/d\Omega$ of photoelectrons emitted from s-, p- and d-orbitals using s-polarized light ($\xi = 0$), and p-polarized light ($\xi = 90°$). For s-polarized light, calculations show vanishing intensity along the y-axis at $k_{fx} = 0$. (c) Measured Fermi surface map of $PtTe_2$ using s-polarized light ($\xi = 0$) and for $\alpha = 54.7°$. (d) Energy-momentum bands dispersion map $E(k_y)$ at $k_{fx} = 0$, probed along the magenta dashed line in (c). (a) Produced based on discussion in Ref. [104] to adapt our experimental data. (b) Produced based on the free-electron model discussed in Ref. [152].

Using the so-called Jones notation, the light polarization $\boldsymbol{\epsilon}$ can be expressed in terms of its conventional components along the x, y, and z axes [155–157], with z representing the out-plane axis[9]

[9]The x- and y-axes in this section are inverted compared to the rest of figures in this thesis to be consistent with Ref. [104].

$$\boldsymbol{\epsilon} = \epsilon e^{i\eta} \begin{pmatrix} cos(\xi) \\ e^{i\delta} sin(\xi) cos(\alpha) \\ e^{i\delta'} sin(\xi) sin(\alpha) \end{pmatrix} \tag{4.1}$$

Here, the angle ξ, referenced to the x-axis, determines the polarization orientation of the incident light's electric field $\boldsymbol{\epsilon}$. Therefore, it defines the ratio between the principal components of $\boldsymbol{\epsilon}$. While δ defines the relative phase between the principal components of $\boldsymbol{\epsilon}$ such that $\delta = \varphi_y$-φ_x and $\delta' = \varphi_z$-φ_x taking φ_x as reference, where φ_j is the phase offset of the electric field in the j^{th} direction. η is the absolute phase of the light. The modulus square of the polarization part of the matrix element can be rewritten in term of the so-called Stokes parameters to investigate the degree of polarization [155, 158, 159]

$$|\boldsymbol{\epsilon} \cdot (i\boldsymbol{k}_f - \frac{1}{\lambda}\boldsymbol{e}_\perp)|^2 = \frac{S_0}{2}\left(k_{fx}^2 + k_{fy}'^2 + \frac{sin^2\alpha}{\lambda^2}\right) + \frac{S_1}{2}\left(k_{fx}^2 - k_{fy}'^2 - \frac{sin^2\alpha}{\lambda^2}\right) + S_2 k_{fx} k_{fy}' - S_3 k_{fx} \frac{sin\alpha}{\lambda}$$

where $k_{fy}' = cos(\alpha)k_{fy} + sin(\alpha)k_{fz}$, $S_0 = \epsilon^2$, $S_1 = \epsilon^2 cos(2\xi)$, $S_2 = \epsilon^2 cos(\delta) sin(2\xi)$ and $S_3 = \epsilon^2 sin(\delta') sin(2\xi)$ [104]. Using linearly ($\delta = \delta' = 0$) and s-polarized light ($\xi = 0$), the electric field will oscillate along the x-direction perpendicular to the reaction plane yz which is defined by the incidence direction of the photons and the normal to the sample surface (see Fig. 4.18(a)). Therefore, the only non-vanishing Stokes parameters would be $S_0 = S_1 = \epsilon^2$ and the polarization term (I) becomes $|\boldsymbol{\epsilon} \cdot (i\boldsymbol{k}_f - \frac{1}{\lambda}\boldsymbol{e}_\perp)|^2 = S_0 k_{fx}^2$ which would lead to a vanishing matrix element for $k_{fx} = 0$. This is clearly verified in Fig. 4.18(b) for the calculated angular distributions $\sqrt{d\sigma/d\Omega}$ and $d\sigma/d\Omega$ of photoemitted electrons from s-, p- and d-atomic orbitals using s-polarized light ($\xi = 0$), where the calculated photoemission distribution exhibits zero intensity along the y-axis at $k_{fx} = 0$[10].

Figure 4.18(c) shows a measured ARPES Fermi surface map of $PtTe_2$. This measurement was done using the experimental geometry of Fig. 4.18(a) with s-polarized light $\xi = 0$ and incidence angle $\alpha = 54.7°$. One can clearly see a nearly vanishing photoemission intensity at $k_{fx} = 0$. Additionally, the energy-momentum map in Fig. 4.18(d) was measured along the magenta-dashed line in Fig. 4.18(c) demonstrating a reduced ARPES intensity in the region of $k_{fx} = 0$.

Figure 4.19(a)-(d) presents a summary of the $PtTe_2$ spectral function measured using the UV $\sim$ 6.02 eV laser system, discussed in Sec. 3.3, centered at the normal emission of the sample as illustrated schematically in Fig. 4.19(e). Panel (a) shows the ARPES Fermi surface map of $PtTe_2$. The corresponding energy-momentum map along the magenta line is shown in panel (b). Both panels (a) and (b) were measured using p-polarized light. Panels (c),(d) are same but measured using s-polarized light.

To verify the reduced photoemission intensity within the reaction plane when using the light with polarization perpendicular to this plane, we employed the high-resolution laser-driven ARPES spectrometer to investigate the effect on the topological surface states near the Fermi level, which have been discussed in Sec. 4.3.

[10] Calculations presented in Fig. 4.18(b) were done using the free-electron final state formula discussed in Note 8

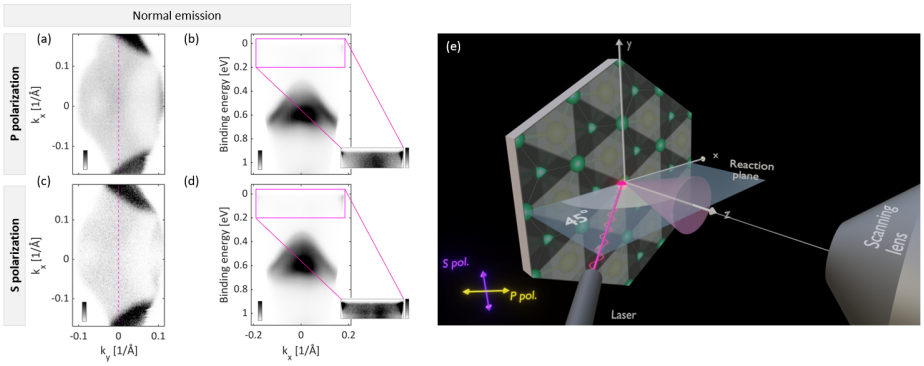

Figure 4.19: **$PtTe_2$ spectral function measured using $\sim$ 6 eV laser in normal emission geometry.** (a) Laser ARPES Fermi surface map of $PtTe_2$ measured using p-polarized light. (b) Corresponding energy-dispersion map $E(k_x)$ for $k_y = 0$, as indicated by the magenta dashed line in (a). (c),(d) Equivalent Fermi surface and energy dispersion maps, respectively, obtained using s-polarized light. (e) Schematic of the ARPES experimental geometry used for measurements in (a)-(d), highlighting the lens deflector system that collects emission angles (red cone) with the sample *normal* to the lens axis.

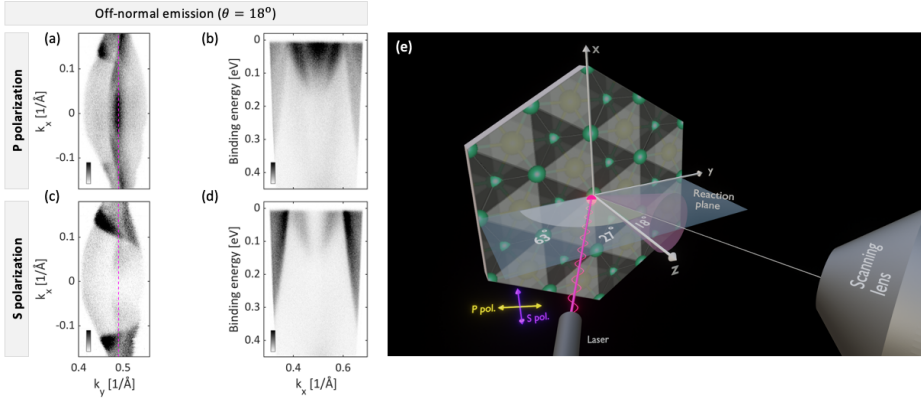

Figure 4.20: **$PtTe_2$ spectral function measured using $\sim$ 6 eV laser in off-normal emission geometry.** (a) Laser ARPES Fermi surface map of $PtTe_2$ measured using p-polarized light. (b) Corresponding energy-dispersion map $E(k_x)$ for $k_y = 0$, as indicated by the magenta dashed line in (a). (c),(d) Equivalent Fermi surface and energy dispersion maps, respectively, obtained using s-polarized light. (e) Schematic of the ARPES experimental geometry used for measurements in (a)-(d), highlighting the lens deflector system that collects emission angles (red cone) with the sample rotated by $\theta = 18°$ relative to the lens axis.

A summary of the electronic band structure for the related portion of the Brillouin zone is presented in Figs. 4.20(a)-(d). These electronic structure maps were measured for the off-normal geometry in which the sample was rotated by $\theta = 18°$ as schematically illustrated in Fig. 4.20(e). This rotation is needed to probe the Fermi surface states, due to the relatively small size of the reciprocal space probed with $h\nu = 6$ eV, where $k_{||}^{max} \sim 0.63$ Å^{-1}.

In Fig. 4.20(b), measured with p-polarized light, the two electron pockets of the Fermi surface states are distinguishable within the narrow energy window of $\Delta E \sim 0.5$ eV below the Fermi level. Notably, one can see a reduced ARPES intensity at $k_{fx} = 0$ in the Fermi surface map shown in panel (c) measured with s-polarized light compared to its equivalent map in panel (a) measured with p-polarized light. Indeed, the energy-momentum map in panel (d) measured along the magenta line in (c) demonstrates this reduced photoemission intensity at $k_{fx} = 0$.

In Sec. 2.5.1.2, we demonstrated that the matrix element in its velocity form can be expressed as $M_{f,i} \propto \langle \phi_f | \boldsymbol{\epsilon} \cdot \boldsymbol{p} | \phi_i \rangle$, where $\boldsymbol{p}$ is the momentum operator. For a known alignment of the mirror planes of the sample surface, a well-defined light polarization, and a known parity of the initial state under reflection through these mirror planes, it becomes possible to predict the final states that will contribute to a non-vanishing ARPES signal. These predictions are based on the parity of the final states, allowing for the identification of both the allowed states that contribute significantly to the ARPES signal and those with suppressed contributions.

To clarify this, consider a case schematically illustrated in Fig. 4.21. Here, the surface of the sample has a mirror plane defined as the yz-plane, which coincides with the reaction plane. Suppose the initial state $|\phi_i\rangle = p_x$ has odd parity, with the odd reflection through the mirror plane shown by two colors.

For s-polarized light, the electric field will oscillate along the x-axis ($\boldsymbol{\epsilon} = \epsilon \hat{\boldsymbol{x}}$), which means that the momentum operator in the matrix element, $\boldsymbol{p}$, will be $\frac{\partial}{\partial x}$, that is odd with respect to the mirror plane. Thus, an even final state $|\phi_f\rangle$ will produce a detectable ARPES signal *within the yz-plane*, where $\langle \phi_f | \frac{\partial}{\partial x} | \phi_i \rangle = \langle + | - | - \rangle \neq 0$. Conversely, an odd final state will lead to a vanishing signal, where $\langle \phi_f | \frac{\partial}{\partial x} | \phi_i \rangle = \langle - | - | - \rangle = 0$.

In contrast, for p-polarized light, the electric field oscillates within the reaction plane yz, which means that the momentum operator will include $\frac{\partial}{\partial y}$ and $\frac{\partial}{\partial z}$, both are even with respect to the mirror plane. In this case, an odd final state produces a detectable ARPES signal, where $\langle \phi_f | \frac{\partial}{\partial y} + \frac{\partial}{\partial z} | \phi_i \rangle = \langle - | + | - \rangle \neq 0$, while an even final state results in a suppressed signal, where $\langle \phi_f | \frac{\partial}{\partial y} + \frac{\partial}{\partial z} | \phi_i \rangle = \langle + | + | - \rangle = 0$.

We have demonstrated, in Sec. 4.6, that the topological surface states crossing the Fermi level, as measured in Fig. 4.20, are predominantly derived from the out-plane Te $5p$ Y_1^0 ($5p_z$) orbital. From an atomic perspective, transitions involving a change in orbital angular momentum must adhere to the dipole selection rule, which specifies that $\Delta l = \pm 1$, while the change in the magnetic quantum number is constrained to $\Delta m_l = 0, \pm 1$ [160, 161]. Consequently, the permitted photoemission transitions that originate from the $5p$ Y_1^0 orbital include $Y_0^0 \sim s$, $Y_2^0 \sim d_{z^2}$, $Y_2^1 \sim (d_{xz} - i d_{yz})$ and $Y_2^{-1} \sim (d_{xz} + i d_{yz})$.

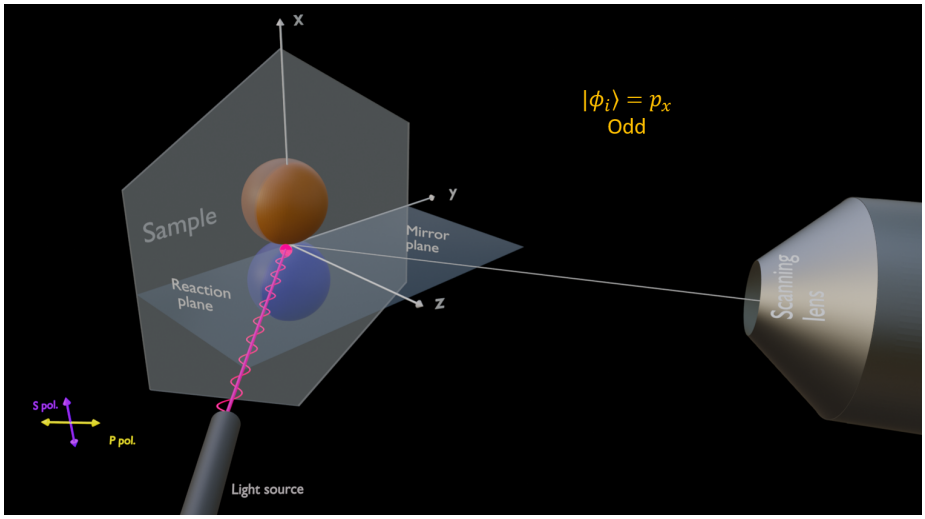

Figure 4.21: **Effect of experimental geometry symmetries on the selection rules for initial and final orbitals.** A mirror plane of the sample surface is shown coinciding with the reaction plane. Initial state $|\phi_i\rangle = p_x$ is shown with an odd parity upon reflection through the mirror plane demonstrated by the two colors of the orbital. For s-polarized light with electric field $\boldsymbol{\epsilon} = \epsilon\hat{\boldsymbol{x}}$, odd with respect to the mirror plane, an ARPES signal within the reaction plane is detectable for an even final state, while a vanishing signal within the plane is measured for an odd final state. For polarized light with electric field within the reaction plane, e.g. p-polarization, even with respect to the mirror plane, an ARPES signal within the reaction plane is detectable for an odd final state, while a vanishing signal within the plane is measured for an even final state.

s-polarization				
ϕ_i \ ϕ_f	Y_0^0	Y_2^0	Y_2^1	Y_2^{-1}
$Y_1^0 = p_z$	$\langle s\vert\text{s-pol.}\vert\ p_z\rangle$ = $\langle +\vert - \vert +\rangle$ = 0	$\langle d_{z^2}\vert\text{s-pol.}\vert\ p_z\rangle$ = $\langle +\vert - \vert +\rangle$ = 0	$\langle d_{xz}\vert\text{s-pol.}\vert\ p_z\rangle$- $i\langle d_{yz}\vert\text{s-pol.}\vert\ p_z\rangle$ = $\langle -\vert - \vert +\rangle$ - $i\langle +\vert - \vert +\rangle$ = $\langle -\vert - \vert +\rangle$	$\langle d_{xz}\vert\text{s-pol.}\vert\ p_z\rangle$+ $i\langle d_{yz}\vert\text{s-pol.}\vert\ p_z\rangle$ = $\langle -\vert - \vert +\rangle$ + $i\langle +\vert - \vert +\rangle$ = $\langle -\vert - \vert +\rangle$

Table 4.1: **Matrix elements using s-polarized light.** Summary of the photoemission matrix elements, within the yz-plane defined in Fig. 4.21, for the allowed transitions into the final states Y_0^0, Y_2^0, Y_2^1 and Y_2^{-1} using s-polarized light, and staring with the out-plane orbital p_z, based on the parity of the initial state, s-polarized light and the final state.

p-polarization				
ϕ_i \ ϕ_f	Y_0^0	Y_2^0	Y_2^1	Y_2^{-1}
$Y_1^0 = p_z$	$\langle s\text{\|p-pol.\| } p_z\rangle$ = $\langle +\| + \|+\rangle$ $\neq 0$	$\langle d_{z^2}\text{\|p-pol.\| } p_z\rangle$ = $\langle +\| + \|+\rangle$ $\neq 0$	$\langle d_{xz}\text{\|p-pol.\| } p_z\rangle$- $i\langle d_{yz}\text{\|p-pol.\| } p_z\rangle$ = $\langle -\| + \|+\rangle$ - $i\langle +\| + \|+\rangle$ $= -i\langle +\| + \|+\rangle$	$\langle d_{xz}\text{\|p-pol.\| } p_z\rangle$+ $i\langle d_{yz}\text{\|p-pol.\| } p_z\rangle$ = $\langle -\| + \|+\rangle$ + $i\langle +\| + \|+\rangle$ $= i\langle +\| + \|+\rangle$

Table 4.2: **Matrix elements using p-polarized light.** Summary of the photoemission matrix elements, within the yz-plane defined in Fig. 4.21, for the allowed transitions into the final states Y_0^0, Y_2^0, Y_2^1 and Y_2^{-1} using p-polarized light, and staring with the out-plane orbital p_z, based on the parity of the initial state, p-polarized light and the final state.

Tables 4.1 and 4.2 summarize the matrix elements for the allowed photoemission transitions starting from the out-plane p_z orbital, which is even with respect to the yz-mirror plane defined in Fig. 4.21. In Table 4.1, we utilized s-polarized light (odd), while Table 4.2 employs p-polarized light (even). Depending on the parity of the final state with respect to the yz-mirror plane, the analysis reveals that, for s-polarized light, two photoemission channels completely vanish, and the other two are significantly suppressed. In contrast, none of the photoemission transitions are absent when p-polarized light is employed.

One can conceptualize s-polarized light, with its electric field oscillating along the x-axis and perpendicular to the yz-plane, as an effective force that oscillates the charge density of the orbitals along the x-direction. This interaction leads to the formation of a region of suppressed intensity within the reaction plane. Therefore, within the free-electron final state picture, and the analysis presented for the photoemission matrix element based on the parity of atomic orbitals and light polarization we could explain the suppressed photoemission signal at $k_{fx} = 0$ within the reaction plane.

However, in Figs. 4.18(c), 4.18(d), 4.20(c) and 4.20(d) the photoemission intensity is not completely zero at $k_{fx} = 0$. This is further supported by the band dispersion map presented in Fig. 4.17(h), which indeed exhibits a well-defined band dispersion despite being obtained using s-polarized light and a sample alignment shown by the corresponding Fermi surface map in Fig. 4.17(a), similar to the alignment represented in the Fermi surface map of Fig. 4.18(c).

The plane-wave approximation for the final state remains valid at the detector, which is effectively at an infinite distance from the sample. However, within the solid, this approximation breaks down due to the significant influence of the local neighboring atomic potentials on the wave function of the photoemitted electron, resulting in scattering events from neighboring atoms.

A more accurate approach to the photoemission process involves considering a scattering final-state wave function, $\psi_f^{scattering}$, for the entire system. This wave function can be expressed as a partial-wave expansion around each atomic site, which, at each site, adheres to the dipole selection rules known from atomic physics

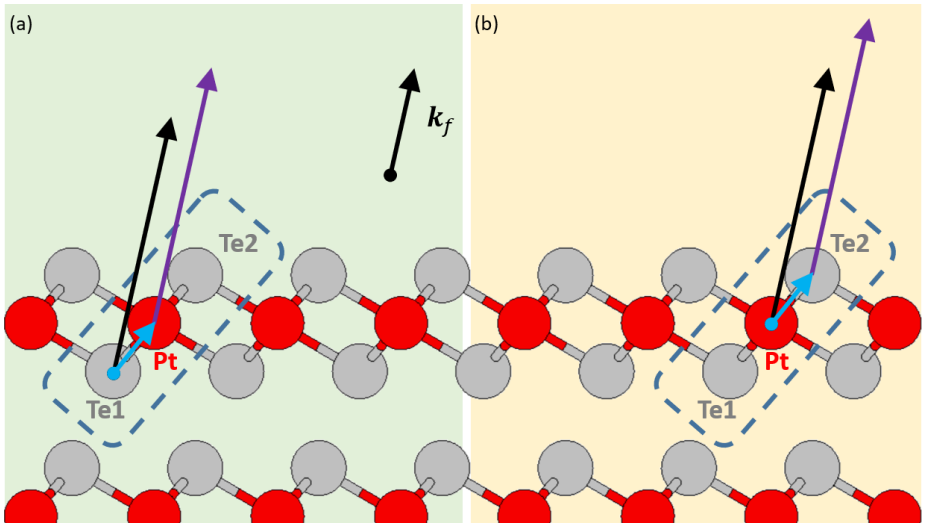

Figure 4.22: **Schematic representation of elastically scattered photoemitted electrons.** (a) Te1,Te2 and Pt atoms within the primitive unit cell, and a final state wave vector $\boldsymbol{k}_f$ are indicated. Black arrow indicates a photoemitted electron from the Te1 atom leaving the surface of bulk $PtTe_2$ along $\boldsymbol{k}_f$ without being scattered. Process of elastic scattering is illustrated by the blue arrow indicating a photoemitted electron from Te1 atom being elastically scattered by the Pt atom leaving the surface at $\boldsymbol{k}_f$ as indicated by the purple arrow. (b) Same as (a), but for electrons emitted from the source atom Pt while the scatterer atom is Te2.

[102, 103].

Figures 4.22(a) and 4.22(b) illustrate the process of elastic scattering of photoemitted electrons along the final wave vector $\boldsymbol{k}_f$. In Fig. 4.22(a), the emitter is the bottom Te atom (Te1) of the top surface monolayer in bulk $PtTe_2$, while the Pt atom acts as the scatterer. In Fig. 4.22(b), the emitter is the Pt atom, while the scatterer is the top Te atom (Te2). Now within the LEED picture (TR-photoemission), the scattering waves from individual atomic sites are coherently summed, as discussed in Sec. 2.6.

To distinguish between the free-electron final-state approximation and the scattering wave final state, photoelectron diffraction calculations were performed using the EDAC code [51]. The angular distribution projections, $|M_{nlm}^{\boldsymbol{k}_f}|$ and $|M_{nlm}^{\boldsymbol{k}_f}|^2$, are presented in Fig. 4.23. These projections correspond to scattering spherical waves emitted from the $4p_x$, $4p_y$, and $4p_z$ orbitals of the Te1 atoms[11], as illustrated in Fig. 4.22(a). The calculations involve the use of both s- and p-polarized light, incident at an angle $\alpha = 54.7°$ (see Fig. 4.18(a)), with electrons emitted at kinetic energies of 104 eV and 500 eV, relevant to the work presented in this thesis. In the first two vertical channels of Fig. 4.23, the emission is modeled from an isolated Te atom. In contrast, the third and fourth vertical channels represent emissions from Te1 atoms

[11] As discussed in Note 6, a portion of the charge from the outermost valence orbitals extends beyond the Muffin-tin spheres, therefore, Te $4p$ orbitals were used in the calculations instead of Te $5p$. For the same reason, the Pt $5s$ orbital was used instead of Pt $6s$ in the calculations presented in Fig. 4.24. Nevertheless, the underlying concept remains valid.

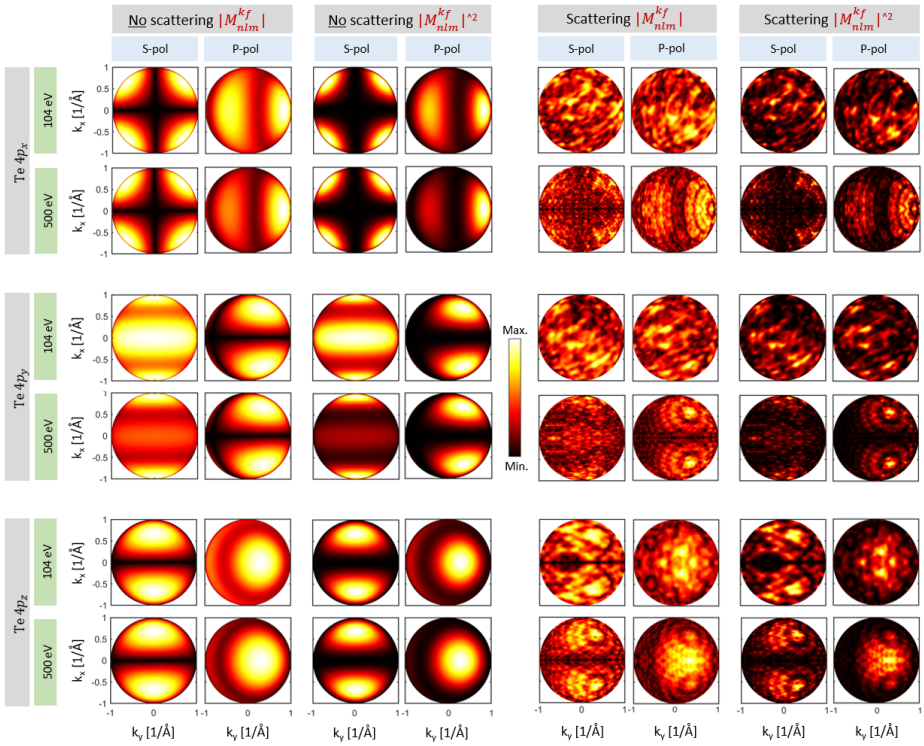

Figure 4.23: **Angular distribution of photoelectrons emitted from Te p-orbitals.** Projection of the angular distribution $|M^{\boldsymbol{k}_f}_{nlm}|$ and $|M^{\boldsymbol{k}_f}_{nlm}|^2$ of photoelectrons emitted from Te 4p-orbitals (Te1-labeled atom in Fig. 4.22) for s- and p-polarized light and incidence angle of light $\alpha = 54.7°$ (see Fig. 4.18(a)), and for electrons emitted with kinetic energies of 104 eV and 500 eV. In the first two vertical channels maps show atomic emission, where scattering effect was neglected and zero inner potential was used. In the third and fourth vertical channels, scattering effect was included within a cluster of radius 20 Å , IMPF of 3 Å and inner potential $V_\circ = 15$ eV.

embedded within a cluster of 775 atoms, with a radius of 20 Å , an inelastic mean free path (IMFP) of 3 Å , and an inner potential $V_\circ = 15$ eV. Figure 4.24 presents analogous calculations for photoemission from the outermost Pt orbitals, specifically the 5s and 5d orbitals (see Fig. 4.22(b)). In both Figs. 4.23 and 4.24, the emission is analyzed from atomic orbitals with significant contributions to the valence bands, as discussed in detail in Sec. 4.6.

From Figs. 4.23 and 4.24, it is evident that the angular distribution exhibits a non-vanishing signal at $k_{fx} = 0$ even for emission from isolated atoms, in contrast to the free-electron model calculations shown in Fig. 4.18(b). This observation accounts for the well-defined band dispersion seen in Fig. 4.17(h) and, more generally, explains the non-vanishing ARPES signal at $k_{fx} = 0$.

Moreover, as the kinetic energy of the photoemitted electrons increases, the angular distribution becomes increasingly similar to that of atomic emission. This trend is apparent in the comparison between photoemitted electrons with kinetic energies of 500 eV and 104 eV. The consistency of this behavior aligns with the understand-

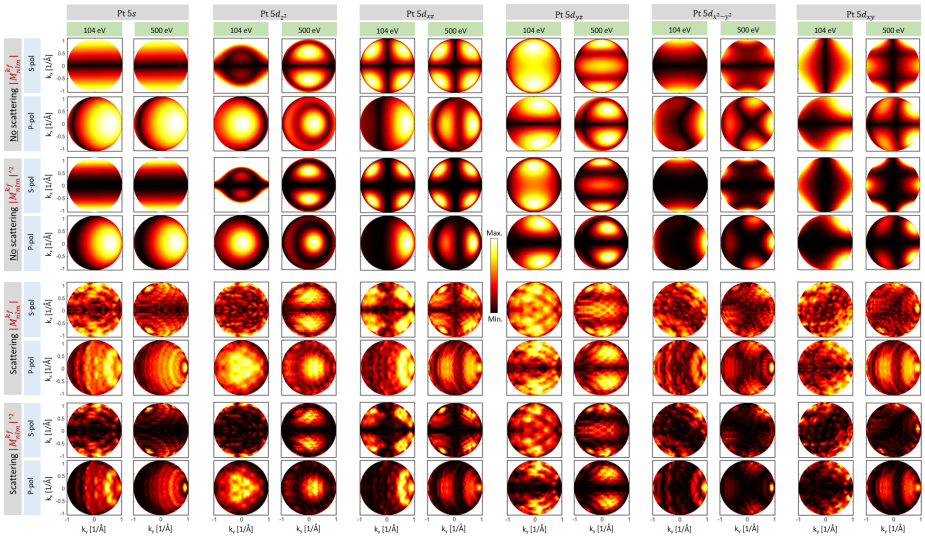

Figure 4.24: **Angular distribution of photoelectrons emitted from Pt s- and d-orbitals.** Projection of the angular distribution $|M^{\boldsymbol{k}_f}_{nlm}|$ and $|M^{\boldsymbol{k}_f}_{nlm}|^2$ of photoelectrons emitted from Pt 5s- and 5d-orbitals (see Fig. 4.22) for s- and p-polarized light and incidence angle of light $\alpha = 54.7°$ (see Fig. 4.18(a)), and for electrons emitted with kinetic energies of 104 eV and 500 eV. In the first two horizontal channels maps show atomic emission, where scattering effect was neglected and zero inner potential was used. In the third and fourth horizontal channels, scattering effect was included within a cluster of radius 20 Å , IMPF of 3 Å and inner potential $V_\circ = 15$ eV.

ing that higher kinetic energy promotes more pronounced forward scattering along atomic bonds, as discussed in Sec. 2.6.

4.10 Asymmetric $E(k_x)$ spin-integrated maps

In this section, I will begin to delve into the central idea of the work presented in my thesis. Figure 4.25 shows an overview of $PtTe_2$ measured spectra via the unpolarized HeI_α discharge lamp with photon energy $h\nu_{(HeI_\alpha)} = 21.22$ eV. In Fig. 4.25, the reaction plane is the yz-plane. Let's divide the work into two main geometries, based on the orientation of the reaction plane with respect to the mirror planes of the crystal. The first geometry: is schematically illustrated in (a) where the sample was rotated around the out-plane z-axis such that the HeI-light impinges the sample within one of the three mirror planes hosted by bulk $PtTe_2$, i.e. the reaction plane coincides with the $\mathcal{M}_x$ mirror plane. This we call *symmetry geometry*.

ARPES data has been collected as a 3D matrix, visualized in (b) with two cuts through this matrix shown in (c) and (d). Figure 4.25(c) shows a constant energy surface at the Fermi level where it is clearly seen that the $\mathcal{M}_x$ mirror plane divides the picture into two mirrored halves regarding the photoemission intensity and the structure features. One would as well expect when probing perpendicular to the mirror plane $\bar{M}$-$\bar{\Gamma}$-$\bar{M}$ along the x-direction to get a mirrored spin-integrated band dispersion maps. This is verified in the energy-momentum map $E(k_x)$ shown in

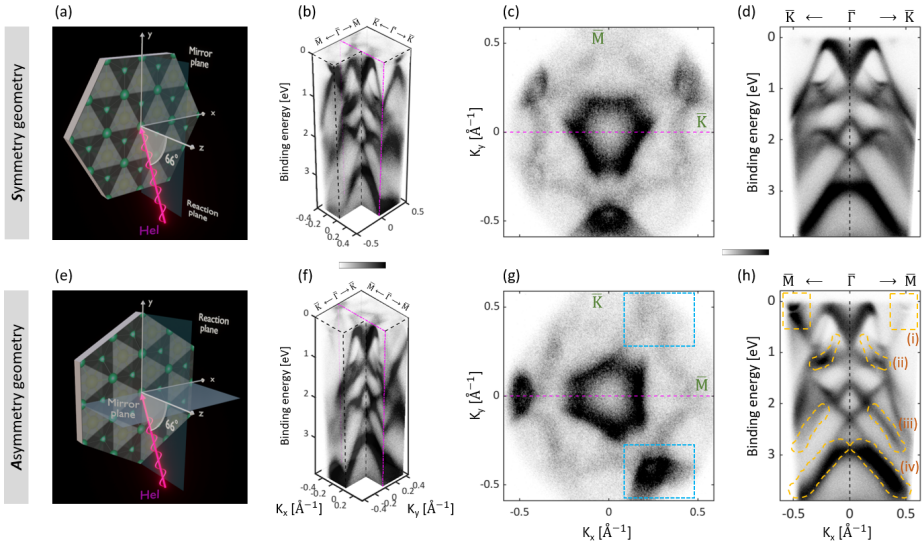

Figure 4.25: **Spin-integrated asymmetries**. Upper panel *symmetry geometry*: (a) schematic geometry showing aligning of the sample such that the unpolarized HeI-light ($h\nu = 21.22$ eV) impinges the sample within one of the three mirror planes of bulk $PtTe_2$ (photoemission reaction plane coincides with a mirror plane) (b) Visualisation of the $E_B(k_{||})$ set of data collected in this geometry. (c) Fermi surface, constant energy surface cut through (b) at the Fermi energy $E_B = 0$ eV. (d) Band dispersion map $E(k_x)$ at $E(k_y) = 0$, indicated by the magenta frame in (b) and probed along the magenta line in (c). Lower panel *asymmetry geometry*: (e)-(h) Same as (a)-(d) but for the geometry shown in (e) which is reachable from (a) by rotating the sample around the z-axis by 30° ending up with one of the sample mirror planes being orthogonal to the reaction plane. Blue rectangles in (g) indicate light induced asymmetries in ARPES signal. Yellow-labeled regions in (h) denote photoemission asymmetries in surface states (i-ii) and bulk states (iii-iv).

(d), indicated by the dashed magenta frame in (b) and the dashed magenta line in (c), in which the black-dashed line at $k_x = 0$ in (d) acts as a mirror line of the spectrum. This is a result of an $\mathcal{M}_x$ mirror plane being conserved by the entire experimental setup, that is sample together with the incident light. It is easy to see from Fig. 4.25(c) that the two remaining sample mirror planes of the sample surface are broken, that is the intensity distribution in (c) does not obey them.

The second geometry: is schematically shown in (e). The sample was rotated around the z-axis by $\varphi = 30°$ referenced to the symmetry geometry such that *none* of the three mirror planes would be within the incidence plane of light, instead the reaction plane is perpendicular to the $\mathcal{M}_y$ mirror plane in this case. This we call *asymmetry geometry*. The corresponding 3D data set $E_B(k_{||})$ is visualized in (f) with the Fermi energy cut in (g) and the energy momentum $E(k_x)$ cut in (h) which is also indicated by the magenta frame in (f) and magenta line in (g). However, In this geometry ARPES maps do not obey any mirror symmetries and in particular the map in Fig. 4.25(h) is very strongly asymmetric, both regarding the intensity distributions and location of the dispersive features along negative and positive k_x. Some of these asymmetries are highlighted and labeled with the numbers (i)-(iv).

It is important to note that the asymmetries in the photoemission signal happening at (i)- and (ii)-labeled regions are assigned to the topological surface state (TSS3) crossing the Fermi level and the surface state (SS) that is buried within the bulk manifold respectively. Conversely, ARPES asymmetries in (iii)- and (iv)-labeled regions can be attributed to bulk-projected momentum space regions. On the other hand, *none of these asymmetries exist in the calculated initial state band dispersion* plotted in Fig. 4.7.

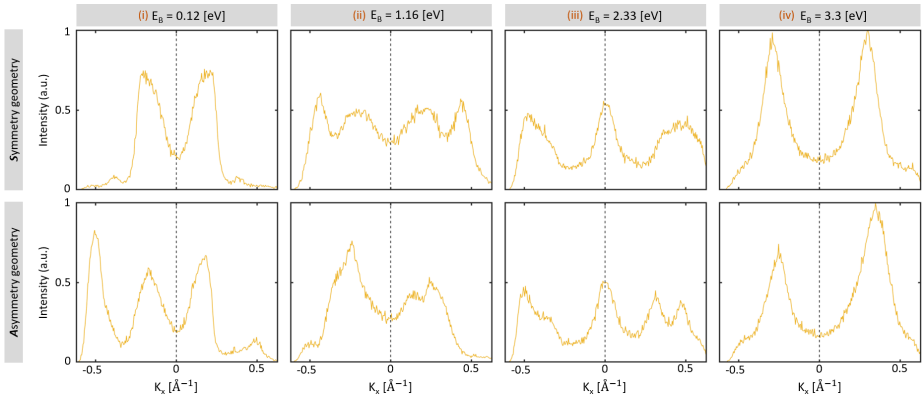

Figure 4.26: **Spin-integrated momentum distribution curves.** Upper panel shows momentum distribution curves at the corresponding indicated binding energies averaged over three energy pixels (ΔE = 20 meV) for the *symmetry* ARPES map Fig. 4.25 (d). Lower panel is equivalent for the upper panel, but for the *asymmetry* ARPES map Fig. 4.25 (h).

To zoom in this picture, a quantitative analysis for the momentum distribution curves (MDCs) is shown in Fig. 4.26 for the two orientations, the *symmetry orientation* in the upper panel and the *asymmetry orientation* in the lower panel for some selected binding energies indicated at the top and also labeled in Fig. 4.25(h). Three energy pixels ($\Delta E = 20$ meV) are averaged over for each of the MDCs plotted in order to reduce the noise. One can see clearly that the MDCs manifest the above observations where the $k_x = 0$ line is a mirror line for all the MDCs in the upper *symmetry geometry* panel. However, the $k_x = 0$ line is no longer a mirror line for any of the corresponding MDCs in the lower *asymmetry geometry* panel.

In order to explain the origin of these spin-integrated asymmetries in the measured spectra, which are absent in the initial state, the projected bulk band structure was calculated along the high symmetry directions K-Γ-K and M-Γ-M as shown in Figs. 4.27(a) and 4.27(b), respectively. The calculations were performed for 61 distinct k_z-values at different heights along the out-plane direction, with the corresponding bulk bands superimposed. The bulk bands corresponding to each specific k_z value were color-coded, with a total of 61 distinct colors used, as indicated by the colorbar. To aid interpretation, a schematic drawing of the bulk Brillouin zone is depicted in Fig. 4.27(c), highlighting a mirror plane and four distinct k_z lines. The bulk bands corresponding to these k_z values are emphasized using thicker lines in Figs. 4.27(a) and 4.27(b), with the associated colors labeled in the colorbar.

Figure 4.27(d) schematically illustrates two distinct cases of the initial state wave function: a surface-localized state and a delocalized bulk state. The primary

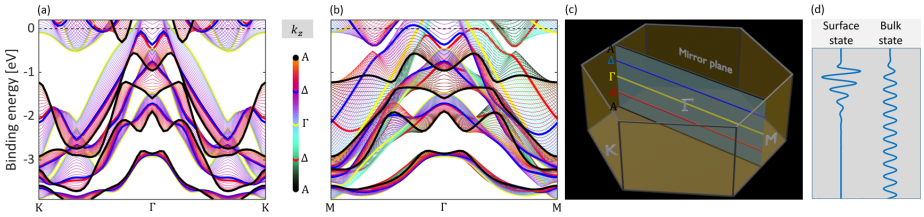

Figure 4.27: **Projected band structure along high symmetry directions of bulk BZ.** (a)-(b) Calculated bulk band structure of $PtTe_2$ projected onto the surface Brillouin zone along the $\bar{K}-\bar{\Gamma}-\bar{K}$ and $\bar{M}-\bar{\Gamma}-\bar{M}$ high-symmetry directions, respectively. The calculations were performed for 61 distinct k_z values along the out-plane direction in reciprocal space, with the bulk bands for each k_z value color-coded, as shown by the colorbar. (c) Schematic of the bulk Brillouin zone, highlighting a mirror plane and four k_z lines, colored according to the corresponding labels in the colorbar. (d) Schematic representation of the charge density distribution for surface and bulk states below the surface.

difference between these cases lies in the behavior of the perpendicular momentum $k_{i\perp}$ of the initial state. Bulk states form continuous bands, whereas surface states manifest as discrete energy levels. As a result, by varying the photon energy, one can observe changes in intensity corresponding to the final perpendicular momentum $k_{f\perp}$. This variation often reflects the bulk dispersion with changing binding energy, particularly at higher photon energies $h\nu$ [162] where the IMFP increases making the photon energy more bulk sensitive (see Sec. 2.5.2). On the other hand, for surface states, only discrete energy levels are detected, with their intensity modulated at different photon energies [149, 150, 163].

The projected bulk band structure along the K-Γ-K direction, depicted in Fig. 4.27(a), exhibits symmetry, with the Γ line serving as a mirror axis for the color distribution on either side, consistent with the presence of a perpendicular mirror plane. In contrast, the projected bulk band structure along the M-Γ-M direction, shown in Fig. 4.27(b), displays asymmetry due to the lack of such a perpendicular mirror plane. This asymmetry is further demonstrated by the thicker bulk bands highlighted in Figs. 4.27(a) and 4.27(b), corresponding to the blue and red lines in Fig. 4.27(c). In Fig. 4.27(a), these bands overlay, whereas they do not align in Fig. 4.27(b). Indeed, this asymmetry is anticipated due to the trigonal crystal structure of bulk $PtTe_2$ discussed in Sec. 4.1, in contrast to what would be expected if it had hexagonal symmetry.

Therefore, we attribute the observed asymmetries in the band dispersion map of Fig. 4.25(h), measured along $\bar{M}-\bar{\Gamma}-\bar{M}$, to bulk-induced effects, particularly in regions (iii) and (iv), which correspond to bulk diffuse manifolds.

A detailed comparison between the projected bulk band structure in Figs. 4.27(a) and 4.27(b) and the corresponding surface band calculations in Figs. 4.7(b) and 4.7(c) reveals that the surface Dirac cone at a binding energy of approximately 2 meV, along with the surface states at $\sim$ 1.5 meV, reside within well-defined bulk-projected gaps. The asymmetries measured in these surface states, which can be considered completely disentangled from the bulk states, can be attributed to geometry-induced asymmetries, as demonstrated in Ref. [46]. In Fig. 4.25(e), the sample was aligned such that the sample surface mirror plane $\mathcal{M}_x$ was broken, leading to an

asymmetry where the positions of atoms on the right side of the plane ($+x$) differ from those on the left side ($-x$). This results to relative shifts in real space between atoms, and as discussed in sec. 2.6 shifts in real space introduce phase shifts in reciprocal space. This in turn creates different phase shifts in reciprocal space for the two emission directions ($+\boldsymbol{k}_x$) and ($-\boldsymbol{k}_x$), contributing to the asymmetries observed in the regions of these surface states in the spectrum depicted in Fig. 4.25(h). The origin of these geometry-induced asymmetries will be discussed in detail later in this thesis, where we will demonstrate that similar asymmetries are also present in the spin-resolved spectra.

Additionally, the surface states at ~ 0.8 meV and those crossing the Fermi level (see Figs. 4.7(b) and 4.7(c)) merge with the surrounding bulk-projected band structure (see Figs. 4.27(a) and 4.27(b)). The asymmetries observed in these surface states, particularly in regions (i) and (ii) of Fig. 4.25(h), can be attributed to a combination of bulk-induced and geometry-induced effects.

Taking a step back, let's examine the Fermi surface map shown in Fig. 4.25(g). As discussed in Sec. 4.2, bulk $PtTe_2$ exhibits a *3-fold* rotational symmetry. Based on the sample alignment in Fig. 4.25(g), the magenta-dashed line represents a mirror plane $\bar{M}$-$\bar{\Gamma}$-$\bar{M}$. Consequently, both the crystal symmetry and alignment require the structure within the blue rectangle in the upper half of the map to be a mirror image, in both intensity and structure, of the corresponding region in the lower half. However, this symmetry is not observed, instead, there is a significant difference in photoemission intensity between the two rectangles. This discrepancy is attributed to light-induced asymmetries in the measured spin-integrated ARPES signal, where the HeI light, as shown in Fig. 4.25(e), breaks the mirror plane indicated by the magenta-dashed line in Fig. 4.25(g). This observation highlights the importance of considering the symmetries of the entire system, which include not only the crystal structure and sample alignment but also the influence of the light.

4.11 Summary

We performed spin-integrated ARPES measurements on $PtTe_2$ using both lab-based light sources at PGI-6 and the PHELIX beamline at the Solaris synchrotron facility in Kraków, Poland. For the first time, we presented ARPES measurements of $PtTe_2$ using Xe ($h\nu = 8.44$ eV) and laser ($h\nu = 6.02$ eV) light sources. Along with detailed band structure calculations, we successfully identified and distinguished between the bulk and surface states of $PtTe_2$.

A significant contribution of this chapter is the systematic analysis of the effects of light polarization, specifically s- and p-polarized light, on the ARPES spectra. Our results demonstrate that the spectral weights and the corresponding band structures exhibit a strong dependence on the polarization of the incident light, a behavior that correlates with the varying orbital characters of the valence bands. Furthermore, we provided experimental evidence of the matrix element effect, showcasing the near-vanishing photoemission intensity, in line with theoretical calculations. This phenomenon is observed when light polarization is perpendicular to the reaction plane and measurements are taken within this plane, or at the zero symmetric line when measurements are made perpendicular to the reaction plane.

The ARPES experiments were conducted with two different sample orientations, each based on the alignment of the mirror planes of crystal surface relative to the reaction plane in which the light impinged the sample. A key finding of this study is the identification of induced asymmetries in the spin-integrated momentum maps. These asymmetries emerged when the sample was rotated such that the incident light beam no longer aligned with a mirror plane of the the crystal, breaking the symmetry of the system. This resulted in significant variations in the photoemission intensity and shifts in the positions of electronic features, especially in the regions corresponding to surface and bulk states. These observed asymmetries are attributed to both the experimental alignment of the crystal and the intrinsic structural asymmetries of the material itself. These findings illustrate a specific instance of how symmetry-breaking in ARPES measurements can influence the observed spectra, providing insight into broader symmetry considerations that have to be taken into account in ARPES experiments.

A thorough comparison of the ARPES data under symmetric and asymmetric configurations highlights the sensitivity of the electronic structure, particularly the topological surface states, to changes in experimental conditions. These findings underscore the importance of considering the experimental setup when interpreting ARPES measurements, as the induced asymmetries significantly affect the observed results and must be taken into account alongside theoretical models for a more accurate understanding of the electronic properties of materials.

5. Spin-resolved electronic structure of $PtTe_2$

In non-magnetic centrosymmetric systems, the combination of time-reversal symmetry (TRS: E(**k**,↑)=E(-**k**,↓)) with the inversion symmetry (IS: E(**k**,↑)=E(-**k**,↑)), where E,±**k**, and ↑↓ denote the electron energy, momentum and spin respectively ensures a net-zero spin polarization and doubly spin-degenerate electronic states throughout the material. However, the current insight that relativistic spin-orbit coupling (SOC) is localized on specific nuclear (atomic) sites in the crystal rather than being a property of the entire crystal structure, is essential for understanding SOC-induced spin polarization [164]. This perspective has led to the concept of hidden spin polarization, which emerges through *local* symmetry breaking at atomic sites. The total spin polarization of the crystal is then the vector sum of these local spin polarizations across all sites [165]. This has led to two forms of such hidden spin polarization, the Dresselhaus D-2 effect resulted from the local inversion asymmetric environment which has been observed at the K and K' points of bulk WSe_2 single crystal [34], and the local Rashba R-2 effect created by the site dipole field which in turn has been verified in the Se $p_{x,y}$-derived bands of the 1T-$PtSe_2$ monolayer [33], and recently in the bulk 1T-$HfSe_2$ single crystal [35].

In previous studies, e.g. [33–42], the accessibility to only limited regions or selected k-points in the energy-momentum space has often hindered the unambiguous confirmation of alignment and has sometimes resulted in unexplainable asymmetries in the spin textures, similar to the asymmetry reported in [33]. These asymmetries have been attributed to defects in the sample or final state effects. However, with the recent advancements in 2D spin detection techniques, such as momentum microscopes, e.g. [45], or lens-deflector systems, e.g. [46] in hemispherical analyzers, it has become possible to image 2D photoemission spin texture maps in certain cases. These maps can be obtained as k_x-k_y maps at a selected binding energy or as E($k_{||}$) maps along a specific $k_{||}$ direction.

In this chapter, we take advantage of the newly developed spin-polarized ARPES (S-ARPES) spectrometer at PGI-6 to study the spin texture of bulk $PtTe_2$ in order to disentangle the final state effects from the initial state.

5.1 Asymmetric $E(k_x)$ spin-resolved maps

In this section I will discuss the main idea of the work presented in this thesis. This work is the demonstration of the existence of asymmetries in the spin-resolved spectra of bulk $PtTe_2$ based on the set-up used during the experiment i.e. the sample alignment together with the incident light. These asymmetries, besides the spin-integrated asymmetries already discussed in Sec. 4.10, are measured taking advantage of the newly developed high-resolution HeI spin-polarized ARPES (S-ARPES) spectrometer.

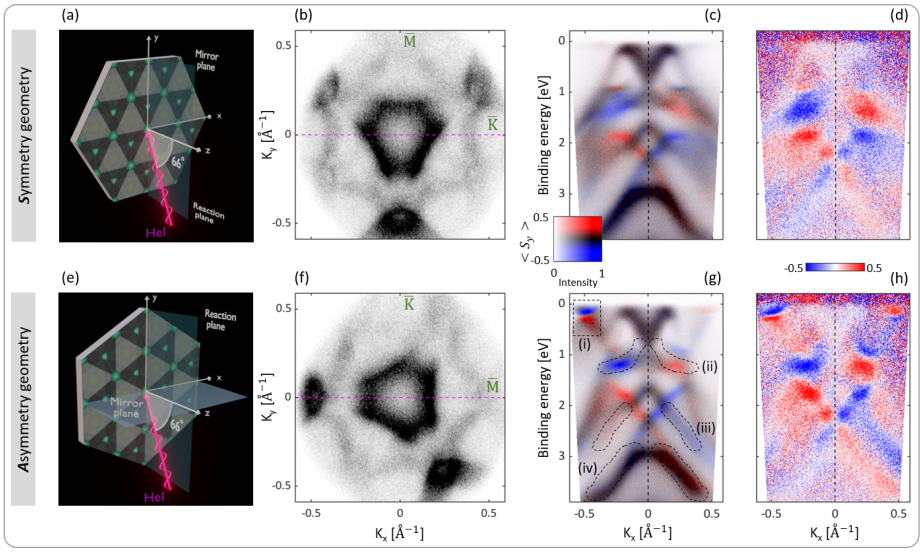

Figure 5.1: **Spin-resolved asymmetries.** Upper panel {***Symmetry geometry***}: (a) schematic geometry where the $\mathcal{M}_x$ mirror plane coincides with the reaction plane. (b) Corresponding Fermi surface map. (c),(d) Experimental HeI spin-resolved (280 × 251 pixels) energy dispersion maps, $E(k_x)$, measured using the lens deflector system probing along the x-axis perpendicular to $\mathcal{M}_x$ mirror plane, as defined in (a) and along the magenta-dashed line in (b), while the sample in normal emission. Lower panel {***Asymmetry geometry***}: (e) Achieved from (a) by rotating the sample around the z-axis by 30°. The reaction plane is now perpendicular to the $\mathcal{M}_y$ mirror plane. (f) Corresponding Fermi surface map. (g),(h) Experimental HeI spin-resolved (280 × 251 pixels) energy dispersion maps, $E(k_x)$, measured using the lens deflector system probing along the x-axis i.e. along the magenta-dashed line in (f), ***not*** perpendicular to any of the system's mirror planes, as defined in (e) while the sample in normal emission. (i-iv) labeled regions in (g) are selected highly asymmetric spin polarized regions. In (c) and (g) the intensity and spin-polarization are simultaneously displayed using the inset 2D color code, where the false color scale refers to the in-plane spin polarization S_y in the ensemble of the photoemitted electrons. (d),(h) The corresponding pure in-plane S_y spin polarization.

The data presented in Fig. 5.1 demonstrates this idea. The way the experiments are done is similar to the spin-integrated experiments discussed in Sec. 4.10. In the upper *symmetry geometry* panel, the sample was rotated around the out-plane z-axis such that one of the three M-Γ-M mirror planes of $PtTe_2$, $\mathcal{M}_x$ in this case, coincides with the reaction plane. Therefore, the symmetry rules of that mirror plane hold

for the spin degree of freedom of an electron. Under symmetry operations, spin polarization transforms as an *axial vector*. The distinction between the axial vector and the polar vector rules under such symmetry mirror operation is summarized in Fig. 5.2. Back to Fig. 5.1(a), the mirror plane under investigation is the $\mathcal{M}_x$ mirror plane perpendicular to the x-axis and labeled in the right panel of Fig. 5.2. When probing along the x-direction perpendicular to the $\mathcal{M}_x$ mirror plane to resolve the in-plane S_y spin component, a reversing in the spin direction of the electron is expected on either side of the $\mathcal{M}_x$ mirror plane based on the axial vector rules summarized in Fig. 5.2.

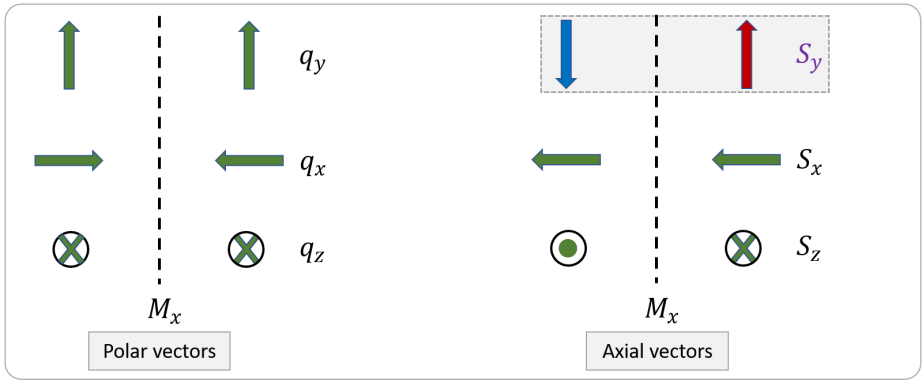

Figure 5.2: **Effects of the symmetry operation $\mathcal{M}_x$ on axial and polar vectors.** In the left panel, the dashed black line represents a mirror plane perpendicular to the x-axis. Under this symmetry operation, the polar vector q_x perpendicular to this plane flips its direction while the other two polar vectors q_y, q_z keep their signs (**q**: e.g. electric dipole). The right panel illustrates the axial vector behaviour under the same symmetry operation. Here, the axial vector S_x spin component perpendicular to the $\mathcal{M}_x$ mirror plane keeps its sign, while the parallel components S_y, S_z flip their signs (**S**: spin vector). The spin component S_y is marked and is the component mainly propped in this thesis, where red and blue indicate flipping of the S_y spin component either side of the mirror plane.

Figures 5.1 (c-d) show spin-polarized energy dispersion maps of bulk $PtTe_2$[1]. These maps are obtained by probing perpendicular to the $\mathcal{M}_x$ mirror plane along the high symmetry direction K-Γ-K in the reciprocal space that is delineated by the magenta-dashed line in (b). In Fig. 5.1(c) the photoemission intensity as well as the spin polarization are plotted together were the spin polarization is saturated to 50% as illustrated by the 2D color code inset. In Fig. 5.1(d) the corresponding pure spin polarization is shown. In Figs. 5.1(c-d), the measured spin polarization maps exhibit symmetric behaviour with respect to the $\mathcal{M}_x$ operation, where the photoemission intensity, spin polarization strength as well as the band structures shapes and positions are copy paste of each other on either side of the $k_x = 0$ line. The only difference between the two halves of each figure is the flipping of the spin-polarization color from *red* (*blue*) $\overset{to}{\Longrightarrow}$ *blue* (*red*) obeying the axial vector rules for the final state measured in-plane S_y spin-component, $S_y(k_x) = -S_y(-k_x)$,

[1]Raw data for the spin-resolved energy dispersion maps presented in Fig. 5.1 are shown in Appendix B.

summarized in Fig. 5.2.

In the lower *asymmetry geometry* panel, the sample was aligned as shown in Fig. 5.1(e). This is achieved via rotating the sample by 30° around the z-axis as compared to Fig. 5.1(a). Now the mirror plane $\mathcal{M}_y$ is perpendicular to the reaction plane. The spin polarized maps Figs. 5.1 (g-h), similar to Figs. 5.1 (c-d), are filtered through probing along the x-direction. However, in this case the probed spectrum along the magenta-dashed line in Fig. 5.1(f) is not perpendicular to any of $PtTe_2$ mirror planes. One can see very strongly asymmetric behavior in these spin polarized maps both regarding the intensity distributions and location of the dispersive features along negative and positive k_x. Some of the highly asymmetric regions are labeled (i)-(iv) in Fig. 5.1(g). Some of these asymmetries are happening for the surface states as for the (i)-labeled surface state as well as (ii)-labeled region. Some asymmetries are happening in the bulk manifold regions labeled (iii) and (iv).

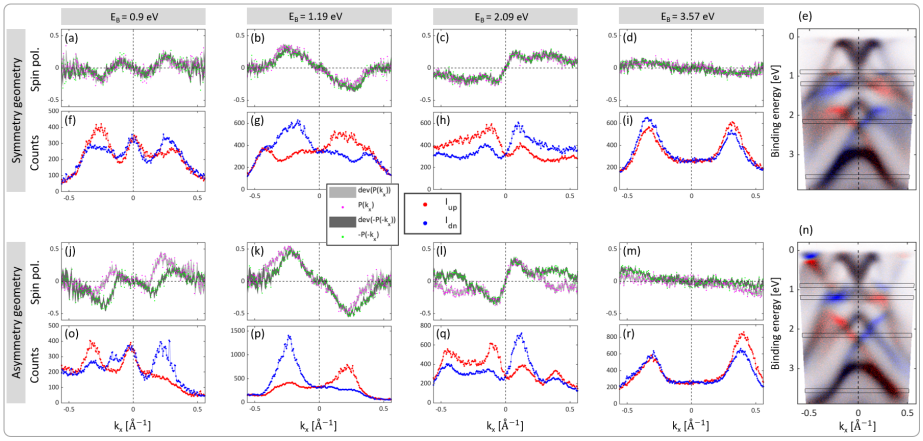

Figure 5.3: **Spin-resolved momentum distribution curves for $PtTe_2$.** Upper panel: (a)-(d) momentum distribution curves (MDCs) for the spin polarization at the indicated binding energies, averaged over 8 energy pixels ($\Delta E \sim 100$ meV) as represented by the black frames in (e). Magenta and green curves show $P(k_x)$ and $-P(-k_x)$, where P is the spin polarization along S_y. Light- and dark gray areas depict standard deviations for spin-polarization curves. (f)-(i) Data from the spin-up (red) and spin-down spectrum (blue) of the spin-detector corrected by the Sherman function S = 0.29, for the magenta $P(k_x)$ curve. Lower panel: (j)-(r) same as upper panel, but for the energy-momentum shown in (n).

To address these asymmetries, a quantitative standard deviation analysis is presented in Fig. 5.3. In the upper symmetry panel of Figs. 5.3(a)-(d) the spin polarization is averaged over 8-energy pixels ($\Delta E \sim 100$ meV), and plotted along k_x with its standard deviation at selected binding energies represented by the black frames in Fig. 5.3(e). Magenta curves represent the spin polarization $P(k_x)$ along S_y with their standard deviations shown by the light gray areas. Additionally, green curves representing $-P(-k_x)$ are also plotted with their standard deviations represented by the dark gray areas.

Figures 5.3(f)-(i) show data from the spin-up (red) and spin-down spectrum (blue) of the spin-detector corrected by the Sherman function S = 0.29, for the magenta $P(k_x)$ curves of the respective panels (a)-(d) of Fig. 5.3. At each k-point

of $E(k_x)$ spin-polarized map, FERRUM detector measures two intensities I_+ and I_- for the target magnetized in opposite directions. Spin polarization is calculated as discussed in Sec. 3.2.2, $P = (1/S)\frac{I_+ - I_-}{I_+ + I_-}$, and the up/down spectra are reconstructed as $I_{up(dn)} = 0.5(I_+ + I_-)(1 \pm P)$. The lower asymmetry panel is same, but for the energy-momentum map in Fig. 5.3(n).

In Figs. 5.3(a)-(d), the $P(k_x)$ and $-P(-k_x)$ curves coincide within the noise level. This confirms the $\mathcal{M}_x$ invariance quantitatively. However, in Fig. 5.3(j-m), the difference between $P(k_x)$ and $-P(-k_x)$ is beyond the noise level. This in turn quantitatively demonstrates asymmetries.

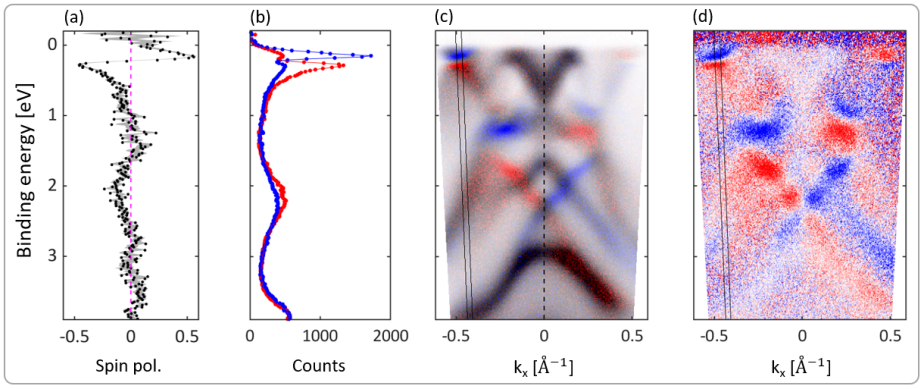

Figure 5.4: **Spin-resolved energy distribution curve for $PtTe_2$.** (a),(b) Polarization vs. binding energy and spin-polarized EDCs, respectively, for the region indicated by the black frame in (c)-(d). Gray areas depict standard deviations for the spin-polarization curve.

Figure 5.4(a) shows the spin polarization energy distribution curve (EDC) for the region indicated by the black frames in Figs. 5.4(c)-(d) with standard deviations represented as gray areas. In Fig. 5.4(b) the respective data from the spin-up (red) and spin-down spectrum (blue) of the spin-detector corrected by the Sherman function S = 0.29 is plotted.

Based on the MDCs of Fig. 5.3 and the EDC of Fig. 5.4, measured spin-polarized maps of $PtTe_2$ show in-plane spin polarization up to $\sim 56\%$.

5.2 Spin-resolved calculations

Figure 5.5 shows the initial state calculations of the S_y spin component of 30-layer $PtTe_2$ slab. A 3D spin polarized calculations is presented in Fig. 5.5(a), while at selected binding energies within an energy window of 100 meV each, are shown in Fig. 5.5(b). Spin-polarized calculations along the high symmetry direction $\bar{K} - \bar{\Gamma} - \bar{K}$ is presented in Fig. 5.5(c) for surface Te1 and Pt atoms, and in Fig. 5.5(d) for the $5p_z$ orbital of the surface Te1 atom. For convenience, Fig. 5.5(g) schematically depicts the outermost Te and Pt atoms from which the majority of the photoemission signal originates through the method's surface sensitivity. Figure 5.5(h) shows 3D spin-polarized calculations for the binding energy window and k-scale range indicated by the black box in Fig. 5.5(f). The black dashed lines in Fig. 5.5(h) refer to the $\bar{K} - \bar{\Gamma} - \bar{K}$ and $\bar{M} - \bar{\Gamma} - \bar{M}$ directions.

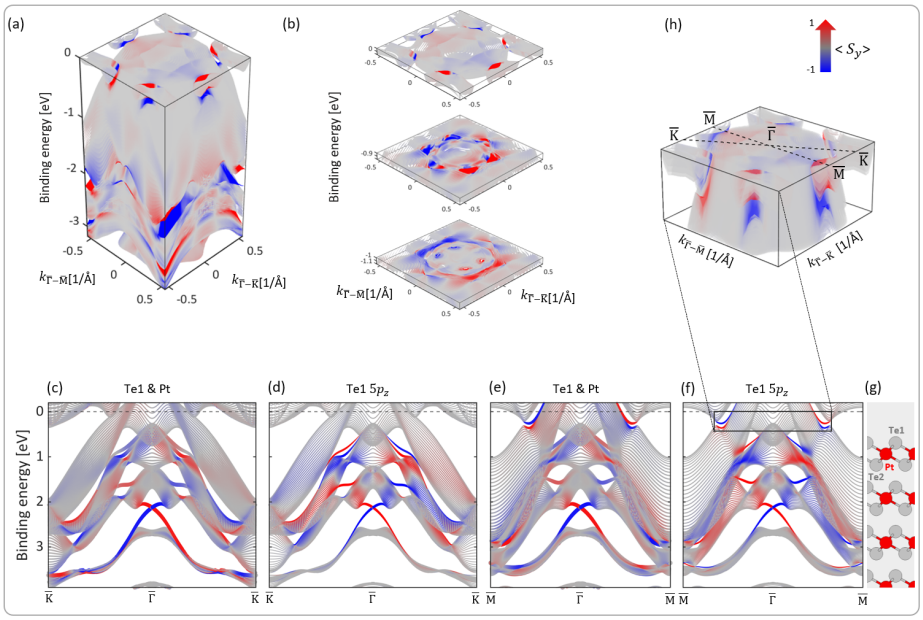

Figure 5.5: **Calculations of the S_y spin component of 30 layer slab of $PtTe_2$.** (a) Theoretical 3D spin-resolved calculations for the in-plane S_y spin component of 30L slab of $PtTe_2$. (b) Spin-resolved momentum maps with energy window 100 meV at the indicated binding energies. (c),(d) Spin-resolved calculations along the high symmetry direction ($\bar{K}-\bar{\Gamma}-\bar{K}$) for the surface (Te1 and Pt atoms) and for Te1 $5p_z$ orbitals, respectively. (e),(f) Same but along ($\bar{M}-\bar{\Gamma}-\bar{M}$). (g) Schematic indication of the surface Te1 atom, the outermost Pt atom and third layer Te2 atom. (h) Spin-resolved calculations for the energy window and k-scale range indicated by the black box in (f). The size of the symbols (thickness of lines in (c)-(f)) indicates the orbitals weight, while the color indicates the spin expectation value S_y.

Calculations show highly spin-polarized surface states close to the Fermi level, at $E_{binding} \sim 0.85$ eV, at $E_{binding} \sim 1.75$ eV as well as the strongly spin-polarized surface Dirac cone at $E_{binding} \sim 2.2$ eV in agreement with the spin polarized measurements of Fig. 5.1. Comparing Figs. 5.5(c) and 5.5(d) with the experimental results in Fig. 5.1(c), Fig. 5.5(d) exhibits better agreement, particularly in the region of ladder states at $E_{\text{binding}} \sim 0.85$ eV. Similarly, Figs. 5.5(e) and 5.5(f), which depict the same analysis along the $\bar{M}-\bar{\Gamma}-\bar{M}$ direction, show better agreement between Fig. 5.5(f) and Fig. 5.1(g).

The theoretical S_y calculations presented in Figs. 5.5(c) and 5.5(e) indicates that the topological ladder wave functions are strongly mixed between the surface-most Pt and Te sites.

However, contrary to the asymmetries in the spin-resolved measurements in Figs. 5.1 (g)-(h), no such asymmetries exist in the calculated spin-polarized initial state.

5.3 Out-plane S_z spin-resolved $E(k_x)$

In this section we present the only out-of-plane S_z measured spin polarization from $PtTe_2$, using the *symmetry geometry* presented in Fig. 5.6(a), in which the reaction plane coincides with the $\mathcal{M}_x$ mirror plane of the sample surface. Figure 5.6(b) presents the corresponding measured ARPES Fermi surface map. A schematic drawing showing the scattering target of the Ferrum spin detector that is rotated by 15° around the y-axis away from the yz-plane and towards the negative x-direction is shown in Fig. 5.6(c). Therefore, using the normal emission of Fig. 5.6(a), we are probing a spin component $S_{15°}$ that is 15° away from the z-axis, which is primarily S_z, but with small component of S_x as indicated in Fig. 5.6(c). A demonstration of such a measurement is presented in Fig. 5.6(d).

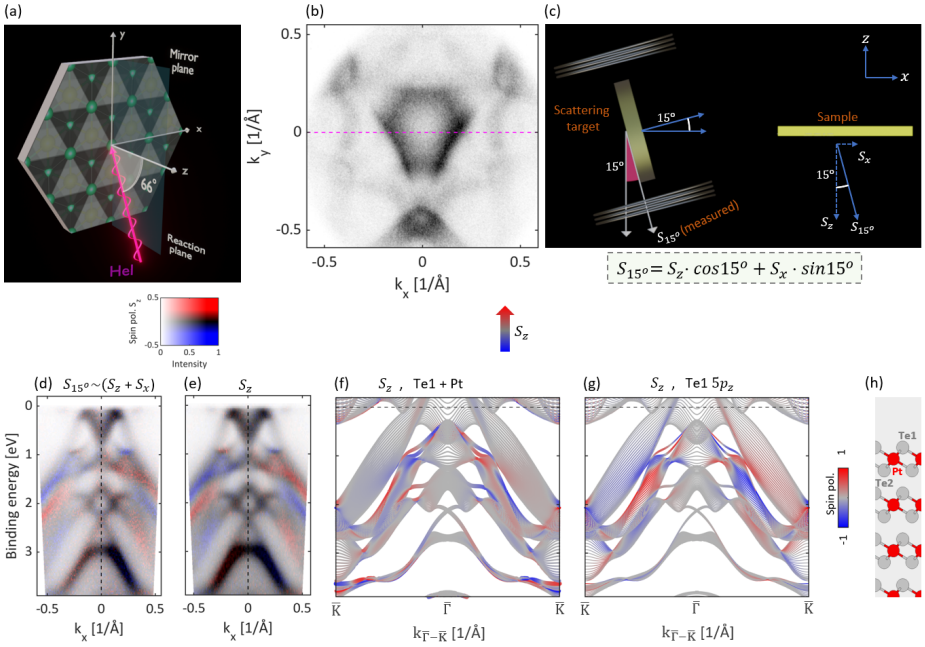

Figure 5.6: **Measured and calculated S_z spin component from $PtTe_2$.** (a) Experimental *symmetry geometry* where the reaction plane coincides with the $\mathcal{M}_x$ mirror plane of the sample's surface. (b) Corresponding measured ARPES Fermi surface map. (c) Schematic drawing shows the rotated scattering target by 15° around the y-axis towards the negative x-direction, indicating the measured spin-polarization component $S_{15°}$. (d) Measured $S_{15°}$ spin component using the geometry presented in (a) for the cut along the magenta line shown in (b). (e) Corrected S_z spin component from (d). (f),(g) Spin-resolved calculations for the out-plane S_z spin component along the high symmetry direction ($\bar{K}-\bar{\Gamma}-\bar{K}$) for the surface (Te1 and Pt atoms) and for Te1 $5p_z$ orbitals, respectively. Thickness of lines indicates the orbitals weight, while the color indicates the spin expectation value S_z. (h) Schematic indication of the surface Te1 atom, the outermost Pt atom and third layer Te2 atom.

In the geometry in Fig. 5.6(a) an $\mathcal{M}_x$ mirror plane is conserved for the experimental setup. Through the $\mathcal{M}_x$ axial vector reflection rules this means that

$S_x(k_x, k_y, E_B) = S_x(-k_x, k_y, E_B)$ and $S_z(k_x, k_y, E_B) = -S_z(-k_x, k_y, E_B)$. These conditions allow, to calculate S_z map presented in Fig. 5.6(e) from the map of Fig. 5.6(d). Spin-polarized calculations for the out-plane spin component S_z, along the high symmetry direction $\bar{K} - \bar{\Gamma} - \bar{K}$, is presented in Fig. 5.6(f) for surface Te1 and Pt atoms, and in Fig. 5.6(g) for the $5p_z$ orbital of the surface Te1 atom. Figure 5.6(h) schematically depicts the outermost Te and Pt atoms. This out-of-plane spin texture results from the intra-layer in-plane dipoles, which are parallel to the $\mathcal{M}_x$ mirror plane [35]. Again, comparing Figs. 5.6(f) and 5.6(g) with Fig. 5.6(e), a favorable agreement is found for the calculations using only the partial charge of $5p_z$ orbital of the surface Te atom. The S_y and S_z spin polarizations in Fig. 5.1(c) and Fig. 5.6(e), respectively, appear to be similar, with the main difference being a small S_z polarization in the Dirac cone, theoretically reproduced in Figs. 5.6(f) and 5.6(g).

5.4 Spin-resolved momentum maps close to the Fermi level

To investigate the highly spin-polarized surface states near the Fermi level, identified in Fig. 5.1(g) by the label (i) and visualized in Fig. 5.4, spin-resolved momentum maps were measured at the corresponding binding energies and are shown in Fig. 5.7. Panels (a)-(i) show the experimental geometry and spin-ARPES constant energy maps for two different binding energies and different sample rotations φ as defined in panel (a). Panels (b)-(e) correspond to measurements at $E_{binding} = 0.1$ eV, while panels (f)-(i) correspond to $E_{binding} = 0.3$ eV. The same 2D color map, displayed in the inset, is applied across all panels. The related calculated initial band structure maps are shown in panels (j)-(k).

In panels (b),(c),(f) and (g), the mirror plane $\mathcal{M}_x$ coincides with the reaction plane. This explains the symmetric spin-APRES maps with respect to the $\mathcal{M}_x$ operation such that $S_y(k_x, k_y) = -S_y(-k_x, k_y)$.

By comparing the structure enclosed by rectangles in panels (b) and (c), one can see a notably reduced photoemission intensity in (b) compared to its equivalent structure in (c). Additionally, one can as well see a decrease in the spin polarization signal in panels (c) and (g) compared to the equivalent geometry in panels (b) and (f). To clarify this, the spin-polarized momentum distribution curves (MDCs) for the two boxes labeled in (f) and (g) are plotted in panel (l), where the green MDC of Box1 demonstrates a stronger spin polarized signal compared to the magenta MDC of Box2. Data from the spin-up (red) and spin-down spectrum (blue) of the spin-detector corrected by the Sherman function S = 0.29, for Box1 (green curve) and Box2 (magenta curve), are presented in panels (m) and (n), respectively. These strong effects are related to incident light direction, where due to the trigonal symmetry of $PtTe_2$ (rather that hexagonal), when φ is changed by 60° the spin-ARPES results are different. This makes the maps of panels (b) and (c) (as well (f) and (g)), not only appearing rotated by $\Delta\varphi = 60°$ but also exhibiting different intensity pattern and different strength of spin polarization.

On the other hand, in panels (d),(e),(h) and (i), the mirror plane $\mathcal{M}_y$ is perpendicular to the reaction plane. A visual inspection suggests that the spin polarized momentum maps of the two asymmetry geometries are connected by the $\mathcal{M}_x$ mirror operation. Indeed, Fig. 5.7(d) can be transformed into Fig. 5.7(e) through the symmetry operations of the $\mathcal{M}_x$ mirror plane by $S_y(k_x, k_y) \rightarrow -S_y(-k_x, k_y)$. The

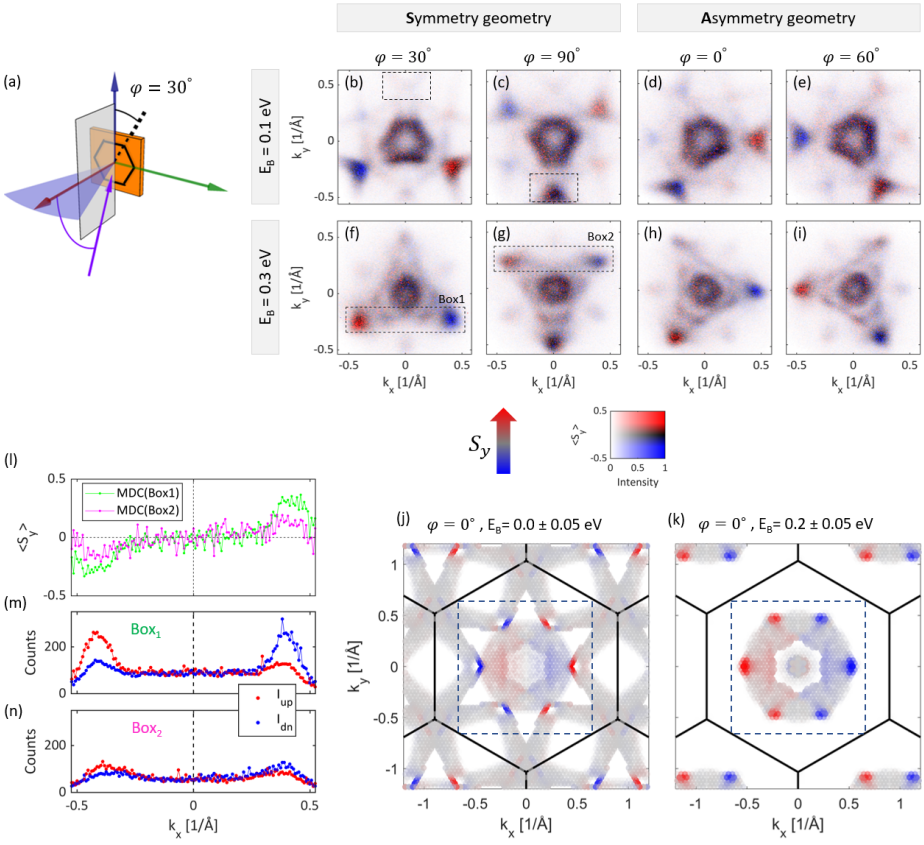

Figure 5.7: **Spin-resolved momentum maps of $PtTe_2$ near Fermi level.** (a) Experimental geometry indicating the rotation of the sample with respect to the z-axis by an angle φ. (b)-(e) Experimental spin-resolved photoemission intensities at $E_{binding} = 0.1$ eV, for $\varphi = 30°, 90°, 0°$ and $60°$, respectively. (f)-(i) Same but measured at $E_{binding} = 0.3$ eV. In (b),(c),(f) and (g) the mirror plane $\mathcal{M}_x$ coincides with the reaction plane. In (d),(e),(h) and (i) the mirror plane $\mathcal{M}_y$ is perpendicular to the reaction plane. (j)-(k) Theoretical spin-polarized constant energy maps at $E_{binding} = E_F \pm 0.05$ eV and at $E_{binding} = 0.2 \pm 0.05$ eV, respectively. Dashed boxes in (j) and (k) represent the probed region of the momentum space in (b)-(e) and (f)-(i), respectively. (l) Spin-polarized MDCs for the structure enclosed by Box1 and Box2 in (f) and (g). (m)-(n) Data from the spin-up (red) and spin-down spectrum (blue) of the spin-detector corrected by the Sherman function S = 0.29, for Box1 (green curve in (l)) and Box2 (magenta curve in (l)), respectively. Boxes in (b) and (c) enclose a measured structure that exhibits a stronger photoemission intensity in (c) compared to (b). (b)-(i) Plotted using the 2D color code inset showing intensity and spin polarization. HeI ($h\nu = 21.22$ eV) used for all maps.

same transformation applies to Figs. 5.7(h) and 5.7(i). This point will be discussed in detail later in this chapter.

Indeed, in all maps one can see spin-polarization sign inversion between $E_{binding} = 0.1$ eV and $E_{binding} = 0.3$ eV. This sign flipping is consistent with the spin polarization sign of the Fermi surface states in Fig. 5.1 (g), Fig. 5.1(h) and Fig. 5.4.

5.5 Spin-resolved $E(k_x)$ maps for two symmetry geometries

Figure 5.8 shows spin-resolved energy-momentum maps measured using the two *symmetry geometries* depicted in Figs. 5.8 (a) and (b)[2]. These geometries are connected by a $\varphi = 60°$ rotation around the z-axis. The spin-resolved maps in panels (c) and (d) were measured using the first symmetry geometry shown in panel (a), which is the same geometry used in measuring Figs. 5.7(b) and 5.7(f). Panels (e) and (f) were measured using the second symmetry geometry shown in panel (b), which is the same geometry used in measuring Figs. 5.7(a) and 5.7(e)[3]. The spin-resolved maps (c)-(f) consistently exhibit a symmetric spin texture with respect to the preserved $\mathcal{M}_x$ mirror plane when *symmetric geometries* are employed during the experiments.

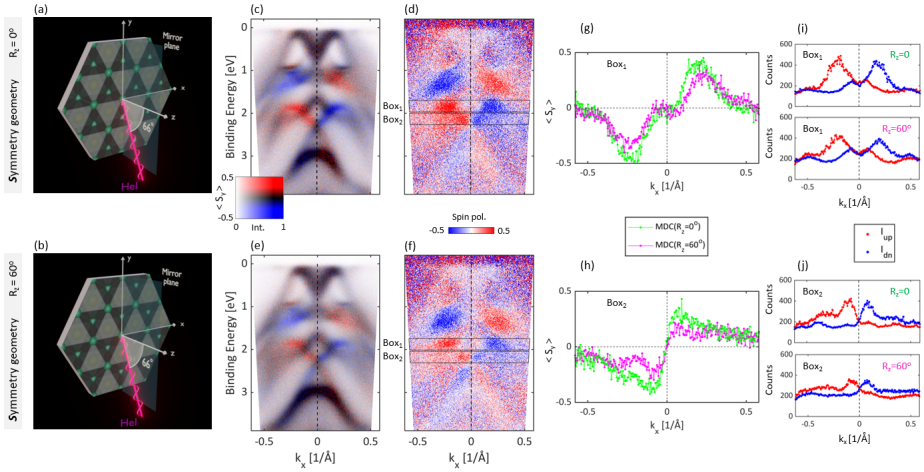

Figure 5.8: **Spin-resolved band dispersion maps for two *symmetry geometries* of $PtTe_2$.** (a),(b) Schematically shown two nonequivalent *symmetry geometries*. Each of the two geometries is a *symmetry geometry* that can be reached from the other via rotating the sample by $\varphi = 60°$ around the z-axis as labeled. (c)-(d), (e)-(f) Experimental HeI-driven ($h\nu = 21.22$ eV) spin-resolved energy dispersion maps $E(k_x)$ (280×251 pixels each), measured using the lens deflector system probing along the x-axis perpendicular to the $\mathcal{M}_x$ mirror plane of the crystal as defined in (a) and (b) respectively while the sample in normal emission. Box_1 in (d) and (f) enclose a structure that exhibits stronger spin polarization signal in (d) compared to (f) as demonstrated by the corresponding not equal MDCs in (g). Box_2 is same, and the corresponding difference in spin signal is demonstrated in (h). Magenta MDCs in (g) and (h) refer to (f), while green MDCs refer to (d). (i),(j) Data from the spin-up (red) and spin-down spectrum (blue) of the spin-detector corrected by the Sherman function S = 0.29, for Box1 (g) and Box2 (h), respectively. (c) and (e) plotted using the spin and intensity color code inset.

However, the spin-resolved maps in panels (c) and (d) display a stronger spin signal compared to those in panels (e) and (f), consistent with the enhanced spin-polarization observed in Figs. 5.7(b) and 5.7(f) relative to Figs. 5.7(a) and 5.7(e),

[2]Raw data for the spin-resolved band dispersion maps presented in Fig. 5.8 are shown in Appendix C.

[3]Determining the absolute assignment of the two geometries requires further investigation.

despite all measurements being conducted under symmetrical geometry.

This shows that light incidence has an effect on the measurements. The difference in spin polarization is illustrated using the spin-polarized momentum distribution curves (MDCs) in panels (g) and (h). In panel (g), the green MDC corresponds to Box_1 in panel (d), while the magenta MDC corresponds to Box_1 in panel (f). The mismatch between these two MDCs indicates a light-induced disparity in spin polarization. The MDCs in panel (h) represent the same analysis but for Box_2. The corresponding data from the spin-up (red) and spin-down spectrum (blue) of the spin-detector corrected by the Sherman function S = 0.29, for Box1 and Box2, are plotted in panels (i) and (j), respectively.

5.6 Spin-resolved $E(k_x)$ maps for four asymmetry geometries

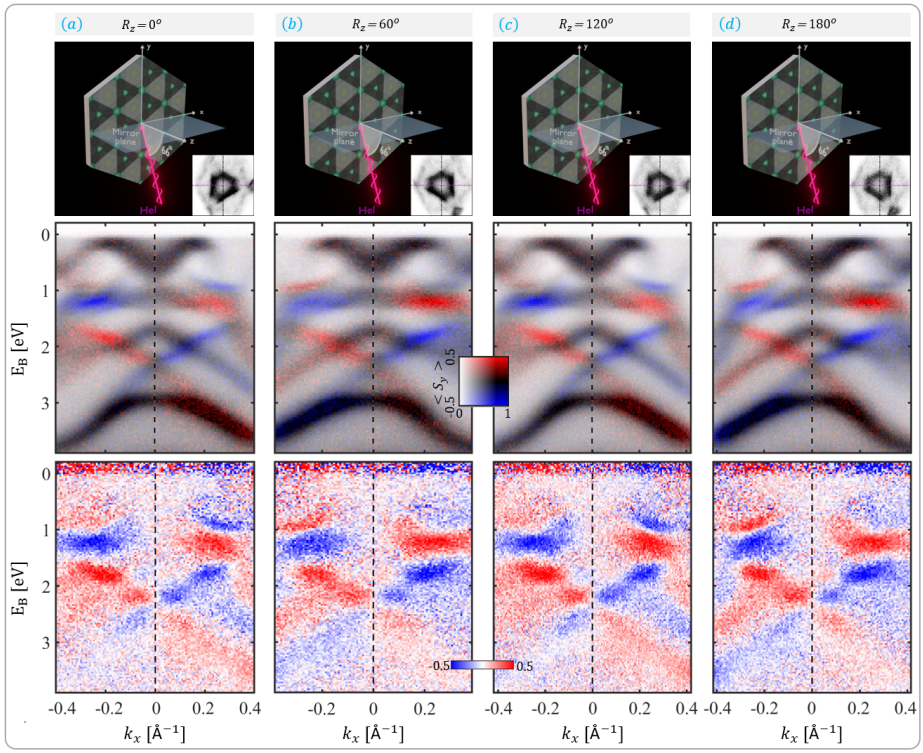

Figure 5.9: **Spin-resolved band dispersion maps for four *asymmetry geometries* of $PtTe_2$.** (a-d) Vertical panels are experimental HeI-driven ($h\nu = 21.22$ eV) highly spin-resolved energy dispersion maps $E(k_x)$, measured using the lens deflector system probing along the x-axis ***not*** perpendicular to any mirror plane of the crystal as defined in the top geometry panel while the sample in normal emission. The corresponding Fermi surface map for each geometry is also plotted. The transition between geometries (a) to (b), (c), and finally (d) was done by successive 60° rotations of the sample around the z-axis. Panel (a) is equivalent to (c), while panel (b) is equivalent to (d).

Panels (a-d) of Fig. 5.9 depict four *asymmetry geometries* alongside their respective spin-resolved $E(k_x)$ maps probed along the magenta line in the corresponding

Fermi surface maps shown in the insets. The transition in Fig. 5.9 between geometries (a) to (b), (c), and finally (d) was done by successive 60° rotations of the sample around the z-axis, having $\mathcal{M}_y$ as the xz mirror plane in all of them.

Contrary to the symmetric spin-resolved maps presented in Sec. 5.5, all the spin-resolved maps in Fig. 5.9 exhibit asymmetric spin texture as a result of the absence of any mirror plane of the crystal preserved in the entire experimental setup, that is the sample and the incidence light.

By examining the crystal structure depicted in the first horizontal panel of Fig. 5.9(a-d), one can observe that the alignment of the crystal in both (a) and (c) is identical, achieved through a 120° rotation of the sample around the z-axis. *This consistency aligns with the crystal's inherent 3-fold rotational symmetry.* Similarly the alignment of the crystal in (b) and in (d) is equivalent. This correspondence is evident in the reciprocal space measurements, as the spin-resolved maps in panels (a) and (c) are identical, as are those in panels (b) and (d)[4].

5.7 Off-center spin-resolved $E(k_x)$ maps

Up to this point, all preceding spin-resolved measurements were conducted via the Γ point along high symmetry directions. Panels (a)-(e) of Fig. 5.10 display spin-resolved $E(k_x)$ maps utilizing both *symmetry* and *asymmetry geometries*, however, the maps are measured probing along the yellow lines of the corresponding Fermi surface maps. Notably, all yellow lines in Fig. 5.10(a)-(e) are off-center. While panels (a)-(c) of Fig. 5.10 depict *symmetry geometries*, panels (d)-(e) of Fig. 5.10 portray *asymmetry geometries*. The spin texture of the symmetry panels shown in Fig. 5.10(a)-(c) demonstrates symmetric behaviour, contrasting with the asymmetric spin-resolved maps of Fig. 5.10(d)-(e). The asymmetries observed in Figs. 5.10(d), 5.10(e) and Fig. 5.9 demonstrate that the origin of these asymmetries are not due to misalignment of the sample neither due to missing the Γ line.

5.8 Spin-resolved momentum maps at $E_b \sim 1.3$ eV

Spin-resolved momentum maps for the in-plane S_y spin component and the corresponding spin-integrated maps of $PtTe_2$ at $E_{binding} \sim 1.13$ eV, close to the lower part of the surface states SS-labeled in Fig. 4.3, are depicted in Fig. 5.11[5].

Panel (a) of Fig. 4.3 shows the spin-integrated momentum map at $E_{binding} \sim 1.13$ eV, for the symmetry orientation of the sample equivalent to the geometry shown in Fig. 5.10(b), measured using the lens deflector system. Panel (b) is the corresponding intensity and spin-polarization simultaneously displayed using the 2D color code inset, while panel (c) is the pure spin-polarization momentum map saturated to 40%. The spin-resolved maps in panels (b) and (c) exhibit strong agreement with the spin-integrated lens deflector map in panel (a), indicating a high degree of consistency between the two measurement techniques. Panels (d)-(f) are similar to panels (a)-(c), but for a rotated sample by $\varphi = 60°$ around the z-axis as shown in the geometry of Fig. 5.10(a).

[4]Raw data for the spin-resolved band dispersion maps presented in Fig. 5.9 are shown in Appendix D.

[5]Raw data for the spin-resolved momentum maps presented in Fig. 5.11 are shown in Appendix E.

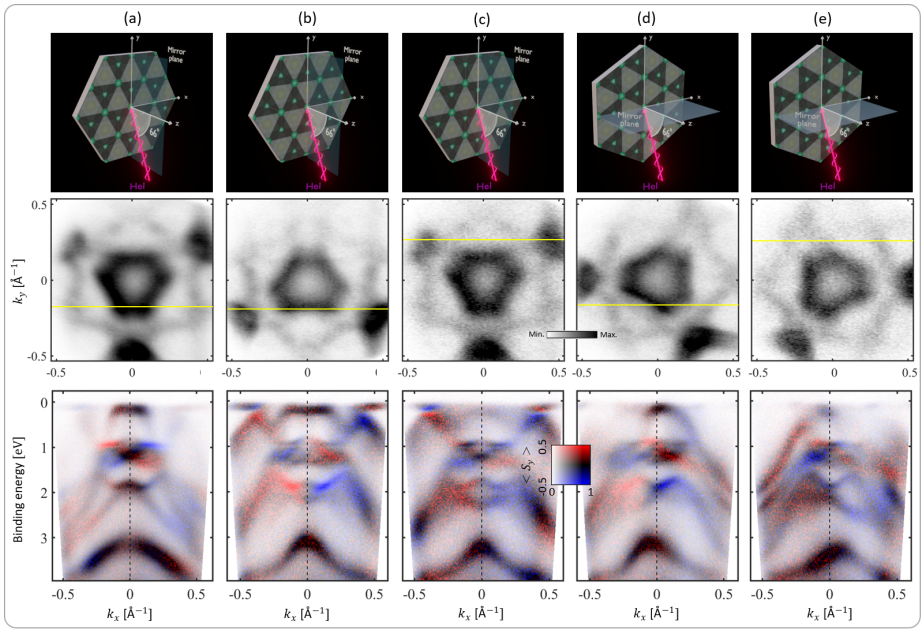

Figure 5.10: **Off-center spin-resolved energy dispersion maps of $PtTe_2$.** (a)-(e) Bottom panel: spin-resolved band dispersion maps of $PtTe_2$ measured using the corresponding geometries illustrated in (a)-(e) upper panel respectively. Second panel shows the corresponding Fermi surface maps with the yellow lines indicating the *off-center* energy cuts along which the spin maps were filtered. (a)-(c) *Symmetry geometries* manifested with the corresponding symmetric spin-resolved maps. (d)-(e) *Asymmetry geometries* demonstrated with the corresponding highly asymmetric spin-resolved maps. Measurements were performed using the unpolarized HeI-light ($h\nu = 21.22$ eV).

For the two geometries used to measure panels (a)-(f), the mirror plane $\mathcal{M}_x$ preserves its symmetry rules. This is demonstrated in the corresponding spin-integrated as well as the spin-resolved momentum maps. In the spin-integrated maps, the positive k_x side is a copy of the negative k_x side. In the spin-resolved maps, similarly, both sides of the k_x axis exhibit mirrored features, additionally, they exhibit switching the spin polarization color from red (blue) to blue (red) obeying the axial vector rules of the $\mathcal{M}_x$ mirror plane as explained in Fig. 5.2 for the S_y spin component.

On the other hand, the geometry used to measure Figs. 5.11(g)-(i) is *asymmetry geometry* equivalent to that shown in Fig. 5.10(e). Panels (j)-(l) are similar to panels (g)-(i), but for a rotated sample by $\varphi = 60°$ around the z-axis as shown in the geometry of Fig. 5.10(d).

Based on these geometries, all crystal mirror planes are broken, including the horizontal $\mathcal{M}_y$ mirror plane. Therefore, one can not compare the negative k_y side with the positive k_y side due to light effects. This leaves the whole system without any preserved mirror plane. As a consequence of this, the negative k_x side does not have to be a mirror of the positive k_x side. This is demonstrated in the corresponding spin-integrated as well as the spin-resolved momentum maps.

Let us analyze the α-labeled region in panel (h) that is plotted using the 2D color

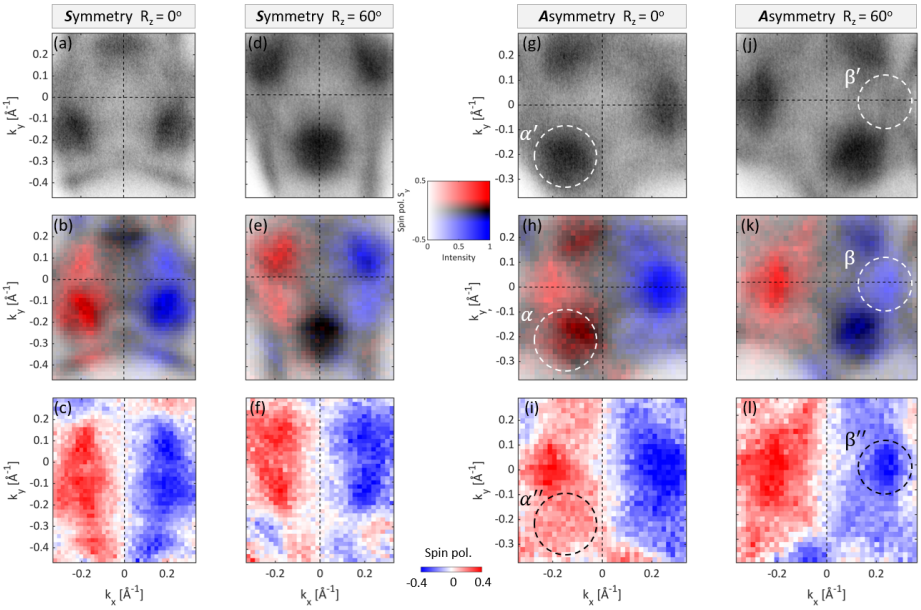

Figure 5.11: **Measured spin-resolved constant energy contours in the** $(k_x - k_y)$ **plane of PtTe$_2$ at** $E_{binding} \sim 1.13$ **eV for the in-plane** S_y **spin component.** (a)-(c) Measured using the symmetry geometry of Fig. 5.10(b). (a) Spin-integrated photoemission map at $E_{binding} \sim 1.13$ eV, measured using the lens deflector system. (b) corresponding photoemission intensity and spin-polarization simultaneously displayed using the inset 2D color code. (c) Corresponding pure S_y spin polarization map. (d)-(f) Equivalent to (a)-(c) but using another symmetry geometry shown in Fig. 5.10(a), that is connected to the first symmetry geometry by $\varphi = 60°$ as labeled. (g)-(i), (j)-(l) Same but measured using geometries of Figs. 5.10 (e) and (d) respectively, which are connected by $\varphi = 60°$. $\boldsymbol{\alpha}$ ($\boldsymbol{\beta}$), $\boldsymbol{\alpha}'$ ($\boldsymbol{\beta}'$) and $\boldsymbol{\alpha}''$ ($\boldsymbol{\beta}''$) refer to regions enclosed inside the corresponding circles. $\boldsymbol{\alpha}$ ($\boldsymbol{\beta}$)-region in the 2D color code momentum map shows stronger (weaker) spin polarization signal compared to $\boldsymbol{\alpha}''$ ($\boldsymbol{\beta}''$)-region in the pure spin-resolved momentum map. Measurements are conducted utilizing the unpolarized HeI-light ($h\nu = 21.22$ eV).

code where intensity and spin polarization are plotted simultaneously[6]. This region shows strong spin polarization. However, comparing this with the corresponding α''-labeled region in the pure spin-resolved momentum map of panel (i) reveals a weaker spin polarization signal. Indeed, α in panel (h) is generated by plotting α'' in panel (i) atop α' in panel (g) with transparency. Consequently, the heightened signal observed in the α-labeled region is attributed to the high intensity of the corresponding spin-integrated α'-labeled region.

Now, let us follow a similar way of analysis for the β, β' and β'' labeled regions in panels (k), (l) and (j) respectively. The β-labeled region in the 2D color code map displays a weaker spin-polarization signal compared to the corresponding β'' labeled region in the pure spin-polarization map. However, in this case it is due to the corresponding weak spin-integrated β' labeled region (β is generated by plotting β'' atop β'). Therefore, relying solely on the intensity-spin maps may occasionally lead

[6]The method for plotting using the 2D color code is detailed in Appendix F.

to misinterpretation, underscoring the necessity of examining the pure spin-resolved maps as well. On the other hand, spin polarization primarily matters in the high intensity regions of the reciprocal space.

5.9 Two asymmetry geometries connected by $\mathcal{M}_x$ mirror plane

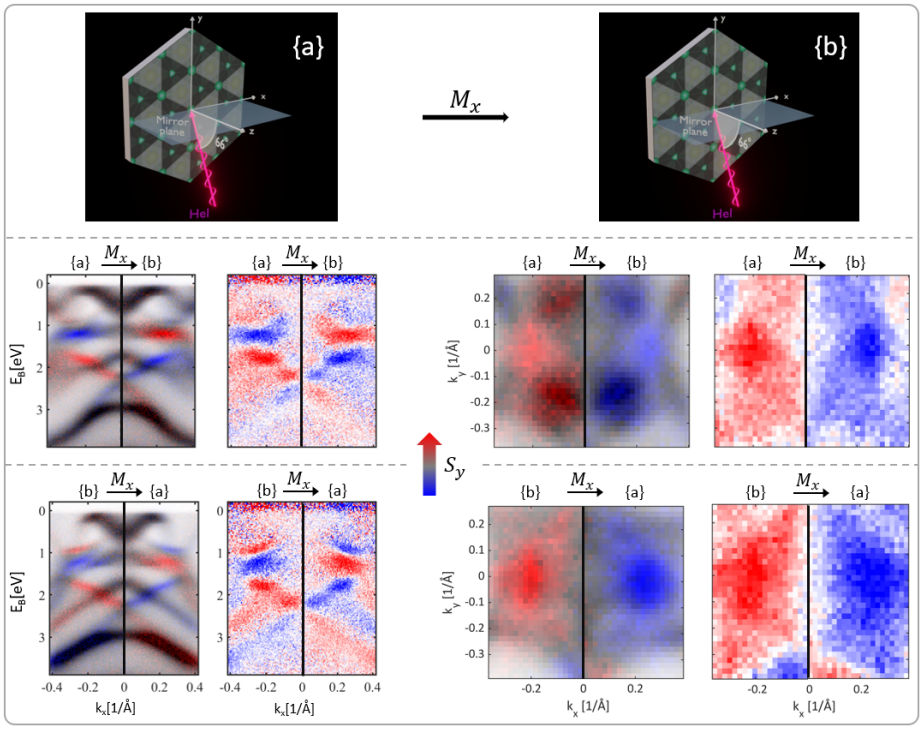

Figure 5.12: **Transitioning between two asymmetry geometries via the mirror plane $\mathcal{M}_x$.** First horizontal panel: (a),(b) Two *asymmetry geometries* connected by 60° rotation around the z-axis. *Geometry (a) can be transformed into geometry (b) via the mirror operation $\mathcal{M}_x$.* Second horizontal panel: left half of each figure in the panel is the negative k_x side corresponds to geometry (a), while the right half of each figure is the positive k_x side corresponds to geometry (b). Third horizontal panel: left half of each figure in the panel is the negative k_x side corresponds to geometry (b), while the right half of each figure is the positive k_x side corresponds to geometry (a). Left and right sides of each spin-polarized momentum map as well as spin-polarized band dispersion map are connected by the symmetry rules of the $\mathcal{M}_x$ mirror plane. Measurements are conducted using the unpolarized HeI-light ($h\nu = 21.22$ eV).

In the previous section 5.8, upon visual inspection, it appears that in Fig. 5.11 transforming panels (g)-(i) into panels (j)-(l), respectively, is achievable through the symmetry operations of the $\mathcal{M}_x$ mirror plane explained in Fig. 5.2. Likewise, in Sec. 5.6, the correspondence in Fig. 5.9 between panels (a ≡ c) and panels (b ≡ d) can be established using a similar reasoning.

In order to provide clarity to this idea, two *asymmetry geometries*, (a) and (b) related by $\varphi = 60°$, are depicted in the first panel of Fig. 5.12. One can see that

geometry (a) can be transformed into geometry (b) by mirroring through the $\mathcal{M}_x$ mirror plane. In the second panel of Fig. 5.12, the left half of each figure of the spin-resolved band dispersion maps as well as the spin-resolved momentum maps is the negative k_x side corresponds to geometry (a), while the right half of each figure is the positive k_x side corresponds to geometry (b). In the third panel of Fig. 5.12, the left half of each figure is the negative k_x side corresponds to geometry (b), while the right half of each figure is the positive k_x side corresponds to geometry (a). One can see that, the right- and left sides of each spin-resolved map in Fig. 5.12 are connected through the symmetry operations of the $\mathcal{M}_x$ mirror plane for the in-plane S_y spin component.

5.10 Spin-resolved measurements and calculations for the surface Dirac cone of $PtTe_2$

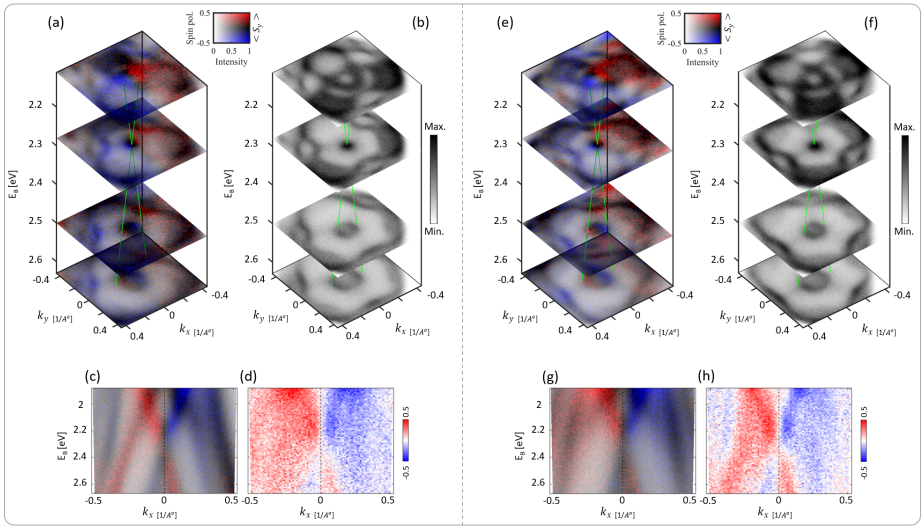

Figure 5.13: **Measured spin-resolved $PtTe_2$ surface Dirac cone.** (a) Spin-resolved photoemission (k_x-k_y) maps measured at selected binding energies below, at, and above the Dirac point of the surface Dirac cone using the 2D color code. (b) Corresponding spin-integrated ARPES maps. (c) Spin-resolved band dispersion map using the 2D color code, and the corresponding pure spin-resolved band dispersion map (d). (a)-(d) Measured using the geometry of Fig. 5.1(a). Right panels (e)-(h) equivalent to (a)-(d) respectively but measured using the *asymmetry geometry* of Fig. 5.1(e). ARPES maps in (b) and (f) were measured using the lens deflector system. Measurements were carried out using the unpolarized HeI-light ($h\nu = 21.22$ eV).

A detailed spin-resolved analysis of the surface Dirac cone centered at $E_{binding} \sim$ 2.3 eV is presented in Fig. 5.13. Measurements in Fig. 5.13 were carried out using the unpolarized HeI-light ($h\nu = 21.22$ eV). The geometry used in panels (a)-(d) was the *symmetry geometry* depicted in Fig. 5.1(a). Spin-resolved momentum maps at selected binding energies below, at, and above the Dirac point are presented in panel (a), while panel (b) displays the corresponding spin-integrated momentum maps acquired using the lens deflector system. The spin-resolved maps in panel

(a) demonstrate strong agreement with the spin-integrated lens deflector maps in panel (b), underscoring the consistency between these measurement techniques and highlighting the high resolution of the spin-detection system. Additionally, spin-resolved band dispersion maps with an energy window covering the surface Dirac cone are depicted in panels (c)-(d). Figure 5.13(a) shows closing and re-opening of the Dirac cone with increasing binding energy. It also shows the flipping of the spin-polarization sign S_y either sides of the Dirac point, red (blue) → blue (red), in agreement with the spin texture behaviour of the surface Dirac cone. Panels (e)-(h) are the same but measured using the *asymmetry geometry* alignment of the crystal as shown in Fig. 5.1(e).

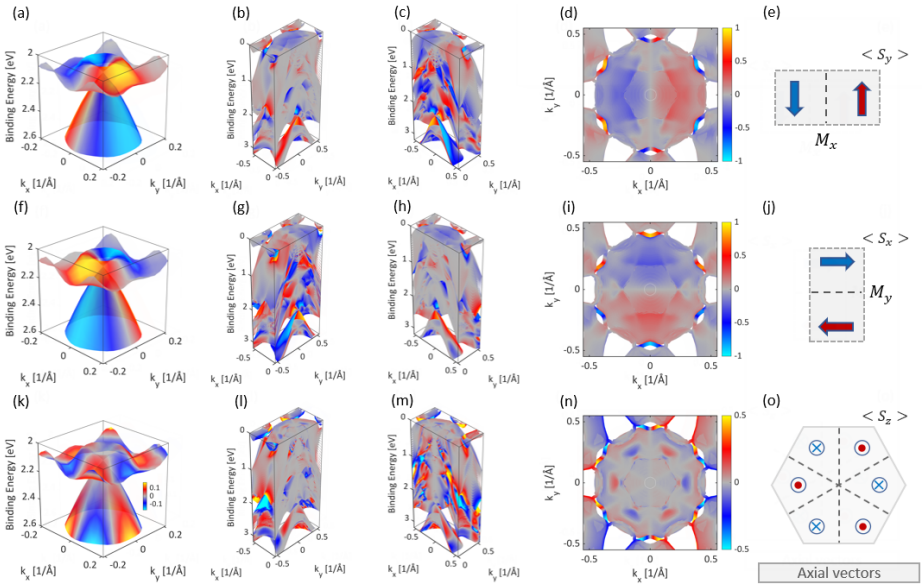

Figure 5.14: **spin-resolved calculations for the surface Dirac cone of $PtTe_2$.** (a) Three-dimensional spin-resolved calculations of the in-plane S_y spin component for the surface Dirac cone of $PtTe_2$. (b), (c) Extended energy range compared to (a), plotted along half of the k-scale for improved visualization of the Dirac cone. (d) Spin-resolved Fermi momentum map ($\Delta E = 100\,\text{meV}$) with the mirror symmetry line $k_x = 0$. The color of the symbols corresponds to the spin polarization as indicated by the false-color scale in (d). (e) Axial vector rule for the S_y spin component mirrored through the M_x mirror plane indicated by the dashed line. (f)-(j) and (k)-(o) Analogous calculations for the S_x and S_z spin components, respectively, with their corresponding axial vector rules depicted in (j) and (o). In (o), the three $\bar{M} - \bar{\Gamma} - \bar{M}$ mirror planes are indicated by the dashed lines. The color scale is saturated to 17% in (k) and to 50% in (l)-(m). These calculations consider contributions from the outermost atomic orbitals of the topmost Pt and Te atoms in the 30-layer slab.

Spin resolved calculations, illustrating the behaviour of the spin-texture of the surface Dirac cone, are presented in Fig. 5.14. Figure 5.14(a) shows the spin-resolved bands contributing to the Dirac cone, over the limited energy and momentum ranges, for the in-plane S_y spin component. Figures 5.14(b) and 5.14(c) present extended energy range with the momentum scale being limited to better visualizing the surface

Dirac cone. Spin-resolved Fermi momentum map ($\Delta E = 100\,\text{meV}$) with the mirror symmetry line $k_x = 0$ is presented in Fig. 5.14(d). The color of the symbols corresponds to the spin polarization as indicated by the false-color scale in (d). The axial vector rule for the S_y spin component, mirrored through the $\mathcal{M}_x$ mirror plane, is shown in (e), with the mirror plane marked by a dashed line. Figures 5.14(f)-(j) and Figs. 5.14(k)-(o) present similar calculations but for the S_x and S_z spin components, respectively. In Fig. 5.14(j), the dashed line indicates the $\mathcal{M}_y$ mirror plane, while the three dashed lines in Fig. 5.14(o) indicate the $\bar{M} - \bar{\Gamma} - \bar{M}$ mirror planes. The axial vector rules associated with these mirror planes directly correspond to the spin-resolved Fermi maps, demonstrating a clear one-to-one correspondence between the axial vector rules and the spin polarization behavior. In Fig. 5.14(k), the color scale is saturated at 17%, while in Figs. 5.14(l)-(n), it is saturated at 50%, indicating a smaller out-of-plane spin polarization in $PtTe_2$ compared to the in-plane component. This is consistent with the spin-resolved measurements presented in Fig. 5.6.

In Fig. 5.1, Fig. 5.9, Fig. 5.10, Fig. 5.11, Fig. 5.12 and Fig. 5.13, the asymmetries in the measured spin-resolved band dispersion maps as well as the $(k_x - k_y)$ spin-resolved energy contours were present when the reaction plane was not coinciding with any of the mirror planes of the crystal. In the next section, various processes that might lead into such asymmetries will be discussed.

5.11 One-step model simulations

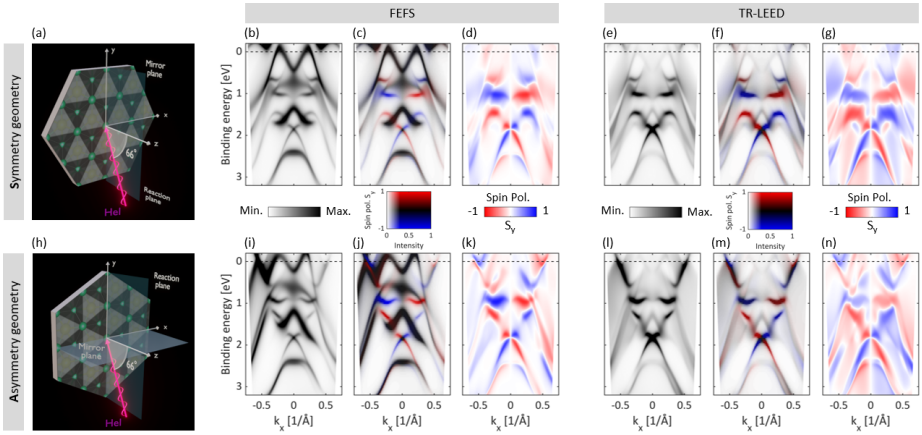

Figure 5.15: $E(k_x)$ **simulated maps for $PtTe_2$.** (a) *Symmetry geometry.* (b) Spin-integrated simulation of Fig. 4.25(d), using the geometry in (a). (c)-(d) Corresponding spin-polarized simulations: (c) shown with a 2D color map, and (d) depicting the spin-polarization magnitude. Maps (b)-(d) were calculated using the FEFS. (e)-(g) Corresponding simulations based on the TR-LEED final state. (h)-(n) Equivalent simulations using the *asymmetry geometry* shown in (h), with (i) and (l) simulating Fig. 4.25(h).

Figure 5.15 presents one-step model calculations, which are simulations that take into account our experimental conditions (i.e., the combined system of light and the symmetries of the sample surface) used in measuring the spin-integrated as well as

the spin-resolved maps of $PtTe_2$ in the PGI-6 spin-ARPES laboratory[7].

Figures 5.15(a)-(g) display $E(k_x)$ simulations at the *symmetry geometry* shown in panel (a). Panels (b)–(d) were simulated using the free-electron final state (FEFS), while panels (e)–(g) were simulated using the time-reversed low-energy electron diffraction (TR-LEED) final state. Figures 5.15(b) and (e) correspond to the experimental data presented in Fig.4.25(d). The 2D spin-polarized maps in panels (c) and (f) simulate the experimental results shown in Fig.5.1(c), whereas panels (d) and (g) simulate the spin-resolved pure map presented in Fig. 5.1(d).

Figures 5.15(h)-(n) present equivalent simulations for the *asymmetry geometry* depicted in panel (h). In this case, panels (i) and (l) correspond to the experimental data shown in Fig.4.25(h). The 2D spin-polarized maps in panels (j) and (m) simulate the experimental results from Fig.5.1(g), while panels (k) and (n) simulate the spin-resolved pure map from Fig. 5.1(h).

Both FEFS and TR-LEED simulations show excellent agreement with experimental data, with FEFS offering particularly stronger correspondence. Since the TR-LEED picture accounts for the scattering events discussed in Sec. 2.6, this indicates that SOC-scattering in $PtTe_2$ (to be discussed in Sec. 5.12.2) is not critical.

5.12 Various contributions to the photoemission spin polarization

Figure 5.16 schematically illustrates various processes which may modify the initial state spin polarization during the photoemission process taking the $PtTe_2$ lattice as an example. Fig. 5.16(a) shows the 3 atomic sites within the primitive unit cell labeled as Te1, Te2, and Pt, and a generic final state wavevector $\boldsymbol{k}_f$ along which the photoelectrons are detected.

Fig. 5.16(b) shows atomic photoemission scattering waves from the 3 sites along $\boldsymbol{k}_f$ within the formalism of IACA discussed in Sec. 2.6. Since $PtTe_2$ valence band wave functions are strongly mixed between Te and Pt sites, as demonstrated in Sec. 4.6, these final states will interfere [90, 112] (see Sec. 2.6). This may lead to a modification of the spin-ARPES spin polarization, as demonstrated in Ref. [46]. This interference is related to different positions of the Te1, Te2, and Pt sites along $\boldsymbol{k}_f$. Indeed, the photoemission amplitude along $\boldsymbol{k}_f$ is a coherent sum of the photoemission amplitudes originating from all the atomic-emitters, Te1, Te2 and Pt, participating in the photoemission process, taking into account the relative phase shift which depends on the relative positions of these emitters leading to the relative phase $e^{i\boldsymbol{k}_f\cdot(\boldsymbol{R}_{Te1}-\boldsymbol{R}_{Te2}-\boldsymbol{R}_{Pt})}$, where $\boldsymbol{R}_j$ is a real space vector from origin to the j^{th} atom; $j \in \{\text{Te1, Te2, Pt}\}$. In this discussion we neglect emission from deeper layers, which must be considered in precise modeling.

Figure 5.16 (c) shows the scenario, where electron photoemitted from the Te1 site is elastically scattered on the Pt site. An intuitive way of thinking of such scattering process is by considering electron plane wave scattering on atomic targets where for atoms with high atomic number Z high spin polarization of the scattered beam can be generated at selected scattering angles [167–169] event at low kinetic energies. Therefore, scattering processes in $PtTe_2$, a material made from large atoms, are expected to lead to spin polarization even if it was not present in the initial state.

[7]The calculations presented in this section were performed by Dr. Jakub Schusser at the University of Würzburg, calculated with the SPR-KKR package [166].

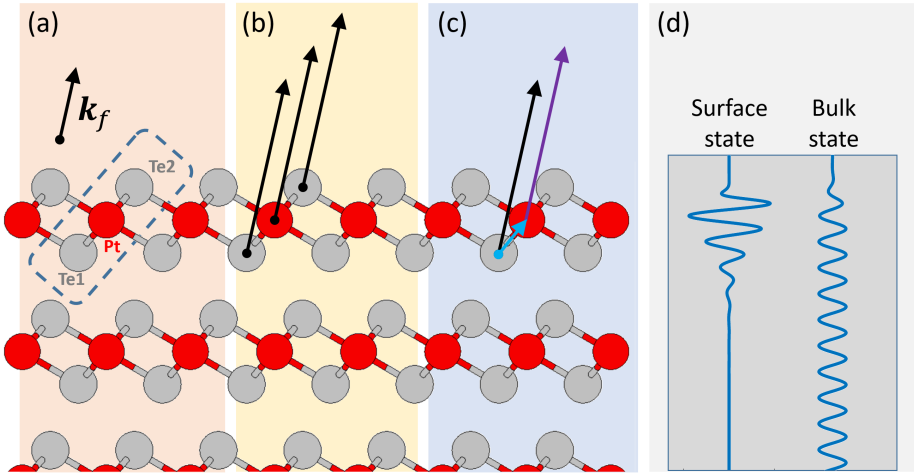

Figure 5.16: **Various processes modifying the initial state spin polarization.** (a) Indication of the Te1, Te2, and Pt atoms within the primitive unit cell of bulk $PtTe_2$, and depiction of a generic final state wavevector $\boldsymbol{k}_f$. (b) Illustration of the interatomic interference process, waves emitted from the three atomic sites will interfere due to different positions of the emission sources. (c) Illustration of the scattering process. Blue arrow depicts an electron emitted from the source atom Te1 and scattered on the Pt atom. (d) Schematic illustration of the charge density of the surface and bulk state below the surface.

In addition, Fig. 4.27(d) schematically illustrates the charge density of the localized surface state and the delocalized bulk state below the surface. This figure was discussed in detail in Sec. 4.10.

In the following subsections, we will discuss the impact of each process, as schematically illustrated in Figs. 4.27(b)-(d), on the measured spin-polarized spectra.

5.12.1 Atomic sites-induced asymmetric spin polarization

Considering that initial parallel momenta components are conserved in the photoemission process, let's relate the regions labeled by squares $S1$ and $S2$ in Fig. 5.17(a). Probing initial parallel momenta $\boldsymbol{k}_{iS1} = k_{ix}$ and $\boldsymbol{k}_{iS2} = -k_{ix}$ indicated by squares $S1$ and $S2$ in Fig. 5.17(a) via ARPES requires measuring electrons emitted along $\boldsymbol{k}_{fS1} = (k_{ix}, k_{fz})$ and $\boldsymbol{k}_{fS2} = (-k_{ix}, k_{fz})$.

Another way of thinking regarding the process illustrated in Fig. 5.16(b) is that, any non-equivalent site within the primitive unit cell will only contribute a phase factor into the matrix element. To have a better visualization of this idea, one can think of photoemission from a simple one-dimensional *zigzag* shape shown in Fig. 5.17(b). Within the FEFS picture, one can intuitively consider a plane wave emitted from Pt atom along the two emission directions $\boldsymbol{k}_{fS1}$ and $\boldsymbol{k}_{fS2}$ shown by the brown- and blue plane waves, respectively. Complex part of the emitted plane wave is also plotted. The real space positions of the Pt atoms are $\delta(x - la)$, and for the Te atoms are $\delta(x - la - d)\delta(z - h)$, where l is an integer, a is the lattice constant and the distances d and h represent the relative displacement of Pt and Te atoms.

As discussed before (see Sec. 2.6), shifts in space introduce phase shifts in recip-

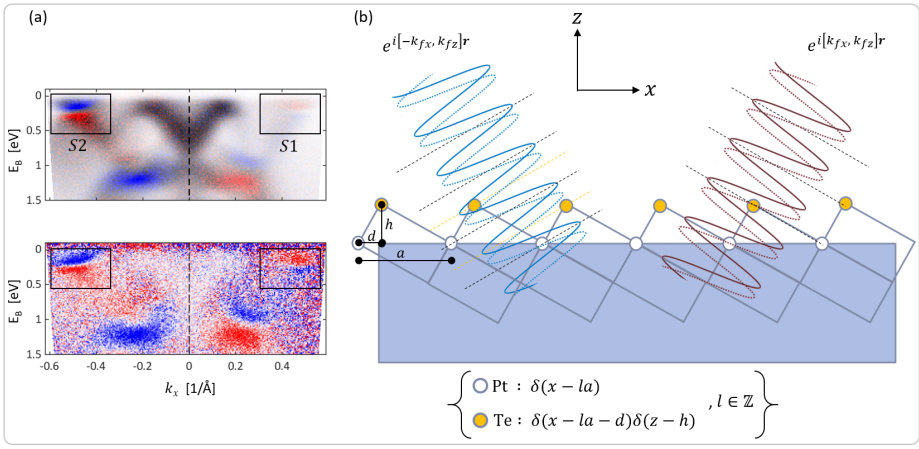

Figure 5.17: **Asymmetric spin polarization by non-equivalent atomic sites.** (a) Part of the spin-polarized energy dispersion map for the *asymmetry geometry*. $S1$ and $S2$ labeled squares represent the surface states close to Fermi level. (b) One dimensional *zigzag* model representing a side view of the *asymmetry geometry* of $PtTe_2$ where $\mathcal{M}_x$ mirror plan is broken. The lattice constant a and the relative displacement of Pt and Te atoms is indicated by the distances d and h. Real space positions of Pt and Te toms are shown in brackets. Probing the squares $S1$ and $S2$ in (a) via ARPES requires measuring electrons emitted along $\boldsymbol{k}_{fS1}$ represented by the brown plane wave, and $\boldsymbol{k}_{fS2}$ represented by the blue plane wave. Real and complex parts of the plane waves are plotted. Wave fronts of the plane waves are indicated by the dashed lines.

rocal space. The *zigzag* model in Fig. 5.17(b) can be considered as equivalent to the *asymmetry geometry* of the $PtTe_2$ lattice once is it extended to 3D. One can see that atomic sites in the *zigzag* model are positioned such that $\mathcal{M}_x$ mirror plane is broken. This will introduce different phase shifts in the $S1$ and $S2$ matrix elements $M_{S1} = \langle e^{i\boldsymbol{k}_{fS1}.\boldsymbol{r}} | \psi_i(\boldsymbol{k}_{iS1}, \boldsymbol{r}) \rangle$ and $M_{S2} = \langle e^{i\boldsymbol{k}_{fS2}.\boldsymbol{r}} | \psi_i(\boldsymbol{k}_{iS2}, \boldsymbol{r}) \rangle$. Indeed, one can show that M_{S1} will have a term with a phase factor $e^{ik_{ix}(a-d)e^{-ik_{fz}h}}$, while M_{S2} will have a term with a different phase factor $e^{ik_{ix}de^{-ik_{fz}h}}$, where the parallel momentum component is conserved and $k_{fx} = k_{ix}$. One can as well show that in a generic case this leads to different final measured spin polarizations for the two emission directions $\boldsymbol{k}_{fS1}$ and $\boldsymbol{k}_{fS2}$, despite equal initial state polarizations $S_{iy}(\boldsymbol{k}_{fS1})$ and $S_{iy}(\boldsymbol{k}_{fS2})$ as shown in the theoretical calculations in Fig. 5.5(d). A full derivation of this interference model for the minimal case of two orbitals on two different sites is presented in the next Sec. 5.12.1.1, while a coupled *zigzag* chains model can be found in Sec. SIV of the Supplemental Material in Ref. [46].

On the other hand, the *zigzag* model for the symmetry orientation will be reshaped such that the relative distance d will be half of the lattice constant a, i.e. $d = a/2$, recovering the $\mathcal{M}_x$ mirror plane. In this case, the phase shift $e^{ik_{ix}de^{-ik_{fz}h}}$ is same for the two emission directions, leading to symmetric final measured spin polarizations for the two emission directions $\boldsymbol{k}_{fS1}$ and $\boldsymbol{k}_{fS2}$ as demonstrated in the measured spin-polarized maps in Fig. 5.8 as well as in the calculated maps in Fig. 5.5(c).

5.12.1.1 Analytical *zigzag* model

We model the experimental geometry by the one-dimensional *zigzag* shape, as depicted in Fig. 5.18. Top surface Pt sites are referred to by α, while top surface Te atoms are referred to by β. In this thesis, spin-resolved $E(k_x)$ band dispersion maps measures spin polarization in the photoemitted ensemble $P_r(k_{fx}, k_{fz})$ and $P_l(-k_{fx}, k_{fz})$ as indicated by the emission directions in Fig. 5.18. To establish the rules of the underlying initial state wave-functions $\Psi_{ini}(k_x, \boldsymbol{r})$ and $\Psi_{ini}(-k_x, \boldsymbol{r})$, we shall define the direction of the quantization axis. Since in most of the experiments presented in this thesis we measure S_y, we should couple it to orbitals with non-zero orbital angular momentum (magnetic quantum number m_l) along y. As it was shown earlier in Sec. 4.6, $PtTe_2$ valence bands are highly mixed of Te $5p$, Pt $6s$ and Pt $5d$ orbitals.

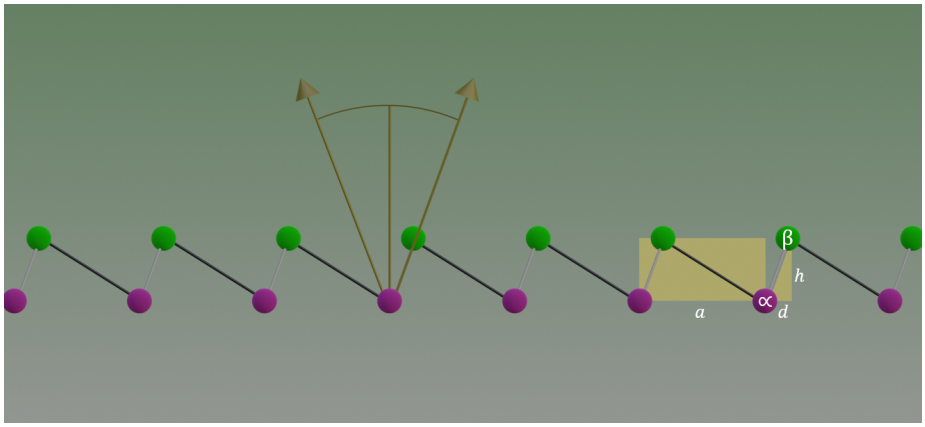

Figure 5.18: **Visualization of the 1D *zigzag* model.** Schematic visualization of the *zigzag* model. The one-dimensional unit cell with the lattice constant a is shown as a yellow rectangle in the $(x - z)$ plane. The relative displacement of α and β atoms is indicated by the yellow triangle with the distances d and h.

For simplicity we consider the orbital angular momentum on Te $5p$, namely $|p_\pm\rangle = |p_z \pm ip_x\rangle$ ($m_l = \pm 1$) orbitals on site β, and the isotropic Pt $|s\rangle$ orbital on site α. We set the spin quantization axis to y and we write for the initial state Bloch wave function

$$\Psi_{ini}(k_x, \mathbf{r}) = e^{ik_x \mathbf{r}} \sum_{l=-\infty}^{\infty} (\delta(x - la)\delta(z) \cdot (\alpha_\uparrow |s_\uparrow\rangle + \alpha_\downarrow |s_\downarrow\rangle) + \delta(x - la - d)\delta(z - h) \cdot (\beta_{+\uparrow} |p_{+\uparrow}\rangle + \beta_{-\uparrow} |p_{-\uparrow}\rangle + \beta_{+\downarrow} |p_{+\downarrow}\rangle + \beta_{-\downarrow} |p_{-\downarrow}\rangle)) \quad (5.1)$$

where a is the lattice constant along x, and $\uparrow, \downarrow$ depict up/down initial state S_y spin, (see Fig. 5.18). Shifting the β site by d along the x direction (see Fig. 5.18) is equivalent to the phase shift of $e^{-ik_x(d+la)}$, where l is an integer[8].

[8] At the Γ points of the Brillouin zone, where $k_x = 2\pi l/a$, the phase shift disappears for $d = a$ and $d = 0$.

We consider wave-vectors in the first Brillouin zone, $0 \leq k_x \leq 2\pi/a$, and follow the convention that Fourier frequencies are positive, therefore we consider a positive phase shift $e^{-ik_x(d-a)} = e^{ik_x(a-d)}$, since $d < a$. Therefore, we can write

$$\Psi_{ini}(k_x, \mathbf{r}) = e^{ik_x \mathbf{r}} \sum_{l=-\infty}^{\infty} \Big(\delta(x - la)\delta(z) \cdot (\alpha_\uparrow |s_\uparrow\rangle + \alpha_\downarrow |s_\downarrow\rangle) + \\ \delta(x - la)\delta(z - h) e^{ik_x(a-d)} \cdot (\beta_{+\uparrow} |p_{+\uparrow}\rangle + \beta_{-\uparrow} |p_{-\uparrow}\rangle + \beta_{+\downarrow} |p_{+\downarrow}\rangle + \beta_{-\downarrow} |p_{-\downarrow}\rangle) \Big) \quad (5.2)$$

Now the goal is to derive $\Psi_{ini}(-k_x, \mathbf{r})$. Since the system is time-reversal invariant, we calculate

$$\Psi_{ini}(-k_x, \mathbf{r}) = \Psi^*_{ini}(k_x, \mathbf{r}) = e^{-ik_x \mathbf{r}} \sum_{l=-\infty}^{\infty} \Big[\delta(x - la)\delta(z) \cdot (\alpha^*_\downarrow |s_\uparrow\rangle + \alpha^*_\uparrow |s_\downarrow\rangle) + \\ \delta(x - la - d)\delta(z - h) \cdot (\beta^*_{-\downarrow} |p_{+\uparrow}\rangle + \beta^*_{+\downarrow} |p_{-\uparrow}\rangle + \beta^*_{-\uparrow} |p_{+\downarrow}\rangle + \beta^*_{+\uparrow} |p_{-\downarrow}\rangle) \Big] \\ = e^{-ik_x \mathbf{r}} \sum_{l=-\infty}^{\infty} \Big[\delta(x - la)\delta(z) \cdot (\alpha^*_\downarrow |s_\uparrow\rangle + \alpha^*_\uparrow |s_\downarrow\rangle) + \\ \delta(x - la)\delta(z - h) e^{ik_x d} \cdot (\beta^*_{-\downarrow} |p_{+\uparrow}\rangle + \beta^*_{+\downarrow} |p_{-\uparrow}\rangle + \beta^*_{-\uparrow} |p_{+\downarrow}\rangle + \beta^*_{+\uparrow} |p_{-\downarrow}\rangle) \Big] \quad (5.3)$$

where we performed the complex conjugation by exchanging the $\uparrow$ / $\downarrow$ and $\pm$ indices and their assignment to the respective orbitals, then we pulled out the phase shift $e^{ik_x d}$ due to the shift of the β site by d (it is positive because now we have $-k_x$ in the Bloch wave exponent).

We consider a simplified form of the photoemission matrix element $\langle e^{i\mathbf{k}_f \mathbf{r}} | \Psi_{ini}(k_x, \mathbf{r}) \rangle$ where the influence of the polarization of the incoming light, the $\mathbf{A} \cdot \mathbf{P}$ operator (see Sec. 2.5.1.1), is neglected. This operator could be added and will lead to additional effects, but it is not needed to derive the effect of the interest.

The goal of the calculation is to show that spin polarizations for two different final state free-electron wave vectors, $\mathbf{k}_{fr} = [k_{fx}, k_{fz}]$ and $\mathbf{k}_{fl} = [-k_{fx}, k_{fz}]$ are different. We will show that this is realized by the matrix elements:

$$w_r = \langle e^{i\mathbf{k}_f \mathbf{r}} | \Psi_{ini}(k_x, \mathbf{r}) \rangle \quad (5.4)$$

$$w_l = \langle e^{i\mathbf{k}_f \mathbf{r}} | \Psi_{ini}(-k_x, \mathbf{r}) \rangle \quad (5.5)$$

We write the w matrix elements as

$$w_r(k_{fx}, k_{fz}) = \langle e^{i[k_{fx}, k_{fz}]\mathbf{r}} | \Psi_{ini}(k_x, \mathbf{r}) \rangle \\ = \int_x \int_z dx dz \, e^{-ik_{fx}x} e^{-ik_{fz}z} \times e^{ik_x \mathbf{r}} \sum_{l=-\infty}^{\infty} \Big[\delta(x - la)\delta(z) \cdot (\alpha_\uparrow |s_\uparrow\rangle + \alpha_\downarrow |s_\downarrow\rangle) \\ + \delta(x - la)\delta(z - h) \cdot e^{ik_x(a-d)} (\beta_{+\uparrow} |p_{+\uparrow}\rangle + \beta_{-\uparrow} |p_{-\uparrow}\rangle \\ + \beta_{+\downarrow} |p_{+\downarrow}\rangle + \beta_{-\downarrow} |p_{-\downarrow}\rangle) \Big] \quad (5.6)$$

$$
\begin{aligned}
w_l(k_{fx},k_{fz}) &= \langle e^{i[k_{fx},k_{fz}]\mathbf{r}}|\Psi_{ini}(-k_x,\mathbf{r})\rangle = \langle e^{i[k_{fx},k_{fz}]\mathbf{r}}|\Psi^*_{ini}(k_x,\mathbf{r})\rangle \\
&= \int_x\int_z dxdz\, e^{-ik_{fx}x}e^{-ik_{fz}z}\times e^{-ik_x\mathbf{r}}\sum_{l=-\infty}^{\infty}\Big[\delta(x-la)\delta(z)\cdot(\alpha^*_\downarrow|s_\uparrow\rangle+\alpha^*_\uparrow|s_\downarrow\rangle) \\
&\quad+\delta(x-la)\delta(z-h)\cdot e^{ik_xd}(\beta^*_{-\downarrow}|p_{+\uparrow}\rangle+\beta^*_{+\downarrow}|p_{-\uparrow}\rangle \\
&\quad+\beta^*_{-\uparrow}|p_{+\downarrow}\rangle+\beta^*_{+\uparrow}|p_{-\downarrow}\rangle)\Big]
\end{aligned}
\tag{5.7}
$$

We see that the non-zero solutions (remembering that we are considering wave functions at a certain energy E) are for $w_r(k_x,k_z)$ and $w_r(k_x,k_z)$, which indicates the parallel momentum conservation[9]. We also see that for the β site, the shift by h along z will result in the $e^{-ik_{fz}h}$. From this we have

$$
\begin{aligned}
&w_r(k_x,k_{fz}) = \\
&\alpha_\uparrow|s_\uparrow\rangle+\alpha_\downarrow|s_\downarrow\rangle+e^{ik_x(a-d)}e^{-ik_{fz}h}\Big(\beta_{+\uparrow}|p_{+\uparrow}\rangle+\beta_{-\uparrow}|p_{-\uparrow}\rangle+\beta_{+\downarrow}|p_{+\downarrow}\rangle+\beta_{-\downarrow}|p_{-\downarrow}\rangle\Big)
\end{aligned}
\tag{5.8}
$$

$$
\begin{aligned}
&w_l(-k_x,k_{fz}) = \\
&\alpha^*_\downarrow|s_\uparrow\rangle+\alpha^*_\uparrow|s_\downarrow\rangle+e^{ik_xd}e^{-ik_{fz}h}\Big(\beta^*_{-\downarrow}|p_{+\uparrow}\rangle+\beta^*_{+\downarrow}|p_{-\uparrow}\rangle+\beta^*_{-\uparrow}|p_{+\downarrow}\rangle+\beta^*_{+\uparrow}|p_{-\downarrow}\rangle\Big)
\end{aligned}
\tag{5.9}
$$

For clarity we can write all $w_\uparrow$ and $w_\downarrow$ parts separately

$$
\begin{aligned}
w_{r\uparrow}(k_x,k_{fz}) &= \alpha_\uparrow|s_\uparrow\rangle+e^{ik_x(a-d)}e^{-ik_{fz}h}(\beta_{+\uparrow}|p_{+\uparrow}\rangle+\beta_{-\uparrow}|p_{-\uparrow}\rangle) \\
w_{r\downarrow}(k_x,k_{fz}) &= \alpha_\downarrow|s_\downarrow\rangle+e^{ik_x(a-d)}e^{-ik_{fz}h}(\beta_{+\downarrow}|p_{+\downarrow}\rangle+\beta_{-\downarrow}|p_{-\downarrow}\rangle) \\
w_{l\uparrow}(-k_x,k_{fz}) &= \alpha^*_\downarrow|s_\uparrow\rangle+e^{ik_xd}e^{-ik_{fz}h}(\beta^*_{-\downarrow}|p_{+\uparrow}\rangle+\beta^*_{+\downarrow}|p_{-\uparrow}\rangle) \\
w_{l\downarrow}(-k_x,k_{fz}) &= \alpha^*_\uparrow|s_\downarrow\rangle+e^{ik_xd}e^{-ik_{fz}h}(\beta^*_{-\uparrow}|p_{+\downarrow}\rangle+\beta^*_{+\uparrow}|p_{-\downarrow}\rangle)
\end{aligned}
\tag{5.10}
$$

This allows calculating the $\uparrow$ and $\downarrow$ intensities as $I_{r\uparrow}=w^*_{r\uparrow}w_{r\uparrow}$, $I_{r\downarrow}=w^*_{r\downarrow}w_{r\downarrow}$, $I_{l\uparrow}=w^*_{l\uparrow}w_{l\uparrow}$ and $I_{l\downarrow}=w^*_{l\downarrow}w_{l\downarrow}$, and subsequently spin polarizations as $P_r=\frac{I_{r\uparrow}-I_{r\downarrow}}{I_{r\uparrow}+I_{r\downarrow}}$ and $P_l=\frac{I_{l\uparrow}-I_{l\downarrow}}{I_{l\uparrow}+I_{l\downarrow}}$.

We can now consider positive k_x and assume the $|p_-\rangle$ band at positive k_x is shifted in energy, because of the broken $\mathcal{M}_z$ mirror plane at the surface-vacuum interface, and does not contribute significantly, that is $\beta_{-\uparrow,\downarrow}=0$. Therefore, we can consider an electron band made from an $|s\rangle$ orbital and hole bands made from $|p_{+\uparrow,\downarrow}\rangle$ orbitals. Due to the spin-momentum locking we consider spin-splitting of $|p_{+\uparrow}\rangle$ and $|p_{+\downarrow}\rangle$ bands. We assume these bands hybridize and anticross, leading to $E(k_x)$ at which the *band characters are mixed*. We can assume all α and β coefficients are real, and we end up with three different coefficients $\alpha_\uparrow=\alpha_\downarrow$, $\beta_{+\uparrow}$ and $\beta_{+\downarrow}$.

At the Fermi level $E_{kin}=h\nu-\Phi_\circ$[10], and we can get the total momentum as $k=\sqrt{\frac{2m}{\hbar^2}E_{kin}}$. We can fix k_x, and get $k_{fz}=\sqrt{k^2-k_x^2}$, making the *zigzag* model $h\nu$

[9] Parallel momentum conservation : $e^{ik_{fx}}=e^{ik_x}$ and $e^{ik_{fy}}=e^{ik_y}$.

[10] The work function $\Phi_\circ$ was set to 4.5 eV in the model.

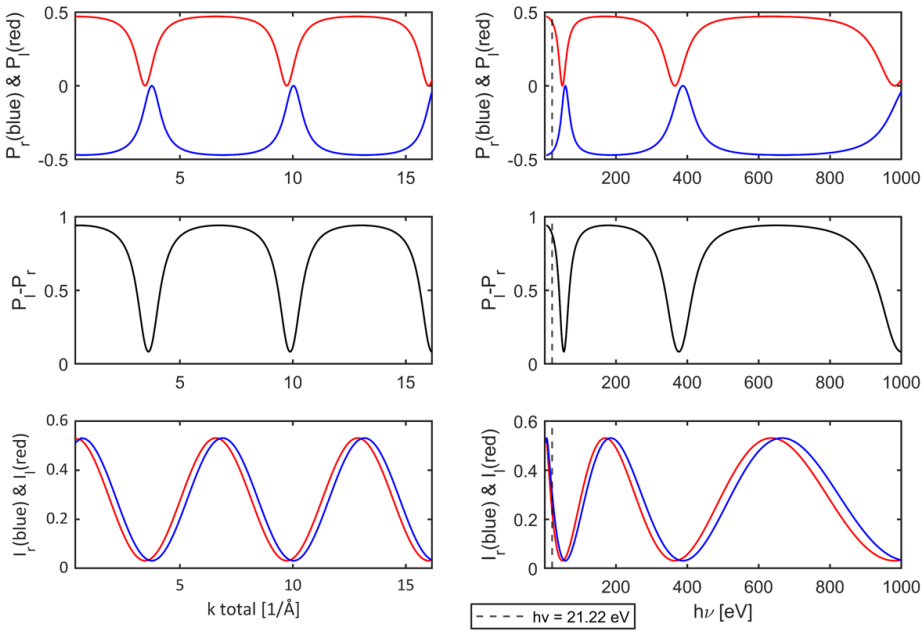

Figure 5.19: **One-dimensional *zigzag* model calculations.** Numerical calculation for the zig-zag model with $a = 3$ Å, $d = 1$ Å, $h = 1$ Å, $\alpha_\uparrow = 2/8$, $\alpha_\downarrow = 2/8$, $\beta_{+\uparrow} = 1/8$, $\beta_{+\downarrow} = 3/8$ and $k_x = 0.3$ Å.

dependent. Figure 5.19 shows the results of the model plotted vs. total momentum and vs. photon energy for selected parameters and hν between 5 and 1000 eV. It is also indicated that at $h\nu = 21.22$ eV using HeI discharge lamp, high asymmetry in the spin polarization is expected, and is demonstrated in e.g. Sec. 5.1.

5.12.2 Scattering-induced asymmetric spin polarization

In materials that contain large atoms such as Pt and Te, the SOC scattering of hot electrons may play a role, as schematically indicated in Fig. 5.16(c). Indeed, such a scattering process can induce spin polarization as will be demonstrated in this section.

To clarify the scattering-induced spin polarization mechanism in $PtTe_2$, let us discuss the scattering event, schematically illustrated in Fig. 5.20, for a beam of photoelectrons emitted from Pt atom and scattered by the potential of the Te atom.

A scattering plane is defined by the unit vector, $\hat{\boldsymbol{n}} = \frac{(\boldsymbol{k}_\circ \times \boldsymbol{k}_1)}{|(\boldsymbol{k}_\circ \times \boldsymbol{k}_1)|}$, perpendicular to it, where $\boldsymbol{k}_\circ$ and $\boldsymbol{k}_1$ are the momenta of the incoming and the scattered electrons respectively. In Fig. 5.20, the incoming beam is defined along the Pt-Te bond which is defined along the z-axis, i.e, $\boldsymbol{k}_\circ = k_\circ \hat{\boldsymbol{z}}$. If $N_\uparrow$ and $N_\downarrow$ are the number of the electrons parallel and antiparallel, respectively, to the normal of the scattering plane $\hat{\boldsymbol{n}}$, where $\hat{\boldsymbol{n}} = \hat{\boldsymbol{y}}$ in Fig. 5.20, then the polarization P of this beam is defined as

$$P = \frac{N_\uparrow - N_\downarrow}{N_\uparrow + N_\downarrow}. \tag{5.11}$$

The differential cross sections of this beam are given by [170–174]

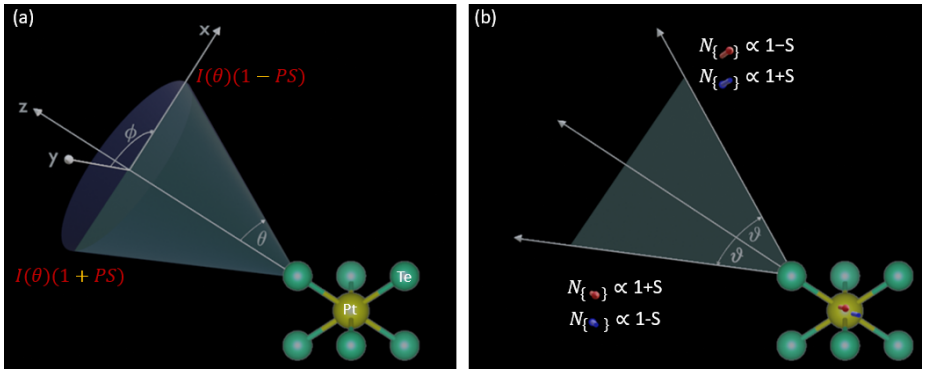

Figure 5.20: **Scattering-induced asymmetric distribution of spin polarization.** (a) Schematic illustration of asymmetrically scattered P polarized beam of electrons for $\phi = 90°$ and $\phi = 270°$ within the green triangular scattering xz-plane. (b) Same as (a) but for initially unpolarized beam that is considered as two fully polarized beams: one with spin $S_{iy,\uparrow}$ and the other with spin $S_{iy,\downarrow}$. Both spins are oriented perpendicular to the same scattering plane as described in (a). θ, ϕ, ϑ are the scattering angles, P is polarization of the beam, and S is the Sherman function.

$$\sigma(\theta, \phi) = I(\theta)(1 - PS(\theta) sin\phi) \tag{5.12}$$

where θ and ϕ are defined in Fig. 5.20(a), and S is the Sherman function. Therefore, for an initially spin-polarized beam with polarization P, the scattered intensity has a left-right asymmetry which depends on the angle ϕ. Figure 5.20 (a) shows this scattering asymmetry for an initially P polarized beam for $\phi = 90°$ and $\phi = 270°$.

To study the scattering case of initially unpolarized beam, $P_\circ = 0$, one can think of this beam as a mixture of two fully polarized beams with opposite spin polarization directions $S_{iy,\uparrow}$ and $S_{iy,\downarrow}$ perpendicular to the scattering green triangular plane defined within the xz-plane in Figs. 5.20(a) and 5.20(b).

Starting with the fully polarized up beam, $S_{iy,\uparrow}$, then from Eq. 5.11 it has polarization $P = 1$. Then, following Eq. 5.12, this beam will have scattering intensity to the right, ($\phi = 90°$), proportional to $(1 - S)$, while the scattering intensity to the left, ($\phi = 270°$), will be proportional to $(1 + S)$, as indicated in Fig. 5.20(b). On the other hand, for the fully polarized down beam, $S_{iy,\downarrow}$, the corresponding values are $(1 + S)$ and $(1 - S)$, respectively.

For the fully polarized beam, with polarization *perpendicular* to the scattering plane, the direction of the polarization vector of the scattered beam is not changed after the scattering [170], as indicated in Fig. 5.20(b). This means that along any scattering angle ϑ within the scattering plane, there will be different number of electrons with spin up and spin down, leading to a scattering-induced spin polarization. Indeed, scattering to the right creates spin polarization of

$$P = \frac{N_\uparrow - N_\downarrow}{N_\uparrow + N_\downarrow} = \frac{(1 - S) - (1 + S)}{(1 - S) + (1 + S)} = -S, \tag{5.13}$$

while scattering to the left will have a polarization of $P = S$.

This will lead in general to a non-vanishing scattering-induced spin polarization as schematically shown in Figs. 5.21(a) and 5.21(b), with respect to the white dashed line, for the *symmetry* and *asymmetry geometries* respectively.

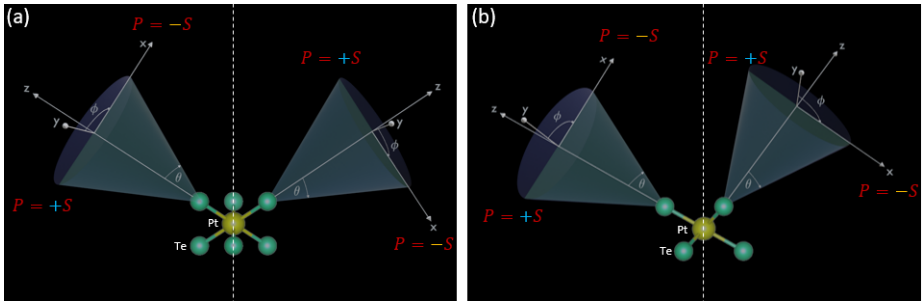

Figure 5.21: **Non-vanishing scattering-induced spin polarization.** (a),(b) Spin polarization induced by scattering in the *symmetry* and *asymmetry geometries*, respectively. To the right of each scattering event: added spin is $(-S)$, while it is $(+S)$ to the left of the same event.

The scattering-induced spin polarization in the *symmetry geometry*, as depicted in Fig. 5.21(a), is symmetrically distributed relative to the white dashed line, indicating a balanced addition of spin polarization. In contrast, in the *asymmetry geometry* shown in Fig. 5.21(b), the scattering-induced spin polarization is added asymmetrically, resulting in scattering-induced asymmetric measured spin polarization.

To estimate the magnitude of such effects in $PtTe_2$, photoelectron diffraction calculations, that include spin-orbit scattering, were performed using the EDAC code [51]. The results are shown in Figs. 5.22(a) and 5.22(b) for the in-plane S_y spin component, and in Figs. 5.22(c) and 5.22(d) for the in-plane S_x spin component. The *s*-wave (an isotropic spherical wave) was emitted from the outermost Pt atoms of the $PtTe_2$ cluster. The cluster radius was 18 Å and contained 574 atoms. We have chosen $E_{kin} = 16$ eV, typical for the Fermi level electrons measured with He-I radiation ($h\nu = 21.22$ eV), and standard values for inner potential $V_\circ = 15$ eV, and IMFP of 3 Å. The results presented in Fig. 5.22 indicate that spin polarization of up to $\approx 15\%$ can be expected purely from SOC scattering. We conjecture that in spin-ARPES spectra the effects are less pronounced through mixing of scattering due to different emitters and their scattering environments and because intense emission appears only at parallel momenta related to the bands, therefore might not coincide with areas of high polarization due to scattering. Figures 5.22(e) and 5.22(f) were calculated using a plane wave emitted from the source, however, in the Muffin-tin approximation spherical waves are emitted and get scattered. Nevertheless, these figures illustrate the mechanism. They as well clearly show that the differential cross sections are at their maxima when the scattering angle is zero, indicating forward scattering along the bond. This is consistent with the discussion made in Sec. 2.6, particularly as illustrated in Fig. 2.11.

For EDAC, the first layer of $PtTe_2$ cluster contained Pt site at (0,0,0) and Te sites at ($\pm$ 1.169 Å, 2.025 Å,$\mp$ 1.365 Å). Subsequent layers were separated by 5.48 Å along the z-axis. Two separate calculation for the initial *s*-wave spin polarized up to down along the y-axis were performed, this initial emission can be written as $S_{i\uparrow}(\theta, \phi)$ and

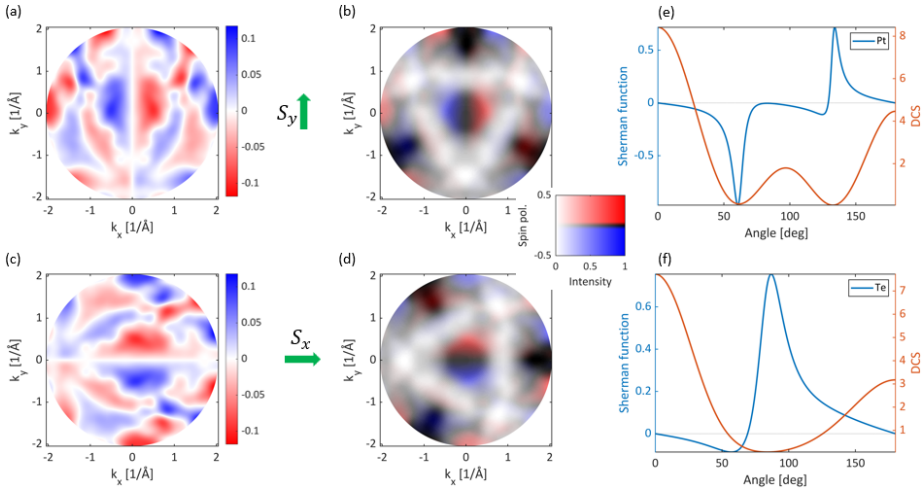

Figure 5.22: **Photoelectron diffraction from Pt s-orbital in $PtTe_2$ at E_{kin} = 16 eV calculated using EDAC [51].** (a) Spin-polarized photoelectron diffraction pattern for s-wave emission from the outermost Pt site in bulk $PtTe_2$. (b) Same as (a), but with the special 2D colormap inset that simultaneously represents both spin polarization and intensity. In (a) and (b), the spin quantization axis is aligned with the y-scale. (c),(d) Same as (a) and (b), but for the spin quantization axis being aligned with the x-scale. (e),(f) Differential cross sections and Sherman functions, for the Pt and Te atoms respectively, corresponding to the muffin-tin potentials employed in the photoelectron diffraction (PED) calculation.

$S_{i\downarrow}(\theta, \phi)$ which are just fully isotropic spin polarized waves emitted from Pt site. This is needed to obtain results from non-spin-polarized initial state. Subsequently, in both cases, the final state spin polarization along the y-axis was calculated, therefore obtaining 2 multiply scattered wave functions $S_{i\uparrow,f\uparrow}(\theta, \phi)$, and $S_{i\downarrow,f\downarrow}(\theta, \phi)$. In order to obtain intensities shown in Fig. 5.22(a), we calculated $I_\uparrow = |S_{i\uparrow,f\uparrow}(\theta, \phi)|^2$ and $I_\downarrow = |S_{i\downarrow,f\downarrow}(\theta, \phi)|^2$.

5.12.3 Bulk-induced asymmetric spin polarization

Bulk $PtTe_2$ has a centrosymmetric crystal structure belonging to the 1T-phase class of TMDCs. In this phase, the two chalcogen Te layers are rotated 180° relative to each other, as discussed in Sec. 4.1 and illustrated in Fig. 5.23 (Te: green atoms; Pt: yellow atom). Thus, the charge across the Te-Pt-Te bond is symmetrically distributed, and inversion symmetry is retained even at the single trilayer limit. However, at a local scale, an effective electric field arises from the Pt-Te bonds, leading to an out-of-plane site dipole field. This dipole field is localized in the upper half of the unit cell (indicated by the upper white arrow) and reverses sign in the lower half, resulting in a vanishing net dipole field.

The local dipole field, combined with spin-orbit coupling, induces in-plane Rashba R-2 spin splitting perpendicular to the dipole field. In centrosymmetric materials, all energy bands must be doubly degenerate. As a result, the compensated spins with opposite signs (depicted by magenta arrows with opposite helicities in Fig. 5.23) exhibit energy degeneracy. Each spin is spatially localized in one of the two

real-space-separated sectors, which correspond to the inversion partners (top and bottom Te layers) [165]. This spatial separation underlies the spin-layer locking effect, a key characteristic of hidden spin polarization.

Therefore, a non-zero spin polarization called hidden spin polarization can only be uncovered with a surface-sensitive probe of the electronic structure, where the topmost layer of the material is primarily probed compared to deeper layers. Such hidden spin polarization has been predicted in the 1T-phase of TMDCs [175] and has been verified in the Se $p_{x,y}$-derived bands of the 1T-$PtSe_2$ monolayer [33], which exhibit a local in-plane Rashba polarization. Recently, this hidden spin polarization has also been reported in bulk 1T-$HfSe_2$ single crystals [35].

Rashba spin splitting can be categorized into two main types: R-1, which arises in systems with structure inversion asymmetry [70, 176–182] and is typically associated with a large internal electric field, and R-2, where spin polarization is layer-dependent and arises even in centrosymmetric structures with local dipole fields. The spin-layer-locked nature of the R-2 Rashba spin polarization provides a distinct advantage over R-1, as it enables easier manipulation of spins via an external electric field. This property makes R-2 particularly promising for electrically tunable spintronic devices [183–185].

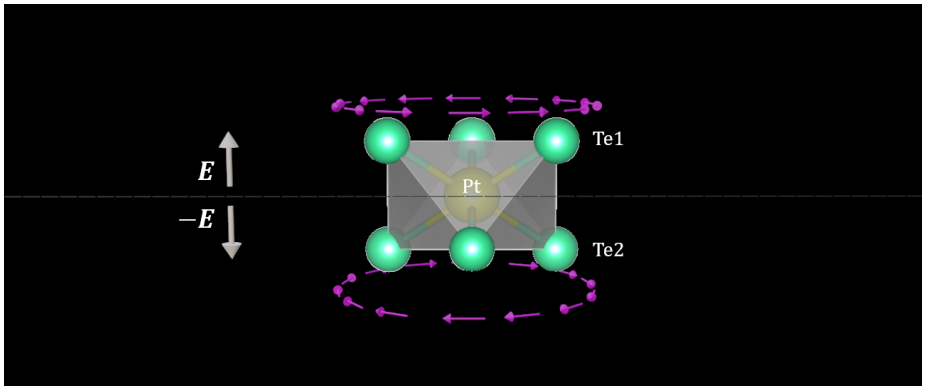

Figure 5.23: **Hidden spin polarization in the 1T-phase structure of TMDCs.** Unit cell structure of bulk 1T-$PtTe_2$ single crystal (Pt: labeled yellow atom; Te: labeled green atoms). White arrows indicate the localized out-of-plane dipoles within the same unit cell, which give rise to in-plane Rashba R-2 spin splitting. Magenta arrows are schematic representation of the spin helicity showing the spin-layer locking mechanism.

Figure 5.16(d) illustrates the delocalization of the bulk state, with its periodic charge density distribution extending up to the sample surface. Consequently, the symmetry of the spin-ARPES measurements is influenced by the intrinsic symmetries of the bulk band structure. As discussed in Sec. 4.1 and Sec. 4.10, $PtTe_2$ exhibits trigonal symmetry in its bulk form, rather than hexagonal symmetry. Thus, when probing along the $\bar{M} - \bar{\Gamma} - \bar{M}$ direction, which is not perpendicular to any mirror plane, the measurements will be affected by the initial asymmetry in the bulk band structure along $M - \Gamma - M$ as shown previously by the projected band structure in Fig. 4.27(b).

5.13 Summary

In its bulk form, $PtTe_2$ adopts an inversion-symmetric 1T-phase structure, satisfying $E(\boldsymbol{k},\uparrow) = E(-\boldsymbol{k},\uparrow)$. As a non-magnetic system, it also preserves time-reversal symmetry, ensuring $E(\boldsymbol{k},\uparrow) = E(-\boldsymbol{k},\downarrow)$. The combination of inversion symmetry (IS) and time-reversal symmetry (TRS) typically enforces a fully spin-degenerate bulk band structure. However, in this chapter, we have presented - for the first time - spin-polarized energy-momentum spectra and constant energy contours of $PtTe_2$, revealing spin polarization reaching up to $\sim 55\%$.

We attribute most of the in-plane spin texture to a Rashba-like mechanism, arising from the out-of-plane potential gradient. In contrast, the out-of-plane spin texture originates from intra-layer in-plane dipoles, a consequence of broken inversion symmetry at the surface. Additionally, we identify spin polarization in the bulk-derived bands as a manifestation of *hidden spin polarization*, which is revealed due to the surface sensitivity of spin-ARPES. Furthermore, calculations using the EDAC code demonstrate that spin polarization of up to $\sim 15\%$ can result from the scattering of photoelectrons on their way to the detector.

Experiments were performed for different orientations of the sample, taking into consideration the alignment of the mirror planes hosted by $PtTe_2$ single crystal relative to the reaction plane of the experiments, within which the unpolarized HeI radiation ($h\nu = 21.22$ eV) impinged the sample.

In the first set of orientations, referred to as the *symmetry geometry*, the reaction plane coincided with one of the mirror planes of the crystal. Under these conditions, the measured $E(k)$ and $(k_x - k_y)$ spin-polarized maps obeyed the symmetry rules associated with the preserved mirror plane, consistent with theoretical calculations. However, for two *symmetry geometries* of the sample, related by a rotation of $\varphi = 60°$, one of these geometries exhibited a stronger spin-polarization signal, even though both geometries showed symmetric spin-polarization maps. We attribute this to the light incidence direction.

In the second set of orientations, termed the *asymmetry geometry*, where the reaction plane did not coincide with any of the mirror planes of the crystal, the symmetry rules of all mirror planes were broken. In this configuration, we observed highly asymmetric spin textures, both in the positions of features and in the magnitude of the spin-polarization signal, contrasting with the corresponding symmetric spin-calculated maps.

We have identified several processes that may have modified the initial state spin polarization during the photoemission process, resulting in these asymmetric spin-polarized maps. The first process is the interference of waves emitted from different atomic sites, where non-equivalent atomic sites in the *asymmetry geometry* create varying phase shifts that can alter the spin-ARPES spin polarization. The second process involves the scattering of photoelectrons by neighboring atoms on their way to the detector, when the *asymmetry geometry* is employed. Finally, the third factor is the inherently asymmetric bulk band structure due to the trigonal crystal structure of bulk $PtTe_2$, rather than a hexagonal one, when the *asymmetry geometry* is used.

6. Electronic structure of $PdTe_2$

6.1 ARPES on bulk $PdTe_2$

$PdTe_2$ is an intrinsic bulk superconductor with $T_c \sim 1.7$ K [186–188]. Single-crystal $PdTe_2$ belongs to the space group $P\bar{3}m1$ hosting three mirror planes. The crystal structure of $PdTe_2$ and the corresponding symmetry operations hosted by the crystal are same as those of $PtTe_2$ discussed in Sec. 4.1 and Sec. 4.2.

Figure 6.1 provides an overview of the ARPES measurements of $PdTe_2$. The first set of measurements were conducted using the *symmetry geometry* as schematically depicted in Fig. 6.1(a), in which the sample was aligned such that the incident light beam coincided with one of the mirror planes of the crystal, preserving its symmetry rules. The data were acquired as a 3D matrix using p-polarized light with photon energy $h\nu = 107$ eV, as presented in Fig. 6.1(b). For better visualization of the band structure, part of the 3D data is visualized in Fig. 6.1(c). The Fermi surface map, representing a constant energy cut at $E_B = 0$, is shown in Fig. 6.1(d), and the energy-momentum map along the $\bar{\Gamma} - \bar{K}$ direction of the surface BZ is presented in Fig. 6.1(e), taken from Fig. 6.1(b) at $k_x = 0$ as indicated by the dashed-black line in Fig. 6.1(d). Fig. 6.1(f) is same as Fig. 6.1(e) indicating the key features by the dashed- and solid yellow lines highlighting the surface states, as will be discussed later in this section. Lower panels (g)-(l) correspond to similar measurements as (a)-(f), but were obtained using the *asymmetry geometry* depicted in Fig. 6.1(g), where in this case the incident light breaks all mirror planes symmetries of the crystal surface, as discussed in Sec. 4.10. Figures 6.1(k) and 6.1(l) show the band dispersion along the $\bar{\Gamma} - \bar{M}$ direction, taken as a cut from Fig. 6.1(h) at $k_x = 0$, as indicated by the dashed-black line in Fig. 6.1(j), with the key features highlighted in Fig. 6.1(l).

The corresponding calculated electronic band structure of $PdTe_2$ is shown in Fig. 6.2(a)-(g). Figure 6.2(a) presents the 3D band structure calculations for a 30-layer slab of $PdTe_2$, with key features visualized in Figs. 6.2(b) and 6.2(c) for enhanced clarity of the band structure. Figure 6.2(d) displays the calculated Fermi surface map, with the magenta frame delineating the surface Brillouin zone. A magnified view of the 3D band structure calculation near the Fermi level is provided in Fig. 6.2(e), offering a clearer view of the surface states near the Fermi surface, which will be discussed in more detail later in this section. Additionally, dispersions of $PdTe_2$ bands along the high symmetry directions $\bar{\Gamma} - \bar{K}$ and $\bar{\Gamma} - \bar{M}$ are plotted in Figs. 6.2(f) and 6.2(g), respectively.

The measured energy-momentum maps presented in Fig. 6.1(e) with its key features highlighted in 6.1(f) and 6.1(k) with its key features highlighted in 6.1(l), along with the corresponding calculated maps in Figs. 6.2(f) and 6.2(g), reflect the similarity between the band structure of $PdTe_2$ and the band structure of its sister

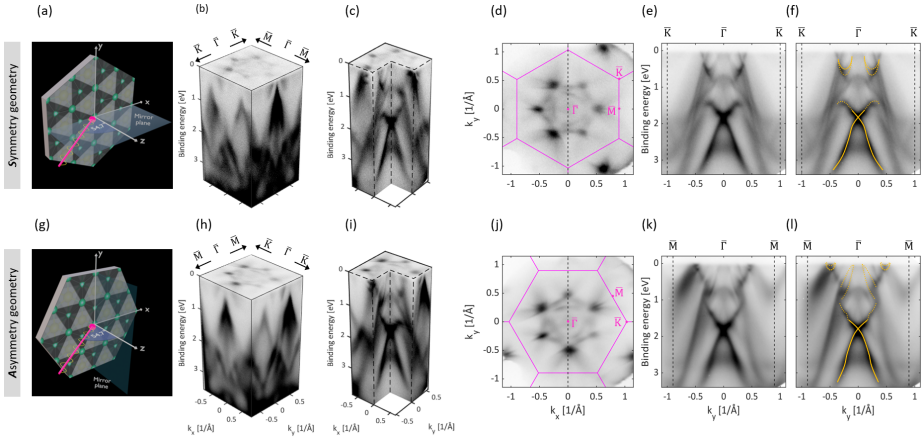

Figure 6.1: **Experimentally determined electronic band structure of $PdTe_2$.** *Upper panel*: (a)-(f) Results obtained using the *symmetry geometry* schematically shown in (a), in which one of the three mirror planes of bulk $PdTe_2$ was aligned such that the light beam impinged the sample within this plane, preserving the symmetry rules of this mirror plane. (b) ARPES 3D matrix data of $PdTe_2$. (c) Three quarters of (b) for better visualization of the band structure. (d) ARPES Fermi surface map of $PdTe_2$ ($E_F \pm 50$ meV). (e) In-plane energy-momentum dispersion $E(k_y)$ along the high symmetry direction in reciprocal space $\bar{\Gamma} - \bar{K}$, indicated by the black-dashed line in (d). (d),(e) Taken as cuts from the measured 3D-stack of data (b) at $E_{binding} = 0$ and at $k_x = 0$ respectively. (f) Same as (e) with the key features indicating surface states highlighted by dotted and solid yellow lines. *Lower panel*: (g)-(l) equivalent measurements, but measured as shown schematically in (g) where one of the three mirror planes of bulk $PdTe_2$ was aligned such that for the complete system of the sample and the incident light, no mirror plane symmetry remained. (Measurements were performed at room temperature, $h\nu = 107$ eV; p-polarized light: probing close to A-plane in the three dimensional Brillouin zone along the k_z-direction; see Notes 2 and 3).

compound $PtTe_2$ which was discussed in Sec. 4.3. Indeed, one can see a pronounced feature situated at $E_B \sim 1.8$ eV below the Fermi level which has been identified as a topological surface Dirac cone in $PdTe_2$ [25, 49]. Similar to $PtTe_2$, the upper legs of the cone emerge and become degenerate with the bulk diffuse spectral weight where they keep their general shape along the $\bar{\Gamma} - \bar{K}$ direction and survive as surface resonances (see Figs. 6.1(e), 6.1(f) and 6.2(f)). However, along the $\bar{\Gamma} - \bar{M}$ direction, these branches diffuse into the bulk manifold and become indistinguishable, though they re-emerge as distinct surface states at lower binding energies (see Figs. 6.1(k), 6.1(l) and 6.2(g)).

The constant energy momentum contours between $E_B = 1.5$ eV and $E_B = 2.2$ eV in Fig. 6.3 show the characteristic closing and re-opening of the Dirac cone with increasing binding energy, a feature that is also clearly captured in the calculations presented in Figs. 6.2(b) and 6.2(c). Additionally, another distinct pair of sharp surface states appear at $E_B \sim 0.55$ eV in Figs. 6.1(e), 6.1(f), 6.1(k) and 6.1(l). Unlike the corresponding surface states in $PtTe_2$ (see Figs. 4.3(e) and 4.3(l)), the two branches of these states exhibit a turning point midway along the $\bar{\Gamma} - \bar{K}$ direction (see Figs. 6.1(e), 6.1(f) and 6.2(f)). This behavior induces pronounced hexagonal

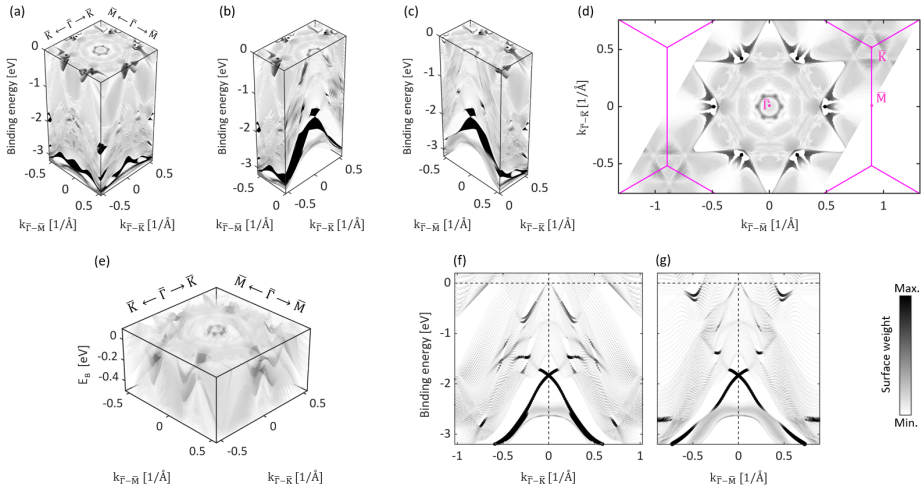

Figure 6.2: **Calculated electronic band structure of $PdTe_2$.** (a) Three-dimensional calculated band structure of a 30-layer slab of $PdTe_2$. (b),(c) Parts of (a) for enhanced visualization of the key features in the band structure. (d) Fermi surface map showing a constant energy cut derived from (a). (e) Narrow energy range close to the Fermi level from (a), showcasing the surface states crossing the Fermi level midway along the $\bar{\Gamma} - \bar{M}$ direction. (f),(g) Calculations of the band structure along the high symmetry directions of the surface Brillouin zone $\bar{\Gamma} - \bar{K}$ and $\bar{\Gamma} - \bar{M}$, respectively. The outermost atomic orbitals of the top surface Pd and Te atoms are included in all calculations (a)-(g) with their spectral weight represented by the colorbar.

warping in the constant energy contours, as shown in Fig. 6.3, over the energy range from $E_B = 0.4$ eV to $E_B = 0.6$ eV as highlighted by the yellow-dotted warping curves in the momentum map at $E_B = 0.6$ eV, that evolve to arc-like features as highlighted in the momentum map at $E_B = 0.7$ eV just below the minimum of the surface states. Furthermore, a pair of sharp spectral features intersecting the Fermi level can be seen approximately midway along the $\bar{\Gamma} - \bar{M}$ direction (see Figs. 6.1(k), 6.1(l) and 6.2(g)), which have been demonstrated to have negligible dispersion along the out-plane direction, and thus, are identified as surface states (see supplementary in Ref. [19]). The 3D calculations in Fig. 6.2(e) provide a clearer visualization of these surface states. Their locations at high $k_{||}$ lead to deviations from circular Fermi surface geometry, instead forming intricate multi-valley pockets [19], as evidenced in the Fermi surface maps of $PdTe_2$ presented in Figs. 6.1(d),(j) and the calculated Fermi map in Fig. 6.2(d), as well as in the constant energy contours at $E_B = 0.1$ eV and $E_B = 0.2$ eV in Fig. 6.3.

In addition to these surface states, several broad diffuse features are observed in the energy-momentum maps, particularly around $E_B \sim 0.8$ eV, where a type-II bulk Dirac cone has been identified in $PdTe_2$ [25, 50]. These surface states as well as the type-II bulk Dirac cone originate from a series of band inversions within the Te p-orbital manifold, driven by the differing bandwidths of the out-of-plane p_z orbitals compared to the in-plane $p_{x,y}$-orbitals along the k_z direction in reciprocal space [25], as discussed in Sec. 4.5.

Figure. 6.4 and Fig. 6.5 show surface orbital characters of the 30 layer $PdTe_2$

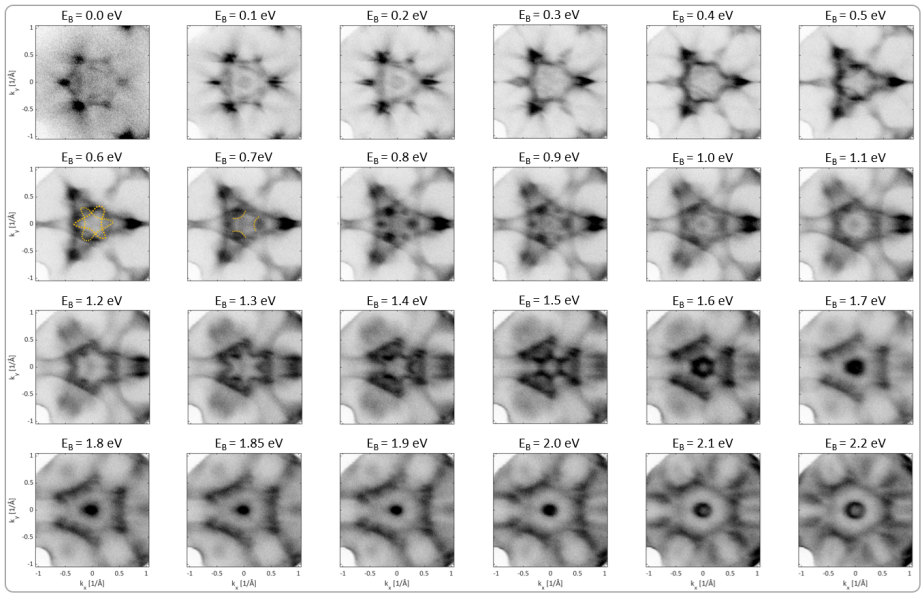

Figure 6.3: **Constant energy-momentum cuts of $PdTe_2$.** Selected constant energy contours ($\Delta E = 20$ meV) of $PdTe_2$ at the indicated binding energies, using p-polarized light and photon energy $h\nu = 107$ eV.

slab calculations. The quantization axis for the complex orbitals is chosen perpendicular to the surface as shown in the right insets. For convenience, the most prominent features in the band structure are highlighted in the left insets named key features. One can see that the surface Dirac cone centered at $E_B \sim 1.8$ eV is formed predominantly from the out-plane orbitals Pd $5d\ Y_2^0 = d_{z^2}$ and Te $5p\ Y_1^0 = p_z$. The surface states at $E_B \sim 1.4$ eV are formed predominantly from Te $5p\ Y_1^0$ and Pd $5d\ Y_2^0$ orbitals with admixtures of Te $5p\ Y_1^{\pm 1}$ and Pd $5d\ Y_2^{\pm 2}$. The surface states at $E_B \sim 0.55$ eV are formed predominantly from Te $5p\ Y_1^0$ and Te $5p\ Y_1^{\pm 1}$ with admixtures of Pd $5d\ Y_2^0$ and Pt $5d\ Y_2^{\pm 2}$ orbitals. The surface states close to Fermi level that appear only along the $(\bar{\Gamma} - \bar{M})$ direction are formed predominantly from the out-plane Te $5p\ Y_1^0$ orbitals with admixtures of Pd $5d\ Y_2^0$, $Y_2^{\pm 1}$ and $Y_2^{\pm 2}$ orbitals. This demonstrates that in $PdTe_2$ the valence bands wave functions are strongly mixed between Te and Pd sites.

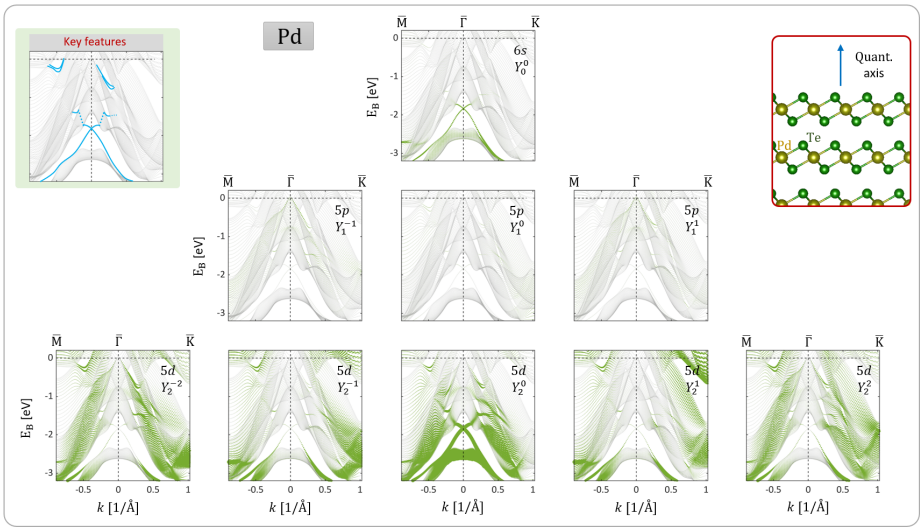

Figure 6.4: **Band characters for the Pd surface atom of the 30L $PdTe_2$ slab calculation.** Band characters for the Pd surface atom of the 30L $PdTe_2$ slab calculation for s, p and d complex orbitals for the quantization axis normal to the surface as indicated in the right inset. The bands are plotted along $\bar{\Gamma} - \bar{K}$ of the reciprocal space. The size of symbols represents the corresponding orbital weight. The left inset highlights the key features of the band structure.

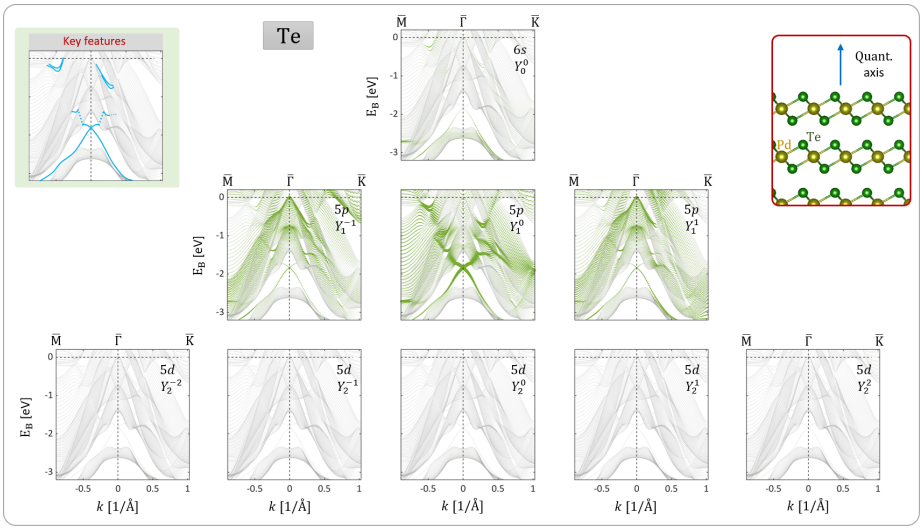

Figure 6.5: **Band characters for the Te surface atom of the 30L $PtTe_2$ slab calculation.** Band characters for the Te surface atom of the 30L $PtTe_2$ slab calculation for s, p and d complex orbitals for the quantization axis normal to the surface as indicated in the right inset. The bands are plotted along $\bar{\Gamma} - \bar{K}$ of the reciprocal space. The size of symbols represents the corresponding orbital weight. The left inset highlights the key features of the band structure.

6.2 Spin-ARPES on bulk $PdTe_2$

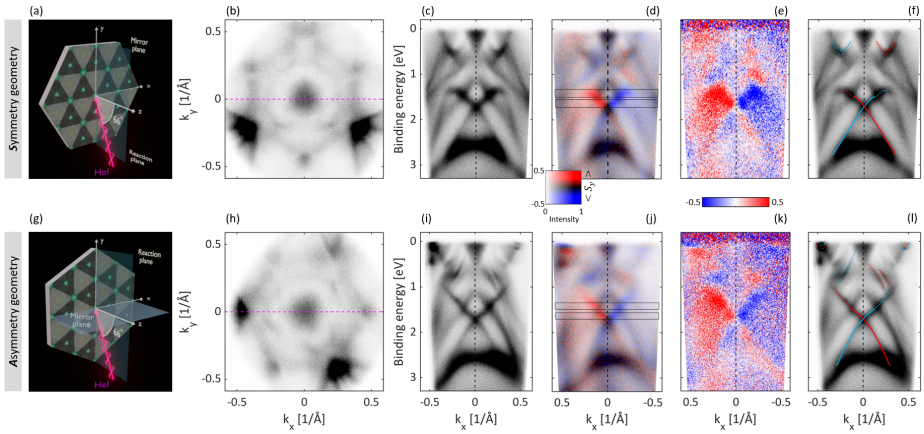

Figure 6.6: **Spin-resolved asymmetries of $PdTe_2$.** Upper panel: (a)-(f) Results obtained within the *symmetry geometry* schematically shown in (a) where the $\mathcal{M}_x$ mirror plane coincides with the reaction plane. (b) Corresponding Fermi surface map. (c) Energy-momentum band dispersion map $E(k_x)$, at $k_y = 0$. (d),(e) Corresponding spin-resolved energy dispersion maps, $E(k_x)$, measured using the lens deflector system probing along the x-axis perpendicular to $\mathcal{M}_x$ mirror plane, as defined in (a) and along the magenta-dashed line in (b), while the sample in normal emission. (f) Same as (c) highlighting the strongly spin-polarized features of the spectrum with the color indicating their spin-polarization sign. Lower panel: (g)-(l) Equivalent to (a)-(f) respectively, but measured using the *asymmetry geometry* schematically shown in (g) where the reaction plane is now perpendicular to the $\mathcal{M}_y$ mirror plane and the spin maps were filtered along the magenta line in (h) ***not*** perpendicular to any of the system's mirror planes. In (d) and (j) the intensity and spin-polarization are simultaneously displayed using the inset 2D color code shown in (d), where the false color scale refers to the in-plane spin polarization S_y in the ensemble of the photoemitted electrons. (e),(k) The corresponding pure in-plane S_y spin polarized maps. (Measurements were performed using the unpolarized HeI radiation $h\nu = 21.22$ eV).

Figure 6.6 presents two spin-resolved measurements from $PdTe_2$, at different experimental geometries, specifically, the relative orientation of the reaction plane (defined in Sec. 4.9) with respect to the mirror planes of the crystal surface. The unpolarized HeI light ($h\nu = 21.22$ eV) was used, as in the experiments conducted on $PtTe_2$ in Sec. 5.1. Figures 6.6(b)-(e) were measured using the *symmetry geometry* shown in Fig. 6.6(a) , where the reaction plane coincides with one of the surface mirror planes, specifically $\mathcal{M}_x$. As seen in Fig. 6.6(b), $\mathcal{M}_x$ is the only preserved mirror plane out of the three present in the crystal. The spin-integrated energy-momentum map in Fig. 6.6(c) was measured along the magenta line in Fig. 6.6(b), perpendicular to $\mathcal{M}_x$. Panels (d) and (e) show the corresponding spin-resolved energy-momentum maps for the in-plane spin component S_y. In Fig. 6.6(d), both photoemission intensity and spin polarization are represented using a 2D color code (see inset), while Fig. 6.6(e) depicts only the spin polarization. Figures 6.6(g)-(j) present equivalent measurements to those in panels (b)-(e), but taken using the *asymmetry geometry* depicted in Fig. 6.6(f), where the reaction plane is perpendicular to another mirror plane, $\mathcal{M}_y$.

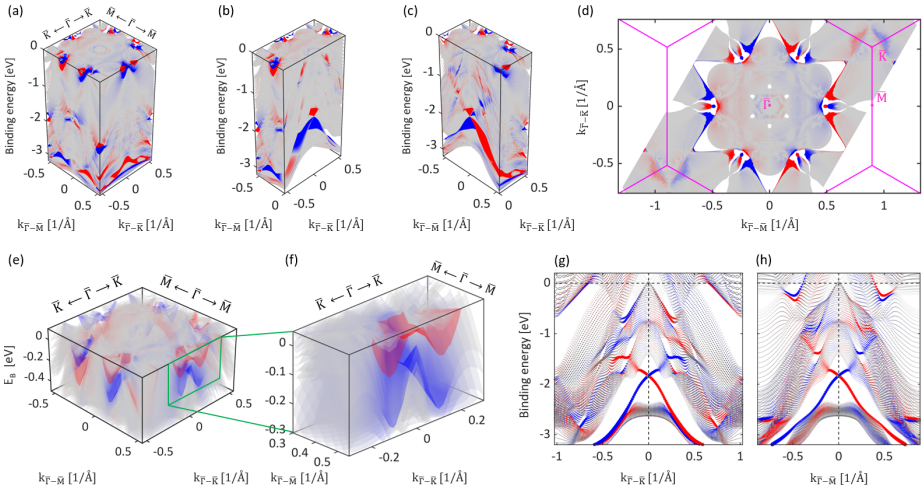

Figure 6.7: **Spin-resolved calculated electronic band structure of $PdTe_2$.** (a) Three-dimensional spin-resolved calculated band structure of a 30-layer slab of $PdTe_2$. (b),(c) Parts of (a) for enhanced visualization of the key spin-polarized features in the band structure. (d) Spin-resolved Fermi surface map showing a constant energy cut derived from (a). (e) Narrow energy range close to the Fermi level from (a), showcasing the highly spin-polarized surface states crossing the Fermi level midway along the $\bar{\Gamma} - \bar{M}$ direction. (f) Magnified view of the portion of (e) highlighted by the green frame, enhancing the visualization of these surface states. (g),(h) Spin-resolved calculations of the band structure along the high symmetry directions of the surface Brillouin zone $\bar{\Gamma} - \bar{K}$ and $\bar{\Gamma} - \bar{M}$, respectively. The outermost atomic orbitals of the top surface Pd and Te atoms are included in all calculations (a)-(h).

Figures 6.7(a)-(c) present 3D spin-resolved calculations of $PdTe_2$, with the spin-polarized Fermi surface map shown in Fig. 6.7(d). A narrower energy range is depicted in Fig. 6.7(e) to better visualize the highly spin-polarized surface states near the Fermi level, particularly along the $\bar{\Gamma} - \bar{M}$ direction. A magnified 3D picture of the green-highlighted portion containing these surface states is shown in Fig. 6.7(f). Additionally, spin-resolved calculations of the band dispersion along the high symmetry directions $\bar{\Gamma} - \bar{K}$ and $\bar{\Gamma} - \bar{M}$ are shown in Figs. 6.7(g) and 6.7(h), respectively, highlighting sharp, spin-polarized surface states, discussed in Sec. 6.1, that are distinct from the surrounding diffuse bulk spectral weight.

In the measured spin-ARPES maps in Figs. 6.6(d) and 6.6(e), the $\mathcal{M}_x$ mirror plane is in effect, and since spin follows the axial vector rules (see Fig. 5.2), the spin polarization reverses as k_x changes sign, $S_y(k_x) = -S_y(-k_x)$, in agreement with the corresponding calculations in Fig. 6.7(g).

In contrast, the spin-polarized maps shown in Figs. 6.6(j) and 6.6(k), are highly asymmetric with respect to $k_x = 0$, where $\mathcal{M}_y$ is the mirror plane of the crystal, not $\mathcal{M}_x$, as shown in Fig. 6.6(g). This asymmetry contrasts with the corresponding symmetric spin-polarized map calculated for the initial state, as shown in Fig. 6.7(h).

To address these asymmetries, a quantitative standard deviation analysis is presented in Fig. 6.8. In panels (a)-(d) of Fig. 6.8, the spin polarization is averaged

over 8-energy pixels with $\Delta E \sim 150$ meV, and plotted along k_x with its standard deviation at selected binding energies, as highlighted by the black frames in Figs. 6.6(d) and 6.6(j). Magenta curves represent $P(k_x)$ with their standard deviations shown by the light gray areas. Additionally, green curves representing $-P(-k_x)$ are also plotted with their standard deviations represented by the dark gray areas.

Figures 6.8 (e)-(h) show data from the spin-up (red) and spin-down spectrum (blue) of the spin-detector corrected by the Sherman function S = 0.29, for the magenta $P(k_x)$ curves of the respective panels (a)-(d) of Fig. 6.8. At each k-point of $E(k_x)$ spin-polarized map, FERRUM detector measures two intensities I_+ and I_- for the target magnetized in opposite directions. Spin polarization is calculated as discussed in Sec. 3.2.2, as $P = (1/S)\frac{I_+ - I_-}{I_+ + I_-}$, and the up/down spectra are reconstructed as $I_{up(dn)} = 0.5(I_+ + I_-)(1 \pm P)$.

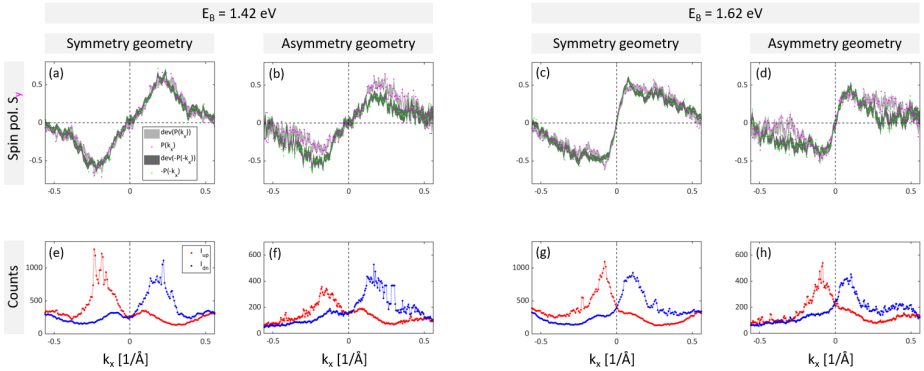

Figure 6.8: **Spin-resolved momentum distribution curves for $PdTe_2$.** (a-d) Momentum distribution curves (MDCs) for the spin polarization at the indicated geometry and binding energies, averaged over 8 energy pixels with $\Delta E \sim 150$ meV. Magenta and green curves show $P(k_x)$ and $-P(-k_x)$, where P is the spin polarization along S_y. Light- and dark gray areas depict standard deviations for spin-polarization curves as indicated by the inset in (a). (e-h) Corresponding data from the spin-up (red) and spin-down spectrum (blue) of the spin-detector, as indicated by the inset in (e), corrected by the Sherman function S = 0.29, for the magenta $P(k_x)$ curve.

In panels (a) and (c) of Fig. 6.8, the $P(k_x)$ and $-P(-k_x)$ curves coincide within the noise level. This confirms the $\mathcal{M}_x$ invariance quantitatively. However, in panels (b) and (d) of Fig. 6.8, the difference between $P(k_x)$ and $-P(-k_x)$ is beyond the noise level. This in turn quantitatively demonstrates asymmetries.

To investigate the spin-polarized surface states near the Fermi level, analogous to the states observed in $PtTe_2$ (see Sec. 5.4), spin-resolved momentum maps for the in-plane S_y spin component were measured at the relevant binding energies using unpolarized HeI radiation ($h\nu = 21.22$ eV), as shown in Fig. 6.9. The corresponding spin-integrated and spin-resolved calculated momentum maps are presented in Figs. 6.10(a)-(d).

Figure 6.9(a) shows the spin-integrated momentum map of $PdTe_2$ measured at $E_{binding} = 0.1$ eV, while Fig. 6.9(b) shows the corresponding spin-resolved momentum map. Similarly, Figs. 6.9(c) and 6.9(d) present the same measurements at $E_{binding} = 0.3$ eV. These measurements were performed using the *symmetry geometry* depicted in Fig. 6.6(a), where the mirror plane $\mathcal{M}_x$ coincides with the reaction

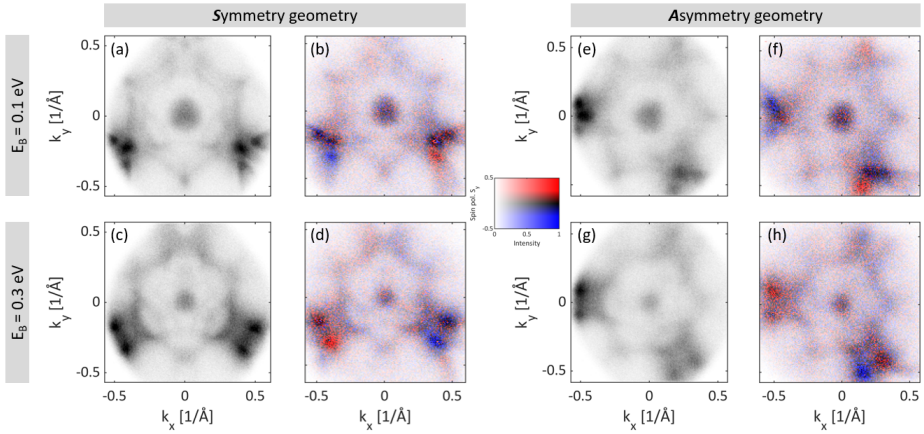

Figure 6.9: **Spin-resolved momentum maps of $PdTe_2$ near the Fermi level.** (a),(b) Spin-integrated and spin-resolved photoemission intensities measured at $E_{binding} = 0.1$ eV. (c),(d) Same but measured at $E_{binding} = 0.3$ eV. (a)-(d) Measured using the *symmetry geometry* of Fig. 6.6 (a). (e)-(h) Same, but measured using the *asymmetry geometry* of Fig. 6.6 (f). Spin-resolved maps plotted using the 2D color code showing intensity and spin polarization. HeI ($h\nu = 21.22$ eV) excitation has been used for all maps.

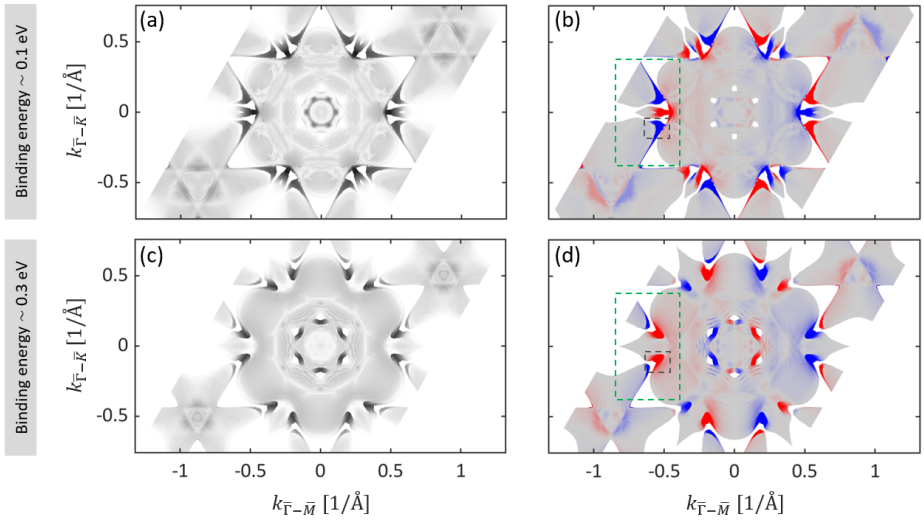

Figure 6.10: **Spin-resolved calculated momentum maps of $PdTe_2$ near the Fermi level.** (a),(b) Spin-integrated and spin-resolved calculated intensities at $E_{binding} = 0.1$ eV. (c),(d) Same but calculated at $E_{binding} = 0.3$ eV. Black frames highlight same structure that shows a spin-polarization sign flipping when moving from $E_B = 0.1$ eV to $E_B = 0.3$ eV. The outermost surface Pd and Te atoms are included in all calculations (a)-(d).

plane. The preserved symmetry of the $\mathcal{M}_x$ mirror plane is evident in the symmetric behavior of the spin-integrated maps in Figs. 6.9(a) and 6.9(c) with respect to the $\mathcal{M}_x$ plane. Furthermore, the spin polarization maps in Figs. 6.9(b) and 6.9(d) obey the axial vector rules for the in-plane S_y spin component relative to the $\mathcal{M}_x$

mirror plane, such that $S_y(k_x, k_y) = -S_y(-k_x, k_y)$. One can also see flipping of the spin polarization between the structures in Fig. 6.9(b) and those in Fig. 6.9(d). This behavior is consistent with the sign reversal in the spin polarization observed in the band dispersion maps in Figs. 6.6(i) and 6.6(j), as well as the calculated spin-polarized map in Fig. 6.7(g). The observed spin polarization sign flip is also in agreement with the calculated spin-polarized momentum maps for the in-plane spin component S_y, as highlighted by the black frames in Figs. 6.10(b) and 6.10(d) where the spin-polarization sign flips between $E_{binding} = 0.1$ eV and $E_{binding} = 0.3$ eV.

On the other hand, Figs. 6.9(e)-(h) were measured using the *asymmetry geometry* depicted in Fig. 6.6(f), where the reaction plane is perpendicular to the crystal's $\mathcal{M}_y$ mirror plane. In this configuration, all symmetries of the mirror planes are broken by the incident light, as evidenced by the absence of any symmetry plane in all panels (e)-(h). However, in panels (f) and (h), the spin polarization still exhibits a tendency to follow the axial vector rules for the in-plane S_y spin component, but now with respect to the $\mathcal{M}_y$ mirror plane. This results in a relation where $S_y(k_x, k_y) \sim S_y(k_x, -k_y)$ at least with respect to the spin-polarization sign.

Focusing on the structure highlighted by the green frame in Fig. 6.10(b), a red spin-polarized feature can be observed sandwiched between two blue structures. This observation closely matches the measured spin-resolved map in Fig. 6.9(f), demonstrating the high resolution of the spin-ARPES apparatus. As the binding energy increases to $E_{binding} = 0.3$ eV, this red spin-polarized structure evolves and opens at its center, as depicted in Fig. 6.10(d). This is also in strong agreement with the measured spin-polarized map in Fig. 6.9(h). Spin-resolved ARPES for the S_x, S_y and S_z spin components for this structure can be found in Ref. [19].

6.3 Summary

In this chapter, we conducted a comprehensive investigation of the spin-resolved electronic structure of $PdTe_2$ over a wide range of energy and momentum, enabling the imaging of the topological ladder in $PdTe_2$. Particular attention was given to the observed asymmetric spin textures in comparison to the symmetric initial states. This research builds upon the observations made in Chapters 3 and 4, which focused on its sister compound, $PtTe_2$. The spin-resolved momentum maps revealed that, in symmetric geometries where the reaction plane coincides with a mirror plane of the crystal, the spin textures followed the expected symmetry rules. Under these conditions, the measured spin polarization demonstrated clear symmetric behavior relative to the preserved mirror plane, with the sign of spin polarization reversing for positive and negative k_x. These results align with theoretical predictions and previous observations in $PtTe_2$, confirming theoretically predicted spin textures of initial states.

However, significant deviations from this symmetry were observed when the experimental geometry was altered, such that the reaction plane no longer coincided with any of the crystal's mirror planes. In this asymmetric geometry, the spin-polarized momentum maps exhibited pronounced asymmetries, both in the positioning of features within the electronic structure and in the magnitude of the spin-polarization signal.

This chapter further demonstrated the similarity in the electronic structure of $PdTe_2$ and $PtTe_2$, both of which exhibit a trigonal structure in their bulk form. Additionally, it was shown that the valence band wavefunctions in $PdTe_2$ are strongly hybridized between Pd and Te sites. As a result, the observed asymmetries in the spin-polarized maps of $PdTe_2$ can be attributed to the same factors discussed in Chapter 4, namely intrinsic bulk asymmetries, non-equivalent atomic sites leading to phase shifts in reciprocal space, and scattering of hot photoemitted electrons on their way to the surface.

These findings underscore the critical influence of both the experimental setup and intrinsic material symmetries on the determination of the spin-polarized electronic structure in $PdTe_2$. The contrast between the symmetric initial states and the observed asymmetric spin textures offers valuable insights into the complexities of spin polarization in this material. These results emphasize the need for careful consideration of experimental geometries when investigating spin-dependent properties, which is crucial for advancing $PdTe_2$ and similar compounds in spintronic and quantum material applications.

7. Electronic structure of $PtSe_2$

$PtSe_2$ is a layered transition-metal dichalcogenide that crystallizes in the 1T-phase structure. Its crystal structure is analogous to that of $PtTe_2$, as described in Sec. 4.1, and exhibits a *3-fold* rotational symmetry about the c-axis in real space, which corresponds to a similar symmetry about the k_z axis in momentum space. Consequently, the surface of $PtSe_2$ features three mirror planes aligned along the $\overline{\Gamma M}$ directions in reciprocal space.

7.1 ARPES on bulk $PtSe_2$

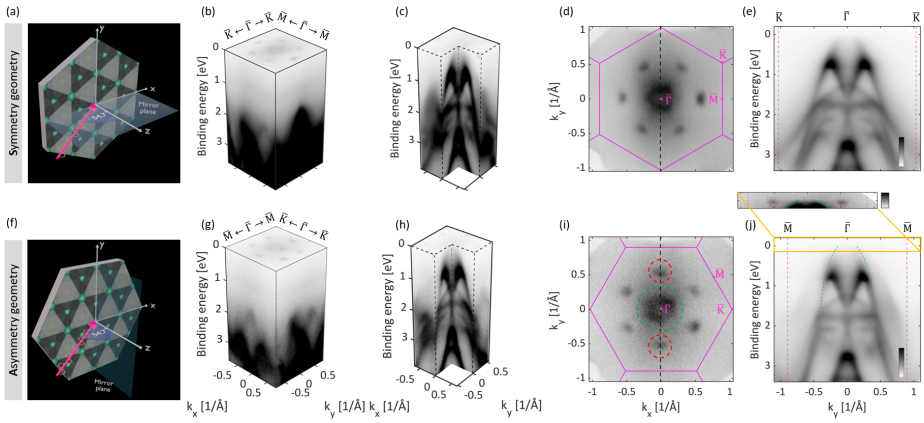

Figure 7.1: **Experimentally determined electronic band structure of $PtSe_2$.** *Upper panel*: (a)-(e) Results obtained using the *symmetry geometry* schematically shown in (a), in which one of the three mirror planes of bulk $PtSe_2$ was aligned such that the light beam impinged the sample within this plane, preserving the symmetry rules of this mirror plane. (b) ARPES 3D matrix data of $PtSe_2$. (c) Three quarters of (b) for better visualization of the band structure. (d) ARPES Fermi surface map of $PtSe_2$ ($E_F \pm 60$ meV). (e) In-plane energy-momentum dispersion $E(k_y)$ along the high symmetry direction in reciprocal space $\bar{\Gamma} - \bar{K}$, indicated by the black-dashed line in (d). (d),(e) Taken as cuts from the measured 3D-stack of data (b) at $E_{binding} = 0$ and at $k_x = 0$ respectively. *Lower panel*: (f)-(j) equivalent measurements, but measured as shown schematically in (f) where one of the three mirror planes of bulk $PtSe_2$ was aligned such that for the complete system of the sample and the incident light, no mirror plane symmetry remained. Electron and hole pockets are marked with red- and green-dashed circles as in (i), and highlighted as well in (j) and its inset. (Measurements were performed at room temperature, $h\nu = 107$ eV; p-polarized light: probing close to A-plane in the three dimensional Brillouin zone along the k_z-direction; see Notes 2 and 3).

An overview of ARPES measurements of $PtSe_2$ is provided in Fig. 7.1. The first set of measurements were conducted using the *symmetry geometry* as schematically depicted in Fig. 7.1(a), in which the sample was aligned such that the incident light beam coincided with one of the mirror planes of the crystal, preserving its symmetry rules. The data were acquired as a 3D matrix using p-polarized light with photon energy $h\nu = 107$ eV, as presented in Fig. 6.1(b). For better visualization of the band structure, part of the 3D data is visualized in Fig. 7.1(c). The Fermi surface map, representing a constant energy cut at $E_B = 0$, is shown in Fig. 7.1(d), and the energy-momentum map along the $\bar{\Gamma} - \bar{K}$ direction of the surface BZ is presented in Fig. 7.1(e), taken from Fig. 7.1(b) at $k_x = 0$ as indicated by the dashed-black line in Fig. 7.1(d). Lower panels (f)-(j) correspond to similar measurements as (a)-(e), but were obtained using the *asymmetry geometry* depicted in Fig. 6.1(f), where in this case the incident light breaks all mirror planes symmetries of the crystal surface, as discussed in Sec. 4.10. Figure 7.1(j) shows the band dispersion along the $\bar{\Gamma} - \bar{M}$ direction, taken as a cut from Fig. 6.1(g) at $k_x = 0$, as indicated by the dashed-black line in Fig. 7.1(i).

The ARPES Fermi surface maps in Figs. 7.1(d) and 7.1(i) exhibit distinct characteristics, including a hole pocket centered at the Brillouin zone and electron pockets located approximately midway along the $\bar{\Gamma} - \bar{M}$ direction. These features are highlighted by green and red dashed circles, respectively, in Fig. 7.1(i). Additional insights are provided in Fig. 7.1(j) and its inset, illustrating that the hole pocket crosses the Fermi level before reaching its apex, while the electron pockets are emphasized by concave-up red frames.

The band dispersion maps in Figs. 7.1(e) and 7.1(j) reveal several pronounced spectral features located at binding energies of approximately $E_b \sim 1.4$ eV, $E_b \sim 2.1$ eV, and $E_b \sim 2.7$ eV. These features are identified as surface states with negligible k_z dispersion, as evidenced by their insensitivity to variations in photon energy [145, 189]. The first two states merge into the bulk diffuse spectral weight near $k_{||} \sim 0$ and away from the Brillouin zone (BZ) center $\bar{\Gamma}$ at $k_{||} \gtrsim 0.5$. The third feature, attributed to a surface Dirac cone, displays distinct behavior compared to Dirac cones observed in $PtTe_2$ and $PdTe_2$, as discussed earlier in this thesis. Specifically, its upper legs bend away from $k_{||} = 0$ and avoid degeneracy with the surrounding bulk states. A more detailed representation of this behavior can be found in [19, 145, 189].

The higher electronegativity of selenium (Se) compared to tellurium (Te) strengthens the metal-chalcogen bonds, thereby diminishing the interlayer hopping in $PtSe_2$ relative to $PtTe_2$ and $PdTe_2$. As a result, the Se p_z-derived band exhibits a narrower bandwidth along the out-plane $\bar{\Gamma} - \bar{A}$ direction in reciprocal space. This reduction in bandwidth prevents the Se p_z-derived band from overlapping with the antibonding Se $p_{x,y}$-derived bands (see Fig. 4.11), thus inhibiting the formation of an inverted band gap above the Fermi level. Consequently, the topological surface states, which would reside within such a band gap, are absent along the $\bar{\Gamma} - \bar{M}$ direction in $PtSe_2$ [145]. This behavior contrasts with that observed in $PtTe_2$ and $PdTe_2$, discussed earlier in this thesis, and is linked to the topological ladder discussed in Sec. 4.5.

Figure 7.2 displays spin-resolved measurements from $PtSe_2$, conducted using unpolarized HeI light ($h\nu = 21.22$ eV), under two distinct experimental geometries. These geometries differ in the orientation of the reaction plane, as defined in Sec. 4.9, relative to the mirror planes of the crystal surface.

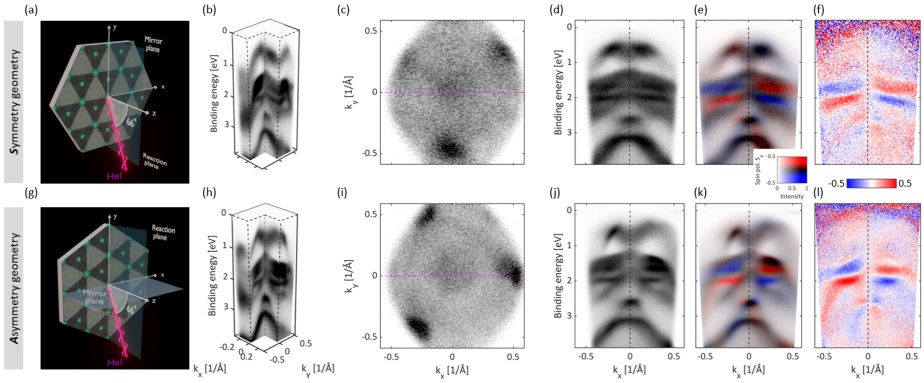

Figure 7.2: **Spin-resolved asymmetries of $PtSe_2$.** Upper panel: (a)-(f) Results obtained within the *symmetry geometry* schematically shown in (a) where the $\mathcal{M}_x$ mirror plane coincides with the reaction plane. (b) Spin-integrated experimental 3D data. (c) Corresponding Fermi surface map. (d) Energy-momentum band dispersion map $E(k_x)$, at $k_y = 0$. (e),(f) Corresponding spin-resolved energy dispersion maps, $E(k_x)$, measured using the lens deflector system probing along the x-axis perpendicular to $\mathcal{M}_x$ mirror plane, as defined in (a) and along the magenta-dashed line in (c), while the sample in normal emission. Lower panel: (g)-(l) Equivalent to (a)-(f) respectively, but measured using the *asymmetry geometry* schematically shown in (g) where the reaction plane is now perpendicular to the $\mathcal{M}_y$ mirror plane and the spin maps were filtered along the magenta line in (i) ***not*** perpendicular to any of the system's mirror planes. In (e) and (k) the intensity and spin-polarization are simultaneously displayed using the inset 2D color code shown in (e), where the false color scale refers to the in-plane spin polarization S_y in the ensemble of the photoemitted electrons. (f),(l) The corresponding pure in-plane S_y spin polarized maps. (Measurements were performed at room temperature using the unpolarized HeI radiation $h\nu = 21.22$ eV).

Figures 7.2(b)-(f) were measured using the *symmetry geometry* shown in Fig. 7.2(a), where the reaction plane coincides with one of the surface mirror planes, specifically $\mathcal{M}_x$. The spin-integrated energy-momentum map presented in Fig. 7.2(d) was measured along the magenta line in Fig. 7.2(c), perpendicular to $\mathcal{M}_x$. Panels (e) and (f) show the corresponding spin-resolved energy-momentum maps for the in-plane spin component S_y. In Fig. 7.2(e), both photoemission intensity and spin polarization are represented using a 2D color code (see inset), while Fig. 7.2(f) depicts only the spin polarization. Figures 7.2(g)-(l) present equivalent measurements, but taken using the *asymmetry geometry* depicted in Fig. 7.2(g), where the reaction plane is perpendicular to another mirror plane, $\mathcal{M}_y$.

Consistent with the spin-integrated and spin-resolved experimental results obtained from the sister compounds $PtTe_2$ (see Sec. 5.1) and $PdTe_2$ (see Sec. 6.2), the energy-momentum maps shown in Figs. 7.2(d)-(f) exhibit symmetry with respect to the $k_x = 0$ line. In contrast, the maps in Figs. 7.2(j)-(l) are asymmetric.

7.2 Summary

Continuing our spin-resolved study of the topological ladder in the band structure of 1T-phase transition-metal dichalcogenides, this chapter visualizes the topological ladder of $PtSe_2$. Using the same methodologies previously applied to its sister compounds, $PtTe_2$ and $PdTe_2$, we employed both *symmetry* and *asymmetry geometries*. Consistent with previous findings, spin-integrated and spin-resolved $E(k_x)$ maps exhibit symmetric behavior, reflecting the preserved mirror plane of the sample surface. However, when the reaction plane does not coincide with any of the sample surface mirror planes, a highly asymmetric spin texture of the topological ladder emerges.

Due to the similarities in the band structure of $PtSe_2$ with $PtTe_2$ and $PdTe_2$, we attribute the observed asymmetries in the spin-polarized maps of $PtSe_2$ to the same factors discussed in Chapters 4 and 5.

Despite its trigonal structure in bulk form, similar to $PtTe_2$ and $PdTe_2$, the high electronegativity of selenium (Se) prevents the formation of an inverted band gap above the Fermi level. As a result, Fermi-crossing topological surface states are absent, unlike in $PtTe_2$ and $PdTe_2$, where these states are strongly spin-polarized.

8. Conclusion

This thesis presents an in-depth investigation into the spin-resolved electronic structure of $PtTe_2$, a type-II Dirac semimetal with a complex *topological ladder* of surface states. Utilizing high-resolution spin-ARPES, we have examined the complex interplay between initial-state properties and final-state effects in photoemission experiments. These final-state effects, arising from various experimental interactions, pose significant challenges in spin-ARPES by altering the intrinsic spin polarization of emitted electrons. Distinguishing these effects is essential for accurate characterization of material properties.

In this work, we systematically examined the manifestation of these effects by varying experimental geometries and comparing results to theoretical calculations. Specifically, we demonstrated that spin asymmetries may arise from interatomic interference due to non-equivalent atomic sites, scattering events, and light-induced asymmetries, all of which can be mistakenly attributed to intrinsic spin polarization.

Our findings confirm that $PtTe_2$ exhibits strong spin-momentum locking within its *topological ladder*, where the spin polarization of surface states evolves as a result of both intrinsic and extrinsic factors. The observed spin-resolved band dispersion and momentum maps support the idea that spin-orbit coupling and crystal symmetry govern the formation of spin textures. Additionally, we extended our analysis to $PdTe_2$ and $PtSe_2$, revealing similar spin polarization and topological surface state behavior, suggesting that the methodologies developed here can be applied to a broader range of spintronic materials.

An important aspect of this work is the necessity to span large energy-momentum and momentum-momentum regions in spin-resolved measurements. The spin textures extracted from these measurements contribute directly to the Bloch wavefunctions, which describe the quantum states of electrons in a crystal. These Bloch wavefunctions, in turn, play a crucial role in transport applications, where spin-polarized currents must be accurately modeled and controlled. The ability to map spin states across an extensive momentum space ensures a more complete understanding of spin-momentum coupling, which is essential for optimizing materials in spintronic devices. Without a comprehensive mapping, the extracted spin textures may be incomplete, leading to uncertainties in predicting material behavior in transport experiments.

Beyond its implications for fundamental condensed matter physics, this work has direct relevance to the advancement of spintronic devices, where control over spin-polarized currents is essential for energy-efficient information processing. The ability to precisely manipulate and understand spin textures in materials like $PtTe_2$ paves the way for their potential integration into next-generation quantum technologies, including spin-orbit torque (SOT) applications. The insights gained here provide a valuable reference for future studies exploring spin-polarized transport and novel

quantum phases in materials with strong SOC.

In conclusion, this thesis has provided a deeper understanding of the electronic properties of $PtTe_2$ and related materials, highlighting the role of final-state effects in spin-resolved photoemission experiments. By carefully distinguishing intrinsic spin textures from extrinsic influences, we have established a more reliable framework for analyzing spin-polarized states in SOC materials. Expanding the energy-momentum coverage in spin-resolved measurements has proven essential for accurately capturing Bloch wavefunctions, which are directly relevant for transport applications. The insights gained here contribute to the broader study of spintronic materials and may help guide future efforts in designing more efficient spin-based devices.

9. Outlook

Following the same methodology used in studying spin-ARPES from $PtTe_2$, Fig. 9.1 presents circular dichroic angle-resolved photoemission (CD-ARPES) maps from $PtTe_2$. The *CD signal* is defined as

$$CD = \frac{I_{\mathrm{LCP}} - I_{\mathrm{RCP}}}{I_{\mathrm{LCP}} + I_{\mathrm{RCP}}},$$

where I_{LCP} and I_{RCP} are the photoemission intensities measured using left- and right-circularly polarized light, respectively. This normalized definition accounts for variations in total intensity.

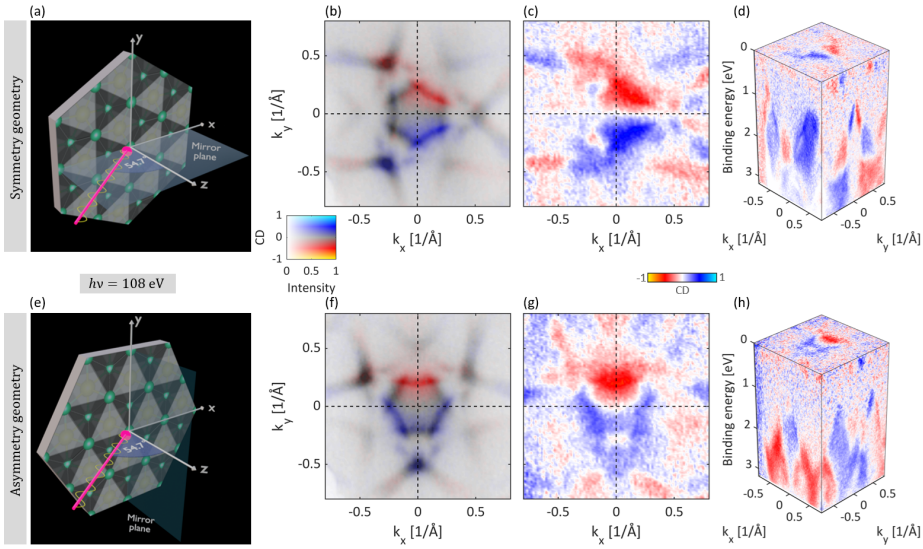

Figure 9.1: **Experimental Fermi-surface CD-ARPES from $PtTe_2$.** (a) *Symmetry geometry* where the reaction plane coincides with the mirror plane $\mathcal{M}_y$ of the sample surface. (b) Fermi surface CD-ARPES map, plotted using the colormap shown in the left inset. (c) Corresponding CD magnitude, plotted according to the colormap in the right inset. (d) 3D CD-ARPES data from which (b) and (c) are extracted. (e)-(h) Equivalent measurements performed in the *asymmetry geometry*, where the reaction plane is perpendicular to the mirror plane $\mathcal{M}_x$, as depicted in (e). Photon energy $h\mu = 108$ eV used for all measurements.

Figures 9.1(a)-(d) show CD maps from $PtTe_2$ measured using the *symmetry geometry*, visualized in (a), where the reaction plane coincides with the $\mathcal{M}_y$ mirror plane of the sample surface. Figure 9.1(b) presents the CD Fermi surface map,

displayed using the 2D colormap provided in the left inset. Panel (c) represents the absolute CD signal from (b), plotted according to the colormap in the right inset. Both panels (b) and (c) are taken as cuts from (d) at $E_B = 0$ eV, and they exhibit odd symmetry with respect to k_y, as the mirror plane $\mathcal{M}_y$ is preserved.

Figures 9.1(e)-(h) show equivalent CD maps from $PtTe_2$, but measured using the *asymmetry geometry*, visualized in (e), where the reaction plane is perpendicular to the $\mathcal{M}_x$ mirror plane of the sample surface. Using this geometry, all mirror symmetries of the crystal are broken, and consequently, the CD-ARPES maps in panels (f) and (g) are not symmetric. Specifically, the CD signal is no longer odd with respect to the $\mathcal{M}_x$ mirror plane.

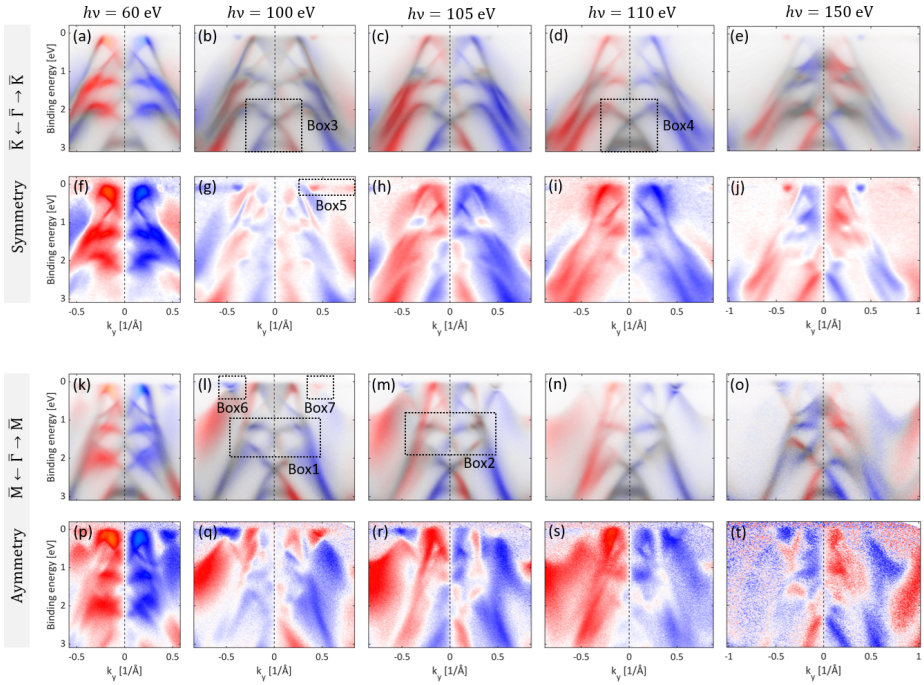

Figure 9.2: **Experimental $E(k_y)$ CD-ARPES from $PtTe_2$.** (a)-(f) CD-ARPES energy-momentum maps along $\bar{\Gamma}$-$\bar{K}$ reciprocal direction, plotted using the 2D colormap from Fig. 9.1, and measured using the *symmetry geometry* visualized in Fig. 9.1(a). (g)-(l) Corresponding CD magnitude maps according to the colormap from Fig. 9.1. (m)-(x) Same, but probed along the $\bar{\Gamma}$-$\bar{M}$ reciprocal direction and measured using the *asymmetry geometry* shown in Fig. 9.1(e). Spectra taken at $\sim$ 40K. Features indicated by boxes 1 to 5 in (b),(d),(h) and (n) are discussed in the text.

Energy-momentum CD maps from $PtTe_2$ are shown in Figs. 9.2(a)-(t). Panels (a)-(j) were measured using the *symmetry geometry* shown in Fig. 9.1(a), where panels (a)-(e) are plotted using the 2D colormap, while panels (f)-(j) show the corresponding absolute CD signal, each measured using the indicated photon energy. In all panels (a)-(j), conservation of the $\mathcal{M}_y$ mirror plane is demonstrated by the symmetric odd CD signal in k_y. On the other hand, panels (k)-(t) were measured using the *asymmetry geometry* shown in Fig. 9.1(e). The demonstration of the resultant asymmetries in CD is indicated, for example, by Box1 in (l) and Box2 in (m), where

both the CD sign and the energy positions of bands are asymmetric for $\pm k_y$. These observations confirm the asymmetries shown in Figs. 9.1(f)-(g). These asymmetries originate primarily from interatomic interferences [46], as detailed in Sec. 5.12.1, and asymmetric multiple scattering, as discussed in Sec. 5.12.2. Additionally, the trigonal symmetry of the bulk band structure, in connection with approximate $k_\perp$ sensitivity of ARPES, may also contribute to these effects, as elaborated in Sec. 4.10.

As extensively analyzed in this thesis, $PtTe_2$ exhibits a surface Dirac cone that is part of the *topological ladder* centered at $\bar{\Gamma}$ at $E_B \sim 2.3$ eV, as indicated by Box3 in panel (b) and Box4 in panel (d). This Dirac cone exhibits pronounced spin polarization and spin-momentum locking, resulting in two branches with opposite spin polarization, as confirmed by our spin-resolved measurements and corroborated by the theoretical calculations presented in Sec. 5.10. Previous studies have suggested that CD-ARPES can serve as a potential probe for spin-momentum locking in topological insulators [190, 191]. However, this behavior is not observed in our experiments. Specifically, in Box3, for positive k_y, both upper and lower branches of the Dirac cone exhibit the same CD sign, and in Box4, the CD signal is nearly absent.

A comparison of panels (a)-(e) with (f)-(j), and (k)-(o) with (p)-(t), reveals that a non-vanishing CD signal is also present in regions corresponding to projected band structure gaps. As exemplified by Box5 in Fig. 9.2(g), a flat CD-ARPES feature emerges at the Fermi level, where inelastic scattering effects are expected to be minimal.

The projected band structure consists of overlapping continuous regions in energy-momentum space, which typically originate from a specific type of orbital [192]. As a result, distinct regions within the projected band structure can exhibit different CD responses. This phenomenon is illustrated in Box6 and Box7 of Fig. 9.2(l), where the topological surface states, located within the projected bulk gap (see Fig. 4.6(c)), display a CD sign opposite to that of the surrounding projected bands. A similar behavior is observed for the small electron pockets crossing the Fermi level along the $\bar{\Gamma}$-$\bar{K}$ direction, see Fig. 9.2(j).

A promising direction for future research involves integrating spin-resolved measurements with circular dichroism to further probe spin textures in $PtTe_2$ and related materials. While CD-ARPES has provided valuable insights into electronic states and symmetry properties, its ability to reveal spin-momentum locking remains debated. The lack of a clear correlation between CD signals and spin polarization in our experiments suggests that spin-resolved CD-ARPES could help disentangle intrinsic spin properties from extrinsic influences. Future studies could refine experimental methodologies by optimizing photon energy, sample orientation, or detector configurations to enhance sensitivity to spin-dependent effects. Extending such investigations to other transition metal dichalcogenides may uncover new topological and spintronic functionalities, contributing to the broader understanding of spin-orbit interactions in condensed matter physics. Furthermore, the integration of spin-resolved CD-ARPES with advanced theoretical modeling could provide a more comprehensive picture of orbital contributions, potentially leading to the discovery of novel materials with engineered spin textures for next-generation spintronic applications.

Appendix A

Tight binding model

In Sec. 2.1 we looked at the band structure through the free-electron and the nearly-free electron point of view, which would fit more the metallic case where the electronic states are highly delocalized. In this section I will introduce another important method called *tight binding model* that is highly used in describing mostly the electronic structure of insulators and the electronic bands arising from the partially filled heavy d-shells of the transition metal atoms [53, 54]. Within the frame of this model, the potential is large such that electrons spend most of their time bound to the ionic cores and rarely hope from atom to another. To describe the system one can divide the crystal Hamiltonian $\mathcal{H}$ into atomic Hamiltonian $\mathcal{H}_{at}$ and the remaining all other potentials

$$\mathcal{H} = \mathcal{H}_{at} + \Delta U(\boldsymbol{r}) \tag{A.1}$$

If $\phi_n(\boldsymbol{r})$ is an atomic wavefunction, $\mathcal{H}_{at}\phi_n(\boldsymbol{r}) = E_n\phi_n(\boldsymbol{r})$, then an approximate Bloch shaped normalized wavefunction, equivalent to Eq. 2.1, for one electron in the whole crystal can be taken as a linear combination of these atomic wavefunctions[1][2]

$$\psi_{n\boldsymbol{k}}(\boldsymbol{r}) = \frac{1}{\sqrt{N}} \sum_{\boldsymbol{R}} e^{i\boldsymbol{k}\cdot\boldsymbol{R}} \phi_{n\boldsymbol{k}}(\boldsymbol{r} - \boldsymbol{R}) \tag{A.2}$$

where $\boldsymbol{R}$ is a real space translation vector of the crystal and the sum runs over all N lattice sites. The heart assumptions of this model are, close to a lattice site $\mathcal{H} \sim \mathcal{H}_{at}$, and the atomic orbitals are highly localized such that $\phi_n(\boldsymbol{r})$ decays exponentially away from the lattice site, hence, $\Delta U(\boldsymbol{r}) \to 0$ at the centre of each atom in the crystal. This makes $\phi_n(\boldsymbol{r})$ a good approximation for a crystal stationary state [193]. To illustrate this picture we consider the simplest example of one-site per unit cell contributing with the non-degenerate s-orbital $\phi_s(\boldsymbol{r})$ to the crystal structure, hence, a single s-orbital character band $n = 1$ is expected. The energy dispersion inside the crystal $\mathcal{E}(\boldsymbol{k})$ is then given by finding the expectation value of $\mathcal{H}$

[1] Hence, it is also known by the (linear combination of atomic orbitals) approximation LCAO.

[2] A more accurate treatment would require writing the crystal wave function $\psi_{n\boldsymbol{k}}(\boldsymbol{r})$ as a linear combination of functions Θ that are *not* precisely atomic orbitals but can be expanded in relatively small number of atomic orbitals $\psi_{n\boldsymbol{k}}(\boldsymbol{r}) = \sum_{\boldsymbol{R}} e^{i\boldsymbol{k}\cdot\boldsymbol{R}}\Theta_{n\boldsymbol{k}}(\boldsymbol{r} - \boldsymbol{R}); \Theta(\boldsymbol{r}) = \sum_m C_m\phi_m(\boldsymbol{r})$. This will produce a dispersion relation for a single s-orbital case given by $\mathcal{E}(\boldsymbol{k}) = E_s - \frac{\beta + \sum_{\boldsymbol{\delta}=n.n} e^{i\boldsymbol{k}\cdot\boldsymbol{\delta}}\boldsymbol{\gamma}(\delta)}{1 + \sum_{\boldsymbol{\delta}=n.n} e^{i\boldsymbol{k}\cdot\boldsymbol{\delta}}\boldsymbol{\alpha}(\delta)}$ where $\boldsymbol{\alpha}(\delta) = \langle\phi(\boldsymbol{r})|\phi(\boldsymbol{r} - \boldsymbol{R})\rangle$ and usually the term containing it is neglected due to its small magnitude [54], while β= I-labeled term in the context which is also neglected, to end up with similar dispersion as Eq. A.3.

$$
\begin{aligned}
\mathcal{E}(\boldsymbol{k}) &= \langle \psi_{\boldsymbol{k}}(\boldsymbol{r})|\mathcal{H}|\psi_{\boldsymbol{k}}(\boldsymbol{r})\rangle \\
&= \frac{1}{\sqrt{N}}\cdot\frac{1}{\sqrt{N}}\sum_{\boldsymbol{R}}\sum_{\boldsymbol{R}'} e^{i\boldsymbol{k}\cdot(\boldsymbol{R}'-\boldsymbol{R})}\langle\phi_s(\boldsymbol{r}-\boldsymbol{R})|\mathcal{H}|\phi_s(\boldsymbol{r}-\boldsymbol{R}')\rangle \\
&= \frac{1}{N}\sum_{\boldsymbol{R}}\sum_{\boldsymbol{R}'} e^{i\boldsymbol{k}\cdot(\boldsymbol{R}'-\boldsymbol{R})}\langle\phi_s(\boldsymbol{r})|\mathcal{H}|\phi_s(\boldsymbol{r}-(\boldsymbol{R}'-\boldsymbol{R}))\rangle \\
&= \sum_{\boldsymbol{R}''} e^{i\boldsymbol{k}\cdot\boldsymbol{R}''}\langle\phi_s(\boldsymbol{r})|\mathcal{H}|\phi_s(\boldsymbol{r}-\boldsymbol{R}'')\rangle \\
&= E_s + \underbrace{\langle\phi_s(\boldsymbol{r})|\Delta U|\phi_s(\boldsymbol{r})\rangle}_{\text{I}} + \ldots \\
&\sum_{\boldsymbol{R}''\neq 0} e^{i\boldsymbol{k}\cdot\boldsymbol{R}''}\Big(\underbrace{\langle\phi_s(\boldsymbol{r})|\mathcal{H}_{at}|\phi_s(\boldsymbol{r}-\boldsymbol{R}'')\rangle}_{\text{II}} + \underbrace{\langle\phi_s(\boldsymbol{r})|\Delta U|\phi_s(\boldsymbol{r}-\boldsymbol{R}'')\rangle}_{\text{III}}\Big) \\
&\approx E_s + \sum_{\boldsymbol{R}''=\boldsymbol{\delta}=n.n} e^{i\boldsymbol{k}\cdot\boldsymbol{R}''}\underbrace{\langle\phi_s(\boldsymbol{r})|\mathcal{H}_{at}|\phi_s(\boldsymbol{r}-\boldsymbol{R}'')\rangle}_{-\boldsymbol{\gamma}(\delta)} \\
&= E_s - \sum_{\boldsymbol{\delta}=n.n} e^{i\boldsymbol{k}\cdot\boldsymbol{\delta}}\boldsymbol{\gamma}(\delta)
\end{aligned}
\tag{A.3}
$$

In the 4^{th} line the translation vector $\boldsymbol{R}''=\boldsymbol{R}'-\boldsymbol{R}$ is used, hence, the sum over $\boldsymbol{R}$ contributes by N terms. The sum over lattice sites has been separated into $\boldsymbol{R}''=0$ case which produced the onsite energies E_s and the I-labeled term that can be neglected because it is a product of two atomic wavefunctions on the same site with a potential that goes to zero at that site. The other case is for $\boldsymbol{R}''\neq 0$ that produces a term labeled II requiring multiplication of atomic orbitals on different lattice sites, and due to the exponentially decaying nature of the atomic orbitals as indicated before, the sum is typically limited just up to *near neighbors* ($\boldsymbol{\delta}=n.n$) as shown in the 6^{th} and 7^{th} equalities, additionally, it produces the III-labeled term which can also be neglected due to a combination of the reasons explained for the I- and II- labeled terms. Most importantly, is the $\boldsymbol{\gamma}(\delta)$ term in the last two equalities which gives an indication for the hopping energy needed for an electron to jump from lattice site into its neighboring site (hopping matrix element).

A.1 Chain of s-orbitals

To illustrate this, we can imagine a *chain* of atoms with only a single *s*-orbital per site and one site pet unit cell as shown in Fig. A.1 (a). Then, there are *two* nearest neighbors such that $\boldsymbol{\delta}$ in Eq. A.3 will be given by $\boldsymbol{\delta}=\pm a\hat{x}$, where a is the lattice constant, and the crystal band dispersion becomes

$$
\begin{aligned}
\mathcal{E}(\boldsymbol{k}) &= E_s - \sum_{\boldsymbol{\delta}=\{a\hat{x},-a\hat{x}\}} e^{i\boldsymbol{k}\cdot\boldsymbol{\delta}}\boldsymbol{\gamma}(\delta) = E_s - (e^{i\boldsymbol{k}\cdot a\hat{x}} + e^{-i\boldsymbol{k}\cdot a\hat{x}})\boldsymbol{\gamma}(a) \\
&= E_s - 2\boldsymbol{\gamma}(a)\left(\frac{e^{ik_x a}+e^{-ik_x a}}{2}\right) = E_s - 2\boldsymbol{\gamma}(a)cos(k_x a)
\end{aligned}
\tag{A.4}
$$

A plot of this cosine band dispersion $\mathcal{E}(\boldsymbol{k})$ is shown in Fig. A.1 (b) with the *bandwidth*, $4\boldsymbol{\gamma}$, also marker which is defined as the difference between the maximum

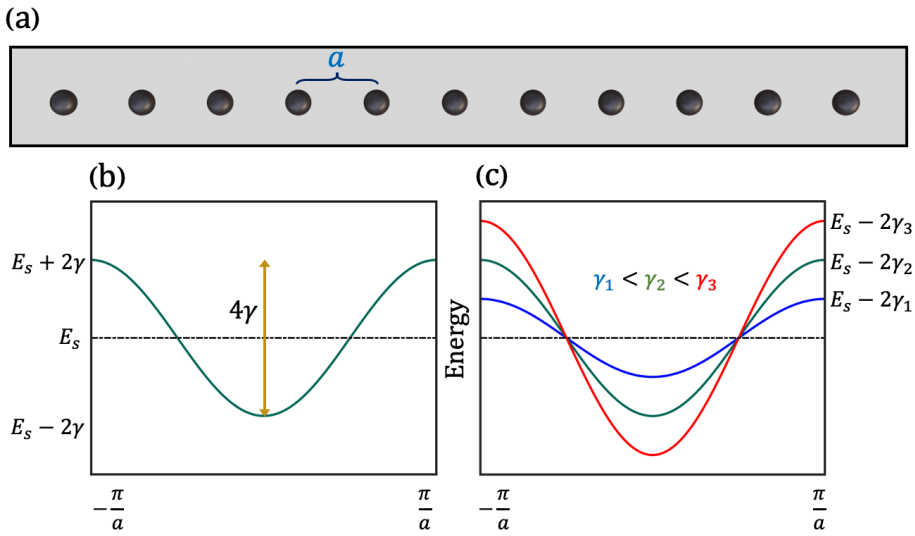

Figure A.1: **Tight binding model for 1D lattice with a single *s*-orbital per site.** (a) Shows a chain of atoms with a single s-orbital per site, and a lattice constant a. (b) The cosine shaped band dispersion $\mathcal{E}(\boldsymbol{k})$ showing the *bandwidth*, $4\boldsymbol{\gamma}$, plotted over a complete reciprocal space unit cell. (c) $\mathcal{E}(\boldsymbol{k})$ plotted for different values of the hopping matrix element (overlap integral) $\boldsymbol{\gamma}$.

and minimum of the band either sides of the onsite energy E_s. The band spreads out from the *s*-orbital and its energy E_s due to the hopping between adjacent sites. One can see also in Fig. A.1 (c) that reducing the hopping matrix element, $\boldsymbol{\gamma}$, decreases the *bandwidth* of the band (*red* $\rightarrow$ *blue*) and if $\boldsymbol{\gamma}$ is reduced totally to zero the band flattens into completely localized *s*-orbitals with energies all equal to E_s independent of k_x.

A.2 2D crystal of s-orbitals

In the case of *square* lattice with again single s-orbital per site as shown in Fig. A.2 (a) (upper panel), there will be *four* nearest neighbors (pink-colored sites surrounding the red-colored site) such that $\boldsymbol{\delta}= \{\pm a\hat{x}, \pm a\hat{y}\}$ and the dispersion relation Eq. A.3 becomes

$$\begin{aligned}\mathcal{E}(\boldsymbol{k}) &= E_s - \sum_{\boldsymbol{\delta}=\{a\hat{x},-a\hat{x},a\hat{y},-a\hat{y}\}} e^{i\boldsymbol{k}\cdot\boldsymbol{\delta}}\boldsymbol{\gamma}(\delta) = E_s - (e^{i\boldsymbol{k}\cdot a\hat{x}} + e^{-i\boldsymbol{k}\cdot a\hat{x}} + e^{i\boldsymbol{k}\cdot a\hat{y}} + e^{-i\boldsymbol{k}\cdot a\hat{y}})\boldsymbol{\gamma}(a) \\ &= E_s - 2\boldsymbol{\gamma}(a)\left\{\left(\frac{e^{ik_x a} + e^{-ik_x a}}{2}\right) + \left(\frac{e^{ik_y a} + e^{-ik_y a}}{2}\right)\right\} \\ &= E_s - 2\boldsymbol{\gamma}(a)\Big\{cos(k_x a) + cos(k_y a)\Big\} \end{aligned} \tag{A.5}$$

A 3D visualization, a top view, as well as $\mathcal{E}(k_x)$ of the band dispersion are shown in Fig. A.2 (a) (lower panel) with the colorbar indicating the different energy values. One can note the concave up shape of the 3D band dispersion representing a minimum energy of $E_s - 4\boldsymbol{\gamma}(a)$ via substituting (k_x,k_y)=(0,0) in Eq. A.5.

This picture can also be extended to include the second nearest neighbors, as indicated by the blue-colored sites in Fig. A.2 (b) (upper panel), so $\boldsymbol{\delta}=\{\pm a\hat{x}, \pm a\hat{y}, \pm a\hat{x}\pm a\hat{y}\}$

$$
\begin{aligned}
\mathcal{E}(\boldsymbol{k}) &= E_s - \sum_{\boldsymbol{\delta}=\{\pm a\hat{x},\pm a\hat{y},\pm a\hat{x}\pm a\hat{y}\}} e^{i\boldsymbol{k}\cdot\boldsymbol{\delta}}\boldsymbol{\gamma}(\delta) \\
&= E_s - \boldsymbol{\gamma}(a)(e^{i\boldsymbol{k}\cdot a\hat{x}} + e^{-i\boldsymbol{k}\cdot a\hat{x}} + e^{i\boldsymbol{k}\cdot a\hat{y}} + e^{-i\boldsymbol{k}\cdot a\hat{y}}) + ... \\
&\quad - \boldsymbol{\gamma}(a\sqrt{2})(e^{i\boldsymbol{k}\cdot(a\hat{x}+a\hat{y})} + e^{i\boldsymbol{k}\cdot(-a\hat{x}+a\hat{y})} + e^{i\boldsymbol{k}\cdot(-a\hat{x}-a\hat{y})} + e^{i\boldsymbol{k}\cdot(a\hat{x}-a\hat{y})}) \\
&= E_s - 2\boldsymbol{\gamma}(a)\Big\{cos(k_x a) + cos(k_y a)\Big\} + ... \\
&\quad - \boldsymbol{\gamma}(a\sqrt{2})\Big\{e^{ik_y a}\Big(e^{ik_x a} + e^{-ik_x a}\Big) + e^{-ik_y a}\Big(e^{ik_x a} + e^{-ik_x a}\Big)\Big\} \\
&= E_s - 2\boldsymbol{\gamma}(a)\Big\{cos(k_x a) + cos(k_y a)\Big\} + ... \\
&\quad - \boldsymbol{\gamma}(a\sqrt{2})\Big\{4\Big(\frac{e^{ik_x a} + e^{-ik_x a}}{2}\Big)\Big(\frac{e^{ik_y a} + e^{-ik_y a}}{2}\Big)\Big\} \\
&= E_s - 2\boldsymbol{\gamma}(a)\Big\{cos(k_x a) + cos(k_y a)\Big\} - 4\boldsymbol{\gamma}(a\sqrt{2})\Big\{cos(k_x a)cos(k_y a)\Big\} \qquad \text{(A.6)}
\end{aligned}
$$

Again the 3D visualization, a top view, as well as $\mathcal{E}(k_x)$ of the band dispersion are plotted in the lower panel of Fig. A.2 (b). Now the minimum of the band is *deeper* in energy and is given from Eq. A.6 by $\Big\{E_s - 4\boldsymbol{\gamma}(a) - 4\boldsymbol{\gamma}(a\sqrt{2})\Big\}$.

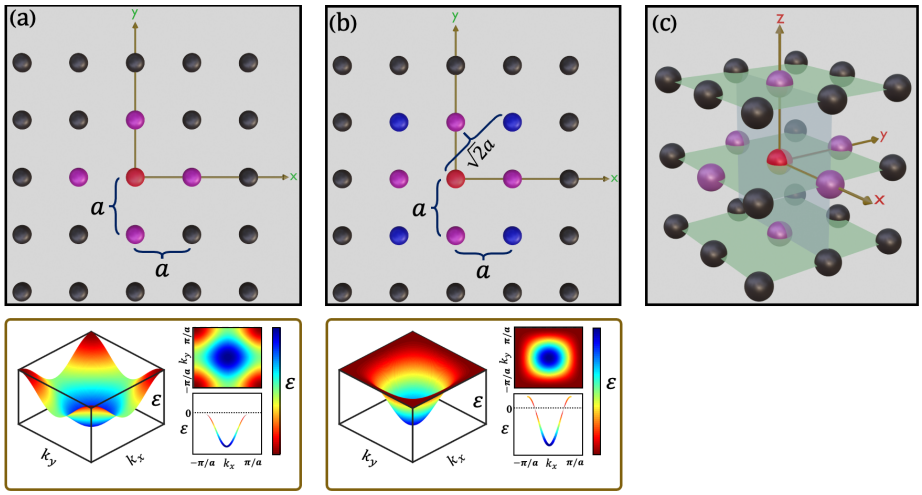

Figure A.2: **Tight binding model for 2D and 3D lattices with a single *s*-orbital per site.** (a) (upper panel): square lattice with a single *s*-orbital per site with a lattice constant a, and the corresponding tight binding 3D, top view and $\mathcal{E}(k_x)$ of the energy dispersion are shown in the (lower panel) where only nearest neighbors represented as pink-colored sites are included. Upper and lower panels in (b) are similar to (a) but second nearest neighbors marked with blue color are included as well in the model. (c) Real space 3D lattice with six nearest neighbors marked with pink color. Colorbars represent energy scales.

A.3 3D crystal of s-orbitals

The method can also be generalized for the 3D lattice case as illustrated in Fig. A.2 (c). However, now it is not trivial to visualize the 4D space of $\mathcal{E}(k_x, k_y, k_z)$, but this still can be visualized for any desired k_z value which will reduce the energy dispersion relation into a similar dispersion to Eq. A.5.

$$\begin{aligned}\mathcal{E}(\boldsymbol{k}) &= E_s - \sum_{\boldsymbol{\delta}=\{\pm a\hat{x},\pm a\hat{y},\pm a\hat{z}\}} e^{i\boldsymbol{k}\cdot\boldsymbol{\delta}}\boldsymbol{\gamma}(\delta) \\ &= E_s - \boldsymbol{\gamma}(a)(e^{i\boldsymbol{k}\cdot a\hat{x}} + e^{-i\boldsymbol{k}\cdot a\hat{x}} + e^{i\boldsymbol{k}\cdot a\hat{y}} + e^{-i\boldsymbol{k}\cdot a\hat{y}} + e^{i\boldsymbol{k}\cdot a\hat{z}} + e^{-i\boldsymbol{k}\cdot a\hat{z}}) \\ &= E_s - 2\boldsymbol{\gamma}(a)\Big\{cos(k_x a) + cos(k_y a) + cos(k_z a)\Big\} \end{aligned} \tag{A.7}$$

A.4 Multi atoms/orbitals per unit cell

In reality, materials will have more than one atom per unit cell, and each atom will contribute with more than one atomic orbital into the band structure. Even though, the problem is still solvable through defining a Bloch wavefunction like [194]

$$\Phi_{\boldsymbol{k}}^{(j\alpha)}(\boldsymbol{r}) = \frac{1}{\sqrt{N}}\sum_{\boldsymbol{R}_j} e^{i\boldsymbol{k}\cdot\boldsymbol{R}_j}\phi_\alpha(\boldsymbol{r}-\boldsymbol{R}_j) \tag{A.8}$$

where j=A,B,C ... represent the different atomic sites per unit cell, $\boldsymbol{R}_j$ are the translation vectors that run over all lattice sites of type j, and $\alpha = s, p_x, p_y, p_z$ ... are the atomic orbitals. Therefore, $\Phi_{\boldsymbol{k}}^{(j\alpha)}$ will represent a linear combination of the α^{th} atomic orbitals on site j. Now, the crystal momentum wavefunction will be a linear combination of these Bloch wavefunctions summed over all different atomic sites j's per unit cell and over all α's atomic orbitals per site j, so

$$\psi_{n\boldsymbol{k}}(\boldsymbol{r}) = \sum_\alpha \sum_j c_{\boldsymbol{k}}^{(j\alpha)}\Phi_{\boldsymbol{k}}^{(j\alpha)}(\boldsymbol{r}) \tag{A.9}$$

Using the variation theorem, the ground state of the system is achieved via minimizing the expectation value of the energy with respect to the basis set coefficients $c_{\boldsymbol{k}}^{(j\alpha)}$, which will form a system of simultaneous linear equations of the form $\Big\{\mathcal{H}_{(i\alpha)(j\beta)} - \mathcal{E}(\boldsymbol{k})S_{(i\alpha)(j\beta)}c_{\boldsymbol{k}}^{(j\alpha)}\Big\} = 0$, where $\mathcal{H}_{(i\alpha)(j\beta)} = \langle\Phi_{\boldsymbol{k}}^{(i\alpha)}|\Phi_{\boldsymbol{k}}^{(j\beta)}\rangle$. This will have a non-trivial solution if the corresponding secular determinant is zero [195, 196]

$$|\boldsymbol{\mathcal{H}} - \mathcal{E}(\boldsymbol{k})\boldsymbol{S}| \approx |\boldsymbol{\mathcal{H}} - \mathcal{E}(\boldsymbol{k})\boldsymbol{I}| = 0 \tag{A.10}$$

Here, $\boldsymbol{\mathcal{H}}$ is the energy matrix of elements $\mathcal{H}_{(i\alpha)(j\beta)}$, $\boldsymbol{I}$ is the identity matrix, and $\boldsymbol{S}$ is the overlap matrix of elements $S_{(i\alpha)(j\beta)}$, where

$$S_{(i\alpha)(j\beta)} = \begin{cases} \delta_{(ij)}\delta_{(\alpha\beta)} & \text{orthogonality of atomic orbitals on same site.} \\ \sim 0 & \text{well-separated orbitals on different sites (origin of} \approx) \\ & \text{as explained in note 2.} \end{cases}$$

A simple but non-trivial example that is enough to examine how to proceed in this situation, is to have two different atomic sites per unit cell with 1s-orbital on

one site and $2p_x$-orbital on the other as illustrated in Fig. A.3. This will require solving the following 2×2 secular determinant[3]

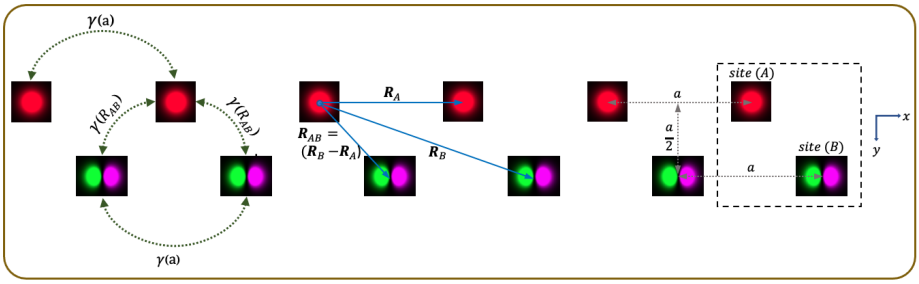

Figure A.3: **Tight binding model for two different atomic sites per unit cell with a single atomic orbital per site.** A theoretical model showing two different atomic sites pet unit cell, that is denoted by the dashed square, with $1s$-orbital on site (A) and $2p_x$-orbital on site (B). The $1s$-orbitals as well as $2p_x$-orbitals are separated by the lattice constant a along the x-direction. $\boldsymbol{R}_A$ and $\boldsymbol{R}_B$ represent the translation vectors that run over the lattice sites (A) and (B) respectively, wile $\boldsymbol{R}_{AB}$ are the translation vectors that connect both sites. $\boldsymbol{\gamma}(a)$, $\boldsymbol{\gamma}(b)$ are the hopping matrix elements between $1s$-orbitals and $2p_x$-orbitals respectively, while $\boldsymbol{\gamma}(R_{AB})$ refer for the hopping between $1s$- and $2p_x$-orbitals.

$$\begin{vmatrix} \mathcal{H}_{(A_{1s})(A_{1s})} - \mathcal{E}(\boldsymbol{k}) & \mathcal{H}_{(A_{1s})(B_{2p_x})} \\ \mathcal{H}_{(B_{2p_x})(A_{1s})} & \mathcal{H}_{(B_{2p_x})(B_{2p_x})} - \mathcal{E}(\boldsymbol{k}) \end{vmatrix} = 0 \tag{A.11}$$

that leads to the following band dispersion

$$\mathcal{E}(\boldsymbol{k}) = -\frac{1}{2}\Big(\mathcal{H}_{(A_{1s})(A_{1s})}+\mathcal{H}_{(B_{2p_x})(B_{2p_x})}\Big)\pm\sqrt{\frac{1}{4}\Big(\mathcal{H}_{(A_{1s})(A_{1s})} - \mathcal{H}_{(B_{2p_x})(B_{2p_x})}\Big)^2+|\mathcal{H}_{(A_{1s})(B_{2p_x})}|^2} \tag{A.12}$$

One can see that two atoms per unit cell with one orbital per atom has led to a dispersion relation with two energy values at each wavevector $\boldsymbol{k}$, that is two bands. All needed is to determine the Hamiltonian matrix elements.

$$\begin{aligned} \mathcal{H}_{(A_{1s})(A_{1s})} &= \langle \Phi_{\boldsymbol{k}}^{(A_{1s})} | \mathcal{H} | \Phi_{\boldsymbol{k}}^{(A_{1s})} \rangle \equiv \{\text{chain of } s\text{-orbitals separated by } a = \text{Eq. A.4}\} \\ &= E_{A_{1s}} - 2\boldsymbol{\gamma}(a) cos(k_x a) \end{aligned} \tag{A.13}$$

with the hopping matrix integrals up to nearest neighbors only, that is $\boldsymbol{\delta} = \{\pm a\hat{x}\}$. Similarly,

$$\mathcal{H}_{(B_{2p_x})(B_{2p_x})} = \langle \Phi_{\boldsymbol{k}}^{(B_{2p_x})} | \mathcal{H} | \Phi_{\boldsymbol{k}}^{(B_{2p_x})} \rangle = E_{B_{2p_x}} - 2\boldsymbol{\gamma}(a) cos(k_x a) \tag{A.14}$$

Now, let's evaluate the off-diagonal matrix elements

[3]If there is additionally p_y-orbital on site (B), one would need to solve the following 3×3 secular determinant $\begin{vmatrix} \mathcal{H}_{(A_{1s})(A_{1s})} - \mathcal{E}(\boldsymbol{k}) & \mathcal{H}_{(A_{1s})(B_{2p_x})} & \mathcal{H}_{(A_{1s})(B_{2p_y})} \\ \mathcal{H}_{(B_{2p_x})(A_{1s})} & \mathcal{H}_{(B_{2p_x})(B_{2p_x})} - \mathcal{E}(\boldsymbol{k}) & \mathcal{H}_{(B_{2p_x})(B_{2p_y})} \\ \mathcal{H}_{(B_{2p_y})(A_{1s})} & \mathcal{H}_{(B_{2p_y})(B_{2p_x})} & \mathcal{H}_{(B_{2p_y})(B_{2p_y})} - \mathcal{E}(\boldsymbol{k}) \end{vmatrix} = 0$ with $\mathcal{H}_{(A_\alpha)(B_\beta)}$ being determined same as explained in the context.

$$
\begin{aligned}
\mathcal{H}_{(A_{1s})(B_{2p_x})} &= \langle \Phi_{\boldsymbol{k}}^{(A_{1s})} | \mathcal{H} | \Phi_{\boldsymbol{k}}^{(B_{2p_x})} \rangle \\
&= \frac{1}{N} \sum_{\boldsymbol{R}_A} \sum_{\boldsymbol{R}_B} e^{i\boldsymbol{k}\cdot(\boldsymbol{R}_B - \boldsymbol{R}_A)} \langle \phi^*_{(A_{1s})}(\boldsymbol{r} - \boldsymbol{R}_A) | \mathcal{H} | \phi_{(B_{2p_x})}(\boldsymbol{r} - \boldsymbol{R}_B) \rangle \\
&\sim \sum_{\boldsymbol{R}_{AB}} e^{i\boldsymbol{k}\cdot\boldsymbol{R}_{AB}} \underbrace{\langle \phi^*_{(A_{1s})}(\boldsymbol{r}) | \mathcal{H}_{at} | \phi_{(B_{2p_x})}(\boldsymbol{r} - \boldsymbol{R}_{AB}) \rangle}_{\boldsymbol{\gamma}(R_{AB})} \\
&= \sum_{\boldsymbol{R}_{AB}} e^{i\boldsymbol{k}\cdot\boldsymbol{R}_{AB}} \boldsymbol{\gamma}(R_{AB}) \sim \sum_{\substack{\boldsymbol{R}_{AB} = n.n = \\ \{(\frac{a}{2}, \frac{a}{2}), (\frac{-a}{2}, \frac{a}{2})\}}} e^{i\boldsymbol{k}\cdot\boldsymbol{R}_{AB}} \boldsymbol{\gamma}(R_{AB}) \\
&= 2\boldsymbol{\gamma}(R_{AB}) \Big\{ \frac{e^{i\frac{a}{2}k_x} + e^{-i\frac{a}{2}k_x}}{2} \Big\} = 2\boldsymbol{\gamma}(R_{AB}) cos\Big(k_x \frac{a}{2}\Big) \\
&= 2\boldsymbol{\gamma}\Big(\frac{a}{\sqrt{2}}\Big) cos\Big(k_x \frac{a}{2}\Big) = \mathcal{H}^*_{(B_{2p_x})(A_{1s})}
\end{aligned}
\tag{A.15}
$$

Here, $\boldsymbol{R}_A$ and $\boldsymbol{R}_B$ are translation vectors that run over the two different lattice sites (A) and (B) respectively, where $\boldsymbol{R}_A = \pm ma\hat{x}$ and $\boldsymbol{R}_B = \boldsymbol{R}_{AB} \pm na\hat{x}$ such that $\{m,n\} \in \mathbb{Z}$. While, $\boldsymbol{R}_{AB} = \boldsymbol{R}_B - \boldsymbol{R}_A$ are translation vectors that connect the two sites as shown in Fig. A.3. Moving from the second line into the third line was done like this, $\boldsymbol{r}' = \boldsymbol{r} - \boldsymbol{R}_A \Rightarrow \boldsymbol{r} - \boldsymbol{R}_B = \boldsymbol{r}' + \boldsymbol{R}_A - \boldsymbol{R}_B = \boldsymbol{r}' - (\boldsymbol{R}_B - \boldsymbol{R}_A) = \boldsymbol{r}' - \boldsymbol{R}_{AB}$ then replacing the dummy variable $\boldsymbol{r}' \rightarrow \boldsymbol{r}$, additionally reducing $\mathcal{H} \rightarrow \mathcal{H}_{at}$ following the same logic in deriving Eq. A.3. Finally, putting all terms together to have the following energy band dispersion

$$
\begin{aligned}
\mathcal{E}(\boldsymbol{k}) = -\frac{1}{2} \Big\{ -4\boldsymbol{\gamma}(a) cos(k_x a) + (E_{A_{1s}} + E_{B_{2p_x}}) \Big\} \pm \\
\sqrt{\frac{1}{4}(E_{A_{1s}} - E_{B_{2p_x}})^2 + \Big\{ 2\boldsymbol{\gamma}(\frac{a}{\sqrt{2}}) cos(k_x \frac{a}{2}) \Big\}^2}
\end{aligned}
\tag{A.16}
$$

The corresponding two energy bands are plotted in Fig. A.4.[4] It is also important to notice that because $\Big(R_{12} = n.n = \frac{a}{\sqrt{2}} < a \Big) \overset{\text{then}}{\Longrightarrow} \Big(\boldsymbol{\gamma}(\frac{a}{\sqrt{2}}) > \boldsymbol{\gamma}(a) \Big)$ which was taken into consideration in plotting the band dispersion.

One can see through the discussed examples that, the energy bands reflect the atomic orbital characters that contribute in producing these bands. Moreover, near the bottom of a tight binding band, the dispersion looks locally parabolic similar to the free electron dispersion, hence, when an electron at this position an effective mass $m^* \propto \frac{1}{\boldsymbol{\gamma}(\delta)} \cdot \frac{1}{a^2}$ can be associated with the band[5]. This inverse relation means that the smaller the hopping matrix element, the heavier the effective mass of the electron and the harder for it to hope from site to another, hence, the narrower the *bandwidth*. On the over hand, the larger the matrix element is, the lighter the electrons effective mass and the easier for it to jump, hence, the wider the *bandwidth*.

[4] If both sites (A) and (B) were occupied by 1*s*-orbital, Eq. A.16 becomes, after replacing $E_{B_{2p_x}} \rightarrow E_{A_{1s}}$, into $\mathcal{E}(\boldsymbol{k}) = -E_{A_{1s}} + 2\boldsymbol{\gamma}(a) cos(k_x a) \pm 2\boldsymbol{\gamma}(\frac{a}{\sqrt{2}}) cos(k_x \frac{a}{2})$.

[5] Expanding the energy dispersion e.g. in Eq. A.5 at the bottom of the band $\{(k_x,k_y)=(0,0)\}$ will give: $\mathcal{E}(\boldsymbol{k}) = E_s - 2\boldsymbol{\gamma}(\delta) \big\{ 1 - \frac{(k_x a)^2}{2} + 1 - \frac{(k_y a)^2}{2} \big\} = E_s - 4\boldsymbol{\gamma}(\delta) + \underbrace{\boldsymbol{\gamma}(\delta) a^2 \{k_x^2 + k_y^2\}}_{\frac{\hbar^2 \boldsymbol{k}^2}{2m^*}} \Rightarrow m^* = \frac{\hbar^2}{2a^2 \boldsymbol{\gamma}(\delta)}$

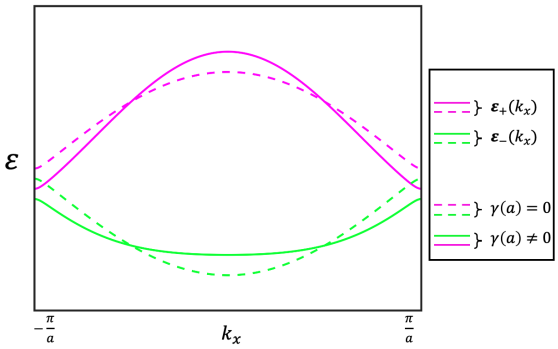

Figure A.4: **Energy dispersion of two different atomic sites per unit cell and a single orbital per site.** Energy dispersion in the 1^{st} Brillouin zone for the tight binding model of Fig. A.3, where the solid lines correspond for a non-zero hopping matrix element between $1s$-orbitals as will as between $2p_x$-orbitals, while the dashed lines include only zigzag hopping between $1s$- and $2p_x$-orbitals. the magenta color refers to $\mathcal{E}_+$ band while the green color is for the $\mathcal{E}_-$ band.

Similarly, the larger the real space lattice constant a along a direction, the farther the distance separating the atoms and the harder for the electron to hope, consistent with the larger effective mass and hence narrow *bandwidth* expected in reciprocal space along that direction and vice versa.

Now we look shortly at the example discussed in Appendix A.4, with a *zigzag*-lattice structure with site (B) off-center as shown in Fig. A.5.

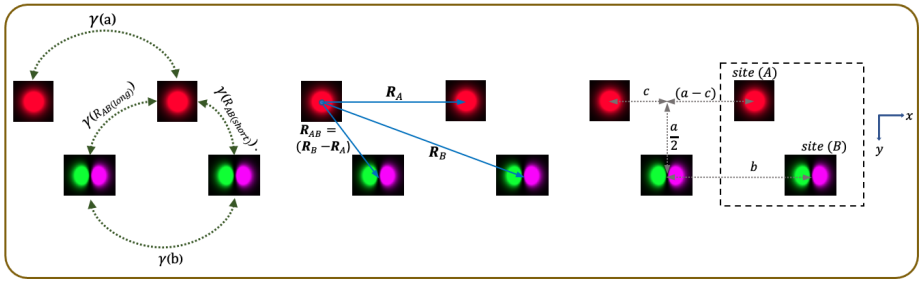

Figure A.5: **Tight binding model for two different atomic sites per unit cell with a single atomic orbit per site in a *zigzag* sites arrangement.** A theoretical model showing two different atomic sites pet unit cell, that is denoted by the dashed square, with $1s$-orbit on site (A) and $2p_x$-orbit on site (B). The $1s$-orbits are separated by a and $2p_x$-orbits are separated by b along the x-direction. $\boldsymbol{R}_A$ and $\boldsymbol{R}_B$ represent the translation vectors that run over the lattice sites (A) and (B) respectively, while $\boldsymbol{R}_{AB}$ are the translation vectors that connect both sites. $\boldsymbol{\gamma}(a)$, $\boldsymbol{\gamma}(b)$ are the hopping matrix elements between $1s$-orbits and $2p_x$-orbits respectively. $\boldsymbol{\gamma}(R_{AB(short)})$ refer for the hopping between $1s$- and $2p_x$-orbits along the *short* path, while $\boldsymbol{\gamma}(R_{AB(short)})$ refer for the hopping between $1s$- and $2p_x$-orbits along the *long* path.

$$\mathcal{H}_{(A_{1s})(A_{1s})} = E_{A_{1s}} - 2\boldsymbol{\gamma}(a)cos(k_x a) \tag{A.17}$$

$$\mathcal{H}_{(B_{2p_x})(B_{2p_x})} = E_{B_{2p_x}} - 2\boldsymbol{\gamma}(b)cos(k_x b) \tag{A.18}$$

$$\begin{aligned}
\mathcal{H}_{(A_{1s})(B_{2p_x})} &= \langle \Phi_{\boldsymbol{k}}^{(A_{1s})} | \mathcal{H} | \Phi_{\boldsymbol{k}}^{(B_{2p_x})} \rangle \\
&= \frac{1}{N} \sum_{\boldsymbol{R}_A} \sum_{\boldsymbol{R}_B} e^{i\boldsymbol{k}\cdot(\boldsymbol{R}_B - \boldsymbol{R}_A)} \langle \phi^*_{(A_{1s})}(\boldsymbol{r} - \boldsymbol{R}_A) | \mathcal{H} | \phi_{(B_{2p_x})}(\boldsymbol{r} - \boldsymbol{R}_B) \rangle \\
&\sim \sum_{\boldsymbol{R}_{AB}} e^{i\boldsymbol{k}\cdot\boldsymbol{R}_{AB}} \underbrace{\langle \phi^*_{(A_{1s})}(\boldsymbol{r}) | \mathcal{H}_{at} | \phi_{(B_{2p_x})}(\boldsymbol{r} - \boldsymbol{R}_{AB}) \rangle}_{\boldsymbol{\gamma}(R_{AB})} \\
&= \sum_{\boldsymbol{R}_{AB}} e^{i\boldsymbol{k}\cdot\boldsymbol{R}_{AB}} \boldsymbol{\gamma}(R_{AB}) \\
&\sim \sum_{\substack{\boldsymbol{R}_{AB} = n.n = \\ \{\boldsymbol{\gamma}(R_{AB(short)}), \boldsymbol{\gamma}(R_{AB(long)})\}}} e^{i\boldsymbol{k}\cdot\boldsymbol{R}_{AB}} \boldsymbol{\gamma}(R_{AB}) \\
&= \sum_{\substack{\boldsymbol{R}_{AB} = n.n = \\ \{(c, \frac{a}{2}), (-(a-c), \frac{a}{2})\}}} e^{i\boldsymbol{k}\cdot\boldsymbol{R}_{AB}} \boldsymbol{\gamma}(R_{AB}) \\
&= \boldsymbol{\gamma}(R_{AB(short)}) e^{ik_x c} + \boldsymbol{\gamma}(R_{AB(long)}) e^{-ik_x(a-c)} \\
&= e^{ik_x c} \Big\{ \boldsymbol{\gamma}(R_{AB(short)}) + e^{-ik_x a} \boldsymbol{\gamma}(R_{AB(long)}) \Big\} \\
&= e^{ik_x c} \Big\{ \boldsymbol{\gamma}\Big(\sqrt{c^2 + (\frac{a}{2})^2}\Big) + e^{-ik_x a} \boldsymbol{\gamma}\Big(\sqrt{(a-c)^2 + (\frac{a}{2})^2}\Big) \Big\} = \mathcal{H}^*_{(B_{2p_x})(A_{1s})}
\end{aligned} \tag{A.19}$$

Note: $\Big((a-c) > c\Big) \Rightarrow \boldsymbol{\gamma}\Big(\sqrt{c^2 + (\frac{a}{2})^2}\Big) > \boldsymbol{\gamma}\Big(\sqrt{(a-c)^2 + (\frac{a}{2})^2}\Big)$

Appendix B

Raw data of spin-resolved band dispersion maps of $PtTe_2$

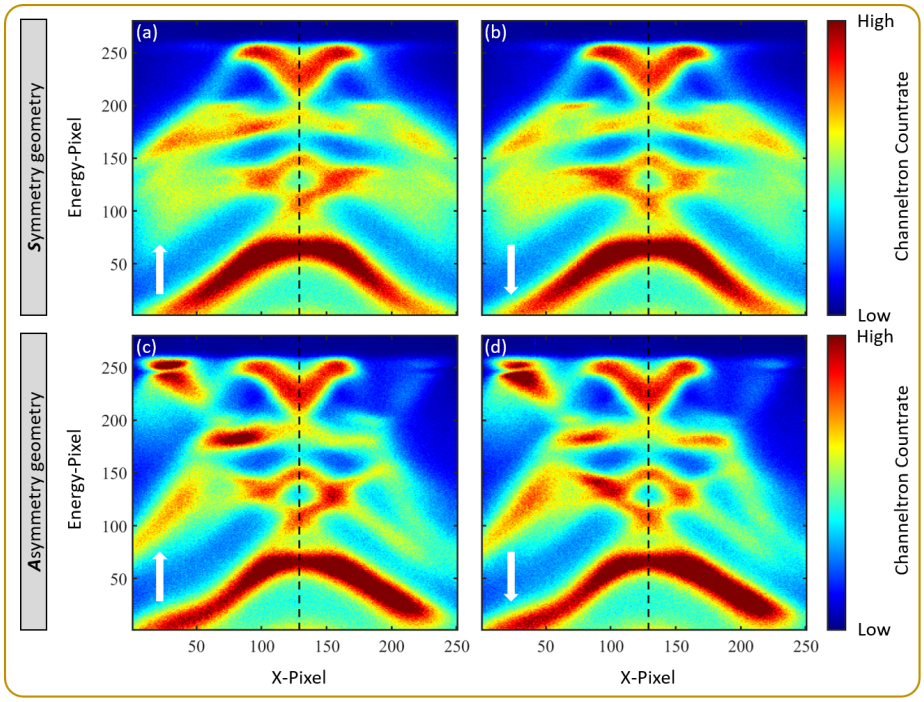

Figure B.1: **Raw data of for the spin-polarized band dispersion maps of $PtTe_2$ presented in Fig. 5.1 of the main text.** The upper ***S***ymmetry geometry panel shows the intensity maps $I_\uparrow$ and $I_\downarrow$ for the opposite scattering target magnetizations measured pixel-by-pixel. While the x-deflection is fixed, 280-energy pixels are scanned. This corresponds to a vertical line in (a). At energy-pixel 280, the scattering target is being re-magnetized and an equivalent vertical line in (b) is being scanned. This is done similarly for the 251-points along the x-direction. The whole process is done equivalently for the lower ***A***symmetry geometry panel (c-d).

Appendix C

Raw data of spin-resolved band dispersion maps for two symmetry geometries of $PtTe_2$

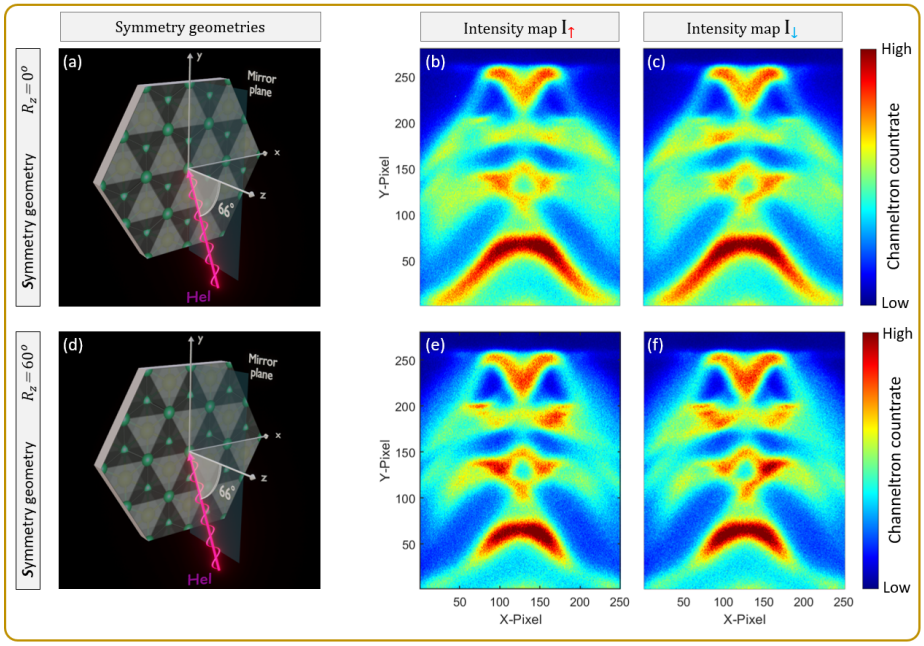

Figure C.1: **Raw data of spin-resolved band dispersion maps for two symmetry geometries of $PtTe_2$ presented in Fig. 5.8 of the main text.** (b),(c) Intensity maps $I_\uparrow$ and $I_\downarrow$ respectively for the opposite scattering target magnetizations measured pixel-by-pixel using the geometry shown in (a). While the x-deflection is fixed, 280-energy pixels are scanned. This corresponds to a vertical line in (b). At energy-pixel 280, the scattering target is being re-magnetized and an equivalent vertical line in (c) is being scanned. This is done similarly for the 251-points along the x-direction. The whole process is done equivalently for (e-f), that are measured using the other symmetry geometry (d).

Appendix D

Raw data of spin-resolved band dispersion maps for four asymmetry geometries of $PtTe_2$

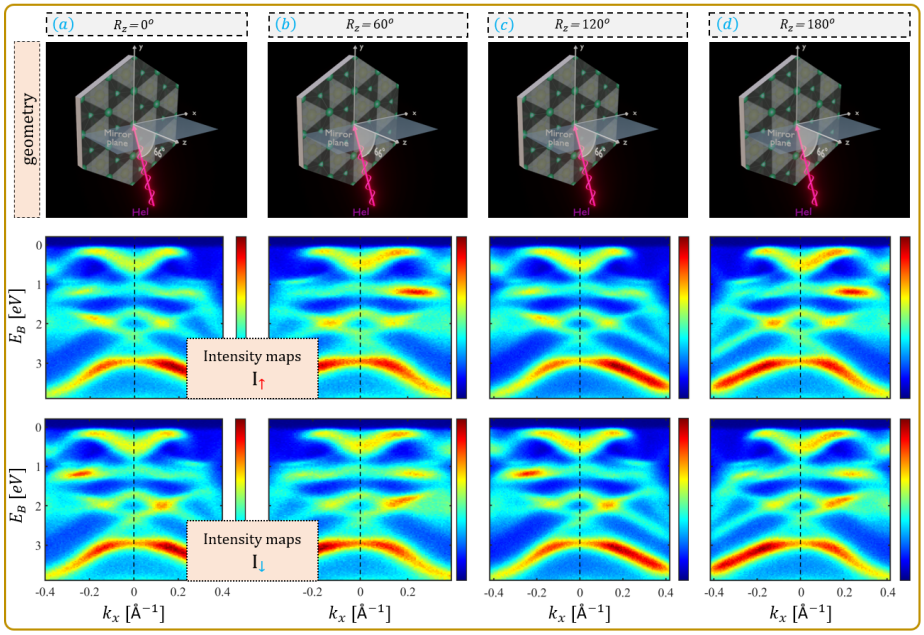

Figure D.1: **Raw data of the spin-resolved band dispersion maps of $PtTe_2$ presented in Fig. 5.9 of the main text.** First row in panels (a-d) shows the set-up geometry used in the corresponding panel. Second row in panels (a-d) displays the intensity maps $I_\uparrow$ with the scattering target being magnetized along one direction of the quantization axis y. Third row in panels (a-d) displays the intensity maps $I_\downarrow$ with the scattering target being re-magnetized along the opposite direction of the same quantization axis y. For panel (a): While the x-deflection is fixed, the energy scale is scanned. This corresponds to a vertical line in $I_\uparrow$-map. At last energy-pixel, the scattering target is being re-magnetized and an equivalent vertical line in $I_\downarrow$-map is being scanned. This is done similarly for all k_x-points along the x-direction. Same for panels (b-d).

Appendix E

Raw data of spin-resolved momentum maps of $PtTe_2$

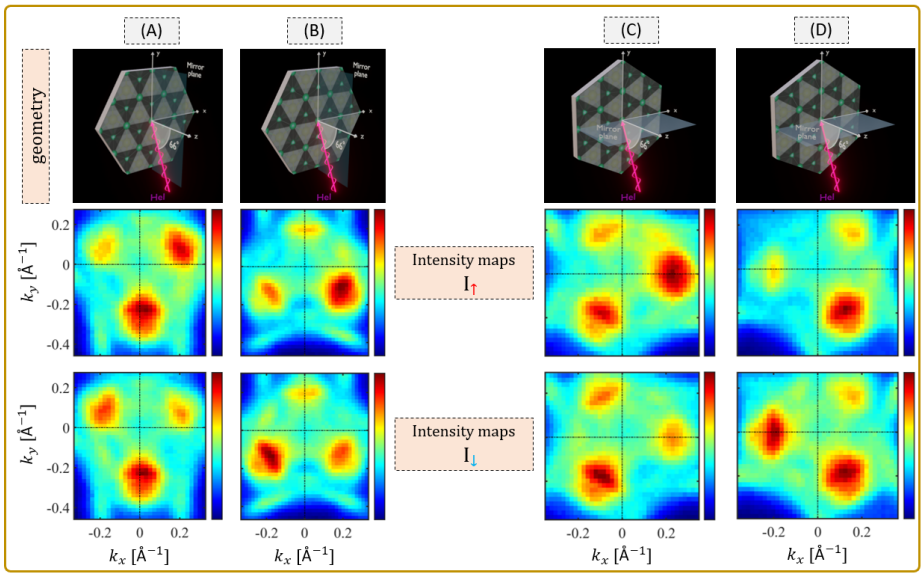

Figure E.1: **Raw data of the spin-resolved band dispersion maps of $PtTe_2$ presented in Fig. 5.11 of the main text.** First row in panels (A-D) shows the set-up geometry used in the corresponding panel. Second row in panels (A-D) displays the intensity maps $I_\uparrow$ with the scattering target being magnetized along one direction of the quantization axis y. Third row in panels (A-D) displays the intensity maps $I_\downarrow$ with the scattering target being re-magnetized along the opposite direction of the same quantization axis y. For panel (A): While the y-deflection is fixed, the x-deflection is scanned. This corresponds to a horizontal line in $I_\uparrow$-map. At last x-pixel, the scattering target is being re-magnetized and an equivalent horizontal line in $I_\downarrow$-map is being scanned. This is done similarly for all k_y-points along the y-direction. Same for panels (B-D).

Appendix F

Visualization of Spin Polarization with 2D Color Mapping

The following MATLAB code snippet demonstrates a method to plot a three-dimensional surface representing spin polarization as a function of parallel momentum $k_{||}$ and binding energy E_B. The plot is color-coded to visually represent the magnitude of spin polarization SP together with the photoemission intensity simultaneously.

MATLAB Code

```
surf(k_parallel, Binding_energy, Spin_polarization, ...
'edgecolor', 'none','facealpha', 'flat','alphadata', ...
(Spin_up + Spin_down) / max(max(Spin_up + Spin_down));
```

Explanation of parameters:

- surf:
  surf function generates a 3D surface plot, where $k_{||}$ is plotted along the x-axis, E_B along the y-axis, and SP along the z-axis. Color coding is used to visually encode variations in spin polarization across different values of $k_{||}$ and E_B.
- 'edgecolor', 'none':
  setting the 'edgecolor' option to 'none' removes gridlines from the plot surface, giving a smooth appearance. This reduces visual noise, allowing the color representation of SP to stand out.
- 'facealpha', 'flat':
  the 'facealpha' property controls the transparency of the surface plot. By setting it to 'flat', the transparency is applied independently to each face (cell) of the surface, enhancing contrast.
- 'alphadata':
  alphadata is used to set the transparency based on the intensity of the underlying data. Here, the transparency is scaled by the combined spin components Spin up and Spin down, normalized by their maximum value using max(max(Spin up + Spin down)). This normalization ensures consistent transparency scaling across all values, highlighting regions with higher spin polarization.

Bibliography

[1] P. Dey and J. N. Roy, *Spintronics: Fundamentals and Applications*. Springer Singapore, 1st edition, 2021, ISBN: 9789811600692. DOI: 10.1007/978-981-16-0069-2 [Online]. Available: http://dx.doi.org/10.1007/978-981-16-0069-2

[2] S. C. Ray, "1 - the fundamental aspects of spintronics," in *Magnetism and Spintronics in Carbon and Carbon Nanostructured Materials*, ser. Micro and Nano Technologies, S. C. Ray, Ed., Elsevier, 2020, pp. 1–21, ISBN: 978-0-12-817680-1. DOI: https://doi.org/10.1016/B978-0-12-817680-1.00001-9 [Online]. Available: https://www.sciencedirect.com/science/article/pii/B9780128176801000019

[3] M. Z. Hasan and C. L. Kane, "Colloquium: Topological insulators," *Rev. Mod. Phys.*, vol. 82, pp. 3045–3067, 4 Nov. 2010. DOI: 10.1103/RevModPhys.82.3045 [Online]. Available: https://link.aps.org/doi/10.1103/RevModPhys.82.3045

[4] A. Hirohata et al., "Review on spintronics: Principles and device applications," *Journal of Magnetism and Magnetic Materials*, vol. 509, p. 166 711, 2020, ISSN: 0304-8853. DOI: https://doi.org/10.1016/j.jmmm.2020.166711 [Online]. Available: https://www.sciencedirect.com/science/article/pii/S0304885320302353

[5] S. A. Wolf et al., "Spintronics: A spin-based electronics vision for the future," *Science*, vol. 294, no. 5546, pp. 1488–1495, 2001. DOI: 10.1126/science.1065389 eprint: https://www.science.org/doi/pdf/10.1126/science.1065389. [Online]. Available: https://www.science.org/doi/abs/10.1126/science.1065389

[6] I. Žuti ć, J. Fabian, and S. Das Sarma, "Spintronics: Fundamentals and applications," *Rev. Mod. Phys.*, vol. 76, pp. 323–410, 2 Apr. 2004. DOI: 10.1103/RevModPhys.76.323 [Online]. Available: https://link.aps.org/doi/10.1103/RevModPhys.76.323

[7] J. Kirschner, *Polarized Electrons at Surfaces* (Springer Tracts in Modern Physics), Softcover reprint of the original 1st ed. Berlin, Heidelberg: Springer, 1985, vol. 106. DOI: 10.1007/978-3-642-82360-0

[8] R. Feder, *Polarized Electrons in Surface Physics*. WORLD SCIENTIFIC, 1986. DOI: 10.1142/0158 eprint: https://www.worldscientific.com/doi/pdf/10.1142/0158. [Online]. Available: https://www.worldscientific.com/doi/abs/10.1142/0158

[9] J. Kessler, *Polarized Electrons* (Springer Series on Atoms and Plasmas), 2nd. Berlin: Springer, 1985, vol. 1.

[10] W. Schattke and M. A. van Hove, Eds., *Solid-State Photoemission and Related Methods: Theory and Experiment*. Weinheim: Wiley-VCH, 2003.

[11] J. Osterwalder, "Magnetism: A synchrotron radiation approach," in *Lecture Notes in Physics*, vol. 697, Berlin: Springer, 2006, p. 95.

[12] U. Heinzmann and J. H. Dil, "Spin–orbit-induced photoelectron spin polarization in angle-resolved photoemission from both atomic and condensed matter targets," *Journal of Physics: Condensed Matter*, vol. 24, no. 17, p. 173 001, Apr. 2012. DOI: 10.1088/0953-8984/24/17/173001 [Online]. Available: https://dx.doi.org/10.1088/0953-8984/24/17/173001

[13] A. V. Kolobov and J. Tominaga, *Two-Dimensional Transition-Metal Dichalcogenides* (Springer series in materials science). Cham, Switzerland: Springer International Publishing, Jul. 1st edition 2016. DOI: https://doi.org/10.1007/978-3-319-31450-1

[14] H. Yuan et al., "Zeeman-type spin splitting controlled by an electric field," *Nature Physics*, vol. 9, no. 9, pp. 563–569, Sep. 2013, ISSN: 1745-2481. DOI: 10.1038/nphys2691 [Online]. Available: https://doi.org/10.1038/nphys2691

[15] J. Sklenar et al., "Spin Hall effects in metallic antiferromagnets – perspectives for future spin-orbitronics," *AIP Advances*, vol. 6, no. 5, p. 055 603, Mar. 2016, ISSN: 2158-3226. DOI: 10.1063/1.4943758 eprint: https://pubs.aip.org/aip/adv/article-pdf/doi/10.1063/1.4943758/12839649/055603_1_online.pdf. [Online]. Available: https://doi.org/10.1063/1.4943758

[16] L. Yang et al., "Long-lived nanosecond spin relaxation and spin coherence of electrons in monolayer mos2 and ws2," *Nature Physics*, vol. 11, no. 10, pp. 830–834, Oct. 2015, ISSN: 1745-2481. DOI: 10.1038/nphys3419 [Online]. Available: https://doi.org/10.1038/nphys3419

[17] K. Deng et al., "Experimental observation of topological fermi arcs in type-ii weyl semimetal mote2," *Nature Physics*, vol. 12, no. 12, pp. 1105–1110, Dec. 2016, ISSN: 1745-2481. DOI: 10.1038/nphys3871 [Online]. Available: https://doi.org/10.1038/nphys3871

[18] D. MacNeill, G. M. Stiehl, M. H. D. Guimaraes, R. A. Buhrman, J. Park, and D. C. Ralph, "Control of spin–orbit torques through crystal symmetry in wte2/ferromagnet bilayers," *Nature Physics*, vol. 13, no. 3, pp. 300–305, Mar. 2017, ISSN: 1745-2481. DOI: 10.1038/nphys3933 [Online]. Available: https://doi.org/10.1038/nphys3933

[19] O. J. Clark et al., "Fermiology and superconductivity of topological surface states in $PdTe_2$," *Phys. Rev. Lett.*, vol. 120, p. 156 401, 15 Apr. 2018. DOI: 10.1103/PhysRevLett.120.156401 [Online]. Available: https://link.aps.org/doi/10.1103/PhysRevLett.120.156401

[20] A. Manchon et al., "Current-induced spin-orbit torques in ferromagnetic and antiferromagnetic systems," *Rev. Mod. Phys.*, vol. 91, p. 035 004, 3 Sep. 2019. DOI: 10.1103/RevModPhys.91.035004 [Online]. Available: https://link.aps.org/doi/10.1103/RevModPhys.91.035004

[21] I. Mihai Miron et al., "Current-driven spin torque induced by the rashba effect in a ferromagnetic metal layer," *Nature Materials*, vol. 9, no. 3, pp. 230–234, Mar. 2010, ISSN: 1476-4660. DOI: 10.1038/nmat2613 [Online]. Available: https://doi.org/10.1038/nmat2613

[22] L. Liu, C.-F. Pai, Y. Li, H. W. Tseng, D. C. Ralph, and R. A. Buhrman, "Spin-torque switching with the giant spin hall effect of tantalum," *Science*, vol. 336, no. 6081, pp. 555–558, 2012. DOI: 10.1126/science.1218197 eprint: https://www.science.org/doi/pdf/10.1126/science.1218197. [Online]. Available: https://www.science.org/doi/abs/10.1126/science.1218197

[23] G. Yu et al., "Switching of perpendicular magnetization by spin–orbit torques in the absence of external magnetic fields," *Nature Nanotechnology*, vol. 9, no. 7, pp. 548–554, Jul. 2014, ISSN: 1748-3395. DOI: 10.1038/nnano.2014.94 [Online]. Available: https://doi.org/10.1038/nnano.2014.94

[24] M. Cubukcu et al., "Ultra-fast perpendicular spin–orbit torque mram," *IEEE Transactions on Magnetics*, vol. 54, no. 4, pp. 1–4, Apr. 2018, ISSN: 1941-0069. DOI: 10.1109/TMAG.2017.2772185

[25] M. S. Bahramy et al., "Ubiquitous formation of bulk dirac cones and topological surface states from a single orbital manifold in transition-metal dichalcogenides," *Nature Materials*, vol. 17, no. 1, pp. 21–28, Jan. 2018, ISSN: 1476-4660. DOI: 10.1038/nmat5031 [Online]. Available: https://doi.org/10.1038/nmat5031

[26] S. Hao et al., "Low-temperature eutectic synthesis of ptte2 with weak antilocalization and controlled layer thinning," *Advanced Functional Materials*, vol. 28, no. 36, p. 1 803 746, 2018. DOI: https://doi.org/10.1002/adfm.201803746 eprint: https://onlinelibrary.wiley.com/doi/pdf/10.1002/adfm.201803746. [Online]. Available: https://onlinelibrary.wiley.com/doi/abs/10.1002/adfm.201803746

[27] H. Xu et al., "High spin hall conductivity in large-area type-ii dirac semimetal ptte2," *Advanced Materials*, vol. 32, no. 17, p. 2 000 513, 2020. DOI: https://doi.org/10.1002/adma.202000513 eprint: https://onlinelibrary.wiley.com/doi/pdf/10.1002/adma.202000513. [Online]. Available: https://onlinelibrary.wiley.com/doi/abs/10.1002/adma.202000513

[28] H. Huang, S. Zhou, and W. Duan, "Type-ii dirac fermions in the $\mathbf{PtSe_2}$ class of transition metal dichalcogenides," *Phys. Rev. B*, vol. 94, p. 121 117, 12 Sep. 2016. DOI: 10.1103/PhysRevB.94.121117 [Online]. Available: https://link.aps.org/doi/10.1103/PhysRevB.94.121117

[29] M. Yan et al., "Lorentz-violating type-ii dirac fermions in transition metal dichalcogenide ptte2," *Nature Communications*, vol. 8, no. 1, p. 257, Aug. 2017, ISSN: 2041-1723. DOI: 10.1038/s41467-017-00280-6 [Online]. Available: https://doi.org/10.1038/s41467-017-00280-6

[30] A. R. Mellnik et al., "Spin-transfer torque generated by a topological insulator," *Nature*, vol. 511, no. 7510, pp. 449–451, Jul. 2014, ISSN: 1476-4687. DOI: 10.1038/nature13534 [Online]. Available: https://doi.org/10.1038/nature13534

[31] Y. Wang et al., "Topological surface states originated spin-orbit torques in Bi_2Se_3," *Phys. Rev. Lett.*, vol. 114, p. 257 202, 25 Jun. 2015. DOI: 10.1103/PhysRevLett.114.257202 [Online]. Available: https://link.aps.org/doi/10.1103/PhysRevLett.114.257202

[32] K. Deng et al., "Crossover from 2d metal to 3d dirac semimetal in metallic ptte2 films with local rashba effect," *Science Bulletin*, vol. 64, no. 15, pp. 1044–1048, 2019, Two-Dimensional Materials: New Opportunities for Electronics, Photonics and Optoelectronics, ISSN: 2095-9273. DOI: https://doi.org/10.1016/j.scib.2019.05.023 [Online]. Available: https://www.sciencedirect.com/science/article/pii/S2095927319303172

[33] W. Yao et al., "Direct observation of spin-layer locking by local rashba effect in monolayer semiconducting ptse2 film," *Nature Communications*, vol. 8, no. 1, p. 14 216, Jan. 2017, ISSN: 2041-1723. DOI: 10.1038/ncomms14216 [Online]. Available: https://doi.org/10.1038/ncomms14216

[34] J. M. Riley et al., "Direct observation of spin-polarized bulk bands in an inversion-symmetric semiconductor," *Nature Physics*, vol. 10, no. 11, pp. 835–839, Nov. 2014, ISSN: 1745-2481. DOI: 10.1038/nphys3105 [Online]. Available: https://doi.org/10.1038/nphys3105

[35] O. J. Clark, O. Dowinton, M. S. Bahramy, and J. Sánchez-Barriga, "Hidden spin-orbital texture at the $\overline{\Gamma}$-located valence band maximum of a transition metal dichalcogenide semiconductor," *Nature Communications*, vol. 13, no. 1, p. 4147, Jul. 2022, ISSN: 2041-1723. DOI: 10.1038/s41467-022-31539-2 [Online]. Available: https://doi.org/10.1038/s41467-022-31539-2

[36] B. Feng et al., "Spin texture in type-ii weyl semimetal WTe_2," *Phys. Rev. B*, vol. 94, p. 195 134, 19 Nov. 2016. DOI: 10.1103/PhysRevB.94.195134 [Online]. Available: https://link.aps.org/doi/10.1103/PhysRevB.94.195134

[37] M. Fanciulli et al., "Spin, time, and angle resolved photoemission spectroscopy on WTe_2," *Phys. Rev. Res.*, vol. 2, p. 013 261, 1 Mar. 2020. DOI: 10.1103/PhysRevResearch.2.013261 [Online]. Available: https://link.aps.org/doi/10.1103/PhysRevResearch.2.013261

[38] Y. Wan et al., "Selective observation of surface and bulk bands in polar WTe_2 by laser-based spin- and angle-resolved photoemission spectroscopy," *Phys. Rev. B*, vol. 105, p. 085 421, 8 Feb. 2022. DOI: 10.1103/PhysRevB.105.085421 [Online]. Available: https://link.aps.org/doi/10.1103/PhysRevB.105.085421

[39] E. Razzoli et al., "Selective probing of hidden spin-polarized states in inversion-symmetric bulk MoS_2," *Phys. Rev. Lett.*, vol. 118, p. 086 402, 8 Feb. 2017. DOI: 10.1103/PhysRevLett.118.086402 [Online]. Available: https://link.aps.org/doi/10.1103/PhysRevLett.118.086402

[40] Y. Zhang et al., "The origin of the band-splitting and the spin polarization in bulk 2H-WSe2," *Applied Physics Letters*, vol. 122, no. 14, p. 142 402, Apr. 2023, ISSN: 0003-6951. DOI: 10.1063/5.0146774 eprint: https://pubs.aip.org/aip/apl/article-pdf/doi/10.1063/5.0146774/16820543/142402_1_5.0146774.pdf. [Online]. Available: https://doi.org/10.1063/5.0146774

[41] R. Suzuki et al., "Valley-dependent spin polarization in bulk mos2 with broken inversion symmetry," *Nature Nanotechnology*, vol. 9, no. 8, pp. 611–617, Aug. 2014, ISSN: 1748-3395. DOI: 10.1038/nnano.2014.148 [Online]. Available: https://doi.org/10.1038/nnano.2014.148

[42] L. Bawden et al., "Spin–valley locking in the normal state of a transition-metal dichalcogenide superconductor," *Nature Communications*, vol. 7, no. 1, p. 11 711, May 2016, ISSN: 2041-1723. DOI: 10.1038/ncomms11711 [Online]. Available: https://doi.org/10.1038/ncomms11711

[43] A. Gianfrate et al., "Measurement of the quantum geometric tensor and of the anomalous hall drift," *Nature*, vol. 578, no. 7795, pp. 381–385, Feb. 2020, ISSN: 1476-4687. DOI: 10.1038/s41586-020-1989-2 [Online]. Available: http://dx.doi.org/10.1038/s41586-020-1989-2

[44] M. Kang et al., "Measurements of the quantum geometric tensor in solids," *Nature Physics*, vol. 21, no. 1, pp. 110–117, Nov. 2024, ISSN: 1745-2481. DOI: 10.1038/s41567-024-02678-8 [Online]. Available: http://dx.doi.org/10.1038/s41567-024-02678-8

[45] C. Tusche, Y.-J. Chen, L. Plucinski, and C. M. Schneider, "From Photoemission Microscopy to an “All-in-One” Photoemission Experiment," *e-J. Surf. Sci. Nanotec.*, vol. 18, pp. 48–56, 2020. DOI: 10.1380/ejssnt.2020.48

[46] T. Heider et al., "Geometry-induced spin filtering in photoemission maps from WTe_2 surface states," *Phys. Rev. Lett.*, vol. 130, p. 146 401, 14 Apr. 2023. DOI: 10.1103/PhysRevLett.130.146401 [Online]. Available: https://link.aps.org/doi/10.1103/PhysRevLett.130.146401

[47] M.-K. Lin et al., "Dimensionality-mediated semimetal-semiconductor transition in ultrathin $PtTe_2$ films," *Phys. Rev. Lett.*, vol. 124, p. 036 402, 3 Jan. 2020. DOI: 10.1103/PhysRevLett.124.036402 [Online]. Available: https://link.aps.org/doi/10.1103/PhysRevLett.124.036402

[48] K. Zhang et al., "Experimental evidence for type-ii dirac semimetal in $PtSe_2$," *Phys. Rev. B*, vol. 96, p. 125 102, 12 Sep. 2017. DOI: 10.1103/PhysRevB.96.125102 [Online]. Available: https://link.aps.org/doi/10.1103/PhysRevB.96.125102

[49] Y. Liu et al., "Identification of topological surface state in pdte2 superconductor by angle-resolved photoemission spectroscopy*," *Chinese Physics Letters*, vol. 32, no. 6, p. 067 303, Jun. 2015. DOI: 10.1088/0256-307X/32/6/067303 [Online]. Available: https://dx.doi.org/10.1088/0256-307X/32/6/067303

[50] H.-J. Noh, J. Jeong, E.-J. Cho, K. Kim, B. I. Min, and B.-G. Park, "Experimental realization of type-ii dirac fermions in a $PdTe_2$ superconductor," *Phys. Rev. Lett.*, vol. 119, p. 016 401, 1 Jul. 2017. DOI: 10.1103/PhysRevLett.119.016401 [Online]. Available: https://link.aps.org/doi/10.1103/PhysRevLett.119.016401

[51] F. J. García de Abajo, M. A. Van Hove, and C. S. Fadley, "Multiple scattering of electrons in solids and molecules: A cluster-model approach," *Phys. Rev. B*, vol. 63, p. 075 404, 7 Jan. 2001. DOI: 10.1103/PhysRevB.63.075404 [Online]. Available: https://link.aps.org/doi/10.1103/PhysRevB.63.075404

[52] K. W. Böer and U. W. Pohl, "The origin of band structure," in *Semiconductor Physics*. Cham: Springer International Publishing, 2023, ch. 6.

[53] C. Kittel, *Introduction to Solid State Physics*. John Wiley and Sons, 2005, ch. 7.

[54] N. W. Ashcroft and N. D. Mermin, *Solid State Physics*. Holt-Saunders, 1976, ch. 8.

[55] D. P. A. M., "The quantum theory of the electron," *Proc. R. Soc.*, vol. A, no. 117, pp. 610–624, 1928.

[56] P. A. M. Dirac, "The quantum theory of the electron. part ii," *Proceedings of the Royal Society of London. A*, vol. 118, pp. 351–361, 1928. DOI: 10.1098/rspa.1928.0056

[57] B. G., *Electronic States in Solids, chapter A1*. Forschungszentrum Jülich GmbH, 40th IFF Springschool 2009.

[58] S. R., *Principles of Quantum Mechanics*. Springer, 2014.

[59] B. H. A. and S. E. E., *Quantum Mechanics of One- and Two-Electron Atoms*. Springer Berlin, Heidelberg, 1957.

[60] G. K., "Symmetry-allowed spin-orbit coupling in quantum materials," Ph.D. dissertation, UC Berkeley, 2017.

[61] B. G., *Relativistic effects in solids, chapter A10*. Forschungszentrum Jülich GmbH Zentralbibliothek, Verlag, 45th IFF Spring School 2014.

[62] G. D. J. and S. D. F., *Introduction to Quantum Mechanics*. Cambridge University Press, 2018.

[63] S. J. J., *Modern quantum mechanics*. Addison-Wesley Pub. Co, 1994.

[64] P. D. T. et al., "The gaas spin polarized electron source," *Rev. Sci. Instrum. 51, 478–499*, 1980.

[65] W. R., *Spin—Orbit Coupling Effects in Two-Dimensional Electron and Hole Systems, chapter: Introduction*. Springer-Verlag Berlin Heidelberg, 2003.

[66] Y. A. Bychkov and E. I. Rashba, "Oscillatory effects and the magnetic susceptibility of carriers in inversion layers," *Journal of Physics C: Solid State Physics*, vol. 17, no. 33, p. 6039, Nov. 1984. DOI: 10.1088/0022-3719/17/33/015 [Online]. Available: https://dx.doi.org/10.1088/0022-3719/17/33/015

[67] B. Y. A. and E. I. Rashba, "Properties of a 2d electron gas with lifted spectral degeneracy," *Experimental and Theoretical Physics Letters*, vol. 39, no. 2, p. 78, 1984. [Online]. Available: https://api.semanticscholar.org/CorpusID:118743600

[68] K. V. Shanavas and S. Satpathy, "Electric field tuning of the rashba effect in the polar perovskite structures," *Phys. Rev. Lett.*, vol. 112, p. 086 802, 8 Feb. 2014. DOI: 10.1103/PhysRevLett.112.086802 [Online]. Available: https://link.aps.org/doi/10.1103/PhysRevLett.112.086802

[69] S. Gupta and B. I. Yakobson, "What dictates rashba splitting in 2d van der waals heterobilayers," *Journal of the American Chemical Society*, vol. 143, no. 9, pp. 3503–3508, Mar. 2021, ISSN: 0002-7863. DOI: 10.1021/jacs.0c12809 [Online]. Available: https://doi.org/10.1021/jacs.0c12809

[70] S. LaShell, B. A. McDougall, and E. Jensen, "Spin splitting of an au(111) surface state band observed with angle resolved photoelectron spectroscopy," *Phys. Rev. Lett.*, vol. 77, pp. 3419–3422, 16 Oct. 1996. DOI: 10.1103/PhysRevLett.77.3419 [Online]. Available: https://link.aps.org/doi/10.1103/PhysRevLett.77.3419

[71] C. Tusche, A. Krasyuk, and J. Kirschner, "Spin resolved bandstructure imaging with a high resolution momentum microscope," *Ultramicroscopy*, vol. 159, pp. 520–529, 2015, Special Issue: LEEM-PEEM 9, ISSN: 0304-3991. DOI: https://doi.org/10.1016/j.ultramic.2015.03.020 [Online]. Available: https://www.sciencedirect.com/science/article/pii/S0304399115000698

[72] K. Wu, J. Chen, H. Ma, L. Wan, W. Hu, and J. Yang, "Two-dimensional giant tunable rashba semiconductors with two-atom-thick buckled honeycomb structure," *Nano Letters*, vol. 21, no. 1, pp. 740–746, Jan. 2021, ISSN: 1530-6984. DOI: 10.1021/acs.nanolett.0c04429 [Online]. Available: https://doi.org/10.1021/acs.nanolett.0c04429

[73] G. Dresselhaus, "Spin-orbit coupling effects in zinc blende structures," *Phys. Rev.*, vol. 100, pp. 580–586, 2 Oct. 1955. DOI: 10.1103/PhysRev.100.580 [Online]. Available: https://link.aps.org/doi/10.1103/PhysRev.100.580

[74] S. Hüfner, *Photoelectron Spectroscopy, Principles and Applications*. Springer Berlin, Heidelberg, 3^{rd} edition 2003.

[75] H. Hertz, "Ueber einen einfluss des ultravioletten lichtes auf die electrische entladung," *Annalen der Physik*, vol. 267, no. 8, pp. 983–1000, 1887. DOI: https://doi.org/10.1002/andp.18872670827 eprint: https://onlinelibrary.wiley.com/doi/pdf/10.1002/andp.18872670827. [Online]. Available: https://onlinelibrary.wiley.com/doi/abs/10.1002/andp.18872670827

[76] A. Einstein, "Über einen die erzeugung und verwandlung des lichtes betreffenden heuristischen gesichtspunkt," *Annalen der Physik*, vol. 322, no. 6, pp. 132–148, 1905. DOI: https://doi.org/10.1002/andp.19053220607 eprint: https://onlinelibrary.wiley.com/doi/pdf/10.1002/andp.19053220607. [Online]. Available: https://onlinelibrary.wiley.com/doi/abs/10.1002/andp.19053220607

[77] G. Marr, *Handbook on Synchrotron Radiation. Vacuum Ultraviolet and Soft X-ray Processes*. North Holland, 1987.

[78] Ponor, *Photoemission Spectroscopy*. Wikipedia, June 4, 2020. [Online]. Available: https://en.wikipedia.org/wiki/Photoemission_spectroscopy

[79] B. Lv, T. Qian, and H. Ding, "Angle-resolved photoemission spectroscopy and its application to topological materials," *Nature Reviews Physics*, vol. 1, no. 10, pp. 609–626, Oct. 2019, ISSN: 2522-5820. DOI: 10.1038/s42254-019-0088-5 [Online]. Available: https://doi.org/10.1038/s42254-019-0088-5

[80] A. Damascelli, Z. Hussain, and Z.-X. Shen, "Angle-resolved photoemission studies of the cuprate superconductors," *Rev. Mod. Phys.*, vol. 75, pp. 473–541, 2 Apr. 2003. DOI: 10.1103/RevModPhys.75.473 [Online]. Available: https://link.aps.org/doi/10.1103/RevModPhys.75.473

[81] F. Reinert and S. Hüfner, "Photoemission spectroscopy—from early days to recent applications," *New Journal of Physics*, vol. 7, no. 1, p. 97, Apr. 2005. DOI: 10.1088/1367-2630/7/1/097 [Online]. Available: https://dx.doi.org/10.1088/1367-2630/7/1/097

[82] J. A. Sobota, Y. He, and Z.-X. Shen, "Angle-resolved photoemission studies of quantum materials," *Rev. Mod. Phys.*, vol. 93, p. 025 006, 2 May 2021. DOI: 10.1103/RevModPhys.93.025006 [Online]. Available: https://link.aps.org/doi/10.1103/RevModPhys.93.025006

[83] C. Schneider, *Photoelectron Emission Spectroscopy, chapter F3*. Forschungszentrum Jülich GmbH, 43rd IFF Spring School 2012.

[84] A. Damascelli, "Probing the electronic structure of complex systems by arpes," *Physica Scripta*, vol. 2004, no. T109, p. 61, Jan. 2004. DOI: 10.1238/Physica.Topical.109a00061 [Online]. Available: https://dx.doi.org/10.1238/Physica.Topical.109a00061

[85] H. Yang, A. Liang, C. Chen, C. Zhang, N. B. M. Schroeter, and Y. Chen, "Visualizing electronic structures of quantum materials by angle-resolved photoemission spectroscopy," *Nature Reviews Materials*, vol. 3, no. 9, pp. 341–353, Sep. 2018, ISSN: 2058-8437. DOI: 10.1038/s41578-018-0047-2 [Online]. Available: https://doi.org/10.1038/s41578-018-0047-2

[86] H. Zhang et al., "Angle-resolved photoemission spectroscopy," *Nature Reviews Methods Primers*, vol. 2, no. 1, p. 54, Jul. 2022, ISSN: 2662-8449. DOI: 10.1038/s43586-022-00133-7 [Online]. Available: https://doi.org/10.1038/s43586-022-00133-7

[87] M. P. Seah and W. A. Dench, "Quantitative electron spectroscopy of surfaces: A standard data base for electron inelastic mean free paths in solids," *Surface and Interface Analysis*, vol. 1, no. 1, pp. 2–11, 1979. DOI: https://doi.org/10.1002/sia.740010103 eprint: https://analyticalsciencejournals.onlinelibrary.wiley.com/doi/pdf/10.1002/sia.740010103. [Online]. Available: https://analyticalsciencejournals.onlinelibrary.wiley.com/doi/abs/10.1002/sia.740010103

[88] D. W. Lynch and C. G. Olson, "Contents," in *Photoemission Studies of High-Temperature Superconductors* (Cambridge Studies in Low Temperature Physics), Cambridge Studies in Low Temperature Physics. Cambridge University Press, 1999, pp. v–viii.

[89] S. Goldberg, C. Fadley, and S. Kono, "Photoionization cross-sections for atomic orbitals with random and fixed spatial orientation," *Journal of Electron Spectroscopy and Related Phenomena*, vol. 21, no. 4, pp. 285–363, 1981, ISSN: 0368-2048. DOI: https://doi.org/10.1016/0368-2048(81)85067-0 [Online]. Available: https://www.sciencedirect.com/science/article/pii/0368204881850670

[90] P. Krüger, "Photoelectron diffraction from valence states of oriented molecules," *Journal of the Physical Society of Japan*, vol. 87, no. 6, p. 061 007, 2018. DOI: 10.7566/JPSJ.87.061007 eprint: https://doi.org/10.7566/JPSJ.87.061007. [Online]. Available: https://doi.org/10.7566/JPSJ.87.061007

[91] S. Hasegawa, H. Inokuchi, K. Seki, and N. Ueno, "Angle-resolved photoemission from oriented thin films of naphthacene: Comparison with theoretical spectra," *Journal of Electron Spectroscopy and Related Phenomena*, vol. 78, pp. 391–394, 1996, ISSN: 0368-2048. DOI: https://doi.org/10.1016/S0368-2048(96)80106-X [Online]. Available: https://www.sciencedirect.com/science/article/pii/S036820489680106X

[92] D. Sébilleau, K. Hatada, and H. Ebert, *Multiple Scattering Theory for Spectroscopies: A Guide to Multiple Scattering Computer Codes*. Springer International Publishing, 2018, vol. 24, pp. 3–34.

[93] R. Fitzpatrick, *Quantum Mechanics*. World Scientific, Singapore, 2015.

[94] L. D. Landau and E. M. Lifshitz, *Quantum Mechanics:Non-Relativistic Theory, Course of Theoretical Physics*. Pergamon Press, 1977, vol. 3, pp. 469–475.

[95] S. Gasiorowicz, *Quantum Physics*. John Wiley & Sons Inc, 3^{rd} edition 2003, pp. 287–291.

[96] W. Moritz and M. A. Van Hove, *Surface Structure Determination by LEED and X-rays*. Cambridge: Cambridge University Press, 2022, pp. 114–123. DOI: 10.1017/9781108284578 [Online]. Available: https://www.cambridge.org/core/books/surface-structure-determination-by-leed-and-xrays/275456004BB6CF653214D238D14D4BBB

[97] M.-L. Xu, J. J. Barton, and M. A. Van Hove, "Electron scattering by atomic chains: Multiple-scattering effects," *Phys. Rev. B*, vol. 39, pp. 8275–8283, 12 Apr. 1989. DOI: 10.1103/PhysRevB.39.8275 [Online]. Available: https://link.aps.org/doi/10.1103/PhysRevB.39.8275

[98] T. M. Project, "Materials data on te2pt by materials project," Jul. 2020. DOI: 10.17188/1207707

[99] N. J. Shevchik, "Atomic dipole theory of photoemission from molecules adsorbed on surfaces," *Journal of Physics C: Solid State Physics*, vol. 11, no. 16, p. 3521, Aug. 1978. DOI: 10.1088/0022-3719/11/16/021 [Online]. Available: https://dx.doi.org/10.1088/0022-3719/11/16/021

[100] P. Puschnig et al., "Reconstruction of molecular orbital densities from photoemission data," *Science*, vol. 326, no. 5953, pp. 702–706, 2009. DOI: 10.1126/science.1176105 eprint: https://www.science.org/doi/pdf/10.1126/science.1176105. [Online]. Available: https://www.science.org/doi/abs/10.1126/science.1176105

[101] A. R. Edmonds, *Angular Momentum In Quantum Mechanics*. Princeton University Press, 1957, p. 63.

[102] J. S. Townsend, *A Modern Approach to Quantum Mechanics*. University Science Books, 2^{nd} edition 2012, ch. 14.

[103] A. C. Phillips, *Introduction to Quantum Mechanics*. John Wiley & Sons, Chichester, UK, 2003, ch. 8.

[104] S. Moser, "An experimentalist's guide to the matrix element in angle resolved photoemission," *Journal of Electron Spectroscopy and Related Phenomena*, vol. 214, pp. 29–52, 2017, ISSN: 0368-2048. DOI: https://doi.org/10.1016/j.elspec.2016.11.007 [Online]. Available: https://www.sciencedirect.com/science/article/pii/S0368204816301724

[105] Z.-H. Zhu et al., "Layer-by-layer entangled spin-orbital texture of the topological surface state in Bi_2Se_3," *Phys. Rev. Lett.*, vol. 110, p. 216 401, 21 May 2013. DOI: 10.1103/PhysRevLett.110.216401 [Online]. Available: https://link.aps.org/doi/10.1103/PhysRevLett.110.216401

[106] A. Liebsch, "Theory of angular resolved photoemission from adsorbates," *Phys. Rev. Lett.*, vol. 32, pp. 1203–1206, 21 May 1974. DOI: 10.1103/PhysRevLett.32.1203 [Online]. Available: https://link.aps.org/doi/10.1103/PhysRevLett.32.1203

[107] P. Puschnig et al., "Orbital tomography: Deconvoluting photoemission spectra of organic molecules," *Phys. Rev. B*, vol. 84, p. 235 427, 23 Dec. 2011. DOI: 10.1103/PhysRevB.84.235427 [Online]. Available: https://link.aps.org/doi/10.1103/PhysRevB.84.235427

[108] A. M. Bradshaw and D. P. Woodruff, "Molecular orbital tomography for adsorbed molecules: Is a correct description of the final state really unimportant?" *New Journal of Physics*, vol. 17, no. 1, p. 013 033, Jan. 2015. DOI: 10.1088/1367-2630/17/1/013033 [Online]. Available: https://dx.doi.org/10.1088/1367-2630/17/1/013033

[109] M. Dauth et al., "Perpendicular emission, dichroism, and energy dependence in angle-resolved photoemission: The importance of the final state," *Phys. Rev. Lett.*, vol. 117, p. 183 001, 18 Oct. 2016. DOI: 10.1103/PhysRevLett.117.183001 [Online]. Available: https://link.aps.org/doi/10.1103/PhysRevLett.117.183001

[110] W. D. Grobman, "Angle-resolved photoemission from molecules in the independent-atomic-center approximation," *Phys. Rev. B*, vol. 17, pp. 4573–4585, 12 Jun. 1978. DOI: 10.1103/PhysRevB.17.4573 [Online]. Available: https://link.aps.org/doi/10.1103/PhysRevB.17.4573

[111] S. Hasegawa et al., "Molecular orientation in thin films of bis(1,2,5-thiadiazolo)-p-quinobis(1,3-dithiole) on graphite studied by angle-resolved photoelectron spectroscopy," *Phys. Rev. B*, vol. 48, pp. 2596–2600, 4 Jul. 1993. DOI: 10.1103/PhysRevB.48.2596 [Online]. Available: https://link.aps.org/doi/10.1103/PhysRevB.48.2596

[112] W. Schattke, M. A. Van Hove, F. J. G. de Abajo, R. D. Muiño, and N. Mannella, "Overview of core and valence photoemission," in *Solid-State Photoemission and Related Methods*. John Wiley and Sons, Ltd, 2003, ch. 2, pp. 86–88, 102–104, ISBN: 9783527602506. DOI: https://doi.org/10.1002/9783527602506.ch2 eprint: https://onlinelibrary.wiley.com/doi/pdf/10.1002/9783527602506.ch2. [Online]. Available: https://onlinelibrary.wiley.com/doi/abs/10.1002/9783527602506.ch2

[113] Y. Fujimura and S. Lin, "Multiphoton spectroscopy," in *Encyclopedia of Physical Science and Technology (Third Edition)*, R. A. Meyers, Ed., Third Edition, New York: Academic Press, 2003, pp. 199–229, ISBN: 978-0-12-227410-7. DOI: https://doi.org/10.1016/B0-12-227410-5/00464-6 [Online]. Available: https://www.sciencedirect.com/science/article/pii/B0122274105004646

[114] R. L. Dubs, S. N. Dixit, and V. McKoy, "Circular dichroism in photoelectron angular distributions from adsorbed atoms," *Phys. Rev. B*, vol. 32, pp. 8389–8391, 12 Dec. 1985. DOI: 10.1103/PhysRevB.32.8389 [Online]. Available: https://link.aps.org/doi/10.1103/PhysRevB.32.8389

[115] P. Blaha, *WIEN2k, An Augmented Plane Wave Plus Local Orbitals Program for Calculating Crystal Properties*. 2023.

[116] S. Cottenier, *Density Functional Theory and the Family of (L)APW-methods: a Step-by-step Introduction*. 2nd edition 2002-2013. [Online]. Available: http://www.wien2k.at/reg_user/textbooks

[117] S. Hofmann, "Instrumentation," in *Auger- and X-Ray Photoelectron Spectroscopy in Materials Science: A User-Oriented Guide*. Berlin, Heidelberg: Springer Berlin Heidelberg, 2013, pp. 11–41, ISBN: 978-3-642-27381-0. DOI: 10.1007/978-3-642-27381-0_2 [Online]. Available: https://doi.org/10.1007/978-3-642-27381-0_2

[118] F. GmbH, *EFM Evaporators | FOCUS - Instruments for electron spectroscopy and surface analysis*, May 2024. [Online]. Available: https://www.focus-gmbh.com/efm-evaporators/

[119] G. Schonhense and U. Heinzmann, "A capillary discharge tube for the production of intense vuv resonance radiation," *Journal of Physics E: Scientific Instruments*, vol. 16, no. 1, p. 74, Jan. 1983. DOI: 10.1088/0022-3735/16/1/015 [Online]. Available: https://dx.doi.org/10.1088/0022-3735/16/1/015

[120] M. Budke and M. Donath, "Ar gas discharge lamp with heated lif window: A monochromatized light source for photoemission," *Applied Physics Letters*, vol. 92, no. 23, p. 231 918, Jun. 2008, ISSN: 0003-6951. DOI: 10.1063/1.2945641 eprint: https://pubs.aip.org/aip/apl/article-pdf/doi/10.1063/1.2945641/13139813/231918_1_online.pdf. [Online]. Available: https://doi.org/10.1063/1.2945641

[121] J. Stöhr and H. C. Siegmann, "Exchange, spin–orbit, and zeeman interactions," in *Magnetism: From Fundamentals to Nanoscale Dynamics*, S. S. in Solid-State Sciences, Ed. Springer Berlin Heidelberg, 2006, pp. 175–180. DOI: https://doi.org/10.1007/978-3-540-30283-4

[122] C. J. Foot, "Helium," in *Atomic Physics*. Oxford University Press, 2005, pp. 45–53.

[123] F. GmbH, *His 13-high intensity vuv source. focus-instruments for electron spectroscopy and surface analysis*, Jan. 2025. [Online]. Available: https://www.focus-gmbh.com/his13/?utm_source=chatgpt.com

[124] C. Tusche, Y.-J. Chen, C. M. Schneider, and J. Kirschner, "Imaging properties of hemispherical electrostatic energy analyzers for high resolution momentum microscopy," *Ultramicroscopy*, vol. 206, p. 112 815, 2019, ISSN: 0304-3991. DOI: https://doi.org/10.1016/j.ultramic.2019.112815 [Online]. Available: https://www.sciencedirect.com/science/article/pii/S030439911830439X

[125] S. Suga et al., "High resolution, low $h\nu$ photoelectron spectroscopy with the use of a microwave excited rare gas lamp and ionic crystal filters," *Review of Scientific Instruments*, vol. 81, no. 10, p. 105 111, Oct. 2010, ISSN: 0034-6748. DOI: 10.1063/1.3488367 eprint: https://pubs.aip.org/aip/rsi/article-pdf/doi/10.1063/1.3488367/15978353/105111_1_online.pdf. [Online]. Available: https://doi.org/10.1063/1.3488367

[126] G. Funabashi et al., "Ultrahigh-resolution vacuum ultraviolet light source system for extremely low energy photoelectron spectroscopy," *Japanese Journal of Applied Physics*, vol. 47, no. 4R, p. 2265, Apr. 2008. DOI: 10.1143/JJAP.47.2265 [Online]. Available: https://dx.doi.org/10.1143/JJAP.47.2265

[127] S. Suga and A. Sekiyama, "Instrumentation and methodology," in *Photoelectron Spectroscopy: Bulk and Surface Electronic Structures*, Springer Berlin, Heidelberg, 1^{st} edition 2014, ch. 3, pp. 33–89. DOI: https://doi.org/10.1007/978-3-642-37530-9

[128] M. Escher, N. B. Weber, M. Merkel, L. Plucinski, and C. M. Schneider, "Ferrum: A new highly efficient spin detector for electron spectroscopy," *e-Journal of Surface Science and Nanotechnology*, vol. 9, pp. 340–343, 2011. DOI: 10.1380/ejssnt.2011.340

[129] E. Hecht, *Optics, chapters {8,13}*. Essex, England: Pearson Education Limited, Global Edition 5^{th}e, 2017.

[130] S. J. Orfanidis, *Electromagnetic waves and antennas, chapter 4*. 2016 [Online]. [Online]. Available: https://eceweb1.rutgers.edu/~orfanidi/ewa/

[131] *Create Circularly Polarized Light Using a Quarter-Wave Plate (QWP)*. Thorlabs Insights, YouTube, January 19, 2021. [Online]. Available: https://www.youtube.com/watch?v=P0asuzX4x-Q

[132] *Circular Polarization*. Wikipedia, January 16, 2024. [Online]. Available: https://en.wikipedia.org/wiki/Circular_polarization#cite_ref-IAU_8-1

[133] K. J. Kim, "A synchrotron radiation source with arbitrarily adjustable elliptical polarization," *Nuclear Instruments and Methods in Physics Research*, vol. 219, no. 2, pp. 425–429, 1984, ISSN: 0167-5087. DOI: https://doi.org/10.1016/0167-5087(84)90354-5 [Online]. Available: https://www.sciencedirect.com/science/article/pii/0167508784903545

[134] H. Onuki, "Elliptically polarized synchrotron radiation source with crossed and retarded magnetic fields," *Nuclear Instruments and Methods in Physics Research Section A: Accelerators, Spectrometers, Detectors and Associated Equipment*, vol. 246, no. 1, pp. 94–98, 1986, ISSN: 0168-9002. DOI: https://doi.org/10.1016/0168-9002(86)90053-7 [Online]. Available: https://www.sciencedirect.com/science/article/pii/0168900286900537

[135] S. Yamamoto and H. Kitamura, "Generation of quasi-circularly polarized undulator radiation with higher harmonics," *Japanese Journal of Applied Physics*, vol. 26, no. 10A, p. L1613, Oct. 1987. DOI: 10.1143/JJAP.26.L1613 [Online]. Available: https://dx.doi.org/10.1143/JJAP.26.L1613

[136] S. Sasaki, K. Miyata, and T. Takada, "A new undulator for generating variably polarized radiation," *Japanese Journal of Applied Physics*, vol. 31, no. 12B, p. L1794, Dec. 1992. DOI: 10.1143/JJAP.31.L1794 [Online]. Available: https://dx.doi.org/10.1143/JJAP.31.L1794

[137] Y. Taira, M. Fujimoto, S. Ri, M. Hosaka, and M. Katoh, "Measurement of the phase structure of elliptically polarized undulator radiation," *New Journal of Physics*, vol. 22, no. 9, p. 093 061, Sep. 2020. DOI: 10.1088/1367-2630/abb54a [Online]. Available: https://dx.doi.org/10.1088/1367-2630/abb54a

[138] H. Wang, P. Bencok, P. Steadman, E. Longhi, J. Zhu, and Z. Wang, "Complete polarization analysis of an APPLE II undulator using a soft X-ray polarimeter," *Journal of Synchrotron Radiation*, vol. 19, no. 6, pp. 944–948, Nov. 2012. DOI: 10.1107/S0909049512034851 [Online]. Available: https://doi.org/10.1107/S0909049512034851

[139] C. Schmitz-Antoniak, "X-ray absorption spectroscopy on magnetic nanoscale systems for modern applications," *Reports on Progress in Physics*, vol. 78, no. 6, p. 062 501, Jun. 2015. DOI: 10.1088/0034-4885/78/6/062501 [Online]. Available: https://dx.doi.org/10.1088/0034-4885/78/6/062501

[140] H. Petersen, C. Jung, C. Hellwig, W. B. Peatman, and W. Gudat, "Review of plane grating focusing for soft x-ray monochromators," *Review of Scientific Instruments*, vol. 66, no. 1, pp. 1–14, Jan. 1995, ISSN: 0034-6748. DOI: 10.1063/1.1145258 eprint: https://pubs.aip.org/aip/rsi/article-pdf/66/1/1/19220573/1_1_online.pdf. [Online]. Available: https://doi.org/10.1063/1.1145258

[141] M. Szczepanik-Ciba, T. Sobol, and J. Szade, "Phelix – a new soft x-ray spectroscopy beamline at solaris synchrotron," *Nuclear Instruments and Methods in Physics Research Section B: Beam Interactions with Materials and Atoms*, vol. 492, pp. 49–55, 2021, ISSN: 0168-583X. DOI: https://doi.org/10.1016/j.nimb.2021.01.021 [Online]. Available: https://www.sciencedirect.com/science/article/pii/S0168583X21000598

[142] L. F. Mattheiss, "Band structures of transition-metal-dichalcogenide layer compounds," *Phys. Rev. B*, vol. 8, pp. 3719–3740, 1973.

[143] M. Chhowalla et al., "The chemistry of two-dimensional layered transition metal dichalcogenide nanosheets," *Nature Chemistry*, vol. 5, no. 4, pp. 263–275, 2013.

[144] T. Hahn, *International Tables for Crystallography*. Netherlands: Springer, 2005, vol. 8.

[145] O. J. Clark et al., "A general route to form topologically-protected surface and bulk dirac fermions along high-symmetry lines," *Electronic Structure*, vol. 1, no. 1, p. 014 002, 2019.

[146] S. Mukherjee et al., "Fermi-crossing type-ii dirac fermions and topological surface states in nite2," *Scientific Reports*, vol. 10, no. 1, p. 12 957, 2020.

[147] H. Zhang et al., "Topological insulators in bi2se3, bi2te3 and sb2te3 with a single dirac cone on the surface," *Nature Physics*, vol. 5, no. 6, pp. 438–442, 2009.

[148] J. Yeh and I. Lindau, "Atomic subshell photoionization cross sections and asymmetry parameters: $1 \leq z \leq 103$," *Atomic Data and Nuclear Data Tables*, vol. 32, no. 1, pp. 1–155, 1985, ISSN: 0092-640X. DOI: https://doi.org/10.1016/0092-640X(85)90016-6 [Online]. Available: https://www.sciencedirect.com/science/article/pii/0092640X85900166

[149] S. G. Louie, P. Thiry, R. Pinchaux, Y. Pétroff, D. Chandesris, and J. Lecante, "Periodic oscillations of the frequency-dependent photoelectric cross sections of surface states: Theory and experiment," *Phys. Rev. Lett.*, vol. 44, pp. 549–553, 8 Feb. 1980. DOI: 10.1103/PhysRevLett.44.549 [Online]. Available: https://link.aps.org/doi/10.1103/PhysRevLett.44.549

[150] V. Strocov, "Photoemission response of 2d electron states," *Journal of Electron Spectroscopy and Related Phenomena*, vol. 229, pp. 100–107, 2018, ISSN: 0368-2048. DOI: https://doi.org/10.1016/j.elspec.2018.09.001 [Online]. Available: https://www.sciencedirect.com/science/article/pii/S0368204818300860

[151] G. Landolt et al., "Disentanglement of surface and bulk rashba spin splittings in noncentrosymmetric bitei," *Phys. Rev. Lett.*, vol. 109, p. 116 403, 11 Sep. 2012. DOI: 10.1103/PhysRevLett.109.116403 [Online]. Available: https://link.aps.org/doi/10.1103/PhysRevLett.109.116403

[152] S. Goldberg, C. Fadley, and S. Kono, "Photoelectric cross-sections for fixed-orientation atomic orbitals: Relationship to the plane-wave final state approximation and angle-resolved photoemission," *Solid State Communications*, vol. 28, no. 6, pp. 459–463, 1978, ISSN: 0038-1098. DOI: https://doi.org/10.1016/0038-1098(78)90838-4 [Online]. Available: https://www.sciencedirect.com/science/article/pii/0038109878908384

[153] J. Henk, "Chapter 10 - theory of low-energy electron diffraction and photoelectron spectroscopy from ultra-thin films," in *Handbook of Thin Films*, H. Singh Nalwa, Ed., Burlington: Academic Press, 2002, pp. 479–526, ISBN: 978-0-12-512908-4. DOI: https://doi.org/10.1016/B978-012512908-4/50029-1 [Online]. Available: https://www.sciencedirect.com/science/article/pii/B9780125129084500291

[154] J. Henk, W. Schattke, H. Cartensen, R. Manzke, and M. Skibowski, "Surface-barrier and polarization effects in the photoemission from gaas(110)," *Phys. Rev. B*, vol. 47, pp. 2251–2264, 4 Jan. 1993. DOI: 10.1103/PhysRevB.47.2251 [Online]. Available: https://link.aps.org/doi/10.1103/PhysRevB.47.2251

[155] C. J. R. Sheppard, "Jones and stokes parameters for polarization in three dimensions," *Phys. Rev. A*, vol. 90, p. 023 809, 2 Aug. 2014. DOI: 10.1103/PhysRevA.90.023809 [Online]. Available: https://link.aps.org/doi/10.1103/PhysRevA.90.023809

[156] Gil, J. J., "Polarimetric characterization of light and media - physical quantities involved in polarimetric phenomena," *Eur. Phys. J. Appl. Phys.*, vol. 40, no. 1, pp. 1–47, 2007. DOI: 10.1051/epjap:2007153 [Online]. Available: https://doi.org/10.1051/epjap:2007153

[157] J. J. Gil, "Interpretation of the coherency matrix for three-dimensional polarization states," *Phys. Rev. A*, vol. 90, p. 043 858, 4 Oct. 2014. DOI: 10.1103/PhysRevA.90.043858 [Online]. Available: https://link.aps.org/doi/10.1103/PhysRevA.90.043858

[158] J. Bahrdt, R. Follath, W. Frentrup, A. Gaupp, and M. Scheer, "Compensation of Beam Line Polarizing Effects at UE112 of BESSY II," *AIP Conference Proceedings*, vol. 1234, no. 1, pp. 335–338, Jun. 2010, ISSN: 0094-243X. DOI: 10.1063/1.3463205 eprint: https://pubs.aip.org/aip/acp/article-pdf/1234/1/335/11959486/335_1_online.pdf. [Online]. Available: https://doi.org/10.1063/1.3463205

[159] P. Finetti, D. Holland, C. Latimer, and C. Binns, "Polarisation analysis of vuv synchrotron radiation emitted from a bending magnet source in the energy range 20–50 ev: A comparison between measurements and theoretical predictions," *Nuclear Instruments and Methods in Physics Research Section B: Beam Interactions with Materials and Atoms*, vol. 215, no. 3, pp. 565–576, 2004, ISSN: 0168-583X. DOI: https://doi.org/10.1016/j.nimb.2003.08.034 [Online]. Available: https://www.sciencedirect.com/science/article/pii/S0168583X03019505

[160] N. Zettili, *Quantum Mechanics: Concepts and Applications*, 2nd. Chichester, UK: Wiley, 2009, pp. 593–594.

[161] L. van Dommelen, *Quantum Mechanics for Engineers*. 2012, pp. 358–364, Version 5.55 alpha.

[162] V. N. Strocov et al., "High-energy photoemission final states beyond the free-electron approximation," *Nature Communications*, vol. 14, no. 1, p. 4827, Aug. 2023, ISSN: 2041-1723. DOI: 10.1038/s41467-023-40432-5 [Online]. Available: https://doi.org/10.1038/s41467-023-40432-5

[163] P. Hofmann et al., "Unexpected surface sensitivity at high energies in angle-resolved photoemission," *Phys. Rev. B*, vol. 66, p. 245 422, 24 Dec. 2002. DOI: 10.1103/PhysRevB.66.245422 [Online]. Available: https://link.aps.org/doi/10.1103/PhysRevB.66.245422

[164] F. Herman, C. D. Kuglin, K. F. Cuff, and R. L. Kortum, "Relativistic Corrections to the Band Structure of Tetrahedrally Bonded Semiconductors," *Phys. Rev. Lett.*, vol. 11, no. 0, pp. 541–545, 1963.

[165] X. Zhang, Q. Liu, J.-W. Luo, A. J. Freeman, and A. Zunger, "Hidden spin polarization in inversion-symmetric bulk crystals," *Nat. Phys.*, vol. 10, no. 5, pp. 387–393, 2014.

[166] H. Ebert, D. Ködderitzsch, and J. Minár, "Calculating condensed matter properties using the kkr-green's function method—recent developments and applications," *Reports on Progress in Physics*, vol. 74, no. 9, p. 096 501, Aug. 2011. DOI: 10.1088/0034-4885/74/9/096501 [Online]. Available: https://dx.doi.org/10.1088/0034-4885/74/9/096501

[167] F. Salvat, A. Jablonski, and C. J. Powell, "Elsepa—dirac partial-wave calculation of elastic scattering of electrons and positrons by atoms, positive ions and molecules (new version announcement)," *Computer Physics Communications*, vol. 261, p. 107 704, 2021, ISSN: 0010-4655. DOI: https://doi.org/10.1016/j.cpc.2020.107704 [Online]. Available: https://www.sciencedirect.com/science/article/pii/S0010465520303465

[168] M. Fink and J. Ingram, "Theoretical electron scattering amplitudes and spin polarizations: Electron energies 100 to 1500 ev part ii. be, n, o, al, cl, v, co, cu, as, nb, ag, sn, sb, i, and ta targets," *Atomic Data and Nuclear Data Tables*, vol. 4, pp. 129–207, 1972, ISSN: 0092-640X. DOI: https://doi.org/10.1016/S0092-640X(72)80003-2 [Online]. Available: https://www.sciencedirect.com/science/article/pii/S0092640X72800032

[169] M. Dapor, "Polarized electron beams elastically scattered by atoms as a tool for testing fundamental predictions of quantum mechanics," *Scientific Reports*, vol. 8, no. 1, p. 5370, Mar. 2018, ISSN: 2045-2322. DOI: 10.1038/s41598-018-23660-4 [Online]. Available: https://doi.org/10.1038/s41598-018-23660-4

[170] J. Kessler, *Polarized Electrons*. pringer Berlin, Heidelberg, 1976, ch. Polarization Effects in Electron Scattering from Unpolarized Targets, pp. 21–86. DOI: https://doi.org/10.1007/978-3-662-12721-6

[171] J. KESSLER, "Electron spin polarization by low-energy scattering from unpolarized targets," *Rev. Mod. Phys.*, vol. 41, pp. 3–25, 1 Jan. 1969. DOI: 10.1103/RevModPhys.41.3 [Online]. Available: https://link.aps.org/doi/10.1103/RevModPhys.41.3

[172] M. Fink and A. C. Yates, "Theoretical electron scattering amplitudes and spin polarizations: Selected targets, electron energies 100 to 1500 ev," *Atomic Data and Nuclear Data Tables*, vol. 1, pp. 385–456, 1969, ISSN: 0092-640X. DOI: https://doi.org/10.1016/S0092-640X(69)80029-X [Online]. Available: https://www.sciencedirect.com/science/article/pii/S0092640X6980029X

[173] M. Dapor, "Spin-polarization after scattering," *Physics Open*, vol. 14, p. 100 134, 2023, ISSN: 2666-0326. DOI: https://doi.org/10.1016/j.physo.2022.100134 [Online]. Available: https://www.sciencedirect.com/science/article/pii/S2666032622000357

[174] K. Bartschat and P. G. Burke, "Electron scattering from heavy atoms," in *Coherence in Atomic Collision Physics: For Hans Kleinpoppen on His Sixtieth Birthday*, H. J. Beyer, K. Blum, and R. Hippler, Eds. New York, NY: Springer US, 1988, pp. 1–39, ISBN: 978-1-4757-9745-9. DOI: 10.1007/978-1-4757-9745-9_1 [Online]. Available: https://doi.org/10.1007/978-1-4757-9745-9_1

[175] C. Cheng, J.-T. Sun, X.-R. Chen, and S. Meng, "Hidden spin polarization in the 1t-phase layered transition-metal dichalcogenides mx2 (m=zr, hf; x=s, se, te)," *Science Bulletin*, vol. 63, no. 2, pp. 85–91, 2018, ISSN: 2095-9273. DOI: https://doi.org/10.1016/j.scib.2017.12.003 [Online]. Available: https://www.sciencedirect.com/science/article/pii/S2095927317306229

[176] A. Manchon, H. C. Koo, J. Nitta, S. M. Frolov, and R. A. Duine, "New perspectives for rashba spin–orbit coupling," *Nature Materials*, vol. 14, no. 9, pp. 871–882, Sep. 2015, ISSN: 1476-4660. DOI: 10.1038/nmat4360 [Online]. Available: https://doi.org/10.1038/nmat4360

[177] E. Rashba, "Properties of semiconductors with an extremum loop. i. cyclotron and combinational resonance in a magnetic field perpendicular to the plane of the loop," *2*, p. 1109, 1960. [Online]. Available: https://ci.nii.ac.jp/naid/10018760249

[178] Y. M. Koroteev et al., "Strong spin-orbit splitting on bi surfaces," *Phys. Rev. Lett.*, vol. 93, p. 046 403, 4 Jul. 2004. DOI: 10.1103/PhysRevLett.93.046403 [Online]. Available: https://link.aps.org/doi/10.1103/PhysRevLett.93.046403

[179] A. Kimura et al., "Strong rashba-type spin polarization of the photocurrent from bulk continuum states: Experiment and theory for bi(111)," *Phys. Rev. Lett.*, vol. 105, p. 076 804, 7 Aug. 2010. DOI: 10.1103/PhysRevLett.105.076804 [Online]. Available: https://link.aps.org/doi/10.1103/PhysRevLett.105.076804

[180] A. Varykhalov et al., "Ir(111) surface state with giant rashba splitting persists under graphene in air," *Phys. Rev. Lett.*, vol. 108, p. 066 804, 6 Feb. 2012. DOI: 10.1103/PhysRevLett.108.066804 [Online]. Available: https://link.aps.org/doi/10.1103/PhysRevLett.108.066804

[181] K. Ishizaka et al., "Giant rashba-type spin splitting in bulk bitei," *Nature Materials*, vol. 10, no. 7, pp. 521–526, Jul. 2011, ISSN: 1476-4660. DOI: 10.1038/nmat3051 [Online]. Available: https://doi.org/10.1038/nmat3051

[182] M. S. Bahramy, R. Arita, and N. Nagaosa, "Origin of giant bulk rashba splitting: Application to bitei," *Phys. Rev. B*, vol. 84, p. 041 202, 4 Jul. 2011. DOI: 10.1103/PhysRevB.84.041202 [Online]. Available: https://link.aps.org/doi/10.1103/PhysRevB.84.041202

[183] Q. Liu, Y. Guo, and A. J. Freeman, "Tunable rashba effect in two-dimensional laobis2 films: Ultrathin candidates for spin field effect transistors," *Nano Letters*, vol. 13, no. 11, pp. 5264–5270, Nov. 2013, ISSN: 1530-6984. DOI: 10.1021/nl4027346 [Online]. Available: https://doi.org/10.1021/nl4027346

[184] Q. Liu et al., "Search and design of nonmagnetic centrosymmetric layered crystals with large local spin polarization," *Phys. Rev. B*, vol. 91, p. 235 204, 23 Jun. 2015. DOI: 10.1103/PhysRevB.91.235204 [Online]. Available: https://link.aps.org/doi/10.1103/PhysRevB.91.235204

[185] M. Kepenekian, R. Robles, C. Katan, D. Sapori, L. Pedesseau, and J. Even, "Rashba and dresselhaus effects in hybrid organic–inorganic perovskites: From basics to devices," *ACS Nano*, vol. 9, no. 12, pp. 11 557–11 567, Dec. 2015, ISSN: 1936-0851. DOI: 10.1021/acsnano.5b04409 [Online]. Available: https://doi.org/10.1021/acsnano.5b04409

[186] C. Raub, V. B. Compton, T. H. Geballe, B. T. Matthias, J. P. Maita, and G. W. Hull, "The occurrence of superconductivity in sulfides, selenides, tellurides of pt-group metals," *Journal of Physics and Chemistry of Solids*, vol. 26, no. 12, pp. 2051–2057, Dec. 1965, ISSN: 0022-3697. [Online]. Available: https://www.sciencedirect.com/science/article/pii/0022369765902441

[187] A. Kjekshus and W. B. Pearson, "Constitution and magnetic and electrical properties of palladium tellurides (pdte–pdte2)," *Canadian Journal of Physics*, vol. 43, no. 3, pp. 438–449, 1965. DOI: 10.1139/p65-041 eprint: https://doi.org/10.1139/p65-041. [Online]. Available: https://doi.org/10.1139/p65-041

[188] G. Ryu, "Superconductivity in cu-intercalated cdi2-type pdte2," *Journal of Superconductivity and Novel Magnetism*, vol. 28, no. 11, pp. 3275–3280, Nov. 2015, ISSN: 1557-1947. DOI: 10.1007/s10948-015-3195-2 [Online]. Available: https://doi.org/10.1007/s10948-015-3195-2

[189] Y. Li et al., "Topological origin of the type-ii dirac fermions in $PtSe_2$," *Phys. Rev. Mater.*, vol. 1, p. 074 202, 7 Dec. 2017. DOI: 10.1103/PhysRevMaterials.1.074202 [Online]. Available: https://link.aps.org/doi/10.1103/PhysRevMaterials.1.074202

[190] Y. H. Wang et al., "Observation of a warped helical spin texture in Bi_2Se_3 from circular dichroism angle-resolved photoemission spectroscopy," *Phys. Rev. Lett.*, vol. 107, p. 207 602, 20 Nov. 2011. DOI: 10.1103/PhysRevLett.107.207602 [Online]. Available: https://link.aps.org/doi/10.1103/PhysRevLett.107.207602

[191] J. Sánchez-Barriga et al., "Photoemission of Bi_2Se_3 with circularly polarized light: Probe of spin polarization or means for spin manipulation?" *Phys. Rev. X*, vol. 4, p. 011 046, 1 Mar. 2014. DOI: 10.1103/PhysRevX.4.011046 [Online]. Available: https://link.aps.org/doi/10.1103/PhysRevX.4.011046

[192] W. Shockley, "On the surface states associated with a periodic potential," *Phys. Rev.*, vol. 56, pp. 317–323, 4 Aug. 1939. DOI: 10.1103/PhysRev.56.317 [Online]. Available: https://link.aps.org/doi/10.1103/PhysRev.56.317

[193] J. singleton, *Band Theory and Electronic Properties of Solids*. Oxford University Press, 2^{2d} edition 2001, ch. 4.

[194] M. Roy, "The tight binding method," Rutgers University, Tech. Rep., May 2015.

[195] J. P. Lowe and K. A. Peterson, *Quantum Chemistry*. Elsevier Academic Press, 3^{rd} edition 2006, ch. 7.

[196] E. G. Lewars, *Computational Chemistry*. Springer, 2^{nd} edition 2006, ch. 4.

Band / Volume 106
NeuCoNS and Stacked-Net: Facilitating the Communication for Accelerated Neuroscientific Simulations
R. Kleijnen (2024), xx, 110, xxi-xxxiv pp
ISBN: 978-3-95806-788-2

Band / Volume 107
Construction of a Spiking Network Model of Macaque Primary Visual Cortex: Towards Digital Twins
A. Kurth (2024), xvi, 207 pp
ISBN: 978-3-95806-800-1

Band / Volume 108
Spin selectivity of chiral molecules on surfaces
M.R. Safari (2025), xiv, 165 pp
ISBN: 978-3-95806-810-0

Band / Volume 109
Redox-based Random Access Memory Arrays for Computing-In-Memory and Neuromorphic Computing
H. Chen (2025), x, 154 pp
ISBN: 978-3-95806-814-8

Band / Volume 110
Mechanics of deep neural networks beyond the Gaussian limit
K. Fischer (2025), xvi, 138 pp
ISBN: 978-3-95806-815-5

Band / Volume 111
Characteristics of plastically deformed *fcc* and *bcc* High-Entropy Alloys
T. Meenen (2025), x, 115 pp
ISBN: 978-3-95806-820-9

Band / Volume 112
Software-Configurable Analog-To-Digital Converters for Configurable Pulse Detection
L. Krystofiak (2025), xvii, 113 pp, xxix
ISBN: 978-3-95806-826-1

Band / Volume 113
Development of Superparamagnetic Based Biological Sensor for the Detection of Brucella DNA Using Frequency Mixing Magnetic Detection
A. Abuawad (2025), X, 129 pp
ISBN: 978-3-95806-836-0

Band / Volume 114
A System for the Cryogenic Power Management of Quantum Computing Electronics: Development, Integration, and Test
A. R. Cabrera Galicia (2025), xxv, 110, lviii pp
ISBN: 978-3-95806-844-5

Band / Volume 115
Investigation of 2D Materials using Low Energy Electron Microscopy (LEEM)
H. Yin (2025) viii, 137 pp
ISBN: 978-3-95806-848-3

Band / Volume 116
Topotactic phase transition in $La_{0.6}Sr_{0.4}CoO_{3-\delta}$ thin films: oxygen content, dynamics and reversibility
S. He (2025) ix, 137 pp
ISBN: 978-3-95806-868-1

Band / Volume 117
Electrical anisotropy and shear-resistant topology in the quasi one-dimensional van-der-Waals material α-Bi_4Br_4
J.K. Hofmann (2025) xv, 129 pp
ISBN: 978-3-95806-869-8

Band / Volume 118
Spin-orbital mixing in the topological ladder of the two-dimensional metal $PtTe_2$
M. Qahosh (2025), ix, 170 pp
ISBN: 978-3-95806-872-8

Information
Band / Volume 118
ISBN 978-3-95806-872-8

Mitglied der Helmholtz-Gemeinschaft

JÜLICH
Forschungszentrum